Investigation of the Tumour Vascular Response to Single and Fractionated Irradiation



Jakob Raphael Kaeppler

St Catherine's College

University of Oxford

A thesis submitted to the University of Oxford in partial fulfilment of the requirements for the degree of

Doctor of Philosophy

Trinity 2019

ABSTRACT

Investigation of the Tumour Vascular Response to Single and Fractionated Irradiation

Jakob Raphael Kaeppler, St Catherine's College, Oxford

A thesis submitted to the University of Oxford in partial fulfilment of the requirements for the degree of

Doctor of Philosophy

Trinity 2019

The effect of radiation therapy on tumour vasculature has been a subject of debate over the years. Increased oxygenation and perfusion have been documented during radiation treatments. Conversely, death of irradiated tumour endothelial cells by apoptosis, predicted to impair blood flow, has been proposed as a major determinant of tumour control. To approach these contradictions, we used video 2-photon microscopy to study the vascular response to irradiation in two different murine tumour models: MC38, a highly vascularized model with many non-perfused vessels and B16F10, a moderately vascularized model, both grown in transgenic mice with endothelium marked by the fluorescent protein tdTomato. These tumours received either a single dose of radiation (15 Gy) or a fractionated dose (5 × 3 Gy). Unexpectedly, even these high doses led to little structural change of the perfused vasculature. However, non-perfused vessels and blind ends were substantially impaired after radiation accompanied by apoptosis of their endothelium. These changes did not alter perfusion of the less vascularized B16F10 tumour, but led to increased perfusion in the more vascular MC38 tumour. After irradiation, the proliferation of endothelial cells was blocked resulting in diminished numbers of sprouts. Further, endothelial cells from control and irradiated tumours were subjected to RNA sequencing, which confirmed that irradiation upregulates the expression of genes in apoptotic pathways as well as cell cycle regulation. We now explain how apoptosis of tumour endothelial cells after radiation is not detrimental to function, because the apoptosis occurs primarily in the endothelium of non-functional small or blunt end non-perfused vessels leaving the functional vessels intact

Supervisors

Professor Ruth J Muschel, MD PhD, Professor of molecular Pathology, Department of Oncology, University of Oxford

Bostjan Markelc, PhD, Institute of Oncology Ljubljana, Department of Experimental Oncology

Thesis examiners

Professor Boris Vojnovic, PhD, Professor of Biophysics, Department of Oncology, University of Oxford

Professor Gillian Tozer, PhD, Professor of Tumour Biology, Department of Oncology & Metabolism, The University of Sheffield

ACKNOWLEDGEMENTS

This thesis would not have been possible without all the minds (and hands) I have had the pleasure to meet throughout the last four years, alongside the funding that has been provided by CRUK, EPSRC and MRC to pursue this study.

I am indebted to Ruth Muschel for her valuable guidance and for giving me the freedom to explore this field of cancer research the way I deemed fit. I would also like to thank her for keeping me on track. Without her constant support and astute insights, this work would not have existed.

I am also immensely grateful to Dr Boštjan Markelc for being an excellent supervisor and teaching me many essential techniques throughout this DPhil. He has been an invaluable critic and a steadfast friend during my time at Oxford

I would like to thank Dr Jianzhou Chen, Dr Jenny Vermeer, Dr Serena Lucotti, Dr Pavitra Kannan and Dr Yunhong Chao for their help in the laboratory, many fruitful discussions outside the laboratory, and for making my time here truly one to remember, for years to come!

My sincere gratitude goes out to all the collaborators from the RRI, the Department of Oncology, from the IBME and the Institute of Mathematics, for their help. I am proud of the phenomenal work we have been able to accomplish together.

I would also like to thank my fellow graduate students - Angela, Manon, Niloufar, and Egon for their friendship.

I have also been very fortunate to get to know four people from my college, who have always been there for me and have given me the chance to learn many things, things that go far beyond cancer research. Thank you, Priyanka Bawa, Supratik Paul, Dr Stephen Pates and Ikuya Aizawa for giving me memories worth cherishing.

I would be falling short if I failed to extend an immense thanks to my parents, Rosemarie and Klaus, for their continuous support over the last few years, despite being geographically apart.

CONTRIBUTION OF THE WORK PRESENTED

Figure 2.3: *In vivo* experiment performed by Jakob Kaeppler. Cell staining and flow cytometry analysis of tumour endothelial cells performed by Dr Mario Buono and Jakob Kaeppler.

Figure 3.1D: The Breeding strategy was set up with expert help from the biomedical services of the University of Oxford. Flow Cytometry gating of tumour endothelial cells from VEOM mice was performed with the help of Dr Mario Buono and Dr Bostjan Markelc

Figures 5.7-5.9: Dr Mario Buono, Dr Bostjan Markelc and Jakob Kaeppler performed Experiments. Dr Wei Chen Cheng performed RNAseq Data processing. Jakob Kaeppler performed the evaluation of differentially expressed genes with the advice of Dr Bostjan Markelc.

SCIENTIFIC CONTRIBUTIONS

Kannan P, Kretzschmar WW, Winter H, Warren D, Bates R, Allen PD, Syed N, Irving B, Papiez BW, **Kaeppler J**, Markelc B, Kinchesh P, Gilchrist S, Smart S, Schnabel JA, Maughan T, Harris AL, Muschel RJ, Partridge M, Sharma RA, Kersemans V. Functional Parameters Derived from Magnetic Resonance Imaging Reflect Vascular Morphology in Preclinical Tumors and in Human Liver Metastases. *Clin Cancer Res. 2018 Oct 1;24(19):4694-4704. doi: 10.1158/1078-0432.CCR-18-0033*

Chen J, Markelc B, **Kaeppler J**, Ogundipe VML, Cao Y, McKenna WG, Muschel RJ. STING-Dependent Interferon-λ1 Induction in HT29 Cells, a Human Colorectal Cancer Cell Line, After Gamma-Radiation. *Int J Radiat Oncol Biol Phys. 2018 May 1;101(1):97-106. doi: 10.1016/j.ijrobp.2018.01.091. [Epub 2018 Feb 3.]*

Bates R, Irving B, Markelc B, **Kaeppler J**, Brown G, Muschel RJ, Brady SM, Grau V, Schnabel JA. Segmentation of Vasculature from Fluorescently Labeled Endothelial Cells in Multi-Photon Microscopy Images. *IEEE Trans Med Imaging. 2019 Jan;38(1):1-10. doi: 10.1109/TMI.2017.2725639. [Epub 2017 Aug 9.]*

Chen J, Cao Y, Markelc B, **Kaeppler J**, Vermeer JA, Muschel RJ. Type I IFN protects cancer cells from CD8+ T cell-mediated cytotoxicity after radiation. *J Clin Invest. 2019 Sep 4. pii: 127458. doi: 10.1172/JCI127458. [Epub ahead of print]*

Russell Bates, Benjamin Irving, Bostjan Markelc, **Jakob Kaeppler**, Ruth Muschel, Vicente Grau, Julia A. Schnabel Extracting 3D Vascular Structures from Microscopy Images using Convolutional Recurrent Networks. *arXiv:1705.09597*

Radiation resistant cancer cells enhance the survival and resistance of sensitive cells in prostate spheroids Pavitra Kannan, Marcin Paczkowski, Ana Miar, Joshua Owen, Warren W. Kretzschmar, Serena Lucotti, **Jakob Kaeppler**, Jianzhou Chen, Bostjan Markelc, Leoni A. Kunz-Schughart, Adrian L. Harris, Mike Partridge, Helen Byrne doi: https://doi.org/10.1101/564724

Abnormal morphology biases haematocrit distribution in tumour vasculature and contributes to heterogeneity in tissue oxygenation Miguel O. Bernabeu, Jakub Köry, James A. Grogan, Bostjan Markelc, Albert Beardo, Mayeul d'Avezac, **Jakob Kaeppler**, Nicholas Daly, James Hetherington, Timm Krüger, Philip K. Maini, Joe M. Pitt-Francis, Ruth J. Muschel, Tomás Alarcón, Helen M. Byrne doi: https://doi.org/10.1101/640060

TABLE OF CONTENTS

ACKNOWLEDGEMENTS ..... **I**
CONTRIBUTION OF THE WORK PRESENTED ..... **II**
SCIENTIFIC CONTRIBUTIONS ..... **III**
TABLE OF CONTENTS ..... **IV**
LIST OF ABBREVIATIONS ..... **VII**
LIST OF FIGURES ..... **IX**
LIST OF TABLES ..... **XI**
SUPPLEMENTARY FIGURES AND TABLES ..... **XII**
CHAPTER I INTRODUCTION **1**
1.1 Introduction 2
1.1 Radiotherapy 2
1.2 angiogenesis in normal and pathological settings 5
1.2.1 Molecular mechanism of angiogenesis 7
1.2.2 Development of tumour vasculature 9
1.2.3 Basement membrane in tumour vessels 10
1.2.4 Role of pericytes in tumour vessels 10
1.2.5 Stromal cells in tumour angiogenesis 11
1.2.6 Blood flow in tumour vessels 12
1.2.7 Alternative types of vessel formation in experimental tumours 13
1.3 Effect and response of the tumour vasculature to therapies 16
1.3.1 Antiangiogenic treatments 16
1.3.2 Effect of radiotherapy on tumour blood vessels 17
1.3.3 Endothelial cell apoptosis after irradiation 20
1.3.4 Radiation-induced senescence in endothelial cells 22
1.4 Summary 25
1.5 Aim of the thesis 26
CHAPTER 2 MATERIAL AND METHODS **27**
2.1 Cell lines 28
2.2 In Vivo Assays 29
2.2.1 Animals 29
2.2.2 Tamoxifen treatment 31
2.2.3 Subcutaneous tumour model 32
2.2.4 In vivo radiation treatment 32
2.2.5 In vivo radiation treatment of tumours in abdominal window chambers 34

2.2.6 Tumour drug treatment 37
2.2.7 Tumour allograft model and abdominal window chamber imaging 37
2.2.8 Tissue labelling with injectable agents 39
2.3.1 Flow cytometry profiling of tumour endothelial cells 39
2.3.2 Immunofluorescence staining of mouse tumour and organ sections 42
2.3.4 RNA sequencing: Tumour stromal cell preparation 44
2.3.5 RNA sequencing: Flow cytometry of tumour endothelial 44
2.3.6 RNA sequencing: cDNA libraries using Smart-seq2 protocol 46
2.3.7 RNA sequencing: Illumina library preparation and sequencing 46
2.4 Microscopy 48
2.4.1 In vivo 2-photon microscopy 48
2.4.2 Confocal microscopy 49
2.4.3 Image post-processing 49
2.4.4 Segmentation, skeletonization, and quantification microscopy derived images 50
2.5 Statistical analysis 54
CHAPTER 3 *IN VIVO* IMAGING OF THE TUMOUR VASCULATURE 55
3.1 Introduction 56
3.2 Aims 59
3.3 Results 60
3.3.1 Validation of the Cdh5-cre-ERT2 model 60
3.3.2 Intravital imaging of the tumour vasculature in the MC38 tumour model 67
3.3.3 Intravital imaging of the tumour vasculature in the B16F10 tumour model 76
3.4 Discussion 81
3.4.1 Established mouse model 81
3.4.2 Intravital imaging of the developing tumour vasculature 82
3.4.3 Types of angiogenesis 84
3.4.4 Quantifying vascular parameters 85
3.4.5 Conclusion 88
CHAPTER 4 TUMOUR VASCULAR RESPONSE TO SINGLE AND FRACTIONATED IRRADIATION *IN VIVO* 89
4.1 Introduction 90
4.2 AIMS 94
4.3 RESULTS 95
4.3.1 Tumour growth response to single and fractionated irradiation 95
4.3.2 Structural and functional changes of the tumour vasculature after irradiation in MC38 tumours 96
4.3.3 Comparison of vessel parameters between single-dose and anti-angiogenic treatment 107

4.3.4 Structural and functional changes of the tumour vasculature after irradiation in B16F10 tumours 109
4.3.5 Characterisation of vessels and hypoxia in MC38 and B16F10 tumours 115
4.4 DISCUSSION 119
4.4.1 Irradiation has limited effect on tumour vascular structure and function 119
4.4.2 CONCLUSION 124
CHAPTER 5 TUMOUR ENDOTHELIAL CELL RESPONSE TO SINGLE AND FRACTIONATED IRRADIATION 126
5.1 Introduction 127
5.1.1 Tumour endothelial cell proliferation 127
5.1.2 Radiation-induced apoptosis 128
5.1.3 Radiation-induced inflammation 130
5.2 AIMS 131
5.3 RESULTS 132
5.3.1 Endothelial cell proliferation decreases after irradiation 132
5.3.2 Radiation-induced apoptosis in tumour vessels 141
5.3.3 Tumour endothelial cell gene expression confirms cell cycle arrest and apoptosis 147
5.4 DISCUSSION 155
5.4.1 Tumour endothelial cell proliferation is inhibited after irradiation 155
5.4.2 Tumour vessel apoptosis after irradiation 157
5.4.3 Total RNA sequencing after 15 Gy irradiation in MC38 tumour endothelial cells 159
5.4.4 Conclusion 161
CHAPTER 6 CONCLUDING REMARKS 163
6.1 Conclusion 164
6.2 Potential clinical relevance 165
6.3 Limitations of our research and future perspective 166
REFERENCES 170
APPENDIX SUPPLEMENTARY FIGURES AND TABLES 202

LIST OF ABBREVIATIONS

7-AAD	(7-amino-actinomycin D)
ATM	ataxia telangiectasia-mutated
BSA	Bovine serum albumin
BV	Brilliant violet
CD	Cluster of differentiation
CDH5	Cadherin 5/VE-Cadherin
Cre	Causes recombination
CO2	Carbon dioxide
DAPI	4',6-diamidino-2-phenylindole
DC101	Neutralising anti-VEGFR-2 antibody
DLL4	Delta-like ligand 4
DMEM	Dulbecco's Modified Eagle Medium
DNA	Deoxyribonucleic acid
EF5	(2-(2-Nitro-1H-imidazol-1-yl)-N-(2,2,3,3,3-pentafluoropropyl) acetamide)
FBS	Foetal bovine serum
FCC	Forward scatter
EdU	5-Ethynyl-2´-deoxyuridine
FGF	Fibroblast growth factor
FPKM	Fragments per Kilobase of transcript per million mapped reads
GaAsP	Gallium Arsenide Phosphide
GEMM	Genetically engineered mouse model
EGFP	Green fluorescent protein
Gy	Gray
HBSS	Hank's Balanced Salt Solution

HIF	Hypoxia inducible factor
IgG	Immunoglobulin G
IGRT	Image-guided radiotherapy
LoxP	locus of X(cross)-over in P1
NA	Numerical aperture
O2	Dioxygen
PBS	Phosphate-buffered saline
PCR	Polymerase chain reaction
PDGF	Platelet derived growth factor
PDGFR	Platelet derived growth factor receptor
PFA	Paraformaldehyde
Qdot 705	Quantum dot tracker vascular marker 705
RNA	Ribonucleic acid
ROTO	B6.Cg-Gt(ROSA)26Sortm9(CAG-tdTomato)Hze/J mice
RPMI	Roswell Park Memorial Institute Growth Medium
SARRP	Small Animal Radiation Research Platform
SBRT	Stereotactic body radiotherapy
SD	Standard deviation
SDF-1	Stromal cell-derived factor-1
SEM	Standard error of the mean
SSC	Side scatter
TdTomato	tandem dimer (td) Tomato, red fluorescent protein
TGF-β	Transforming growth factor-β
TNF	Tumour necrosis factor
VCAD	C57BL/6-Tg(Cdh5-cre/ERT2)1Rha transgenic mice
VEGF	Vascular endothelial growth factor
VEGFR	Vascular endothelial growth factor receptor
VEOM	C57BL/6-Tg(Cdh5-cre/ERT2)1Rha-Gt(ROSA)26Sortm9(CAG-tdTomato)Hze/J mice
X-ray	X-radiation

LIST OF FIGURES

CHAPTER 2

- **Figure 2.1 sketch of the breeding strategy of ROTO and VCAD mice.**
- **Figure 2.2 Workflow of subcutaneous tumour experiments.**
- **Figure 2.3 Gulmay tray for subcutaneous tumour radiation.**
- **Figure 2.4 Visualisation of the dose delivered to the tumour growing in a window chamber.**
- **Figure 2.5 workflow of EdU or EF5 experiments.**
- **Figure 2.6 Flow cytometry gating strategy for tumour endothelial cells.**
- **Figure 2.7 Fluorescence-activated cell sorting gating strategy for tumour endothelial cells for RNA sequencing.**

CHAPTER 3

- **Figure 3.1.1 Expression of tdTomato in endothelial cells of VEOM mice after Tamoxifen administration.**
- **Figure 3.1.2 Expression of tdTomato in endothelial cells of VEOM mice after Tamoxifen administration.**
- **Figure 3.1.3 Evaluation of tdTomato labelling in endothelial cells after Tamoxifen induction in mouse organs.**
- **Figure 3.1.4 Immunofluorescence evaluation of tdTomato expression in tumour endothelial cells after irradiation in MC38 and B16F10 tumours.**
- **Figure 3.1.5 *In-vivo* two-photon microscopic image of a GFP MC38 tumour in a VEOM mouse.**
- **Figure 3.2.1 Time-lapse intravital microscopy of MC38 tumours in VEOM mice.**
- **Figure 3.2.2 Segmentation of the acquired intravital images.**
- **Figure 3.2.3. Quantification of time-lapse intravital microscopy images of MC38 tumours in VEOM mice.**
- **Figure 3.2.4 MC38 tumour vascular parameters.**
- **Figure 3.2.5 MC38 tumour vascular parameters.**
- **Figure 3.3.1 Time-lapse intravital microscopy of a B16F10 tumour in VEOM mice.**
- **3.3.2 Quantification of time-lapse intravital microscopy images of B16F10 tumour in VEOM mice.**
- **Figure 3.3.3 B16F10 tumour vascular parameters.**

CHAPTER 4

- **Figure 4.1 Tumour growth and response to irradiation.**
- **Figure 4.2.1 Time-lapse intravital microscopy of MC38 tumours in VEOM mice after ionizing irradiation.**
- **Figure 4.2.2 Time-lapse intravital microscopy of B16F10 tumours in VEOM mice after ionizing irradiation.**
- **Figure 4.3.1 Time-lapse intravital microscopy of MC38 tumours in VEOM mice after irradiation.**
- **Figure 4.3.2 Time-lapse intravital microscopy of MC38 tumours in VEOM mice after irradiation.**
- **Figure 4.4 Time-lapse intravital microscopy of MC38 tumours in VEOM mice after irradiation.**
- **Figure 4.5 Time-lapse intravital microscopy of MC38 tumours in VEOM mice after DC101 antibody treatment.**
- **Figure 4.6.1 Time-lapse intravital microscopy of a B16F10 tumour in VEOM mice after irradiation.**
- **Figure 4.6.2 Time-lapse intravital microscopy of a B16F10 tumour in VEOM mice after irradiation.**
- **Figure 4.7 Time-lapse intravital microscopy of B16F10 tumours in VEOM mice after 15 Gy irradiation.**
- **Figure 4.8.1 Tumour hypoxia in MC38 and B16F10 tumours.**
- **Figure 4.8.2 Tumour vessel coverage by mural cells in MC38 and B16F10 tumours.**

CHAPTER 5

- **Figure 5.1.1 Proliferation of cells in MC38 tumours after single and fractionated irradiation.**
- **Figure 5.1.2 Quantification of the proliferation of total and tumour endothelial cells in MC38 tumours after single and fractionated irradiation.**
- **Figure 5.2 Flow cytometry analysis of tumour endothelial cell apoptosis and proliferation after single and fractionated IR.**
- **Figure 5.3.1 Proliferation of cells in B16F10 tumours after single and fractionated irradiation.**
- **Figure 5.3.2 Proliferation of cells in B16F10 tumours after single and fractionated irradiation**
- **Figure 5.4 Flow cytometry analysis of apoptosis in MC38 tumour and tumour endothelial cells after irradiation.**
- **Figure 5.5 Tumour endothelial cell apoptosis after single and fractionated irradiation.**
- **Figure 5.6 Tumour vessels apoptosis after 15 Gy single-dose irradiation in thick tumour sections.**
- **Figure 5.7 Differential expression analysis of tumour endothelial cells after 15 Gy single-dose irradiation.**
- **Figure 5.8 MetaCore pathway analysis of tumour endothelial cells 48 hours after 15 Gy irradiation.**
- **Figure 5.9 Panther pathway analysis of tumour endothelial cells 48 hours after 15 Gy irradiation.**
- **Figure 5.10 Panther pathway analysis of tumour endothelial cells 48 hours after 15 Gy irradiation.**

LIST OF TABLES

CHAPTER 2

- Table 2.1 Antibodies for Flow cytometry analysis of tumour endothelial cells.
- Table 2.2 Antibodies for immunofluorescence analysis of tumour sections.
- Table 2.3 Antibodies for Fluorescence-Activated Cell Sorting analysis of tumour endothelial cells.

SUPPLEMENTARY FIGURES AND TABLES

- Figure S2 Filter and filter set arrangement of the two-photon microscope
- Table S2.1.1 Nuclei algorithm
- Table S2.1.1 EdU algorithm
- Table S2.1.3 CD31 algorithm
- Table S2.1.4 ERG algorithm
- Table S2.1.5 EC nuclei algorithm
- Table S2.2.1 EF5 algorithm
- Table S2.3.1 Vessel algorithm
- Table S23.2 NG2 algorithm
- Table S2.4.1 small vessel algorithm
- Table S2.4.2 medium vessel algorithm
- Table S2.4.3 large vessel algorithm
- Table S2.4.4 cleaved caspase 3/7 on vessels algorithm
- Table S2.5.1 vessel algorithm
- Table S2.5.2 filament vessel tracer algorithm
- Figure S4.1 Tumour growth and response to irradiation.
- Figure S4.2 Quantified parameters from intravital imaging and DCE-MRI imaging of MC38 tumours.
- Figure S4.3A Time-lapse intravital microscopy of a B16F10 tumour in VEOM mice after irradiation.
- Table S5.1 Differential gene expression of ceramide associated genes
- Table S5.2 Differential gene expression of damage-associated molecular pattern

CHAPTER I

Introduction

1.1 INTRODUCTION

The hallmarks of cancer have been first described by Hanahan and Weinberg in their seminal papers as the six functional capabilities of a tumour acquired through its development (1, 2). This acquisition need not necessarily be through the same mechanistic strategies. The hallmarks encompass:

- sustaining proliferative signalling
- evading growth suppressors
- resisting cell death
- enabling replicative immortality
- induction of angiogenesis
- activating invasion and metastasis

This study specifically focuses on tumour angiogenesis and the effect and consequences of radiotherapy on the structure and functionality of the tumour vasculature.

1.1 Radiotherapy

Radiotherapy plays a central role in the treatment of cancer, with around 50% of cancer patients receiving some form of radiation during their course of cancer treatment (3). Although some tumours respond exceptionally well, tumour recurrence remains a major problem. Radiation not only damage the cancer cells but also the tumour microenvironment, which consists of immune cells, stromal cells and tumour blood vessels. Furthermore, the surrounding normal tissue, in the path of the radiation beam, is also damaged. However, with radiotherapy being a localised treatment, the aim is to reduce the delivered dose to the normal tissue surrounding the tumour and in the field of the radiation beam, due to toxic side effects of

radiation to normal tissue and cells. This is achieved by distributing the total dose of radiation over time, which led to the concept of fractionated irradiation. Fractionated irradiation consists of smaller daily doses of radiation with many sessions over several weeks and has been standard practice of care, due to reduced radiation-induced late effects and normal tissue toxicity (4).

Recent technical advances in radiotherapy, such as stereotactic body radiotherapy (SBRT) and stereotactic radiosurgery (SRS), use few or singular high doses of radiation and have shown remarkable results in certain cancer types (5–11). Due to significant technical improvements such as three-dimensional conformal radiotherapy (3DCRT), intensity-modulated radiotherapy (IMRT) and imaging-guided radiotherapy (IGRT) (12, 13), larger radiation doses can now be delivered more precisely to the tumour. These improvements limit exposure of a particular volume of normal tissue by introducing multiple beams from different directions (3, 14), thus minimising late and normal tissue toxicity effects to a particular normal tissue volume. While the body receives the same amount of radiation, it is distributed over a larger volume, resulting in a potentially lower dose of radiation to one area or cell. Although these technological advances in radiotherapy have been introduced and combined with other treatments such as chemotherapy, the local recurrence of tumours and treatment failure continues to remain high (15).

The tumour response to irradiation has been explained with the 5 Rs of radiobiology (16):

- Repair of sub-lethal cellular damage, influencing the biological effect of dose rate and time between fractions
- Repopulation of cells following radiation, decreasing the effect of radiation over long treatment time frames
- Redistribution of cells in the different cell cycle stages

- Radiosensitivity as an intrinsic factor of tumour cells determining their sensitivity to radiation
- Reoxygenation of the surviving tumour cells that are under hypoxia (16–18)

Over the last few decades, it has become clear that biological factors, within the tumour microenvironment, critically contribute to treatment outcomes and disease progression (19). One important component of the tumour microenvironment is the tumour vasculature. The tumour vasculature not only provides metabolites to the tumour, such as oxygen and nutrients, but can also be the gateway for stromal cells, in particular immune cells. With the advent of immunotherapies exploiting the immune checkpoints, for example, PD-1/PD-L1, the importance of immune cells in the response of the tumour to therapy has grown in recent years (20–23), potentially also leading to questions regarding tumour blood vessels as interacting cells. In the context of cancer treatment, the response of tumour vasculature to irradiation has been investigated over the last decades (24, 25). However, we still have a limited understanding of how repeated low doses, such as in conventionally fractionated radiotherapy and hypofractionated radiotherapy, and single high doses of irradiation affect the tumour vasculature. While there seems to be dose-dependent response in damage response to irradiation (26), there is an ongoing discussion about the contribution of tumour vasculature to treatment outcomes. The early effect of endothelial cells damage (27–29) and general blood vessels structure and function are not adequately understood. Hence a better understanding of the *in vivo* response of tumour blood vessels is much needed.

1.2 ANGIOGENESIS IN NORMAL AND PATHOLOGICAL SETTINGS

Blood vessels are essential structures for blood flow, tissue oxygenation and transportation of molecules and cells. The structure of blood vessels is highly hierarchical and displays an organ-specific arrangement to meet their particular needs (30). The structure differs depending on the size of the vessel, and whether it is an artery, a vein or a capillary. For example, large arteries have thick walls called tunica that consist of different cells, like smooth muscle cells and elastic fibres. In contrast, small capillaries often consist of only a layer of single cells and a basement membrane (31) with some more fenestrated and others more smooth. However, blood vessels are all built from endothelial cells that form the tubular structure by interconnecting with each other to form the inner lining that is in direct contact with blood. In the developmental stage, the first endothelial cells arise from vasculogenesis: the process by which endothelial cells develop from precursor cells (32). The subsequent development of blood vessels, which happens during embryonic development, cancer, inflammation and wound healing or as per metabolic demand, is facilitated mostly through angiogenesis: the creation of new blood vessels through the proliferation of endothelial cells from pre-existing endothelial cells (33).

Throughout the last century from as early as 1908, Goldman (34) and later Ide *et al.* (35) investigated the growth or neo-angiogenesis of the vasculature within the tumour mass, as observed through a transparent ear chamber in rabbits. Later Algire and colleagues showed that tumour actively attracted vasculature from surrounding tissue (36, 37). It was then first suggested by Folkman that neo-vascularisation is probably stimulated by tumour cells and vice versa, and that endothelial cells and blood vessels have effects on tumour growth (38).

In 1971 Folkman proposed that inhibiting of the growth of blood vessels, resulting in a lack of metabolites delivered to the tumour, could prevent tumour growth (38). Later, he and his co-workers also confirmed that a soluble factor acts as a mitogen and has capabilities to

induce the formation of capillary blood vessels and that its inhibition might block tumour growth (39). Soon after, they showed that indeed when tumours grew in the anterior chamber of the eye (where neo-vascularisation appears impossible) tumour implants did not grow larger than 1 – 2 mm^3 in size (40). These nodules often displayed a viable rim and a necrotic core. However, if these small nodules were transplanted into an area where normal vasculature from the underlying bed would be close enough to those same nodules, they would eventually grow exponentially. This was a piece of strong evidence to establish that tumour growth above 1 – 2 mm^3 is undoubtedly dependent on angiogenesis (41). Angiogenesis in these nodules was described initially to resemble stages of pre-vasculature hyperplasia, later evolving to a well-vascularised tumour. Indeed, recently angiogenesis was strongly associated with the onset of hyperplasia in human ductal breast carcinoma (42).

This observation led to the search for angiogenic factors. The first factor to be discovered that was capable of inducing angiogenesis was basic fibroblast growth factor (bFGF) (43–45). Soon after, interferon α was identified as the first anti-angiogenic factor, (46). Since then, many pro- and anti-angiogenic factors have been discovered, with molecules of the vascular endothelial growth factor (VEGF) family being regarded as master regulators (31). It has been suggested that tumours undergo an angiogenic switch through the expression of pro-angiogenic factors by tumour or stromal cells (47). Their expression or release of growth factors induces the normally quiescent vasculature to become activated and through neo-angiogenesis, a vasculature network within the growing tumour mass gets developed.

The angiogenic switch takes place when the natural equilibrium of pro- and anti-angiogenic factors in the microenvironment is destabilised (42, 48). To tip the balance, and favour angiogenesis, either suppression of anti-angiogenic factors or over-expression or release of extracellular matrix-bound pro-angiogenic factors must occur (49). This can be driven, for example, by hypoxia due to lack of oxygen or mutations in tumour cells (49). As a result, tumour

and other cells in the tumour microenvironment produce growth factors (50, 51). While tumour cells contribute to the angiogenic switch and are dependent on it, the microenvironment and its cells play an equally important role in the expression and release of pro-angiogenic factors. Over the last decade, it has been shown in numerous tumour models and patient samples that tumour-associated stromal cells and the extracellular matrix can induce and sustain angiogenesis. The key players contributing critically in initial and recurrence phases are thought to be macrophages and neutrophils (51–58).

1.2.1 Molecular mechanism of angiogenesis

Angiogenesis can be initiated by hypoxia and is governed by a non-trivial process of pro and anti-angiogenic factors. These are released to and from the microenvironment, through the production of growth factors from cells experiencing hypoxia or cleavage of extracellular matrix-bound growth factors (49). The release of pro-angiogenic factors such as vasculature endothelial growth factor-A (VEGF-A) generates a concentration gradient, stimulating endothelial cells embedded in pre-existing vessels in a paracrine fashion (59, 60). Through the interaction of the VEGF-A ligand to its tyrosine kinase receptor and vascular endothelial cell receptor (VEGFR), several downstream signalling pathways in endothelial cells become activated (61–63). As a result, an endothelial cell from the pre-existing vessel becomes a guiding endothelial tip cell with long and numerous dynamic filopodia protrusions initiating the growth of a new vessel (64). This tip endothelial cell leads the direction of growth of the newly forming tube (64). Upon stimulation, matrix metalloproteinases are released from endothelial cells, leading to proteolytic degradation of the extracellular matrix (65, 66).

The pivotal signalling pathway that is crucial for communication and morphogenesis within endothelial cells is the Notch-delta pathway (67). While this pathway has many functions

in general development and disease, in endothelial cells, the delta-notch signalling controls several aspects of endothelial cell specification and phenotype (68). Likewise, if a mutation occurs in these pathways, it has strong phenotypic effects on the development, maintenance and function of blood vessels (69). As VEGF-A binds to its receptor VEGFR-2 on tip cells, an intracellular signalling cascade becomes activated, leading to the expression of several proteins, such as delta-like ligand 4 (Dll-4), a ligand to the notch receptor. Delta-like ligand 4 (Dll4) expressed in tip cell binds to the notch receptor of neighbouring endothelial cells (70) and through lateral inhibition, induces a stalk cell phenotype in the neighbouring cells (71, 72). The stalk endothelial cell phenotype displays lower expression of VEGFR2 receptors on the cell surface and increased decoy receptors (VEGFR-1) expression. Thus, the stalk cells are less responsive to VEGF-A from the microenvironment (73, 74). This mechanism leads to a situation whereby it is thought that there is only one tip cell at a time in a vascular sprout (75). Stalk cells follow the tip cell and are thought to be the main proliferating cells that also elongate and form the lumen. They accomplish this through inverse membrane blebbing (76) or other mechanisms that are not yet fully understood (77).

In the process of connecting the blood vessels, the endothelial cells also interact with other cells at specific stages. For example, macrophages facilitate connection of two growing tip cells for the fusion/formation of a new vessel (78). Further, mural cells stabilise and reduce proliferation in endothelial cells and facilitate cell junctions (79). Shear stress, resulting from blood flow through vessels, further contributes to the remodelling of the vascular structure (80, 81). This finally leads to a hierarchically developed normal vascular network allowing for adequate distribution of oxygen and nutrients by diffusion (82).

On a molecular level, this is influenced and guided by growth-factor families, such as VEGFs, PDGFs, angiopoietins and tumour necrosis factor beta (TGF-β) (83–85). As a result, the developed vasculature becomes stable and the rearrangement of vessels, as well as pruning or

apoptosis of developing vessel sprouts, takes place. While the Delta-Notch axis is a crucial player, there are many other receptors, co-receptors, and signalling pathways, such as the WNT pathway, involved in the process of angiogenesis and maintenance of the vasculature (86, 87). Recently, different types of Ribonucleic acids (RNAs) have also been discovered, adding another layer of complexity to the development of blood vessels (74).

1.2.2 Development of tumour vasculature

Compared to normal vasculature, the tumour vasculature contains abnormalities on a blood vessel, endothelial cell, and molecular level (88–94). The well-distributed and hierarchically developed vasculature in a normal organ setting, with defined distances between vessels to allow for adequate distribution of metabolites, nutrients and oxygen, is not present within a tumour. The microvasculature of tumours does not resemble defined specifications compared to normal vasculature, and hypo- as well as hyper- vascularised areas are present (8). The hierarchy of blood vessels from larger to smaller, such as arteries, arterioles, capillaries, venules and veins, is missing (95). Although, this hierarchy of blood vessels does not exist in tumours, Dvorak described several different types of vessels based on morphology in tumours, mostly distinguishing between larger and smaller vessels that also have been reported to respond differently to treatment (95). For example, it has been shown that anti-angiogenic treatment in cancer can lead to differing results due to the expression of different VEGF isoforms (96, 97) when vessels express a more mature phenotype (98, 99).

Tumour vessels are irregular in shape with dilations, constrictions, and connections between tumour endothelial cells displaying a defective endothelial monolayer. While endothelial cell in normal vessels display tight junctions between each other, in a tumour, gaps between endothelial cells are common, fostering haemorrhage. While in a normal vasculature,

the proliferation and quiescence of endothelial cells are tightly regulated, in angiogenic tumours, endothelial cells remain in a proliferative state and form abnormal sprouts due to the constant release of growth factors (100). Although, the proliferation of tumour endothelial cells continues, at a similar rate as in the placenta (101, 102), tumour cells divide at an even higher rate (103) leading to a situation where the tumour vascular system is often unable to keep pace with the growing tumour cells, thus leading to hypoxia and areas of necrosis.

Not only does the tumour vasculature differ compared to normal vasculature but also there are considerable variations depending on tumour type and stage, such as in primary versus metastatic tumours. In addition, the anatomic site and the composition of stromal cells contribute to tumour vessel architecture, probably through a spatiotemporal expression of the aforementioned pro-angiogenic and anti-angiogenic factors (42, 89, 104–107).

1.2.3 Basement membrane in tumour vessels

The chaotic nature of tumour vessels, however, reaches beyond the endothelial cell level, while it has been shown that tumour vessels display a nearly total basement membrane coverage that consists of proteins and proteoglycans such as laminin, fibronectin, heparan sulphate proteoglycan and type IV collagen. It has been demonstrated that it is only loosely associated with irregular thickness depending on the tumour type (90, 92).

1.2.4 Role of pericytes in tumour vessels

Pericytes are regarded as part of mural cells, usually wrapped tightly around endothelial cells, covering the abluminal side of blood vessels and standing in close interaction with

endothelial cells. They have been described as crucial mediators in endothelial cell proliferation, stabilisation and maturation of blood vessels (108–110) and further participating in blood flow regulation and vessel permeability. However, their full function is not completely understood (111). In tumour vasculature, pericytes display abnormalities, are less frequent and are loosely attached to tumour endothelial cells (111–114). This seems to results in a debilitated vessel wall increasing the chance of haemorrhage (108). The interaction of pericytes with endothelial cells is facilitated through the interaction of platelet-derived growth factor and its receptor (PDGF-PDGFR) and concomitant signalling axis. Genetically deficient mice for the PDGF beta isoform have a similar phenotype in normal vasculature as has been seen in tumour vasculature, indicating altered PDGF signalling pathway (112, 115, 116). Further, it has recently been reported that elevated VEGF levels negatively regulate pericytes coverage (117).

1.2.5 Stromal cells in tumour angiogenesis

Over the last 20 years, it has become evident that while tumour cells contribute to tumour angiogenesis, other cells in the tumour microenvironment significantly influence tumour angiogenesis as well. Several types of immune cells, such as macrophages, have been identified as actively influencing the process of tumour angiogenesis in the initial stages as well as in post-treatment relapses. For example, targeting macrophages by molecular means, such as antibodies or small compound inhibitors, significantly contributed to the inhibition of tumour growth (118, 119).

Macrophages respond to various chemoattractant like chemokines and cytokines released from the cancer cells, for example, colony-stimulating factor 1 (SDF-1). Moreover, they themselves release pro-angiogenic factors and are a major source of VEGF-A (120), tumour necrosis factor (TNF), interleukin-1 beta and chemokine ligands (54, 121, 122) which promote

tumour endothelial cell survival, activation and proliferation. Other cells, which are part of the immune system, also contribute to tumour angiogenesis. Neutrophils, mast cells, and eosinophils express several pro-angiogenic factors such as VEGF, TNF and fibroblast growth factor 2 (FGF2) as well as matrix metalloproteinases (MMPs) and other proteases for matrix degradation, and factor release (123).

Macrophages and neutrophils further have been described to be crucial sources for the initiation of vasculogenesis, by expressing factors that attract circulating endothelial cells or endothelial progenitor cells in a glioblastoma model after irradiation (124). Inhibition of SDF-1/CXCR4 decreases the influx of (Cluster of differentiation) CD11b positive cells and leads to decreased vessel formation resulting in abrogation of tumour regrowth (52, 125, 126).

1.2.6 Blood flow in tumour vessels

Ultimately, the architecture of blood vessels impacts on the functionality. The chaotic structure of tumour blood vessels leads to significantly lower blood flow. Other phenomena observed, are sluggish blood flow and change to blood flow directions within the same vessel (95). Overall this can result in poor perfused areas of a tumour, leading to a lack of oxygen , the delivery of metabolites, with profound consequences on treatment efficacy. Poorly perfused areas in a tumour contribute to hypoxia, the reduction of normal levels of tissue oxygen level, leading to increased treatment resistance (127–129).

While angiogenesis occurs in tumours, lymphatic growth has been reported to mostly occur as peri-tumoral lymph-angiogenesis. This lack of lymphatic vessels has critical implications because draining in normal organs contributes to interstitial fluid pressure and convective flow of fluids (130). The lack of a lymph system leads to elevated interstitial fluid pressure. Higher

pressure in the interstitial space compared to the blood vessels can lead to blood vessel collapse and further negatively affects blood vessel structure and blood flow (131).

1.2.7 Alternative types of vessel formation in experimental tumours

The formation of vessels within a tumour does not entirely depend on angiogenesis and other mechanisms have been proposed. In the early stages of development, the initial growth of blood vessels arises from vasculogenesis, whereby endothelial cells differentiate from progenitors, called angioblasts (132). In pathological settings, recent research has suggested that even before angiogenesis takes over vessel formation, recruitment of circulating endothelial progenitor cells to the site is taking place. They are attracted by matrix metalloproteinase mediated release of soluble kit-ligand and can contribute to vessel growth by vasculogenesis (48, 133). These cells, circulating or derived from bone marrow, contribute to the initial stage of blood vessel growth (134–137). They integrate into the developing blood vessels on the luminal side and are diluted in the later stages of tumour growth, due to mixing with local resident endothelial cells. This type of vessel formation has been observed in several types of experimental cancers and human tumours and has been shown to also contribute to blood vessel growth (125, 126, 138). However, the degree of contribution is still under debate and researchers have reported a range of involvement in neo-vessel formation, varying from 50% to no contribution at all (28, 118, 119, 135, 139–142).

While most tumours induce some sort of vessel growth, there are some, which are not dependent on active angiogenesis, at least in specific stages. These tumours nevertheless rely on a functional vasculature and blood supply which is achieved via vessel co-option, the use of functional pre-existing vessels (143). Tumour cells have been described to as migrating towards vessels and initially populating areas around pre-existing vessels (143). However, the process of

how co-option takes place is less understood with tumour cell adhesion and invasion pathways playing an important role (144). With growing tumour mass, active angiogenesis has been observed, suggesting that perhaps vessel co-option can be a mechanism for initial and early tumour growth (143). Indeed, several experimental and clinical primary and metastatic cancers do not rely solely on angiogenesis, but instead reshape the pre-existing blood vessel system to meet their need (145–149). Not surprisingly, vascular co-option was primarily observed in highly vascularised tissue such as brain, liver, and lung cancer (150–154). Generally, this has important clinical implications as the pre-existing vasculature responds differently to treatments (155, 156).

Vascular mimicry, another type of vessel formation, does not rely on angiogenesis and has provoked controversy over the past decade (157). First described by Maniotis and colleagues in an experimental melanoma model, whereby tumour cells appeared to form tube-like structures in direct contact with fluid or blood without endothelial cells and perivascular cells (157). Some groups have suggested that tumour stem cells with high plasticity undergo trans-differentiation into endothelial cell-like cells (158). However, this finding has not been validated so far by other groups.

Intussusceptive angiogenesis, which is the splitting of a vessel into two 'daughter' vessels, has been described in normal and pathological settings (159, 160). Intussusception of existing blood vessels allows for a proliferation-independent increase in the complexity of the vascular architecture, probably to meet the blood supply needs of the tissue. While the molecular mechanisms are poorly understood, some have suggested that shear stress influences the formation of the initial pillars, seen at a bifurcation, which consecutively expands until the blood vessel splits into two parallel ones (160).

The different mechanisms of vessel formation described above have also been investigated in a therapeutic setting with radiotherapy. Vasculogenesis has been described as a

major source in glioblastoma models after radiation and is responsible for blood vessel formation in recurring tumours (126, 161). Circulating endothelial progenitor cells responsible for vasculogenesis are attracted through other stromal cells (125, 162). Co-opted vessels representing normal vasculature and remaining in a quiescent state seem to respond differently to radiation compared to tumour vessels that remain in a highly proliferative state (102, 103, 163). However, little is known about their response to irradiation. Tumour vessels, that incorporated tumour cells in experimental models mimicking endothelial cells or whole tubes formed by tumour cells, showed increased radioresistance (164) and have been generally described as unfavourable to treatment (131). Intussusception of vessels after irradiation has been described as contributing to tumour recovery after radiotherapy (165) through the capability of remodelling independently on proliferative capacity.

1.3 EFFECT AND RESPONSE OF THE TUMOUR VASCULATURE TO THERAPIES

1.3.1 Antiangiogenic treatments

Folkman introduced the concept of angiogenic inhibitors (38) and subsequently defined a protocol to isolate a soluble factor from tumours that induced angiogenesis (39). This, along with the subsequent discoveries of soluble growth factors (166–169), spiked interest in developing compound inhibitors and antibodies targeting key growth factor receptors and their ligand interaction, for example, VEGF, VEGFR-1, 2 and 3, ANG1 and 2 and FGF (170). This led to the discovery and development of so-called anti-angiogenic therapies that target the interaction of angiogenic growth factors with its receptors, and inhibit subsequent downstream signalling of the angiogenic signalling axis (171–176).

In preclinical settings, these compounds showed a significant effect on tumour growth, and tumour blood vessels responded dramatically to compounds such as antibodies targeting the VEGFR-2 receptor and its ligand interaction with VEGF (177–186). Preclinical experiments show that the treatment induces temporal vascular normalisation (105) such that tumour blood vessels change to a more normal vascular phenotype (187). The change in phenotype results in altered morphology, a decrease of vessel leakiness and an increase in mural cell coverage (188). On the other hand, anti-angiogenic therapies can compromise the delivery of drugs and have been shown to increase hypoxia (189–193). So far, anti-angiogenic drugs have shown significant results. However, progression-free and overall survival benefits are modest. Another class of agents disrupting the tumour vasculature, leading to central necrosis of tumours (97, 194), are currently in clinical trials (195–200). They target proliferating endothelial cells by disrupting the cytoskeleton, inducing apoptosis and inhibiting proliferation (201).

1.3.2 Effect of radiotherapy on tumour blood vessels

Radiotherapy not only affects tumour cells but also the tumour microenvironment. The tumour vasculature provides the tumour with oxygen and nutrients, thus contributing to the tumour response to radiotherapy. The tumour vasculature is also affected by radiotherapy. Various studies in the last decades have investigated the response of the tumour vasculature to different radiation modalities. Early studies lacked vascular markers, while recent studies have largely looked at functional changes of the tumour vasculature without investigating structural changes of the tumour vasculature after irradiation. Generally, with radiation doses between 15 and 50 Gray (Gy), conflicting results are reported. For example, several researchers have shown minor initial changes in several human and murine cancer cell lines (124, 202–204). In later stages, after radiotherapy and tumour regression, a decrease of the microvascular density and perfusion has been observed (125, 202, 205–210). However, longitudinal studies of the same tumour and its vasculature have been scarce, thus the understanding of the effects and response of tumour vasculature to irradiation is still poorly understood.

With single high doses between 15 to 20 Gy, a dose-dependent killing of vessels according to size has been observed. With increased vessel size, a greater dose is needed to destroy tumour vessels (202, 206). With irradiation using 5 Gy per fraction, over three weeks, the vessel density decreases by half, while in another tumour type, a single dose of 25 Gy has shown no change at all in the same study (211). Some decrease was observed after 10 Gy irradiation, but with no change in intratumorally oxygen pressure (pO2) level (212).

In a glioblastoma model in mice, a decrease after 15 Gy in perfusion was observed over 21 days, however, perfusion increased with tumour recurrence after 4 weeks, indicating vasculogenesis (125) with the observation based on lectin perfusion showing that functional vessels remained. Doses of 20 and 30 Gy lead to narrowing of microvessels over a period of one week and the irradiated vessels do not recover in their proliferative capacity (213). In some

studies, after doses of 10 to 30 Gy, a temporal decrease in perfusion was observed. In the same studies recovery of blood flow was reported, although they observed a massive destruction of tumour vessels in the same studies (213–215).

The temporal decrease of blood flow occurs in a time frame of 24 hours from irradiation with doses greater than 10 Gy but increases to normal levels within 2 to 7 days after irradiation (206, 215). A dose of 20 Gy causes progressive decrease in vascular volume, and the vasculature becomes disorganised, aggregated and condensed over several weeks (207). Lower doses such as 5 Gy have little effect, but a slight decrease with recovery within 4 days has been observed. A dose of 45 Gy results in extensive vascular damage (208, 209). But on the other hand, even 60.5 Gy has been reported to result only in a transient decrease in perfusion, with partial recovery after 72 hours (216). Larger doses such as 80 Gy and 160 Gy tend to result in a strong decrease in blood flow (206).

Clinical studies have emphasised that blood flow is either maintained during radiotherapy at a pre-irradiated state or it increases initially, in terms of weeks, and decreases towards later stages, in terms of months (217–222). For example, Mäntylä and colleagues showed increased blood flow during hypofractionated irradiation with a weekly total dose of 10 to 30 Gy split in five fractions per week, and then later, a decrease of blood flow was observed (217). Vascular blood volume also increased after irradiation (221), however, fractionated irradiation was shown to decrease tumour vascularity through the midpoint of treatment (218). Generally, enhanced perfusion would be expected to reduce tumour hypoxia, although other explanations could account for increased oxygenation, such as reduced oxygen demand (18). Some tumours were found to have higher levels of perfusion at intermediate times during radio therapy. However, in a few other cases, perfusion remained unchanged for at least several weeks, for example, in cervical and in head and cancers (223–225). Increased perfusion in Shibuya *et al.* and reduced hypoxia in Lock *et al.* were both associated with improved patient

outcome. However, at the end of a full course of fractionated radiation, perfusion was often decreased. All these studies, it must be noted, were done in a fractionated setting and no data is available for single high dose treatment in human patients (226).

Reoxygenation during radiation therapy is regarded as a basic rule (227–231), that is, one of the 5Rs of radiobiology. However, little detailed evidence is available, with some early studies indicating mixed results about oxygenation during radiotherapy. Thus, overall results remain inconclusive. In a study examining hypoxia with ^{18}F-miso positron emission tomography before, during and after the treatment of head and neck cancer tumours, hypoxia reduced midcourse in some patients and at the end of radiation therapy treatments, for others. Those patients with persistent hypoxia had poorer outcomes; raising the possibility that patients in whom hypoxia did not change could benefit from intensified therapy (223, 232, 233). Radiotherapy in cervical cancer patients leads to increased blood perfusion initially, only to decrease at later stages (220).

Despite the large amount of research conducted on tumour perfusion and oxygenation during radiotherapy, there is still a gap in understanding dynamic vascular changes and the mechanism of tumour vascularisation after radiation. Lower doses of radiation seem to have a limiting effect on the tumour vasculature (24, 25) and very high single doses, above 40 Gy, show destruction of the tumour vasculature in a short time frame. However, single doses of 15 to 30 Gy or repeated high doses result in variable results at large. While researchers have looked at certain time points after irradiation, the dynamic change that potentially can explain functional changes of the tumour vasculature such as blood flow is less well understood and needs further investigation.

1.3.3 Endothelial cell apoptosis after irradiation

Irradiation should ideally lead to the killing of cancerous cells. The mechanism of cell killing after irradiation can be induced through Deoxyribonucleic Acid (DNA) damage as well as through the bystander effect of the release of cytotoxic molecules from cells experiencing irradiation (234). However, the exact mechanisms leading to cell death are manifold and can be induced through different molecular pathways and cell-dependent mechanisms, although finally resulting in macroscopic alterations of the cell (235). A dead cell can be defined as a cell that has lost all vital function irreversibly, such as ATP production and redox homeostasis, and that is gradually and inevitably losing its membrane and compartmental integrity (235).

Mitotic catastrophe is the abrogation of proliferation and or survival of cells that do not achieve to complete through mitosis. This is due to extensive DNA damage or non-functional proteins involved in the mitotic step. Eventually, it can lead to multiple micronuclei or macronuclei as a mechanism potentially leading to cell death and is considered a major route for cancer cells after radiation treatment. It refers to a non-programmed cell death mechanism (235, 236). Mitotic catastrophe implies the absence of two major mechanisms within cells: first, a deficient cell cycle checkpoint in response to DNA damage and second, compromised centrosomes resulting in hyperamplification (237–240). However, it has not been investigated if this form of cell death appears in tumour endothelial cells and it is also unclear if both factors are altered in tumour endothelial cells. If tumour endothelial cells remain as normal endothelial cells with only some phenotypical changes, influenced through tumour cells, one would expect normal P53 signalling and cell cycle checkpoint control, preventing continuous proliferation whilst continuing to cause major DNA damage.

Through evolution, cells have acquired several ways to deal with fatal cell damage, leading to the activation of regulated cell death (235). Apoptosis as a form of programmed cell death is another mechanism of cell killing and a potential response to irradiation. It can be

activated through extrinsic and intrinsic pathways and in the setting of radiation, it is often induced initially in a p53 dependent manner (236, 241). However, p53 is mutated in approximately 50% of all cancers (242–244). Biological processes activated through cell damage, such as autophagy are cell intrinsic mechanism by which parts of the cells cytoplasm undergoes vacuolisation and digestion (245–247); senescence as a permanent cell cycle arrest and therefore considered non-lethal (166–168), also contribute as mechanisms to respond to cell damage.

Normal endothelial cells *in vitro* respond in several ways to irradiation. Largely proliferating endothelial cells undergo apoptosis and senescence *in vitro* after irradiation (248–250) but, significantly, can be rescued from entering apoptosis if growth factors are present (251–254). Non-proliferative endothelial cells show little apoptotic activation but have been shown to undergo senescence (255), resembling the late effect of normal tissue after irradiation (27, 163). However, other mechanisms such as mitotic catastrophe, through different mechanisms, for example, after Combretastatin A-4 (a microtubule destabiliser) treatment (194), have also been described *in vitro*. In normal vascular tissue, similar to non-proliferating endothelial cells *in vitro*, the effects of irradiation become evident only once cells attempt to proliferate. While radiation does lead to DNA damage and proliferative sterilization, it might not interfere with the function of the cell itself (27).

Cell death through apoptosis is mediated through two main mechanisms. On one hand, through extrinsic pathways mediated through paracrine and autocrine release of ligands binding to its receptors, such as tumour necrosis factor receptor (TNFR), fatty acid synthetase receptor (FASR) or death receptor (DR) — leading to activation of caspase proteins. On the other hand, intrinsic pathways are activated through mitochondria outer membrane permeabilization, controlled through members of the BCL-2 family which constitute pro- and anti-apoptotic

members such as BAX, BAK, BOK and BH3-only proteins such as BID, BAD, BIM (256–258). Transcription of these proteins can be activated by p53 (259, 260).

In tumour endothelial cells *in vitro*, Friedman and colleagues suggest apoptosis after irradiation is activated through extrinsic signals initiating TNF receptors that activate the caspase machinery via asmase mediated ceramide release acting as a second messenger (261). In a second experiment, they showed that tumour endothelial cells *in vivo* undergo early ceramide mediated apoptosis, after a singular dose of 15 or 20 Gy irradiation within 6 hours, and that it was inhibited when mice were *asmase* deficient. Thus, they proposed that early apoptosis of tumour endothelial cells acts as a major regulator of tumour response to radiotherapy (28). This theory is controversial. Other effects such as immunogenicity of the cell lines deployed and the very low TCD 50 after radiation in the tumours derived from these cell lines question the validity of the results and sparked a lively discussion within the community. Moding, Kirsch and others showed in a mouse model with either mutation of ATM or BAX in endothelial cells there was no measurable differences in tumour response with similar doses (15 Gy), further questioning the previous findings by Friedman. They also showed that apoptosis in tumour endothelial cell peaks between 48 and 72 hours after irradiation with single dose such as 15 or 20 Gy *in vivo* (262, 263) and with 0.5 to 5 Gy *in vitro* (264–266). Non-programmed cell death, such as necrosis, seems to play less of an important role in the endothelial cell response to radiation, at least *in vitro* (250).

1.3.4 Radiation-induced senescence in endothelial cells

Senescence is the mechanism of continuous cell cycle arrest of cells which prevents them from further proliferation yet maintain their viability ad metabolic activity it is therefore, initially, not necessarily lethal. This has been described after irradiation *in vitro*, generally with

a focus on normal vasculature and late response after irradiation. The data is mostly from endothelial cells, harvested from pulmonary arteries, human umbilical veins, and other types of endothelial cells. In normal tissue, radiation has been linked to cardiovascular diseases.

From a population perspective, several findings have been gathered from those who have been exposed to high doses of radiation: Japanese atomic bomb survivors, or patients with Hodgkin lymphoma, and breast cancer patients treated with high doses of radiation (267). On the endothelial cell level, proteomics analysis suggests oxidative stress and DNA damage leading to senescence, which can be mediated through the p53/p21 signalling axis, activated in endothelial cells through unrepaired DNA damage and persistent oxidative stress. Other factors that have been shown to induce senescence are insulin-like growth factor pathways (268). For example, senescence was suppressed by inhibition of the IGF1-Pi3K-Akt/mTOR signalling axis (269–272). Furthermore, NF-κB and TGF β1 signalling pathways have been linked to the induction of endothelial cell senescence (270, 273). Recently, it has been shown that the time scale for endothelial cell senescence *in vitro* can be measured in days. 15 Gy irradiation leads to significant beta-galactosidase expression after 4 days of irradiation (255).

Various researchers with different techniques and in various tumour models, as well as in small clinical trials, have shown that with radiation doses larger than 10 Gy, a dose and time-dependent decrease of the microvasculature occurs. At the same time, data from other studies suggest that perfusion of blood vessels is either maintained, or, in some cases, shows a temporal increase followed by a decrease of perfusion after several days to weeks. Generally, a time and dose-dependent response of the tumour vasculature has been observed, suggesting differential response to radiation with smaller tumour vessels tending to be more fragile towards irradiation and larger tumour vessels tending to be more radioresistant. Although *in vivo* experiments have been conducted extensively, their data is inconclusive. Earlier studies lacked proper vascular markers and their findings allow only limited conclusions. Denekamp and co-workers showed

limited contribution of the tumour vasculature to the outcome of radiotherapy (27). Later, researchers around Fuks and colleagues showed early apoptosis of tumour endothelial cells after radiotherapy and concluded this as a significant contribution to tumour response to radiation, through secondary effects such as oxygen deprivation (28, 274, 275). More recently, researchers around Kirsch have shown, in a series of well-executed experiments, that endothelial cells do not contribute critically to treatment outcomes after irradiation using a genetic mutation of ATM in tumour or tumour endothelial cells (262, 263, 276).

1.4 SUMMARY

What can we conclude by looking at the current state of knowledge? An issue that becomes clear by analysing the literature is that the reasons for the timeline that tumour models display to specific radiation responses are manifold and likely tumour-specific, such as the expression level of VEGF, the total expression of growth factors, the recruitment of other stromal cells like macrophages, the sensitivity of tumour cells to radiation, the expression of protective factors and other types of vessel formation. Earlier studies, unfortunately, were not able to unambiguously label endothelial cells, therefore relying on only perfusion as a marker.

Recently, researchers around Jain have proposed a staged system of tumour vascular response to irradiation, which tries to harmonise the collective effort of the last couple of decades, to increase our understanding of the response of tumour vasculature to irradiation (24). Separating tumour and tumour vascular response into four stages - starting with an initial response stage that is governed by continuous tumour growth. This stage is followed by a regression phase when the tumour starts to shrink and tumour vasculature tends to decrease in complexity. Later stages are concerned with early and late recurrence of tumours and repopulation of the tumour vasculature governed by the demand and supply for tumour and stromal cells.

This staged approach allows results to be compared despite different periods of radiation response. Interestingly, *in vitro* experiments have suggested that, although apoptosis occurs initially within the first few hours or days, a large part of endothelial cells maintained their integrity and progressed into senescence (255). Still, it is not clear whether gross response of the tumour to radiotherapy is associated with significant vascular damage and this remains an unresolved yet controversial topic (27, 28, 275, 277, 278).

1.5 AIM OF THE THESIS

The aim of this research is to investigate the response of the tumour vasculature to single and fractionated irradiation. To this end, we have taken advantage of genetically engineered mice in combination with two-photon microscopy to perform longitudinal imaging studies. These studies have been accompanied by standard molecular techniques to complement our observations. We hope to shed light on the initial phases of the tumour vasculature response to radiation by resolving the disjunction between two seemingly opposing pieces of evidence, that are dominant in this field. We are attempting to bring together the aspects that has observed massive apoptosis and destruction in tumour endothelial cells and blood vessels with the aspect that has only been able to observe functional change in a limited manner. It is intended that by seeing the relationship between these two we can contribute to the research into radiation effects of the tumour vasculature.

CHAPTER 2

MATERIAL AND METHODS

2.1 CELL LINES

Murine colon adenocarcinoma cells (MC38) were a gift from Dr Lee Gorden (Vanderbilt University, Nashville, TN, USA). Mouse melanoma (B16F10) cells were obtained from American Type Culture Collection. Both cell lines were transduced with EGFP using lentiviruses to obtain MC38 EGFP and B16F10 EGFP cells. Additionally, MC38 cells were separately transduced with a lentivirus expression vector to obtain MC38 mCherry cells. Cells were cultured in DMEM (MC38) and RPMI 1640 medium (B16F10), supplemented with 10% (v/v) fetal bovine serum and 1% penicillin-streptomycin. All cells were cultured in a humidified incubator with 5% CO_2 at 37°C. Cells were used at passage numbers < 8 and were routinely tested negative for Mycoplasma with MycoAlertTM Mycoplasma Detection Kit (Lonza).

For intravital imaging studies EGFP expressing MC38 and B16F10 tumour cell lines were used. For the investigation of the induction percentage of tdTomato after tamoxifen administration in VEOM mice, EGFP expressing MC38 tumour cells were used. For subcutaneous tumour studies investigating tumour growth and response to irradiation, for immunofluorescence and flow cytometry investigations as well as for FACS sorting for whole RNA sequencing, the MC38 or B16F10 WT cell lines were used.

2.2 IN VIVO ASSAYS

All animal studies were performed in accordance with the United Kingdom Animals Scientific Procedure Act 1986 and following local ethics review. All animal studies were conducted under the following Procedure Project Licences (PPLs): 30/3413 and PCDCAFDE0.

2.2.1 Animals

Six to eight week old C57BL/6J female WT mice for subcutaneous tumour studies investigating the effects of radiation on the tumour vasculature with immunofluorescence and flow cytometry were obtained from Charles River Laboratories.

The C57BL/6-Tg(Cdh5-cre/ERT2)1Rha/J transgenic mice (VCAD) were kindly provided by Prof. Sarah de Val (University of Oxford) and permission to use was obtained from Prof. Ralf Adams (Max Planck Institute for Molecular Biomedicine) who generated the mice in the first place. These mice carry an DNA insertion of the VE-cadherin promoter fused to tamoxifen inducible cre/ERT2 sequence. This was inserted into a PAC (P1 artificial chromosome). This cDNA construct was microinjected into C57BL/6 zygotes. The founder lines, whose background was not specified were backcrossed to the C57BL/6J line for at least five generations to obtain congenic mice on the C57BL/6J genetic background in our facility.

B6.Cg-Gt(ROSA)26Sortm9(CAG-tdTomato)Hze/J mice (ROTO) were purchased from Jackson Laboratory (Stock Number: 007909). These mice carry the following gene construct from (http://www.informatics.jax.org/allele/MGI:3809523):

> "The Rosa-CAG-LSL-tdTomato-WPRE targeting vector (woodchuck hepatitis virus posttranscriptional regulatory element) was designed with (from 5' to 3') a **C**MV-IE enhancer (**c**yto**m**egalo**v**irus-**i**mmediate **e**arly)/**c**hicken beta-

actin/rabbit beta-**g**lobin hybrid promoter (CAG) (for high expression), an FRT (flipase recognition target) site, a loxP-flanked STOP cassette (LSL) (with stop codons in all 3 reading frames and a triple polyA signal, to enhance translation blocking), tdTomato sequence (a non-oligomerizing DsRed fluorescent protein variant with a 12 residue linker fusing two copies of the protein (tandem dimer)), a woodchuck hepatitis virus post-transcriptional regulatory element (to enhance the mRNA transcript stability), a polyA signal, and an attB/attP-flanked PGK-FRT-Neo-polyA selection cassette. This entire construct was inserted between exons 1 and 2 of the Gt(ROSA)26Sor locus of a C57Bl/6J mouse"[1].

This mouse strain is congenic on the C57BL/6J genetic background.

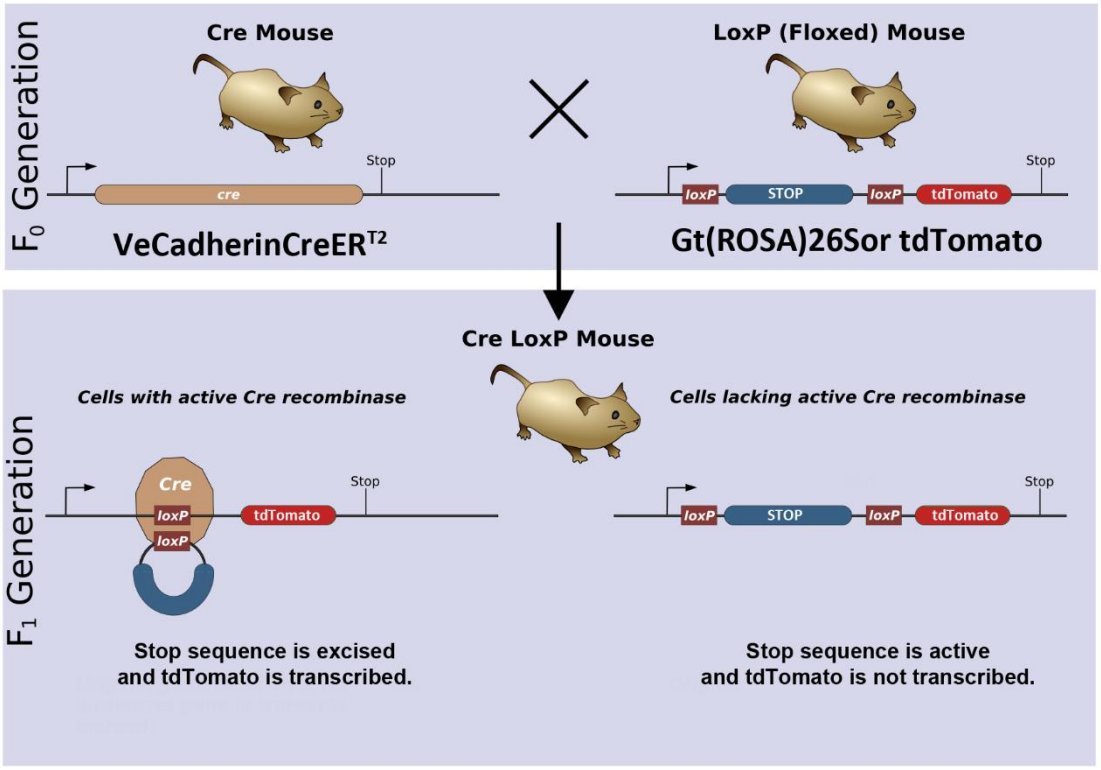


Figure 2.1 The breeding strategy of ROTO and VCAD mice to obtain VEOM mice used in the window chamber experiment. The F1 generation was used and the cre-ert2 was translocated from the cytoplasm to the nucleus via tamoxifen.

[1] With changes from http://www.informatics.jax.org/allele/MGI:3809523

Female VCAD mice and male ROTO reporter mice were crossed to obtain C57BL/6-Tg(Cdh5-cre/ERT2)1Rha-Gt(ROSA)26Sortm9(CAG-tdTomato)Hze/J mice (VEOM mice) and were bred in our facility (Figure 2.1). VCAD and ROTO mice were routinely genotyped to ensure construct integrity within the mouse strains. Genotyping on mouse ear tissue was performed by Transnetyx using a TaqMan-based real-time PCR protocol.

2.2.2 Tamoxifen treatment

Tamoxifen (Sigma-Aldrich) was dissolved in corn oil (Sigma-Aldrich) and 5% ethanol (Sigma-Aldrich) at a concentration of 10 mg ml^{-1} by sonicating the solution in a benchtop sonicator water bath (Fisher Scientific) at 40°C. The solution was sterile filtered in a laminar flow cabinet with a Minisart syringe filter with a pore size < 0.22 µm (Sartorius) and stored at 4°C until further use and for a maximum duration of one week. 100 µl was administered to VEOM mice once they reached an age of 6 weeks via gavage daily for 10 days (5 days of gavage, 2 days of pause, 5 days of gavage) to induce the expression of TdTomato in endothelial cells. This schedule was chosen after initial experiments showed slightly higher induction of tdTomato in VEOM mice with this schedule. In some cases a slight weight loss was observed. However, this was below 5% of total bodyweight. No other side effect or toxicity was observed with this schedule.

Induction efficiency of tdTomato in endothelial cells was checked by observing the epilated ear with an inverted Zeiss LSM 880 microscope (Carl Zeiss) under epifluorescence excitation with a Xenon light source (Carl Zeiss) for excitation (band-pass 545/25) and emission for tdTomato (Fset43wf, band-pass 605/70). Mice deemed good for intravital imaging (approximately 95% or higher induction efficiency, scored by 2 researchers independently and

confirmed via flow cytometry analysis shown in Chapter 3 (Figure 3.1) were chosen without specific gender selection.

2.2.3 Subcutaneous tumour model

The right flank of WT C57Bl/6J mice were shaved. Mice were injected with 100 µl of wild type MC38 or B16F10 cell suspension in 0.9% NaCl (2.5 x 10^5 cells) on the right flank under inhalation anaesthesia with isoflurane (Figure 2.2). Mice were checked daily and tumour volumes were measured every other day using a digital calliper (Vaper). Tumour volumes were calculated using the formula: Length × Width × Depth × π/6.

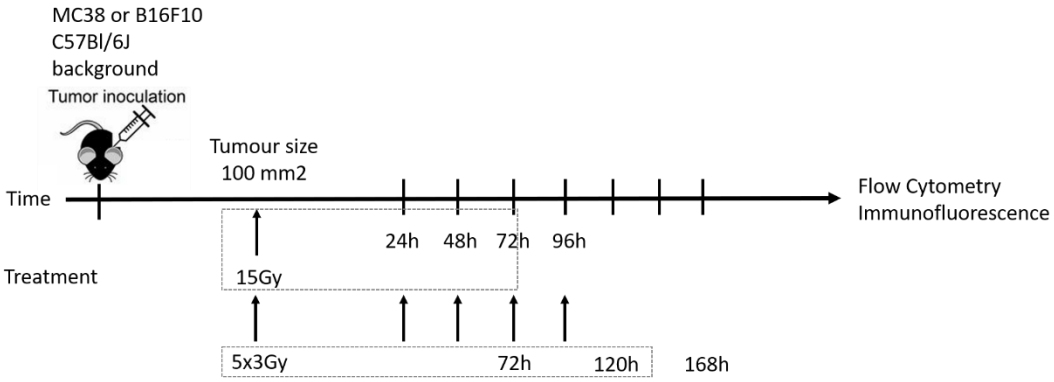


Figure 2.2 Workflow of subcutaneous tumour experiments. Mice were injected with either MC38 or B16F10 tumour cells. Once tumours reached approximately 100 mm^3 the mice were treated either with 15 Gy single dose irradiation or fractionated irradiation at a schedule of 5 times 3 Gy.

2.2.4 In vivo radiation treatment

Once subcutaneous tumours reached 80-100 mm^3 , mice were randomly assigned to experimental groups. Mice were anaesthetised under inhalation with isoflurane and led shielded on a heated stage 37°C with only the tumours exposed to radiation (Figure 2.3). Tumours received either 15 Gy or fractionated 5 × 3 Gy X-ray radiation treatment over five

consecutive days (300 kV, dose rate of 2.25 Gy per minute) delivered to tumours using a Gulmay RS320 irradiation system (Gulmay Medical Ltd). Radiation in the Gulmay irradiator comes from the top of the machine and is targeted towards the ground. The dosimetry done by the facility core team is performed twice a year. The dosimetry was performed using mouse-like phantoms (water equivalent material). They were positioned and used with the shielding as in an actual treatment setting. Gafchromatic film (optical film sensitive to radiation) was sandwiched, placed on top or placed underneath the phantom to mimic tissue penetration of the radiation.

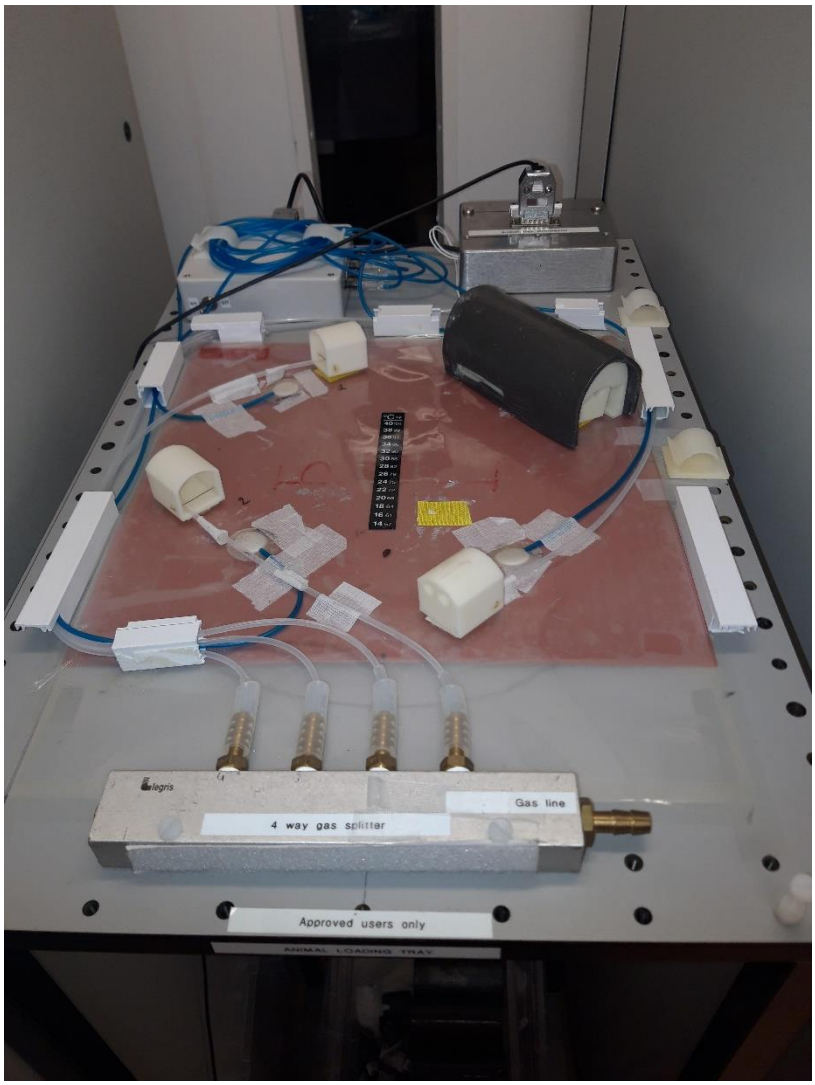


Figure 2.3 Gulmay tray for subcutaneous tumour radiation. The tray consisting of a heating pad (red), four inhalation head chambers and four breathing monitoring units. Lead shielding against radiation (dark grey) can be observed as exemplified on one of the four inhalation head chambers.

The radiation was used at 320keV and 10mA and a range of times was used to calculate a calibration curve. The length of time for the radiation was then chosen such that the bottom of the tumour would receive the desired dose of radiation. Clearly, therefore, there might be a variation in the total dose that tumour cells on the top and the bottom might receive.

This variation and the effect of anaesthesia can affect tumour response to radiation treatment. Anaesthesia of mice undergoing radiation treatment was used for both technical and welfare reasons. First, the current physical set up of the Gulmay irradiator does not allow us to restrain mice in an awake state. Second, under UK legislation, performing a regulated procedure must take place under anaesthesia, unless the anaesthesia itself represents a higher cost (in terms of welfare) to the animal than the procedure itself. Isoflurane is a $GABA_A$ agonist, leading to sedation and relaxation (279). It negatively influences total haemoglobin concentration, tissue oxygen saturation and oxyhaemoglobin in normal and tumour tissue in a time and dose dependent manner (280). Isoflurane further can decrease the respiration rate, blood pressure, peripheral resistance and heart inotropy (281). We are aware of this issue and our findings must be seen in light of these limitations.

2.2.5 In vivo radiation treatment of tumours in abdominal window chambers

Mice were anaesthetised under inhalation with isoflurane and placed in an imaging-guided small animal radiation research platform (SARRP) irradiator (Xstrahl Ltd). A Cone Beam CT scan (computerised tomography) of each mouse was obtained and the treatment was planned using Muriplan (Xstrahl Ltd) to ensure uniformity of dose across the tumour while minimising dose exposure to the surrounding normal tissue. This was achieved using a coronal arc beam with the isocentre positioned a few millimetres above the glass window with a beam at an angle of 65^o to the vertical and the mouse rotated through 360^o horizontally. This setting

ensured that the beam did not pass through the plastic window or glass (Figure 2.4A to D). Ideally an angle close to 90^{o} would have been chosen, sparing the majority of organs, however, spatial constrains between the SARRP collimator and the cradle carrying the animal did not allow for a 365^{o} rotation at 90^{o} without collision: 65^{o} represented the closest possible angle to 90^{o} without collision between the collimator and the cradle. To achieve full coverage of the tumour a 4 mm x 10 mm field size (defined as the isocentre at the long axis parallel to the mouse) was chosen.

The SARRP was used to deliver 15 Gy of X-rays (220 kVp copper filtered beam with HVL of 0.93 mmCu) to the tumour at ~2 Gy per minute. This was given either in a single fraction or at 5 daily fractionations of 3 Gy X-ray radiation to the tumour. Dosimetry of the irradiator was performed as radiochromic film dosimetry previously described in (282). In sum, for the collimator used in our experiment with the SARRP, a set of films at 9 different depths (0, 5, 10, 15, 20, 30, 40, 50, 70mm) in a CIRS Plastic Water LR phantom were irradiated. The films were exposed at three different SSDs (31, 34, 38cm) for 90 seconds, and scanned at [48-bit RGB TIFF images at 300 dpi resolution using an Epson® Expression 10000 XL flatbed scanner (Plainfield) at 24 h post-irradiation. All the measured central axis doses are input into the Xstrahl treatment planning software (MuriPlan), and the doses are calculated using the Xstrahl dose convolution algorithm.

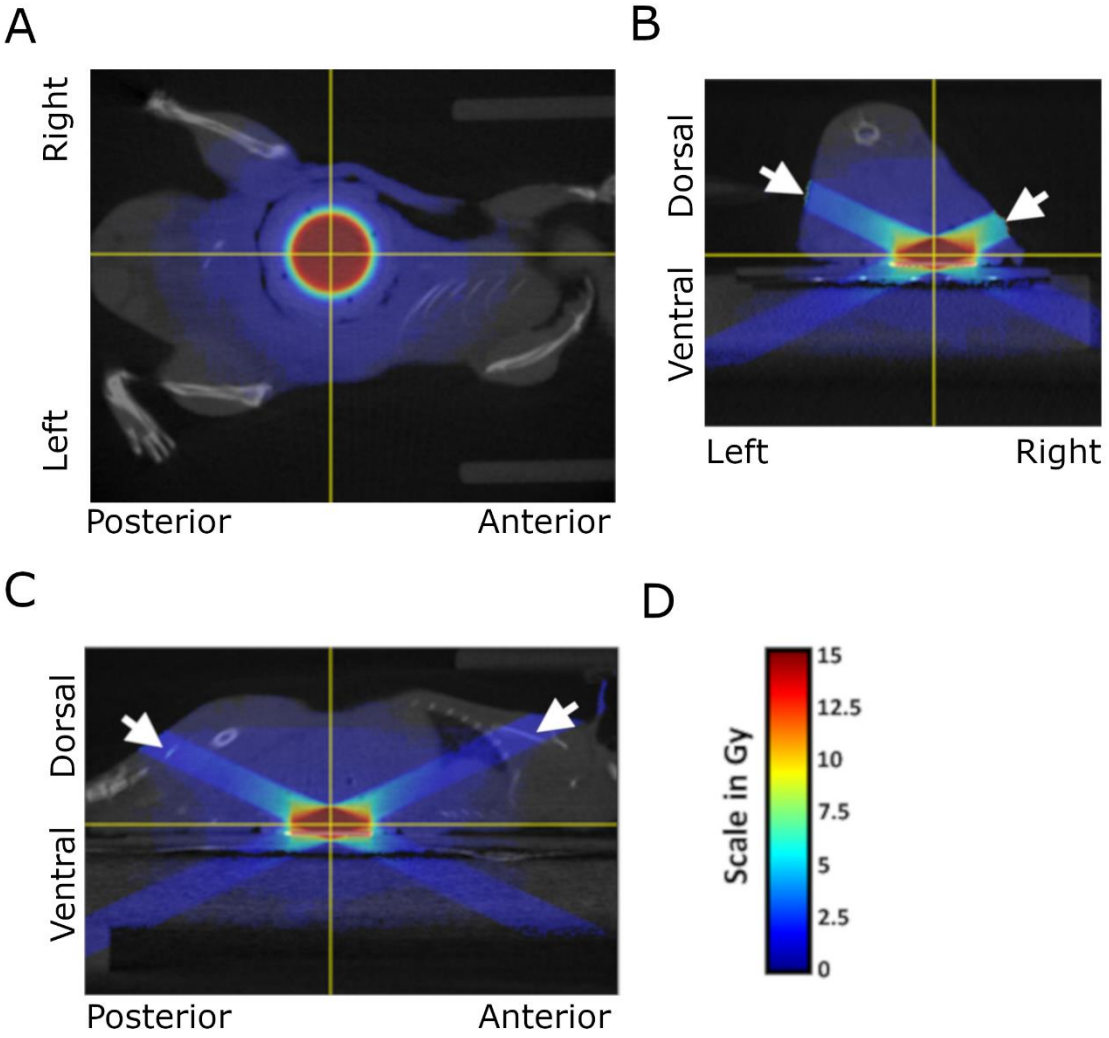


Figure 2.4 Visualisation of the dose delivered to the tumour growing in a window chamber. Radiation was delivered with a SARRP. The dose is presented as an overlaid colour scale ranging from 0 to approximately 15 Gy on the CT scan .

- **A.** CT image of a mouse depicting the posterior – anterior and left – right directions, the isocentre is indicated at the cross section of the two yellow lines, pseudo colours represent confined radiation dose delivered to the area where blue represents a lower dose while red a higher dose (colour scale in **D**).
- **B.** CT image of a mouse Y axis represents the ventral – dorsal axis of a mouse and the X axis represents the left – right axis of the mouse. White arrows indicate the beam direction, incoming at 65^{o} from the vertical yellow line. Colour scale indicates confined radiation dose delivered to the area where blue represents a lower dose while red a higher dose respectively.
- **C.** CT image of a mouse with Y axis representing the ventral – dorsal axis of the animal and the x axis representing the anterior – posterior axis. White arrows indicate the radiation beam direction, incoming at 65^{o} from the vertical axis (yellow line).

Subsequently, the manufacturer's software (Muriplan, Xstrahl) was used to calculate the time to deliver the set dose. A visualisation of the planned dose distribution is presented (Figure 2.4.).

2.2.6 Tumour drug treatment

To determine whether vessel morphology and perfusion were altered due to antiangiogenic treatment, VEOM mice bearing EGFP positive MC38 tumours were treated with anti-mouse VEGFR2 antibody (clone DC101, 500 µg per dose, 27 mg $kg^{-1;}$, BioXCell) or Rat IgG1 (clone HRPN, 500 µg per dose, BioXCell). Intraperitoneal injections were administered when intravital imaging was started and a second administration three days later.

2.2.7 Tumour allograft model and abdominal window chamber imaging

Abdominal window chamber model in mice allowed for intravital imaging of the tumour vasculature. VEOM mice deemed good for intravital imaging, due to good expression of tdTomato in endothelial cells after tamoxifen, underwent consecutive surgery one to two weeks after the last dose of tamoxifen. Mice were anaesthetised with inhalation anaesthesia with isoflurane and kept on a heated stage at 36.5°C throughout the procedure, analgesic (Vertegesic, Ceva) at a concentration of 0.1 mg kg^{-1} body weight was administered preoperatively. An abdominal window chamber made in-house from either titanium or biocompatible plastic (biocompatible plastic windows were used in combination with irradiation treatment) consists of two separate parts that can be joined together. The outer frame was surgically implanted onto shaved and depilated VEOM mice as described previously (283), with the difference that only the skin was cut along the linea alba, whereas the abdominal wall was left intact. The skin was then carefully separated from the underlying muscle. The abdominal window chamber frame was fixed with prolene sutures (Ethicon, Johnson & Johnson) to the skin on the side of the incision of the mouse. Then, murine colon adenocarcinoma MC38 expressing EGFP, or murine melanoma 16F10 tumour cells expressing EGFP in the cytoplasm, were induced

by injecting 5 µl of 2.5×10^5 cells in a 50:50 mixture of saline and matrigel (BD Biosciences) into the thin fat layer on top of the abdominal muscles. The window was closed by joining the inlet into the frame of the already fixed abdominal window chamber.

Mice were transferred onto a heated pad until recovery from anaesthesia. Upon recovery mice were monitored daily to ensure animal health, window integrity and tumour growth. Once the tumours in window chambers reached a size where blood vessels could be detected, which was at ~3 mm of tumour diameter, *in vivo* imaging was initiated. For window imaging with a two-photon microscope, mice were anaesthetised with inhalation anaesthesia with isoflurane and kept on a heated stage at 36.5°C inside a dark air-heated chamber during imaging to 36.5°C. The breathing rate of the mice was monitored with a custom-made in-house breathing monitoring device.

Upon commencing imaging, Qtracker 705 (Invitrogen) vasculature labels in a 1:10 dilution in sterile saline were continuously injected through a tail vein cannulation connected to a syringe and an automated pump (Harvard Instruments) at an injection rate of 75 µl per hour starting with a bolus injection of 12.5 µl. Qtracker 705 are non-targeted Quantum dots (Qdots). These Qdots have a polyethylene glycol surface coating lacking functional groups to prevent interaction that can potentially lead to inflammatory responses. Qdots 705 have an emission peak around 705 nm. Previous studies investigating retaining times show a plasma half-life of around 18 hours. Long term investigation reveals an accumulation of Qdots particularly in the liver, but also the kidneys and the spleen (284).

2.2.8 Tissue labelling with injectable agents

For EdU (5-ethynyl-2´-deoxyuridine) a thymidine analogue labelling of proliferating cells, 200 µl of EdU (Invitrogen) solution in PBS with a concentration of 2 mg ml^{-1} was intraperitoneally injected into mice three hours prior to tumour resection (Figure 2.5).

To label tissue for hypoxic regions between the timeframe of injection and sample collection, 200 µl of EF5, (2-(2-Nitro-1H-imidazol1-yl)-N-(2,2,3,3,3- pentafluoro-propyl) acetamide) obtained from Dr Evans and Koch (University of Pennsylvania, Department of Radiation Oncology), solution in PBS at a concentration of 75 µg ml^{-1} was injected two hours prior sample collection.

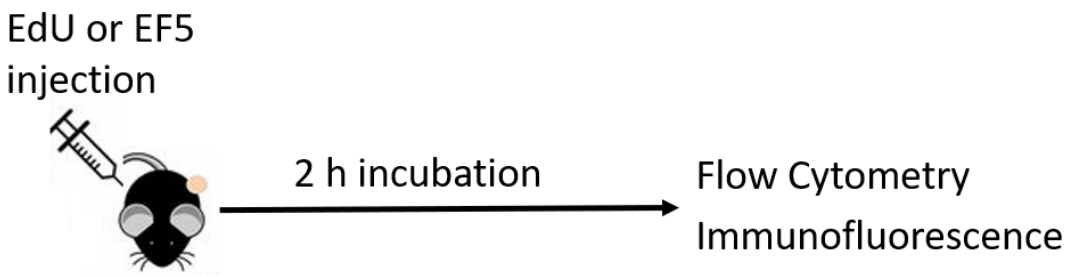


Figure 2.5 workflow of EdU or EF5 experiments. Subcutaneous injection of EdU or EF5 in tumour bearing mice to investigate proliferation and hypoxia in subcutaneous tumours.

2.3.1 Flow cytometry profiling of tumour endothelial cells

MC38 EGFP, MC38 mCherry and B16F10 EGFP tumour-bearing mice were sacrificed by cervical dislocation and the tumours were harvested in ice-cold PBS. Tumours were cut into small pieces and incubated in Hank's Balanced Salt solution (Thermo Fisher Scientific) with collagenase 2 (Worthington; 10 mg ml^{-1}) and DNase I (New England Biolabs; 2 U ml^{-1}) for 45 minutes with regular shaking at 37°C. Cell suspensions were then strained through 50 µm nylon strainers (CellTrix, Sysmex) and centrifuged at 400*g.* Samples were resuspended in PBS and treated with red blood cell lysis buffer (Chemicon). Following this, samples were centrifuged

and resuspended in FACS buffer (PBS containing 2% FBS) and stained for the following markers: CD45 (a transmembrane protein and general marker for identifying differentiated hematopoietic cells except erythrocytes); TER119 (a lineage marker for erythroid cells); CD150 (a transmembrane protein and marker for hematopoietic stem cells); CD31 (detecting the platelet endothelial cell adhesion molecule and therefore a marker for endothelial cells); and LIVE/DEAD markers (Table 2.1).

They were incubated for 30 minutes. Proliferation was analysed with the click-iT® EdU Alexa 488 Flow Cytometry Assay Kit (Thermo Fisher Scientific) according to the manufacturer's instructions. In sum: cells were fixed for 15 minutes and permeabilised for 15 minutes followed by incubation with the click-iT reaction mix for 15 minutes. Cells were washed twice in PBS subsequently.

Apoptosis was analysed with CellEvent™ Caspase-3/7 Green Flow Cytometry Assay Kit (Invitrogen), according to the manufacturer's instructions. Samples were measured using an Attune NxT Flow Cytometer (Thermo Fisher Scientific). Cells were identified based on forward and side scatter, after exclusion of doublets. Tumour endothelial cells were gated as DEAD negative, CD45 negative, CD150 negative, Ter150 negative, EGFP negative (or mCherry negative), CD31+ positive cells (Figure 2.6). The cells relative frequency of each subpopulation from the live-cell gate, or an absolute number of each subset were determined. The data was analysed using FlowJo software (Tree Star Inc.).

Table 2.1 Antibodies for Flow cytometry analysis of tumour endothelial cells

Antibody	Source	Cat#	Dilution	Application
BV421 anti-mouse CD45 (clone 30-F11)	BioLegend	103134	1:600	FC
BV421 anti-mouse TER-119 (clone TER119)	BioLegend	116234	1:100	FC
BV421 anti-mouse CD150 (clone TC15-12F12.2)	BioLegend	115943	1:100	FC
PE/Cy7 anti-mouse CD31 (clone 390)	BioLegend	102418	1:250	FC
FC = Flow Cytometry				

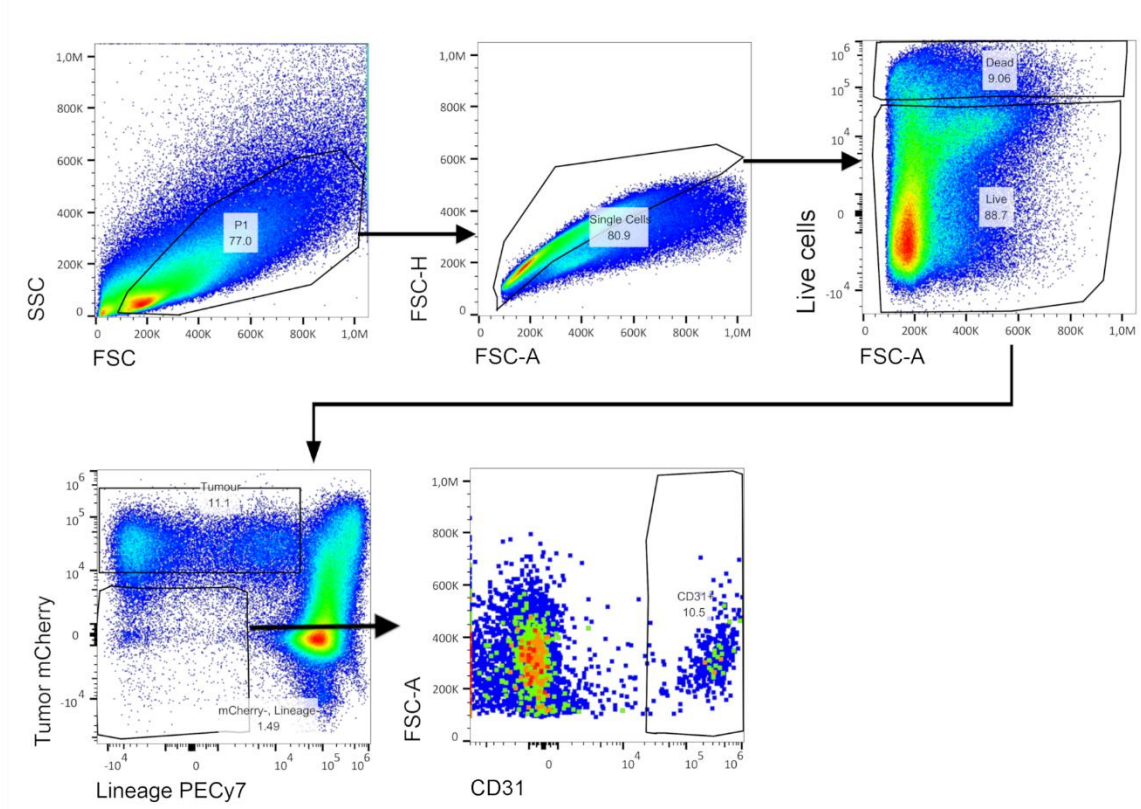


Figure 2.6 Flow cytometry gating strategy for tumour endothelial cells. Forward scatter (FSC), side scatter (SSC), Lineage PECy7 (mix of CD45, TER119 and CD150 all labelled with BV421 or Cy7)

2.3.2 Immunofluorescence staining of mouse tumour and organ sections

An additional tumour bearing group of mice were euthanised and the tumours were resected and immediately placed in 4% Paraformaldehyde (PFA, Sigma-Aldrich) in PBS and incubated overnight at 4°C. Samples were then placed into 30% sucrose (Sigma-Aldrich) in PBS solution (w/v) overnight at 4°C. Subsequently, tumours were embedded in optimal cutting temperature (OCT) medium, frozen in liquid nitrogen and stored at -80°C. Thin 10 µm or 80 µm cryosections were cut with a Leica CM1950 (Leica Biosystems) cryostat onto glass slides (Superfrost Plus, Thermo Scientific) and stored at -80°C until required.

To prepare them for staining, tumour sections were air-dried for 20 minutes and washed once with PBS and blocked with 5% BSA and 5% donkey serum (v/w) in PBS containing 0.25% Triton X-100 (Sigma-Aldrich) for one hour at room temperature in a humidified chamber. Sections were stained for proliferation with the click-iT EdU (5-ethynyl-2´-deoxyuridine) Alexa647 Immunofluorescence staining kit (Invitrogen) according to the manufacturer's instruction followed by incubation with primary antibodies in blocking solution overnight at 4°C. The following primary antibodies were used (Table 2.2): CD31 (R&D, AF3625, 1:200), ERG (Abcam; ab92513, 1:200), CD45 (Abcam; Ab25386, 1:200), GR1 (Abcam; Ab25377, 1:200), CD68 (GeneTex; GTX41865, 1:200) and cleaved caspase 3 (Cell Signaling Technology; #9661, 1:200), NG2 (EMD Millipore; ab5320, 1:200). IgGs from the same species were used at the same concentration as isotype controls. Sections were washed three times for 10 minutes in PBS and incubated with Alexa-Fluor 488-, Alexa Fluor 546- or Alexa-Fluor 647-conjugated secondary antibodies (Invitrogen or Jackson Immuno; 1:400) for one hour at room temperature in a humidified chamber. Sections were washed three times for 10 minutes in PBS and counterstained with Hoechst 33342 (Sigma-Aldrich) for five minutes and washed once in PBS. Sections were mounted with ProLong Diamond Antifade Mountant medium (Molecular Probes).

Table 2.2 Antibodies for immunofluorescence analysis of tumour sections

Antibody	Source	Cat#	Dilution	Application
Goat anti-mouse Endomucin	Thermo Fisher	PA5-47648	1:400	IF
Rabbit anti-mouse ERG	Abcam,	ab92513,	1:200	IF
Rabbit anti-mouse NG2	EMD Millipore	ab5320	1:200	IF
Rat anti-mouse CD45	Abcam	Ab25386	1:200	IF
Rat anti-mouse GR1	Abcam	Ab25377	1:200	IF
Rat anti-mouse CD68	Gene Tex	GTX41865	1:200	IF
Rabbit anti-mouse Cleaved Caspase 3	Cell Signalling	#9661	1:200	IF
Goat anti-mouse CD31	R&D	AF3625	1:200	IF
Donkey anti-goat Alexa Fluor 647	Jackson Immuno	705-605-147	1:400	IF
Donkey anti-goat Alexa Fluor 546	Thermo Fisher	A-21432	1:400	IF
Donkey anti-rabbit Alexa Fluor 488	Thermo Fisher	A-21206	1:400	IF
Donkey anti-rat DyLight 405	Jackson Immuno	712-475-150	1:400	IF
Cy3 labelled anti-EF5 antibody	Drs Evans' and Koch University of Pennsylvania		75 µg/mL	IF
IF = immunofluorescence				

For thick 100 to 200 µm sections, tumours were resected and fixed in 4% PFA in PBS overnight at 4°C and subsequently placed into 30% sucrose (Sigma-Aldrich) in PBS solution (w/v) and incubated overnight at 4°C. Tissues were placed in liquid 0.25% low melting agarose in PBS solution and once solidified cut into 100 to 200 µm sections using a vibratome (Campden Instruments). Tissue was stored at -20°C in antifreeze solution containing sodium azide 0.025% (w/v), sucrose 30% (w/v), ethylene glycol 30% (v/v) and polyvinyl-pyrrolidone (w/v) (all Sigma-Aldrich) in PBS. Subsequent processing of tissues was the same as for the thin sections with incubation and washing times increased three-fold.

2.3.4 RNA sequencing: Tumour stromal cell preparation

Dissected tumours were finely chopped with scalpels and the obtained fragments digested in HBSS (GIBCO; with Calcium and Magnesium) containing a mix of Collagenases 1 and 3 (both Worthington) at a concentration of 3 mg $ml^{-1;}$ dispase II (Roche) at a concentration of 7 mg $ml^{-1;}$ and DNase I (Invitrogen) at a concentration of 2 U ml^{-1}. The samples were incubated at 37°C with gentle agitation for 20 minutes. Tumours up to 100 mm^3 were digested in a final volume of 5 ml. Tumours bigger than 100 mm^3 were digested in 10 ml of HBSS-enzyme mix. The dissociated cells were centrifuged at 500*g* for 5 minutes, resuspended in PBS with 5% FBS and filtered through 70 µm cell strainers (CellTrix, Sysmex) before being counted with a NucleoCounter system (Chemometec), and then used for flow cytometry.

2.3.5 RNA sequencing: Flow cytometry of tumour endothelial

A total of 5×10^6 cells were stained in a final volume of 100 µl of antibody mix for 15-20 minutes, in ice, protected from light. Cells were subsequently washed with 2 ml PBS-5% FBS,

Table 2.3 Antibodies for Fluorescence-Activated Cell Sorting analysis of tumour endothelial cells

Antibody	Source	Cat#	Dilution	Application
PECy7 anti-mouse CD45 (clone 30-F11)	eBioscience	25-0451-82	1:600	FACS
PECy7 anti-mouse Ter119 (clone TER119)	eBioscience	25-5921-82	1:100	FACS
PECy7 anti-mouse CD150 (clone TC15-12F12.2)	Biolegend	115914	1:100	FACS
APC ef780 anti-mouse EpCAM (clone G8.8)	eBioscience	47-5791-82	1:400	FACS
PerCPef710 anti-mouse CD31 (clone 390	eBioscience	46-0311-82	1:250	FACS
APC anti-mouse VE-cadherin (clone BV13)	Biolegend	138006	1:300	FACS
BV786 anti-mouse CD105 (clone MJ7/18)	BD	564746	1:300	FACS
7-AAD Viability Staining Solution	Biolegend	420404		FACS
FACS = Fluorescence-Activated Cell Sorting				

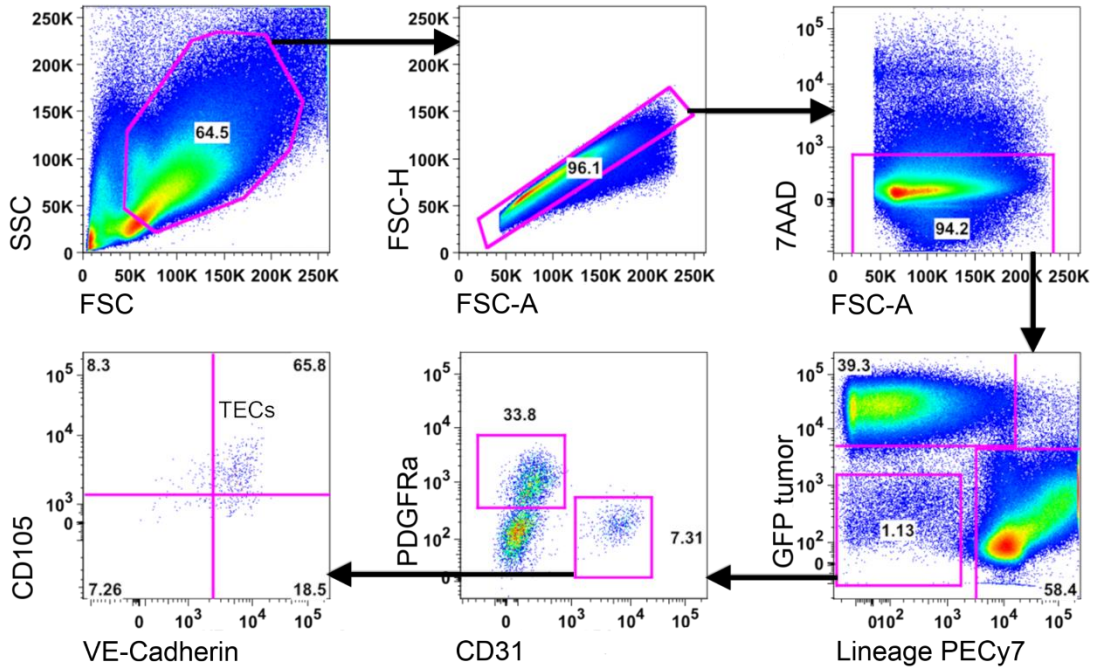


Figure 2.7 Fluorescence-activated cell sorting gating strategy for tumour endothelial cells for RNA sequencing.

centrifuged at 500*g* for 5 minutes and resuspended in 500 µl PBS-5% FBS. 5 µl 7-AAD (7-amino-actinomycin D) was added right before the sample acquisition. Sorting was performed by using a Fusion cell sorter (BD Biosciences). The antibodies used are listed below (Table 2.3). 100 cells per population were sorted in 4 µl of lysis mix (0.4% Triton X + RNAse Inhibitor (1:20) (Figure 2.7), dNTPs (10 mM), Oligo dT (10 µM) - according to the original Smart-seq2 protocol) and immediately processed for RNA-sequencing or stored at -80°C for a few days.

2.3.6 RNA sequencing: cDNA libraries using Smart-seq2 protocol

5.7 µl of the retro-transcription mix (see reference for details) was added to each sample. Retro-transcription was carried out according to the original Smart-seq2 protocol and cDNA was then pre-amplified for 15 cycles (285). After PCR pre-amplification, cDNA was purified using Ampure XP magnetic beads according to the manufacturer's instructions, in a ratio of 0.8 to 1 with cDNA, resuspended in 17.5 µl of buffer EB (Qiagen) and stored at -20°C. The quality and concentration of the cDNA generated were assessed using High-Sensitivity Bioanalyser kit (Agilent).

2.3.7 RNA sequencing: Illumina library preparation and sequencing

1 ng of pre-amplified cDNA was tagmented and indexed with Nextera XT DNA Sample Preparation kit (Illumina) according to the manufacturer's instructions. The product was purified with AMPure XP beads (1:1 ratio) and eluted in 17.5 µl of EB buffer (Qiagen). Samples were loaded on a High-Sensitivity DNA chip (Agilent Technologies) to check for library size and quality and concentration measured with the Qubit High-Sensitivity DNA kit (Invitrogen). Libraries were

pooled to a final concentration ranging between 2 nM and 10 nM and sequenced with Illumina Hiseq 4000 (25 bp single-end read) at the Wellcome Trust Centre for Human Genetics in Oxford.

After the adapters for sequencing were trimmed from single-end reads in samples (n = 8 per group), we aligned the reads to the mouse reference genome GRCm38/mm10 along with transcriptome information by Bowtie 2.2.6 and tophat2 v2.1.0. The aligned reads were used for estimating fold change of normalised expression level, FPKM (Fragments per Kilobase of transcript per Million mapped reads), for each gene by cufflinks-2.2.1. The consistency of significant change, false-positive rate < 0.05, was estimated using the package of non-parametric rank product in R with the contrast between normal and irradiated cells.

The differentially expressed gene set was put into GeneCodis web-based tool (http://genecodis.genyo.es/) to perform Panther Pathways Enrichment Analysis (286). Additionally, the differentially expressed gene set was also analysed with pathway analysis package GeneGo MetaCore (https://portal.genego.com/) to build biological networks and list the associated biological processes and diseases. A p-value of 0.05 was used as a cut off to determine significant enrichment of a pathway or annotated gene groups present in the MetaCore database.

2.4 MICROSCOPY

2.4.1 In vivo 2-photon microscopy

Tumour vasculature images were acquired with an inverted Zeiss LSM 880 microscope (Carl Zeiss AG). The microscope was connected to a tuneable Mai-Tai laser (Newport Spectra-Physics). An excitation wavelength of 940 nm was used. The peak excitation wavelength with a two-photon laser for tdTomato, which was the second fluorescent protein in our system is 1050 nm (287). Although the MaiTai laser can be tuned to up to 1100 nm, the power delivered to the sample dramatically decreases after ~950 nm, thus 940 nm wavelength was chosen as the optimal excitation wavelength to excite both fluorescent proteins at the same time. Moreover, the peak excitation wavelength for Qdot 705 vascular label used in the experiment is also between 920 – 940 nm. Therefore, our chosen excitation wavelength was close to the peak excitation wavelength for EGFP and Qdot's 705 and relatively high tdTomato excitation.

The emitted light was collected through Gallium Arsenide Phosphide (GaAsP) detectors with a steep bandpass filter of 535/22 (Semrock, FF01-535/22-25) for EGFP, and a 575/25 bandpass filter (Semrock, FF03-575/25-25) for tdTomato. A multi-alkali PMT detector with a bandpass filter of 700/75 (Semrock) was used to record Qtracker 705 signal. The alignment of the filters, dichroic beam splitters and detectors is shown in Appendix Figure S2.

A Zeiss 20x magnification water immersion objective (W Plan-Apochromat, 20 ×/1,0 DIC (UV) VIS-IR, Carl Zeiss) with an NA 1.0 was used to acquire Z stack-TileScan images with a dimension of 512 × 512 pixels in x and y. The space between the objective and window chamber was filled with skintact ultrasound gel (Leonhard Lang). Approximately 70 planes in z, with a step size of 5 µm were acquired. Voxel size in the x-y plane was 0.83 µm × 0.83 µm and 5 µm in z. While a 5 µm step throughout the z plane is not ideal, and a smaller step size closer to the objective and a larger step size towards the maximum depth would have increased the

information gained, for several reasons, this was not feasible. First, the ZEN software used with the Zeiss 880 microscope did not permit changing the step size optimization without dramatically slowing down the acquisition time. Second the animal license and protocols did not allow us to extend the acquisition time beyond three hours which would have been a necessary outcome of such alterations. Third, the algorithm that was used for segmentation relied on a step size of 5 microns.

2.4.2 Confocal microscopy

Whole tumour and Z-stack images were acquired with an inverted confocal spinning disc microscope (Andor Dragonfly, Oxford Instruments) equipped with an integrated laser engine, a Plan-Apochromate 20x/0.8 M27 objective. Hoechst, GFP/Alexa488, tdTomato/Alexa546 and Alexa633/647 were excited by 405 nm, 488 nm, 561 nm and 637 nm laser lines respectively through a dichroic, quad-band filter set with excitation ranges: 399-412, 482-495, 558-564 and 631-647. Images were acquired with 10% overlapping for stitching, emission filter band-pass 445/20, 525/30, 595/30, and 705/45. The emission signal was collected with an Andor Zyla 4.2 cMOS camera. Images were processed using Imaris (Bitplane) or FiJi (288).

2.4.3 Image post-processing

Although narrow and steep filters were used during image acquisition within the short wavelength bands for each fluorophore/protein in the two-photon imaging experiments, bleed through from tdTomato into the perfusion channel did appear, due to the extreme brightness of the tdTomato in our system. Reducing the laser intensity or changing the excitation

wavelength of the laser did not solve this issue. Thus, we employed a mathematical approach where we also relied on the fact that the signals from different fluorophores were also spatially separated within the tissue. This is because only tumour cells express the fluorescent protein EGFP while endothelial cells express the fluorescent protein tdTomato. Intravital images were post-processed with Imaris (Bitplane) channel arithmetic whereby signal from one channel was subtracted from the other one. Imaris was also used for visualising the acquired images.

2.4.4 Segmentation, skeletonization, and quantification microscopy derived images

Segmentation and skeletonization of the tumour vasculature from the post-processed intravital images was performed on a previously published segmentation algorithm with computational use at the University of Oxford Advanced Research Computing[2] facility, Oxford (289). For an in-depth description of the algorithm the reader is referred to "Learning to Extract Tumour Vasculature: Techniques in Machine Learning for Medical Image Analysis" by Russell Bates who developed the algorithm (290). In short, the algorithm computes in Python with the TensorFlow[3] and Kras[4] libraries to train and execute the algorithm. The training data set for the algorithm consists of 25 manually segmented tiles from the two-photon intravital images of size 512 × 512 × 70. For manual segmentation of the training set ITK-SNAP[5] and the NeuTube[6] software package for pruning was used.

As the tumour vasculature does not follow a hierarchy known from normal vasculature and, in some tumours, exhibits an extremely dense appearance, segmentation can be

[2] http://dx.doi.org/10.5281/zenodo.22558
[3] https://www.tensorflow.org/
[4] https://keras.io/
[5] http://www.itksnap.org
[6] http://www.neutracing.com/

challenging. To analyse the intravital images a convolutional neuronal network in the form of a U Net style convolutional neural network (U-Net 2D), as proposed by Ronnenberger et al (291), was used. Although analysis is done on slices rather than the whole stack of images, information is shared among neighbouring slices (292) enabling a 2D network to gain some 3D cues by combination with convolutional long short-term memory recurrent neural network units (293) for segmentation and skeletonization. In the final stage of image analysis, a skeletonization algorithm is usually applied. Although the algorithm in our case performs this step, due to uncertainty and variability the obtained skeleton can exhibit skeletons wider than one pixel. To counter this, a homotopic thinning algorithm (294) is applied. Refinement of the skeleton was one by removing artefactual branches shorter than 10 pixels or less than the parental vessel diameter.

Quantification of proliferative endothelial cells was performed with Imaris from fluorescent microscopic images with the following channels:

- Channel 1, representing all nuclei by labelling with Hoechst
- Channel 2 representing endothelial cell nuclei by immunofluorescent labelling of ERG
- Channel 3 representing endothelial cells by immunofluorescent labelling of CD31
- Channel 4 representing proliferating cells that are in a DNA replicative state at the time of EdU labelling

First, a mask and subsequent channel of the tumour area was created to calculate the actual tumour positive area of the image. Then, a mask for all nuclei (DAPI positive) was created with the area algorithm, defining nuclei as structures based on DAPI intensity and size between five and seven microns. The same algorithm was then applied to the EdU signal (channel) to quantify EdU positive nuclei. To define tumour endothelial cells an area algorithm for CD31 was applied and a distance map channel was created based on the CD31 output mask. Next, a mask with the

area algorithm (with the same parameters as for the DAPI algorithm was applied to the ERG channel) including a 0 to 0.5 micrometre distance restriction based on the CD31 area mask. With this approach only ERG positive nuclei within a CD31 positive area are allowed to be counted with high confidence all endothelial cell nuclei within a tumour section. To the quantified ERG positive cell nuclei area, a distance map was applied. Then an area algorithm with a distance of zero micrometre was applied to ERG to count proliferating tumour endothelial cell nuclei. Appendix 2.1 contains five tables with the parameters chosen for each algorithm (Table S2.1.1 -S2.1.5).

Measuring the hypoxic tumour area at the time of EF5 administration was performed with Imaris by first determining the tumour area of the thin tumour tissue sections, followed by applying an Imaris algorithm measuring the EF 5 positive area (Table S2.2.1) from which the percentage area was determined.

To quantify the coverage of the tumour vasculature with perivascular cells, thin tumour sections were immunofluorescent labelled with CD 31 for tumour vessels and NG2, a proteoglycan expressed on perivascular cells, namely pericytes. Immunofluorescent microscopic images were analysed using Imaris with algorithms for CD31 and NG2 displayed in Appendices respectively (Table S2.3.1 and S2.3.2).

Apoptosis in tumour endothelial cells was calculated from immunofluorescently labelled thin tumour sections by applying the area algorithm to CD31 labelled tumour vessels in three different fashions with the only difference being the number of pixels:

Small: 5 to 1500 pixels (Table S2.4.1)

Medium: 1500 to 3000 pixels (Table S2.4.2)

Large: 3000 and above pixels (Table S2.4.3)

Subsequently, distance maps were calculated on each new area masks, resulting in three distance maps for each, small, medium and large. Following this, an area algorithm was applied to the caspase3/7 channel including parameters for, small, medium and larger respectively, with a cut off 0 to 1 micrometre distance restriction (Table S2.4.4).

To analyse 80 micrometre thick tumour tissue sections first the tumour vasculature was segmented (Table S2.5.1) and a new channel was created. On this segmented image a filament trace algorithm was applied (Table S2.5.2). Cleaved caspase 3/7 positive branches and sprouts were then manually evaluated and the numbers for diameter, length and area extracted from the results of the filament algorithm, allowing back trace for each filament to be calculated.

2.5 STATISTICAL ANALYSIS

All statistical analyses were performed in Graph Pad Prism v8.2. A Pearson omnibus normality test was applied to data sets to assess data distribution. Several results were assessed: for normally distributed data; unpaired t-test (two groups); one-way ANOVA with Tukey's multiple comparisons (more than two groups); and one-way ANOVA with Dunnett's multiple comparisons (more than two groups compared to control group comparison). All values in this study represent means (M) and standard deviations (SD) with the exception that the graph bars in the comparison of the vasculature parameters show means and the standard errors of the mean (SEM). No statistical method was used to predetermine sample size. The investigators were not blinded to allocation during the experiments or the outcome assessment. Throughout the manuscript, the following symbols for statistical significance are used: *P<0.05, **P<0.01; ***P<0.001. Mice whose tumours ulcerated during experimental timelines were excluded from the study.

CHAPTER 3

In vivo Imaging of the Tumour Vasculature

3.1 INTRODUCTION

As described in detail in chapter 1.3, the response of the tumour vasculature to irradiation is incompletely understood. Various techniques and models have been deployed to investigate changes of perfusion as a measure of the function of tumour vasculature after irradiation. While several non-invasive techniques are available, such as magnetic resonance imaging, micro-computed tomography, and coherence tomography, they are unable to provide high-resolution information about the vascular network, and in particular, metrics about the perfused and non-perfused parts of the vascular network (295). Other approaches, such as immunofluorescence staining or corrosion casting (89), allow extraction of data at a higher resolution, yet can only be performed once on any tumour, thus eliminating the possibility of detailed longitudinal studies. Immunofluorescence staining has been used with intravital microscopy on hindbrains or postnatal retina models (296, 297). Besides the above-mentioned techniques, all *in vivo* approaches, there are many other *in vitro* and *ex vivo* techniques available to address questions such as signalling in angiogenic sprouting exemplified in the postnatal retina model (33, 298). Finally, different techniques have used tissue sections to attempt to extract the 3-dimensional structure of the blood vessel system, but again these only allow for obtaining information at one time point (88, 299).

We decided to investigate the tumour vasculature and its response to ionising radiation *in vivo* through two-photon fluorescence intravital imaging in combination with an abdominal window chamber. This approach confers some advantages: for example, fluorescent microscopy enables us to record structures at a high spatial resolution on a cellular level. Equipped with a two-photon laser generating photons with wavelengths > 800 nm, enhanced tissue penetration is possible (300, 301). Using both techniques together, produces detailed three-dimensional images of tumour's microvascular structure. Additionally, temporal imaging performed over a

period ranging from several days to weeks, corresponds to the timing of the initial response of the tumour vessels to ionising radiation with a window chamber approach. Furthermore, the abdominal window chamber allows tumours to grow to a larger size than other window chamber models (302, 303), which in turn offers a longer period of observation.

By combining intravital imaging with fluorescently labelled injectable agents, it is possible to trace perfused vessels repeatedly. However, large parts of the tumour vasculature can be poorly or non-perfused (95). Thus, intravital imaging where only injectable fluorescent blood pool labelling agents are used, allows only the perfused parts of the tumour vascular network to be studied (304). To overcome this limitation and visualise perfused and non-perfused tumour vasculature, genetically engineered mice are used. In this technique endothelial cells which express fluorescent proteins can be used (305) to construct a lineage trace . This use of endothelial cells generates labelling of the whole tumour vascular structure.

Several genetically engineered mouse models (GEMMs) with constitutive active or inducible promoters specific for endothelial cells have been generated in the past (305). Combining GEMMs with reporter mouse models, such as the ROSA26 model (306), can lead to the expression of fluorescent reporter proteins such as green fluorescence protein (GFP) or tdTomato, a red fluorescent protein derivate in endothelial cells. Theoretically, combining these two techniques allows labelling and spatiotemporal tracking. However, currently a GEMMs with sufficient labelling of tumour endothelium is missing and many GEMMs in an endothelial cell background report mixed results with different induction efficiencies.

Most GEMMs in the endothelial cell context are based on Cre-recombinase (305). The Cre is either constitutively active within the nucleus or requires induction with an agent such as Tamoxifen (307), to facilitate the recombination. In the latter case, the Cre is genetically engineered forming a chimeric construct with an oestrogen receptor ligand-binding domain keeping it spatially separated in the cytoplasm of the cell. The induction is facilitated by

translocating the protein from the cytoplasm to the nucleus (308, 309). This takes place when the Tamoxifen metabolite 4-hydroxytamoxifen (a synthetic oestrogen antagonist) binds to the Cre-oestrogen fusion protein. As a result, the protein is shuffled from the cytoplasm to the nucleus (306, 310). If a Cre-oestrogen chimeric construct is expressed in cells that also carry a *loxP* (locus of X(cross)-over in P1) floxed gene construct, the catalytic site of the cre-recombinase will detect the LoxP cleavage sides and introduce a site-directed somatic mutation. This leads to the excision of the gene sequence between the two LoxP cleavage sites (311). Although there are at least 12 different transgenic alleles available for endothelial expression, Tek (Tie2) and Cdh5 (VE-cad) are the most commonly used promoters for specifically targeting endothelial cells in GEMMs (305). Yet, there are other endothelial cell specific GEMMs with different induction efficiencies and expression patterns of the transgene. Some label only tip cells and others label not only endothelial cells but also other small subsets of hematopoietic cells that likely share a common progenitor cell with the endothelial cells (305). The inducible Cdh5 (VE-cad) mice are among those transgenic lines with a reported robust induction efficiency over a relative short induction interval of Cre-recombinase in all endothelial cells in early development and adulthood. In total, six different Cdh5-Cre-ERT2 inducible transgenic mouse lines are reported in the literature (312–317). Using the inducible Cre expressed specifically in endothelial cells along with a floxed fluorescent protein should allow for the expression of the fluorescent protein in the majority of endothelial cells. If high levels of the fluorescent protein can be achieved, it should be possible to visualize the entire tumour vascular network including sprouts and non-perfused vessels. Combined with a window chamber model, this would generate longitudinal imaging studies which follow the development of the tumour vascular network and map its response to therapies.

3.2 AIMS

This chapter describes the development of an *in vivo* model that enables the robust generation and imaging of fluorescently labelled endothelial cells in tumours. Development of this model sets the stage to investigate the development of the tumour vasculature and the effect of ionising radiation on a tumour in a window chamber setting. This will be achieved through the following processes/method:

1) Quantifying the percentage of labelled endothelial cells after Tamoxifen induction in genetically engineered mice
2) Evaluating the specificity of endothelial cells labelling: a previously reported subset of monocytes/macrophages was described to express the reporter gene. We have investigated if fluorescently labelled cells that are not endothelial cells were evident in our model.
3) Comparing perfused and non-perfused parts of the tumour vasculature
4) Implementing an abdominal window chamber with the developed transgenic model and intravital two-photon microscopy to image the developing tumour vasculature and analyse the obtained images with a custom-made algorithm to extract parameters describing vessel architecture.

3.3 RESULTS

3.3.1 Validation of the Cdh5-cre-ERT2 model

The need for a model that allows efficient induction of the expression of fluorescent proteins, specifically in endothelial cells of adult mice, led us to choose one of the available VE-cadherin models. Amongst the available transgenic mouse lines, we decided to use the Tg(Cdh5-cre-ERT2)^{1Rha} mice (VCAD) kindly provided by Prof. Sarah de Val (Ludwig Cancer Institute, Oxford, UK) and originally created and obtained from Prof. Ralf Adams (Max Planck Institute for Molecular Biomedicine, Münster, Germany) (314). These mice carry the Tg(Cdh5-cre-ERT2)1Rha transgene leading to the expression of the Tamoxifen-inducible cre-oestrogen receptor fusion protein under the control of the Cdh5 (Vascular Endothelial [VE]-Cadherin) promoter. VCAD female mice were then crossed with male reporter mice (ROTO) obtained from Jackson Laboratory (318). The progenies of the VCAD×ROTO mice (henceforth termed VEOM) carry both, the Ve- Cdh5-cre-ERT2 construct and the loxP-flanked STOP tdTomato cassette.

Upon Tamoxifen induction, the transcribed Cre recombinase-oestrogen receptor fusion protein in cells expressing VE-cadherin, that is, in endothelial cells, is relocated from the cytoplasm to the nucleus leading to the recombination and excision of the LoxP-flanked STOP cassette (Figure 3.1.1A). As a result, the expression of the fluorescent reporter protein tdTomato is enabled, leading to fluorescently labelled endothelial cells, including tumour endothelial cells (Figure 3.1.1B-C and 3.2.1B). This specificity is achieved because VE-cadherin is solely expressed in endothelial cells in adult mice.

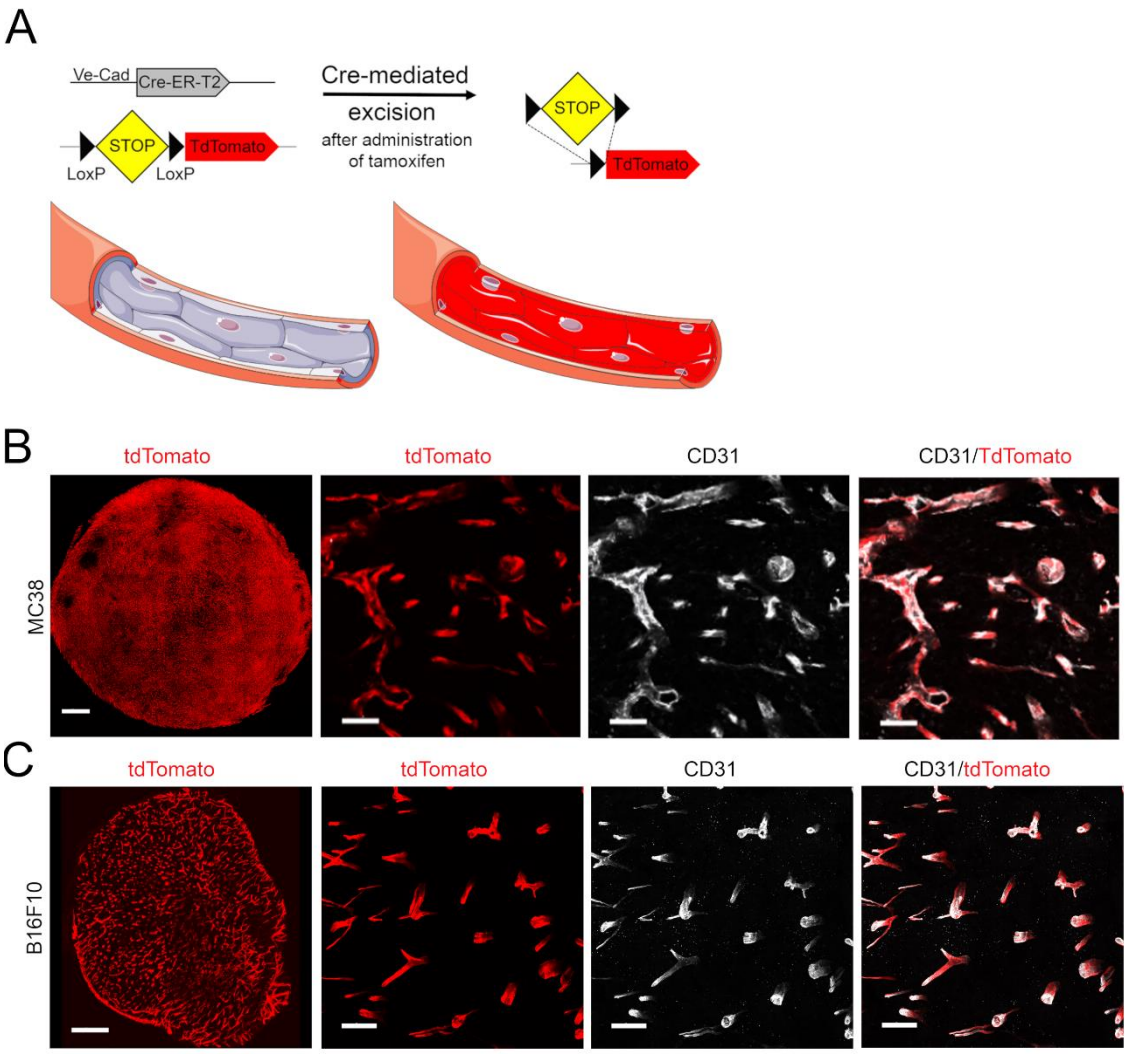


Figure 3.1.1 Expression of tdTomato in endothelial cells of VEOM mice after Tamoxifen administration.

(A) Schematic: Heterozygotes from VCAD and ROTO mice express tdTomato reporter protein in endothelial cells after Tamoxifen administration

(B) Confocal microscopy maximum projection images from an MC38 tumour from mice expressing tdTomato in tumour endothelial cells and magnification of the same tumour stained with CD31 as an endothelial cell marker. Scale bars: 1 mm and 50 µm in magnification; representative immunofluorescent image of n=3 mice.

(C) Confocal microscopy maximum projection images of a B16F10 tumour from mice expressing tdTomato in tumour endothelial cells and magnification of the same tumour stained with CD31 as an endothelial cell marker. Scale bars: 1 mm and 50 µm in magnification; representative immunofluorescent image of n=3 mice.

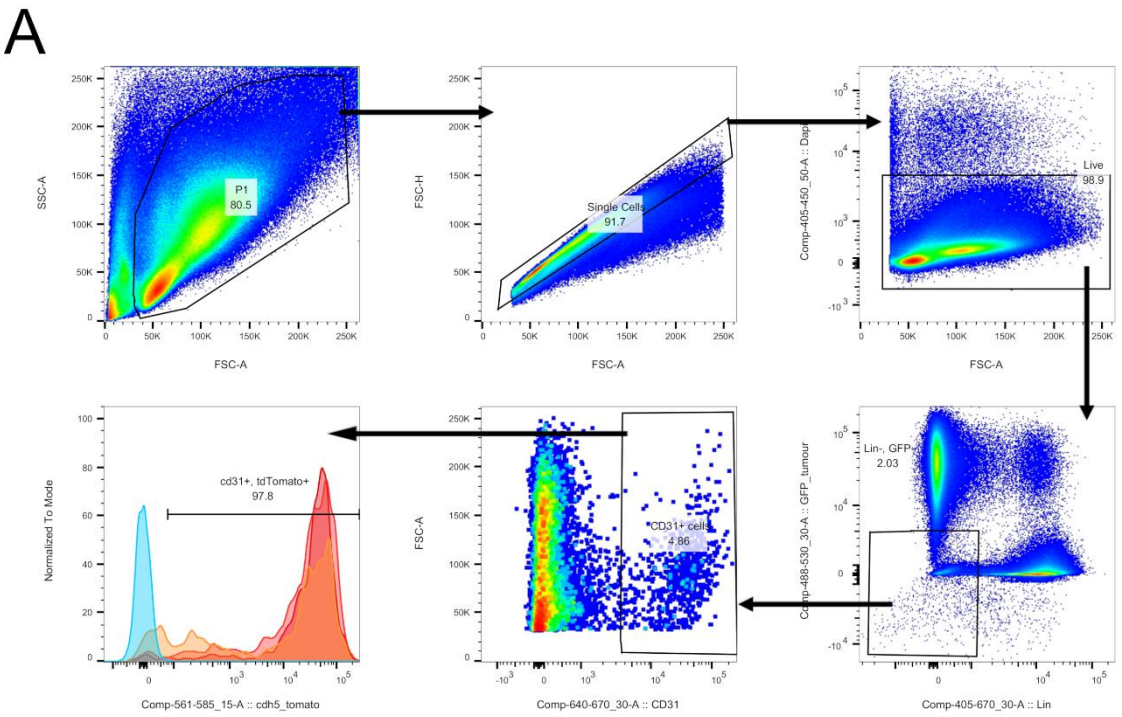


Figure 3.1.2 Expression of tdTomato in endothelial cells of VEOM mice after Tamoxifen administration.

(A) Flow cytometry analysis of tdTomato positive tumour endothelial cells. Gating strategy for Flow Cytometry of GFP positive MC38 tumour samples for quantifying the tdTomato induction efficiency in endothelial cells after Tamoxifen administration. (D to Dv) Gating strategy. (D) Forward scatter vs side scatter, (Di) single cells, (Dii) live cells, (Diii) GFP negative, lineage negative ($CD45^-$, $TER119^-$, $CD150^-$), (Div) Forward scatter vs CD31 positive, (Dv) tdTomato positive of all CD31 positive cells. (n=3 mice).

The mice were screened by visual inspection for induction efficiency by imaging the ear of each mouse after Tamoxifen induction. Mice with an induction greater than approximately 95% were used for subsequent experiments, which was confirmed by FACS analysis of tumour endothelial cells to reinforce the quality of the visual inspection (Figure 3.1.2A). Tamoxifen administration via gavage of 0.1 mL Tamoxifen/oil over 10 days (concentration: 10 mg Tamoxifen/mL) led to approximately 20% of mice with >95% induction. To confirm the efficiency of Cre driven expression of tdTomato in endothelial cells in tumours, flow cytometry analysis of tumours from mice with >95% induction was performed on the dissociated tumours (Figure 3.1.1D).

Flow cytometry-gating shows the strategy used to identify endothelial cells. This strategy excluded cell doublets, dead cells (DAPI positive), as well as the haematopoietic cell lineage population (CD45 positive, TER119 positive and CD150 positive cells), and tumour cells (GFP positive). The remaining cells were gated on CD31 to identify endothelial cells (Figure 3.1Di-Dv). The percentage of tdTomato positive and CD31 positive endothelial cells after Tamoxifen administration measured with flow cytometry confirms the microscopic evaluation of recombination and induction of tdTomato expression after Tamoxifen administration (Figure 3.1.1Dv), with an average induction of tdTomato in endothelial cells of previously selected mice of 97%.

Monvoisin and colleagues who described a similar system *Tg(Cdh5-cre/ERT2)*^{CIVE23Mlia} reported substantial labelling of endothelial cells in normal and disease settings throughout the vascular tree including tip cells, stalk cells, and quiescent endothelial cells. VE-cadherin is mainly expressed in endothelial cells but has also been reported to be expressed in bone marrow-derived cells, in early developmental stages. Roodhart *et al* further reported a small subset of monocytes/macrophages positive for their reporter gene, if activated by the Cdh5-cre-ERT2 system after chemotherapy (29). This subset was also infiltrating the tumour microenvironment and lining the tumour vasculature after chemotherapy. Because we wanted to investigate the tumour vasculature based on fluorescently labelled tumour endothelial cells, we investigated if, in our setting, this reported subset of monocytes/macrophages is detectable in organs, in non-irradiated, and in irradiated tumours.

To this end, VEOM mice injected with MC38 or B16F10 tumour cells were used to obtain 80 to 100-micrometre thick tissue sections from organs (kidney, lung, heart, liver) and tumours (MC38 and B16F10). These sections were fluorescently stained with antibodies for markers for endothelial cells (anti-CD31), macrophages (anti-CD68), monocytes (anti-GR1), and general immune cells (anti-CD45) in organs (Figure 3.1.3) and tumours (Figure 3.1.4). As expected, the

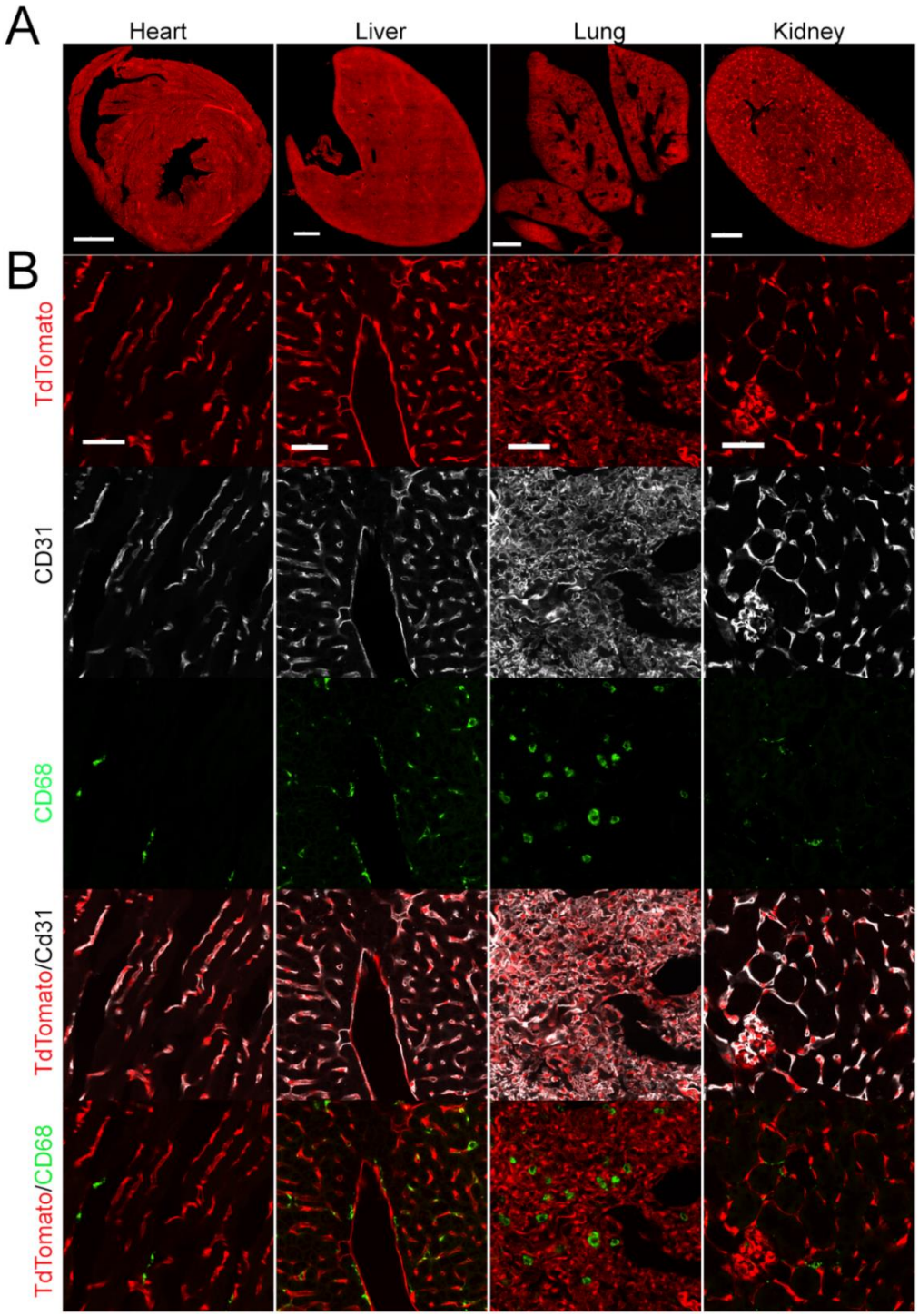


Figure 3.1.3 Evaluation of tdTomato labelling in endothelial cells after Tamoxifen induction in mouse organs.

(A) Representative overview confocal microscopy maximum projection images of mouse organs expressing tdTomato (red) in endothelial cells. From left to right: heart, liver, lung, and kidney. Scale bar: 1mm.

(B) Representative confocal microscopy maximum projection images of mouse organs expressing tdTomato (red) in endothelial cells. Sections were stained for endothelial cell with anti-CD31 (white) and macrophages anti-CD68 (green). Merged images show tissue stained for tdTomato (red) + CD31 (white) and tdTomato (red) + CD68 (green). Scale bar: 50 µm.

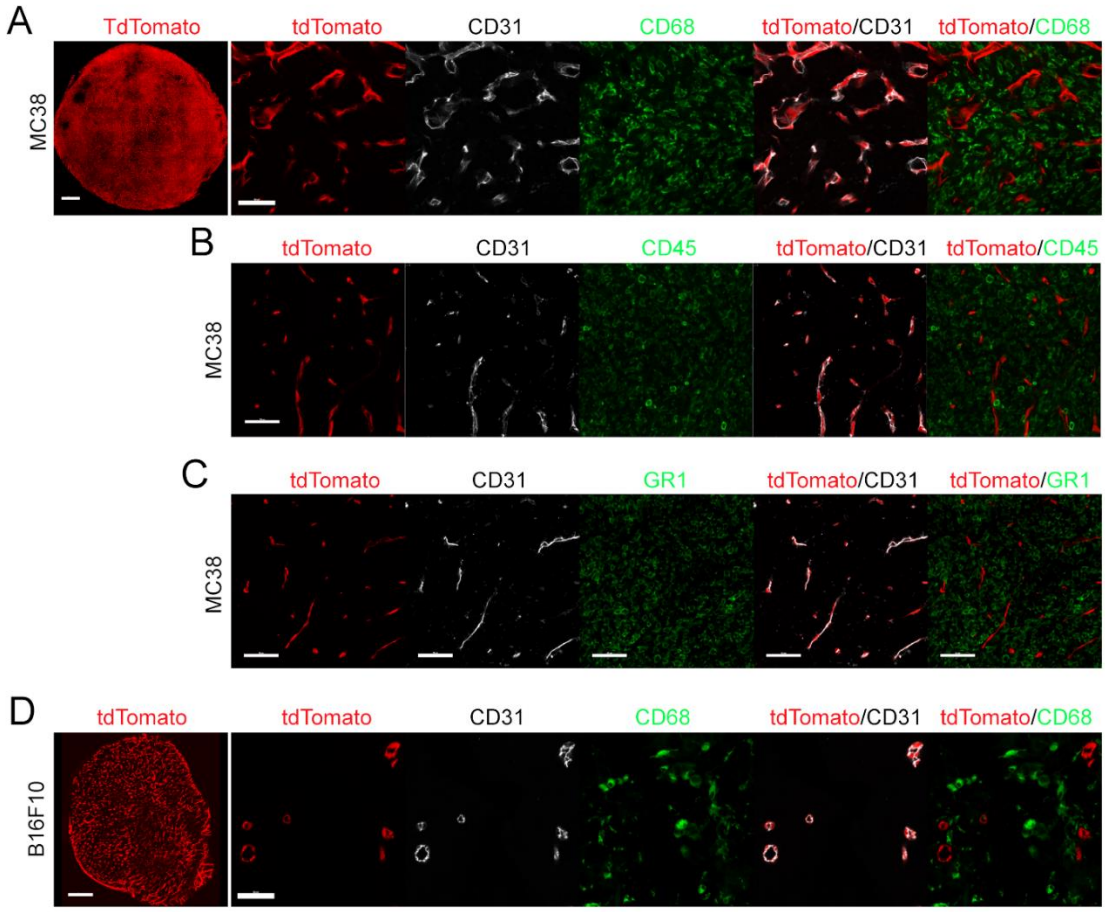


Figure 3.1.4 Immunofluorescence evaluation of tdTomato expression in tumour endothelial cells after irradiation in MC38 and B16F10 tumours.

(A) Representative overview of confocal microscopy maximum projection image (left panel) and of confocal microscopy maximum projection images (right panel) of MC38 tumour sections. Tumours expressing tdTomato in endothelial cells stained for the endothelial cell marker anti-CD31 antibody and macrophage marker anti-CD68 antibody. Merged images display tdTomato + CD31 and tdTomato + CD68. Scale bar: 1 mm in the overview image and 50 µm in the high-power image.

(B) Representative confocal microscopy maximum projection images of MC38 tumour sections. Tumour sections obtained from tumours expressing tdTomato in endothelial cells were stained with the vessel marker anti-CD31 antibody and general immune marker anti-CD45 antibody. Merged images display tdTomato (red) + CD31 (white) and tdTomato (red) + CD45 (green). Scale bar 50 µm in the high-power images.

(C) Representative confocal microscopy maximum projection images of MC38 tumour sections. Tumour sections obtained from tumours expressing tdTomato in endothelial cells were stained with the vessel marker anti-CD31 antibody and monocyte marker anti-GR1 antibody. Merged images display tdTomato + CD31 (white) and tdTomato + GR1 (green). Scale bar 50 µm in the high-power image.

(D) Representative confocal microscopy maximum projection image (left) and confocal microscopy maximum projection images (right panel) of B16F10 tumour sections. Tumour sections obtained from tumours expressing tdTomato in endothelial cells were stained with the vessel marker anti-cd31 antibody and macrophage marker anti-CD68 antibody. Merged images display tdTomato plus anti-CD31 and tdTomato plus anti-CD68. Scale bars 1 mm in the overview image and 50 µm in the high-power image respectively.

immunofluorescence staining with these markers did result in double staining of tdTomato positive, CD31 positive endothelial cells in all examined organs and tumours. While we successfully stained immune cells such as macrophages and monocytes, we could not detect the reported subpopulation of macrophage/monocytes, expressing tdTomato in either organs (Figure 3.1.3) or in tumours (Figure 3.1.4A-D).

We next investigated whether we could discriminate and record differences between perfused and non-perfused tumour vessels. We therefore inoculated GFP labelled MC38 tumour cells and surgically implanted an abdominal window chamber in VEOM mice. Upon tumour growth, we imaged the sprouting tumour vasculature to determine whether perfused and non-perfused vessels could be discriminated (Figure 3.3A). VEOM mice were injected intravenously with a fluorescent blood pool labelling agent (quantum dots 705-vascular marker). This approach enabled us to record and differentiate tumour cells (green), endothelial cells (cyan) and perfused (red) and non-perfused blood vessels. Figure 3.1.5 shows a representative single stack two-photon microscopy image depicting perfused vessels, non-perfused vessels (stars), and sprouting endothelial tip cells (arrows).

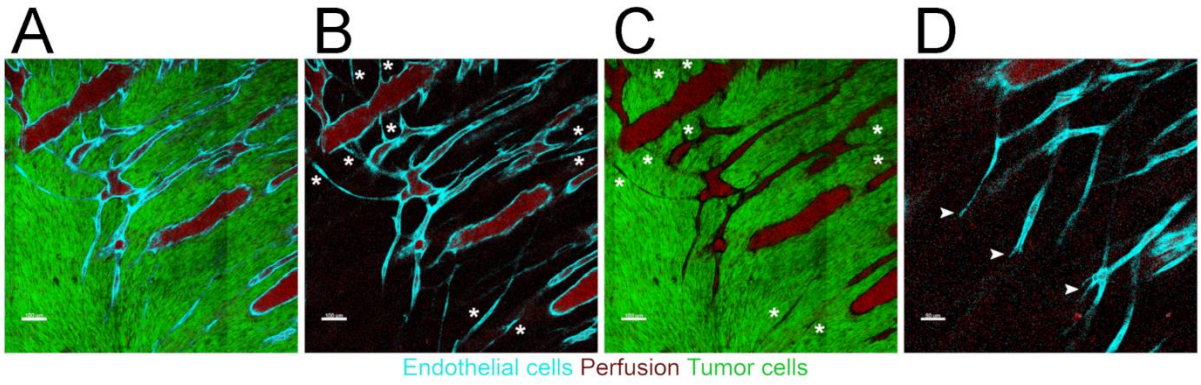


Figure 3.1.5 *In-vivo* two-photon microscopic image of a GFP MC38 tumour in a VEOM mouse.

(A) Representative 2-photon microscopy image of a MC38 tumour. GFP positive tumour cells (green), TECs (cyan), and infused Qdots (red) indicating perfused vessels. **(B/C)** Asterisk, non-perfused tumour vessels. **(D)** Arrowheads, tumour vessel sprouts. Scale bars: A to C 50 µm respectively and D 100 µm.

3.3.2 Intravital imaging of the tumour vasculature in the MC38 tumour model

The verification of the VEOM mouse model and the possibility to image perfused and non-perfused tumour vasculature led us to use these mice to trace tumour vascular development. To investigate how different parameters change over time, we injected 2.5×10^5 MC38 GFP or B16F10 GFP tumour cells into the thin fat layer above the abdominal muscle of VEOM mice. We surgically implanted an abdominal window chamber on top of the tumour injection side. This setting enabled us to follow tumour vascular development for up to 3 weeks after tumour induction. Once the tumour reached a size 3 mm in diameter and perfused vessels were detectable, two-photon microscopy imaging acquisition was performed daily to trace the development of the tumour vascular network (Figure 3.2.1). Intravital imaging of the tumours in 24-hour time intervals revealed the dynamic sprouting angiogenesis in MC38 tumours. We then used a previously published algorithm[7] to segment the acquired fluorescent images (Figure 3.2.2).

[7] R. Bates, B. Irving, B. Markelc, **J. Kaeppler**, R. Muschel, V. Grau, J. A. Schnabel, "Extracting 3d vascular structures from microscopy images using convolutional recurrent networks", *arXiv preprint arXiv:1705.09597*, 2017.

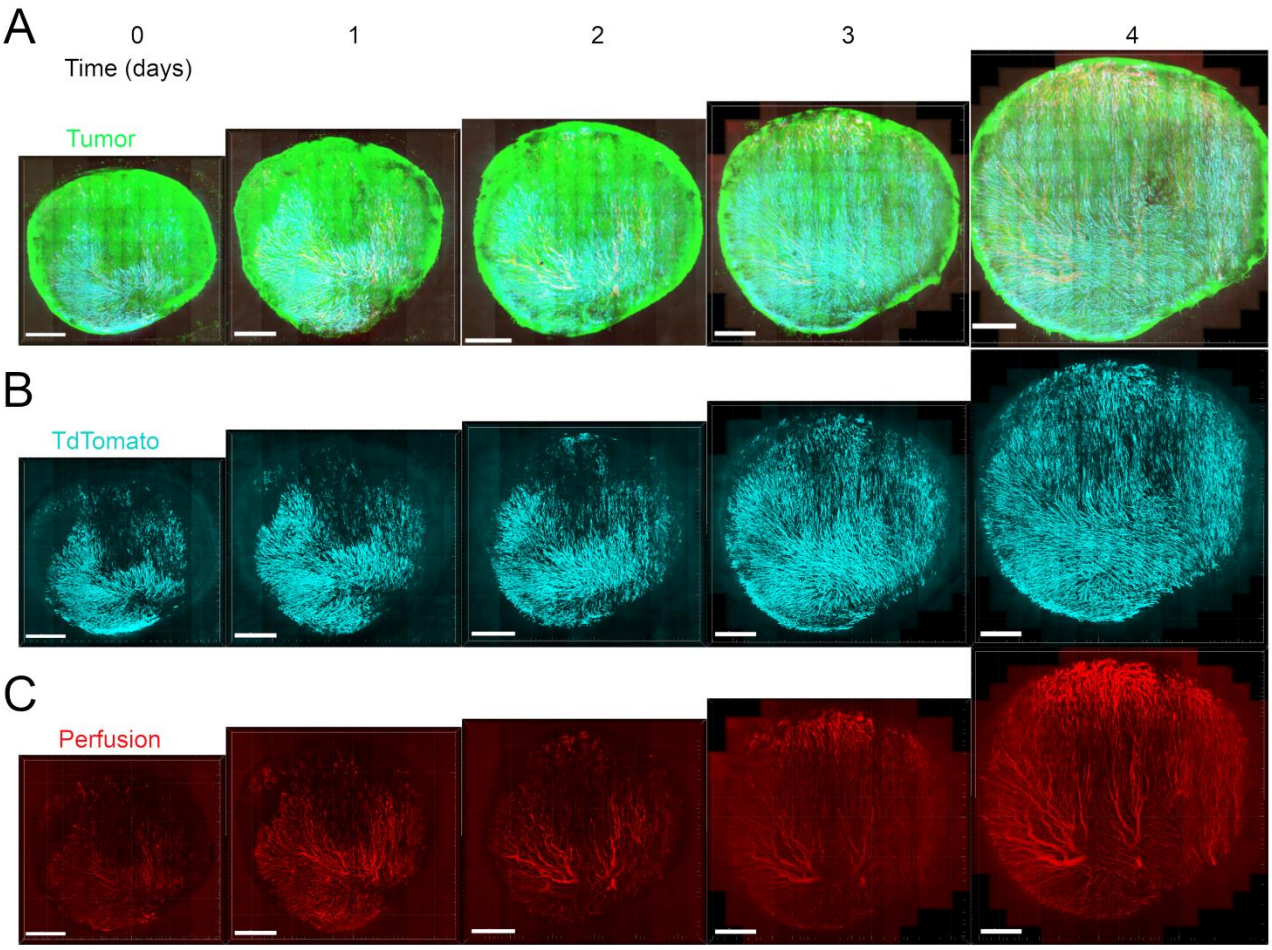


Figure 3.2.1 Time-lapse intravital microscopy of MC38 tumours in VEOM mice. The developing tumour vasculature was imaged over time in an abdominal window chamber model with two-photon microscopy.

(A) Representative two-photon images of GFP-labelled tumour cells with tdTomato labelled tumour endothelial cells (cyan) and perfused blood vessels (red). Scale bars: 1mm.

(B) Representative two-photon images of tdTomato labelled tumour endothelial cells (cyan). Scale bars: 1mm.

(C) Representative two-photon images of perfused blood vessels (red). Scale bars: 1mm.

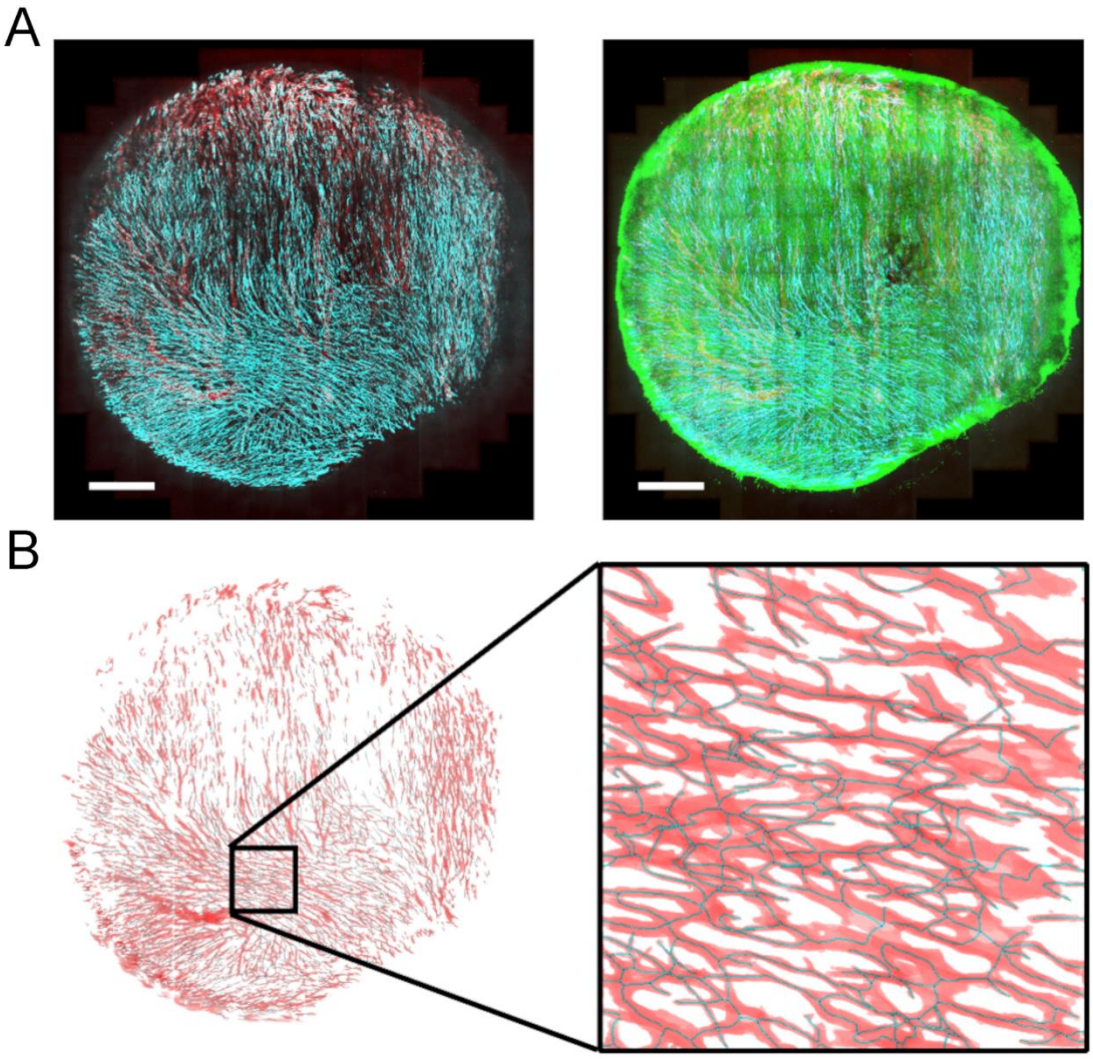


Figure 3.2.2 Segmentation of the acquired intravital images [8]

(A) Representative two-photon images of a tumour vessel network obtained through an abdominal imaging window. Tumour endothelial cells (cyan), perfusion (red), and GFP expressing tumour cells (green). Scale bar: 1 mm.

(B) The obtained 3D images (as shown in **(A)**) are subsequently segmented and skeletonised. Left whole tumour segmented and skeletonised, right zoom of the image. Segmented vessels are represented in red with their centreline (skeleton) as blue lines.

[8] Figure 3.2.2 used from our publication under review, pre-published version available under bioRxiv **doi:** https://doi.org/10.1101/640060 Miguel O. Bernabeu, Jakub Köry, James A. Grogan, Bostjan Markelc ,Albert BeardoRicol, Mayeul d'Avezac, **Jakob Kaeppler**, Nicholas Daly,James Hetherington, Timm Krüger, Philip K. Maini, Joe M. Pitt-Francis, Ruth J. Muschel, Tomás Alarcón, Helen M. Byrne, (2019), Abnormal morphology biases haematocrit distribution in tumour vasculature and contributes to heterogeneity in tissue oxygenation, PNAS [under review]

This algorithm allowed us to extract multiple parameters from the images of the tumour vasculature and follow the changes of those parameters during tumour growth. These were: **vessel length**, representing the length between two vessel branch points; **vessel diameter**, representing the diameter of a vessel between two vessel branch points; **vessel tortuosity**, measured as chord-length-ratio (CLR), the ratio between the chord connecting two ends of a curve and the length of the curve; **vessel direction,** as the local directionality of `branches' within a local radius; **the total number of sprouts**, calculated from the total amount of vessels segments, where one end is not connected to another segmented; **length to diameter ratio**, **the fraction of perfused vessel** over all vessels, the **fraction of vessels shorter or longer** than a given value and the **local density** of branch points. Because X and Y dimensions of the images were much larger than the Z dimension, we measured the local density of branch points in branch points per mm^2.

Some parameters remained unchanged over the time period of imaging in MC38 tumours such as vessel tortuosity measured as cord to length ratio (Figure 3.2.3A). Values maintained on an average between 0.6 to 0.8, where a value closer to = 1 would represent a straighter vessel branch and a value closer to = 0 would represent branch more bent (where a value of zero would represent a circular blood vessel branch). We calculated Pearson's R coefficients of vessel tortuosity to vessel length and found a negative correlation ranging from -0.26 to -0.51 (Figure 3.2.4A). These values indicate that longer vessels were more tortuous on average than shorter ones (Figure S3.2.4B and C). While tortuosity measured by the cord to length ratio displays an intrinsic value for each branch of a blood vessel, it does not supply information about the local spatial direction between two vessels in a tumour. Instead, directional coherence is a measurement of regional tortuosity of the vascular network and reflects the directionality of vessel branches in relation to each other (Figure 3.2.3B). Average directional coherence of tumour vessels detected did not change with tumour growth, indicating that the tumour vasculature does not become more chaotic. However, a dynamic change of the directional values within local tumour areas was observed (Figure S3.1C). This

reflects the dynamic or chaotic nature of tumour vessels during vascular growth as a whole (Figure 3.2.1).

Other parameters that were obtained from segmented tumour vasculature are diameters and lengths of vessel branches where a vessel branch is defined as the section of a vessel between two bifurcations, i.e. the distance between two vessel splits. We first looked at the vessels branch diameters. These increased on average by around 40% from 25 micrometres to 35 micrometres throughout the course of the experiment (Figure 3.2.3C). The development of vessels with larger diameter was accompanied by the development of longer vessels.

We next wanted to know if there was a change of perfused vessels in MC38 tumours over time. The fraction of perfused vessels showed a slight upward trend that, however, did not meet statistical significance (Figure 3.2.3D). Yet, Pearson's correlation of median diameter and perfusion of control samples resulted in positive R-values ranging from 0.24 – 0.66 (Figure 3.2.5A and B). We investigated whether we could detect an increase of perfusion in vessel branches with a larger diameter in control samples. We calculated the diameter of perfused and non-perfused vessels over time (Figure 3.2.5C). Indeed, the diameter across tumours of non-perfused vessels remained at a steady level; in contrast, the diameter of perfused vessels increased over time, suggesting that vessels with a larger diameter are more likely to be perfused.

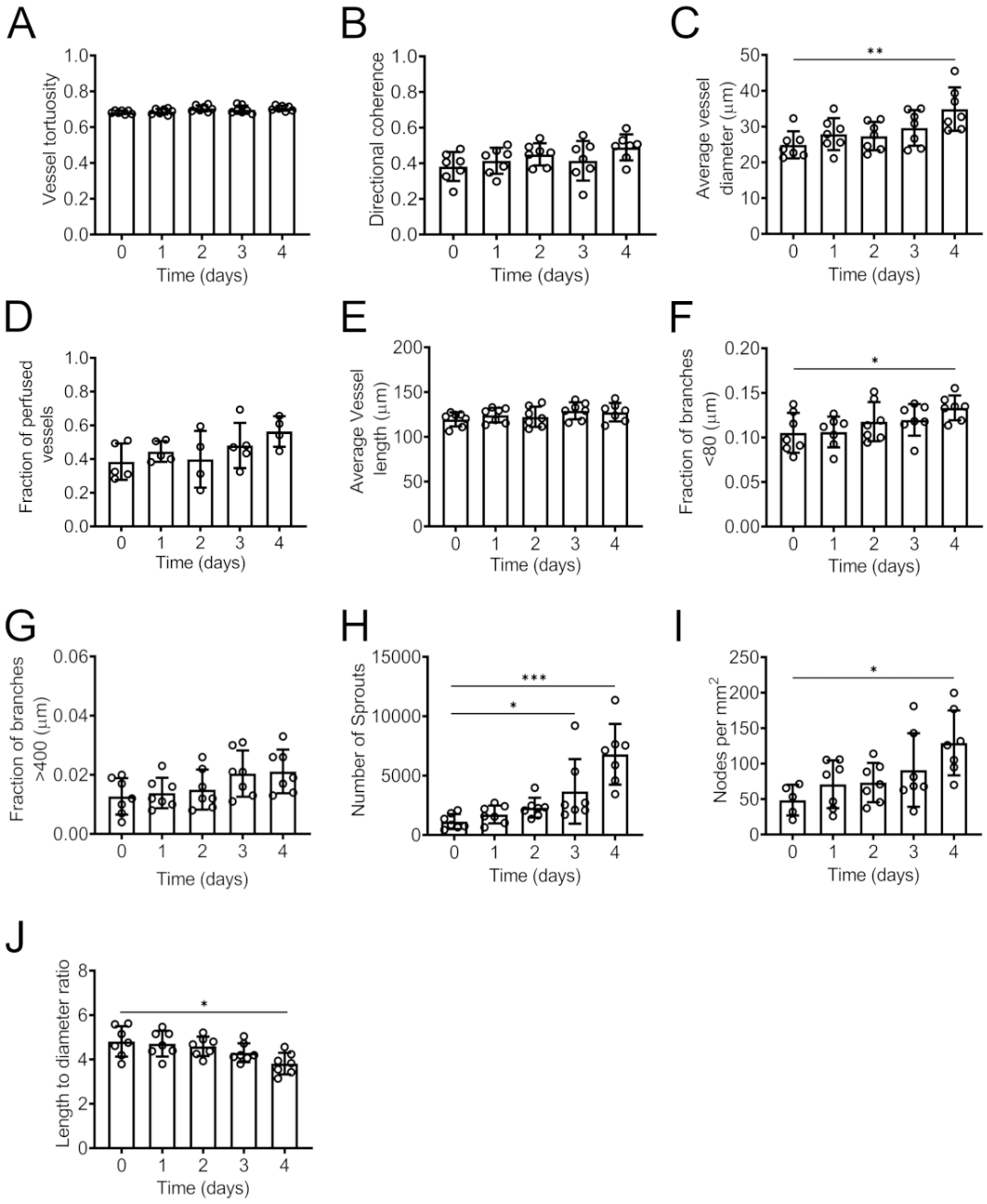


Figure 3.2.3. Quantification of time-lapse intravital microscopy images of MC38 tumours in VEOM mice. The following parameters were quantified from the segmented images: **(A)** vessel tortuosity, **(B)** directional coherence, **(C)** diameter, **(D)** perfusion, **(E)** vessel length, **(F)** fraction of branches <80 µm, **(G)** fraction of branches >400 µm, **(H)** number of sprouts, **(I)** nodes per mm^2, and **(J)** length to diameter ratio. Error bar represents mean ± SD, *P<0.05, **P<0.01 by one-way analysis of variance with Tukey's multiple comparisons (ANOVA) n = 7.

We then asked whether we could observe an increase in tumour vessel length during tumour growth. Average vessel branch length in MC38 tumours ranged from 100 to 150 micrometres and did not increase in length while we observed tumour growth (Figure 3.2.3E). Upon separating vessels according to length, we measured an increase in the fraction of branches that were shorter than 80 micrometres (Figure3.2.3F). This is consistent with ongoing sprouting angiogenesis throughout tumour growth in MC38 tumours. In comparison, longer vessels with a distance between branches of greater than 400 micrometres (Figure 3.2.3G) represented only a small fraction of the total vessels within the tumour. Nevertheless, the fraction of vessels with reduced branching showed a slight upward trend, which, however, was not statistically significant. In the MC38 tumour model, very long vessels, as well as vessels with large diameters, were scarce.

We next quantified the number of sprouts per tumour in MC38 during tumour growth, which increased with time (Figure 3.2.3H), reflecting the high angiogenic capacity of this tumour model. To ask if this was just due to the increased tumour size, we calculated branch density, reflected as the number of vessel branches per square millimetre (Figure 3.2.3I). This parameter increased with tumour size indicating a general increase of sprouting during tumour growth and an increase in interconnectivity between tumour vessels. We then asked whether this would influence the length to diameter ratio. We have recently suggested that a small L/D value (i.e. < 6) might bias haematocrit distribution in the tumour vasculature. Therefore, we were interested to see how this value develops over time in a growing tumour (Figure 3.2.3J). Indeed, the L/D ratio decreases over time in the MC38 tumour model, indicated by the increase of vessel diameter over vessel length that did not change during tumour growth.

A

	Control	tortuosity versus vessel branch length				
Days		0	1	2	3	4
	1	-0.5	-0.51	-0.48	-0.45	-0.37
	2	-0.44	-0.35	-0.43	-0.41	-0.43
	3	-0.49	-0.45	-0.39	-0.31	-0.31
	4	-0.48	-0.43	-0.34	-0.45	-0.47
	5	-0.48	-0.45	-0.46	-0.51	-0.48
	6	-0.42	-0.36	-0.29	-0.35	-0.45
	7	-0.41	-0.38	-0.26	-0.3	-0.4

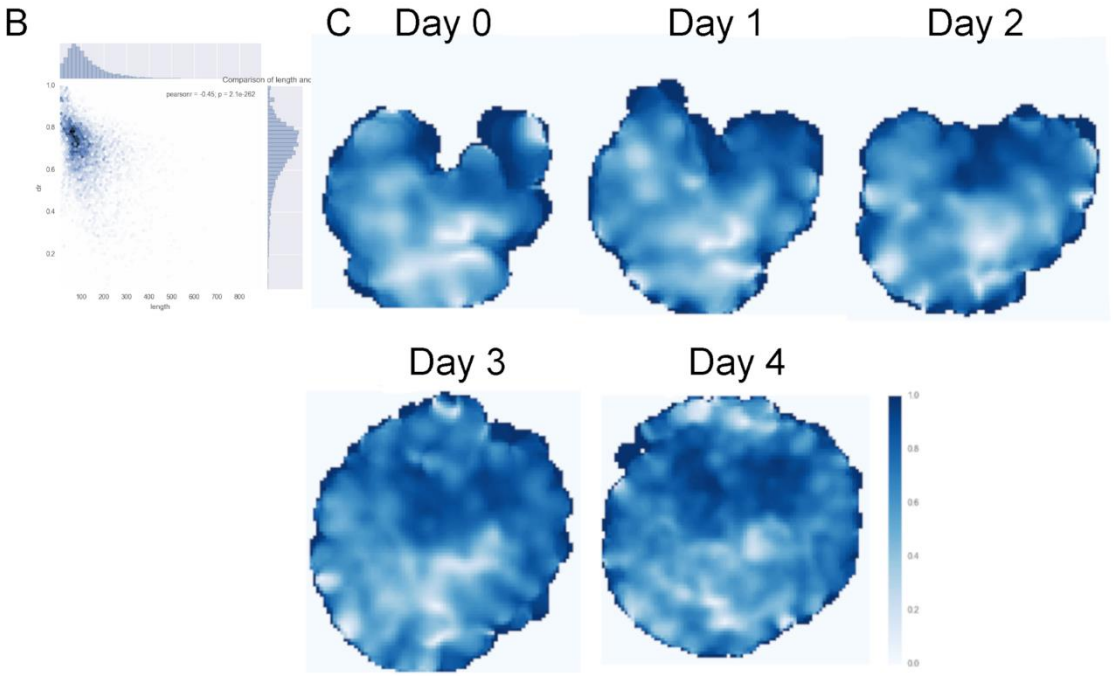


Figure 3.2.4 MC38 tumour vascular parameters:

(A) Table with R-values correlating tortuosity (Y-axis) and length (X-axis) with values for each day and each tumour calculated in the first column second column P-value calculated for each day. N=7.

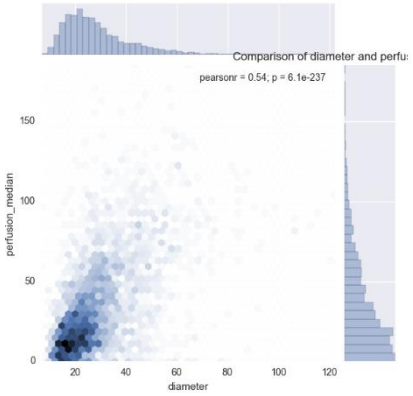
(B) Representative correlation of tortuosity versus length.

(C) Representative directional coherence map originating from fluorescent images and calculated with the algorithm. Blue = a more coherent area. White = a less coherent area.

A

	Control	perfusion vs diameter				
Days		0	1	2	3	4
	1	0.34	0.38	0.34	0.46	0.43
	2	0.32	0.38	0.37	0.45	0.54
	3	0.24	0.53	0.51	0.55	0.61
	4	0.41	0.54	0.54	0.6	0.66

B



C

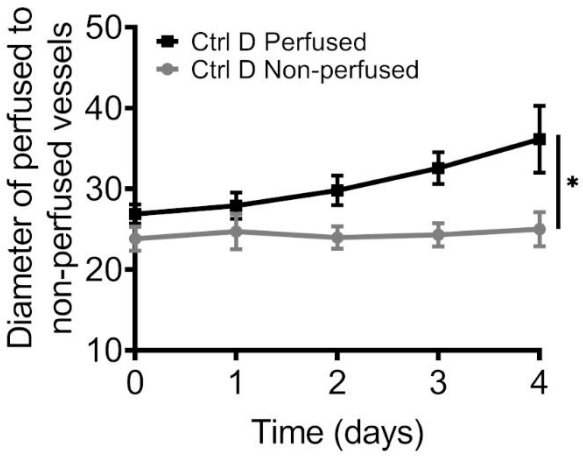


Figure 3.2.5 MC38 tumour vascular parameters

(A) Table with R-values correlating perfusion (Y-axis) and diameter (X-axis) with values for each day and four representative tumours. R-values are followed by the respective P-value. N = 4.

(B) Representative correlation plot of perfusion vs diameter.

(C) Calculation of vessel diameter of perfused to non-perfused vessels. N=7 for control samples. Error bars represents mean ± SEM, *P <0.05, **P <0.01. Statistical analysis of all data by analysis of variance (1 way-ANOVA) with Tuckey's multiple comparison test.

3.3.3 Intravital imaging of the tumour vasculature in the B16F10 tumour model

The tumour vasculature varies greatly between tumour types. Intratumoral heterogeneity of the vasculature has been previously described (33). In contrast to MC38, tumours originating from the B16F10 melanoma cell line grow faster. The vasculature developing from these tumours showed a more heterogeneous vascular network (Figure 3.3.1A and B) and slightly higher perfusion (Figure 3.3.1C) yet demonstrated decreased evidence of angiogenesis. For example, we observed areas that mainly consist of larger vessels with larger diameters and other areas with increased microvessel density.

Like MC38, VEOM mice were injected with 2.5×10^5 B16F10 cells in the thin fat layer above the abdominal muscle followed by surgical implantation of an abdominal window chamber. Two-photon microscopy imaging acquisition was performed with daily imaging of the same tumour. However, due to the aggressive nature of growth of this cell line *in vivo* imaging was started at a smaller tumour size (Figure 3.3.1). For the growth curve, please see Figure 4.1. Daily intravital imaging revealed a vascularised bed with well-perfused vessels from an early stage (Figure 3.3.1C).

As in the previous tumour model, we first quantified vessel tortuosity and directional coherence. Both parameters showed no differences during tumour growth (Figure 3.3.2A and B). Vessel tortuosity stayed roughly at a value of 0.7, indicating relatively straight vessel branches like the MC38 tumour model. To test whether there is a difference in vessel straightness between short and long vessels, we performed Pearson's R coefficient correlating tortuosity to branch length.

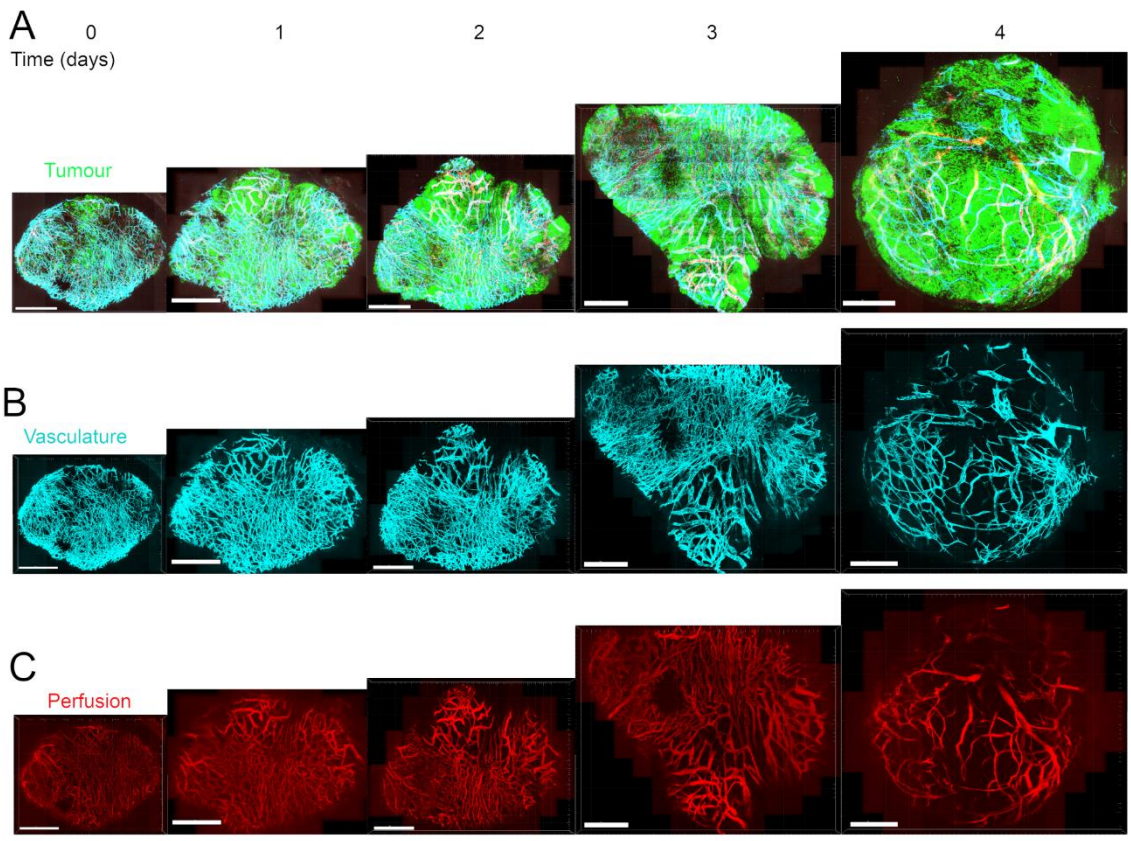
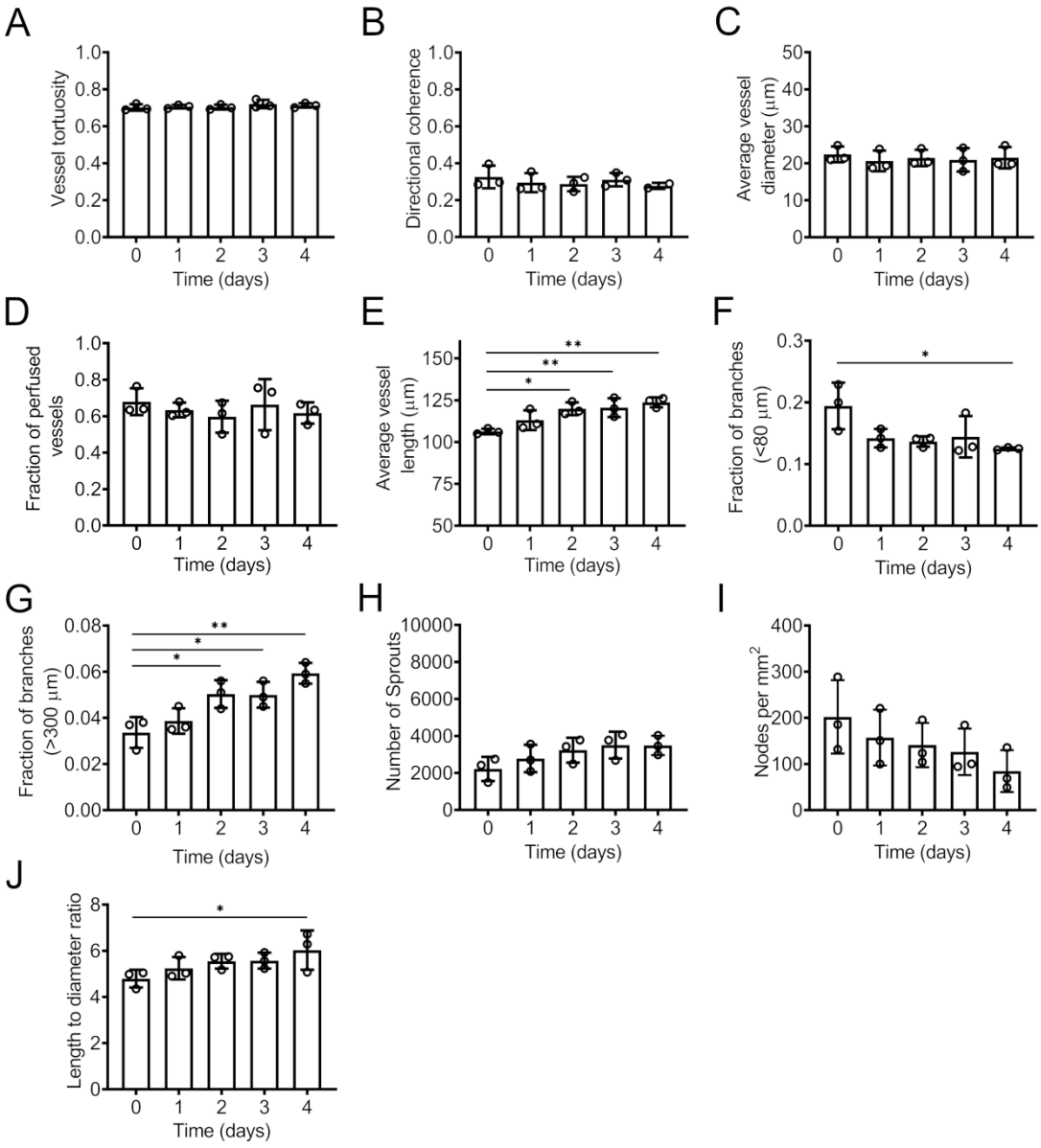


Figure 3.3.1 Time-lapse intravital microscopy of a B16F10 tumour in VEOM mice. Representative intravital images of the developing tumour vasculature growing in an abdominal window chamber model acquired over time with two-photon microscopy with:

(A) Representative two-photon images of GFP-labelled tumour cells (green) with tdTomato labelled tumour endothelial cells (cyan) and perfused blood vessels (red). Scale bars: 1 mm.

(B) Representative two-photon images of tdTomato labelled tumour endothelial cells (cyan). Scale bars: 1 mm.

(C) Representative two-photon images of perfused blood vessels (red) labelled with Qtracker 705. Scale bars: 1 mm.



3.3.2 Quantification of time-lapse intravital microscopy images of B16F10 tumour in VEOM mice. The developing tumour vasculature was imaged over time in an abdominal window chamber model with two-photon microscopy. The following parameters were quantified from the segmented image each day: **(D)** vessel tortuosity, **(E)** directional coherence, **(F)** perfusion, **(G)** number of sprouts, **(H)** fraction of branches <80 µm, **(I)** fraction of branches >400 µm, **(J)** length to diameter ratio, **(K)** nodes per mm^2, **(L)** vessel length, and **(M)** vessel diameter. **(N)** The diameter of perfused to the non-perfused vessel in B16F10 tumours. Error bar represents mean ± SD, *P<0.05, **P<0.01 by one-way analysis of variance with multiple comparisons (ANOVA).

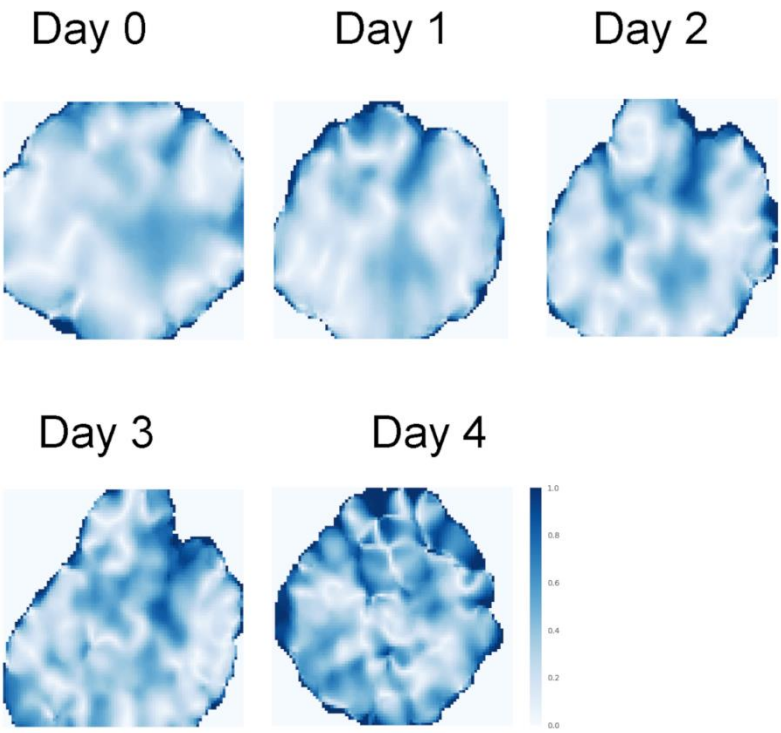
The R-value ranged from -0.23 to -0.45, indicating, as with the MC38 tumour model, that longer vessels display a more tortuous nature (Figure 3.3.3A). Directional coherence was slightly lower in comparison to the MC38 tumours and maintained on an average value of 0.3 (Figure 3.3.2B) on a scale from zero to 1, where zero represents less coherent vessel branches and a value close to 1 represents more coherent vessels branches. However, local differences and changes of the directional coherence were observed, suggesting dynamic sprouting in the tumour and during tumour growth (Figure 3.3.3B). Average vessel diameter across tumours did not change throughout tumour growth and maintained between 20 and 30 micrometres (Figure 3.3.2C).

We then measured the ratio of perfused to non-perfused tumour vessels. Quantification did not reveal significant changes throughout tumour growth (Figure 3.3.2D). Compared to MC38 which displayed 40 to 50% of vessels perfused, in the B16F10 tumour model around 70% of vessels indicated as perfused after the blood pool labelling agent (qDot705) was added. Although imaging was started earlier compared to the MC38 model, most vessels appeared to be well perfused from the early stages of tumour growth (Figure 3.3.2D). Pearson's R coefficient of vessel diameter and median perfusion ranged from 0.02 to 0.4, suggesting larger diameter vessels to be more likely to be perfused like MC38 (Figure 3.3.3C). In the B16F10 model, no increase in the total number of sprouts (Figure 3.3.2H) was observed during tumour growth and there was a decrease in the number of branch nodes per mm^2 (Figure 3.3.2I) compared to the MC38 model. This was accompanied by a significant decrease in the fraction of vessels shorter than 80 micrometres (Figure 3.3.2F) and an increase in the fraction of longer vessels compared to MC38. (Figure 3.3.2G). Furthermore, we measured an increase in the average vessel length (Figure 3.3.2E) but no difference in vessel diameter (Figure 3.3.2C). This resulted in a slight increase of the length to diameter ratio in this tumour model (Figure 3.3.2J). Thus, while MC38 parameters reflect a medium to high level of angiogenesis in the tumour, B16F10 does not display such a high angiogenic capacity (319).

A

	Control	tortuosity versus vessel branch length				
Days		0	1	2	3	4
	1	-0.45	-0.44	-0.34	-0.32	-0.23
	2	-0.31	-0.37	-0.33	-0.25	-0.34
	3	-0.4	-0.42	-0.36	-0.35	-0.36

B



C

	Control	perfusion vs diameter				
Days		0	1	2	3	4
	1	0.028	0.064	0.2	0.24	0.31
	2	0.15	0.033	0.075	0.26	0.21
	3	0.1	0.045	0.27	0.4	0.34

Figure 3.3.3 B16F10 tumour vascular parameters:

(A) Table with R-values correlating tortuosity (Y-axis) and length (X-axis) with values for each day and each tumour calculated in the first column second column P-value calculated for each day. N = 3.

(B) Representative directional coherence map originating from fluorescent images and calculated with the algorithm. Blue = a more coherent area. White = a less coherent area.

(C) Table with R-values correlating perfusion (Y-axis) and diameter (X-axis) with values for each day and four representative tumours. R-values are followed by their respective P-value. N = 3.

3.4 DISCUSSION

3.4.1 Established mouse model

In order to understand the effect and response of tumour vasculature to irradiation, we have chosen the Cdh5-cre-ERT2 inducible mouse model as a host for tumours because it allows for the specific modification of other genes in the context of loxP cleavage sites. Here we used this system to activate the expression of a fluorescent reporter gene tdTomato in all endothelial cells including tumour endothelial cells and so to create fluorescently labelled tumour vessels. While there are several different models available leading to the labelling of endothelial cells (305) the Cdh5-cre-ERT2 model was, to the best of our knowledge, the most reliable in terms of high induction efficiency of fluorescent proteins.

However, in our experience even 10 daily doses of Tamoxifen administration (10 mg ml^{-1}) resulted in only around 20% of mice with a > 95percentage induction of tdTomato positive endothelial cells. The other 80% of mice that received Tamoxifen were not usable for this kind of imaging studies due to a less than 95% of labelling, leading to scarcely labelled tumour vasculature. Our studies rely on fully labelled tumour vasculature in mice with approximately > 95% of endothelial cells expressing tdTomato.

There are several reasons for the difference in induction efficiency. Based on reports describing the expression of Cdh-5 as ubiquitous in endothelial cells, one would expect the cre-recombinase to be active in all endothelial cells reflecting its activation after Tamoxifen administration. However, there are some reports suggesting that whether the cre recombinase comes from the maternal or paternal germline can affect its cre activity (320). This so-called parent-of-origin effect (321) can either result in the mosaic expression of cre, or off-target effects leading to widespread expression in other tissues (320). While in the model we used, the mosaic phenotype was detectable by means of incomplete induction, revealed in our

experience that only 20% of mice displayed high recombination, nevertheless, we did not observe widespread expression in other cells in our setting (Figure 3.1.3 and 3.1.4). This might be due to our breeding strategy using female mice carrying the cre-ERT2 gene and male mice carrying the reporter gene. Heffner et al reported that both effects (mosaics and off targeted effects) can occur when male mice carrying the cre-ERT2 transgene over female mice. We, however, decided to use female Cdh5-Cre-ERT2 mice and male ROSA26 reporter mice for breeding and production of VEOM mice.

3.4.2 Intravital imaging of the developing tumour vasculature

To collect comprehensive information of the tumour vasculature we used intravital two-photon microscopy in combination with an algorithm that enabled us to obtain several parameters describing the vessel architecture, such as diameter and length, but also other parameters that might be of relevance to perfusion of the tumour blood vessels. Changes in perfusion can lead to hypoxia which can affect the response to treatment (322–324). There are several fluorescent injectable molecules available to label the perfused vasculature. However, because of the leakiness of the tumour vasculature, molecule size preventing the extravasation into the interstitial space is crucial to ensure that one can differentiate between perfused vessel lumen and extra vascular space. Lectins, for example, are often used to label perfused blood vessels. In fact, they label endothelial cells by binding to the inner lining of endothelial cells exposed to flowing blood.

Another example are fluorescently labelled dextrans which are inert to binding to cells, yet they can size-dependently extravasate into the interstitial space and are taken up by immune cells, such as macrophages through pinocytosis. As a result, repetitive imaging is not feasible because the macrophages become fluorescent, leading to a false-positive signal. Qdots

in comparison are nanocrystals that are larger in size 10 to 20 nm and are PEG-coated to minimise nonspecific interactions particularly with cells from the immune system. These properties allow for repeated imaging without the interference of Qdots extravasation or uptake by cells inside or outside of the bloodstream (325, 326). Therefore, Qdots as vascular labelling agents have advantages over other labelling agents such as lectins or fluorescently labelled dextrans.

The abdominal window chamber allows for following tumour development over a slightly longer period compared to other chamber models, because as the tumours grow, especially in the case of the untreated tumours, they can outgrow the window in other models (302, 303). A limitation of the window imaging is the confined size restriction that may affect tumour growth. Late or large tumour stage observations are therefore difficult to investigate. Another limitation is the depth of imaging with 2-photon microscopy. While it is possible to image tissues to a depth of up to 1 mm in the brain, tumours have a different makeup of cells and extracellular matrix resulting in a more opaque tissue type (301, 327, 328). This feature has a direct effect on the recovery of emitted photons and thus imaging depths. Laser light emitted from the two-photon near-infrared laser with a wavelength of 940 nm will penetrate deeper into tissue than the light of a shorter wavelength used in general light microscopy, emitted light from the excited fluorophores in the tissue will be of shorter wavelength. Emitted photons of shorter wavelength, however, are more prone to scattering and absorption resulting in decreased photon collection from the focal area with increased depth. Absorption occurs on a magnitude lower than scattering and therefore has little or no effect on photon recovery and detection (329). Increased laser power can compensate for this to a certain extent. However, phototoxicity becomes a factor that needs to be considered. Together this limited the depths that could feasibly be imaged in our hands to approximately 300 micrometres.

3.4.3 Types of angiogenesis

While sprouting angiogenesis was evident, other types of angiogenesis described in the literature such as the phenomenon of vessel co-option (156, 330) could not be observed in our model because we were relying on a tumour growing outside of an existing organ. We cannot rule out the potential of vessel co-option in the initial stage of tumour growth. This mechanism of abducting pre-existing vessels might occur after tumour cell injection in the fat layer above the abdominal muscle and before the angiogenic switch. We did not observe this kind of development once tumours were resected, as an intact muscle layer was evident.

Another phenomenon described in the literature is called vascular mimicry. In this case, tumour cells form tube-like structures masquerading as endothelial cells. These tubes can be part of the vascular network, contain blood and contribute to blood flow (157). However, in both our tumour models in combination with VEOM mice we did not observe such structures during the intravital imaging. While we cannot exclude the possibility that some tumour cells might form a lining between endothelial cells in the tumour vasculature, due to tumour cell dissemination, whole tubes without endothelial cells were not observed. GFP labelled tumour cells and tdTomato labelled endothelial cells in combination with labelling the blood perfusion would have readily allowed us to detect the development of these structures in which GFP labelled tumour cells would have been extending or developing new tube-like structures in direct contact with flowing blood.

Intussusception of vessels, whereby an existing vessel develops an initial pillar that then expands and splits the initial vessel into two, has also been described in the literature and has been observed in postnatal normal blood vessel development particularly in lung tissue and muscle tissue (159). We did observe initial stages of intussusception in tumour blood vessels.

However, it was a sparse event and was not a major contributor to angiogenesis in our tumour models.

3.4.4 Quantifying vascular parameters

To follow the development of the tumour vasculature, we applied intravital imaging in combination with the VEOM mice in two different murine cancer cell lines MC38 and B16F10. To analyse the obtained microscopic images, we used a custom-made algorithm to segment and extract tumour vessel parameters. While there are other algorithms available (331), our approach was to segment blood vessel structures on the endothelial cell lining rather than the labelled bloodstream with the advantage of being able to differentiate between perfused and non-perfused parts of the vasculature. Further, to define intra and extra-vascular space the algorithm made use of the labelling strategy of GFP = tumour, tdTomato = endothelial cell, and Qdot705 = perfusion. Although the algorithm detected the majority of vessel structures, occasional smaller vessels were sometimes not detected.

To obtain vascular network metrics, different approaches have been applied such as corrosion casting (88, 299), thick tissue sections (332) or intravital imaging (333). Corrosion casting and thick tissue sections do not allow for longitudinal investigations of the same tumour. Tozer et al. (333), for example, used intravital imaging in mice and rats to measure network metrics based on a perfusion marker which allows for longitudinal measurements of the same tumour. What becomes clear after review of these reports is the tumour model-specific vascular architecture (89) which we have observed in our models as well.

In the MC38 tumour model this manifests itself, for example, in intensive sprouting and branch point development, which was the most prominent change over time and tumour growth. The increase in the number of sprouts reflects the increase of tumour size and suggests

that the vasculature remains in a developing stage. The increase in vessel branch points normalised to tumour size also points towards increased interconnectivity between tumour blood vessels resulting in a more branched network. The increased fraction of shorter vessel branches is perhaps not surprising when looking at total number of sprouts and branch points per mm^2. Both parameters increased with time, pointing towards a more dense network over time. Although we saw a slight increase in longer vessels, it was not statistically significant. The increase in the branch point density could explain this as vessels become increasingly interconnected but did not generally increase in length. We thus can conclude that there was almost no increase in the distances between bifurcations in the MC38 model. In addition, this might explain the decrease in the length to diameter ratio measured in the MC38 model.

Furthermore, we did not observe a change in tortuosity and directional coherence. This is in line with our observation that there was no increase in vessel tortuosity, considering that no increase in average vessel length was observed this is not surprising, as we have shown that vessel length does correlate with tortuosity.

Quantification of the developing vasculature in the B16F10 model revealed differences in the vascular pattern during tumour growth. Like the MC38 tumours, no change in tortuosity and directional coherence was observed with tumour growth. However, vessel tortuosity was in the upper quartile, indicating relatively straight vessels. A minor increase in the level of sprouting angiogenesis during tumour growth was seen compared to the MC38 tumour model. While this could be due to space constraints within the window chamber, others have reported a similar development in the B18F10 tumours during tumour growth (319, 334). We observed only a slight increase in the total number of sprouts compared to MC38 indicating that the B16F10 is, in fact, less angiogenic and displays a loss of branching complexity compared to the MC38 model. We demonstrate in Chapter Five that one possibility is the level of proliferation of tumour endothelial cells.

Another finding is that the B16F10 also displays a shorter doubling time and thus faster growth (see Chapter four) contributing to the observations made here. Accordingly, we also quantified a decrease in branch points per mm^2. Together, this might explain why the fraction of smaller vessels decreased and, concordant with this development, we observed an increase in average vessel length, the fraction of longer vessels and an increase of the length to diameter ratio. This indicates that the vascular network in B16F10 tumours is less dense and in fact, we have seen this as well in subcutaneous tumours. A similar phenotype has been described by Mathivet et al. (296) in a glioma model by which the shift in the polarization of macrophages from an M1 to an M2 type fosters these changes in the vascular structure. This might explain what we have observed in our model.

In the MC38 model, the vessel diameter increased over time which has been described in the tumour vasculature by others in different tumour models (208). This was not the case with the B16F10 model where it was maintained at a similar level. Both developments have been described in the past for different tumour models (88, 333). We did see a trend of increased perfusion in the MC38 tumour with increased diameter but not in the B16F10 tumour where no changes in the vessel's diameter were evident.

Previous reports describe great variety in the architecture and measured parameters of the tumour vasculature depending on the tumour model (89). Tozer and colleagues (333) have shown in their models, also measured with intravital microscopy, an increase in vessel length throughout tumour growth. However, their measurements were based on perfused vessels and non-perfused parts of the vasculature were not included in their measurements. On the other hand, Mathivet et al. described vessel expansion in later stage tumours, measured by vessel diameter (296). Taken together our results, as well as reports in the literature, describe a great variety of tumour vascular architecture depending on the tumour model and demonstrating that this architecture changes during tumour growth.

3.4.5 Conclusion

In this Chapter we have established and validated a system in which we were able to image the tumour vasculature with its perfused and non-perfused tumour vessels for over 2 weeks. We have further shown that in our model only endothelial cells express the fluorescent protein tdTomato in detectable levels and that despite reports on similar systems, we did not detect other cell types that express this reporter protein. This made us confident that the microscopy images obtained in the subsequent experiments contained only tumour vessels labelled with tdTomato and that no other cell type would interfere in the quantification of tumour vessel parameters.

Having established a system that robustly labels endothelial cells, including tumour endothelial cells, we introduced a window chamber two-photon approach to follow tumour vascular development. The obtained images were segmented and quantified with a custom-made algorithm to extract parameters describing the architecture of the tumour vascular system. This allowed us to describe the development and changes of these parameters over time. It was clear that, depending on the tumour type, the vascular network develops differently and seems to be tumour model specific. In the next chapter, we compare these parameters of the tumour vasculature obtained from non-irradiated tumours to those obtained from irradiated tumours to delineate the effect of irradiation on the tumour vascular system and its response.

CHAPTER 4

Tumour Vascular Response to Single and Fractionated Irradiation *in vivo*

4.1 INTRODUCTION

In the previous chapter, we introduced GEMMs that enabled robust labelling of endothelial cells with fluorescent protein tdTomato. This model was used in combination with an intravital window chamber to study the development of the tumour vasculature *in vivo* over time. The obtained intravital images were analysed with a machine-learning algorithm to quantify tumour vessel parameters of the developing tumour over time (289). Quantification displayed modest change during tumour vasculature development in our two tumour models over time without treatment. We observed different developments between the two tumour models, with MC38 displaying a highly vascularised tumour while the B16F10 tumour model was less angiogenic. In this chapter, we use both tumour models to investigate the response of tumour blood vessels to ionising radiation and to compare these results to control measurements.

Radiotherapy of a cancer results in irradiation of both the cancer cells and the tumour stromal cells including the tumour vasculature. Although extensively studied in the past, the effects of radiotherapy on the tumour vasculature is incompletely understood in both single-dose and fractionated irradiation settings. In recent years, the technical advances in imaging guidance and targeted delivery of radiation doses to the tumour (while at the same time reducing the radiation dose delivered to the surrounding tissue) have rejuvenated the idea of stereotactic body radiation therapy (SBRT) in patients. Recent clinical studies using SBRT support this notion (21, 335, 336). In some cancer types, such as lung cancer or the treatment of oligometastatic disease (21, 336–341), SBRT showed improved outcomes and overall survival compared to standard treatments of care, including conventional radiotherapy.

Research in rodent models suggests that the response of the tumour vasculature to ionising radiation is dose and time-dependent (24, 25, 342). Kozin and colleagues (24) suggested

a temporal framework of five stages describing the response of the tumour vasculature to ionising radiation for larger doses. Starting from a pre-irradiated stage that recapitulates an active status of angiogenesis to a higher or lower degree (see the previous chapter). After irradiation (with doses between 14 and 50 Gy) a second stage of early response of the tumour vasculature, that includes the initial continued growth of tumours, follows. Several studies have suggested an increase or no change in blood flow and oxygenation after a single-dose of up to 20 Gy that can last for some days (205, 206, 208–210, 231, 343). This phenomenon might be partially attributed to the release of nitric oxide, leading to vasodilation (344, 345) which has been shown to be released after smaller doses. Others have observed no change after irradiating tumours when looking at vascular volume, functional vasculature or vessel density (346, 347). Doses above 20 to 30 Gy or repeated high doses of radiation have also been reported to lead to destruction and vascular death as well as leakiness of blood vessels and the loss of perfusion in parts of the tumour (215, 226). In comparison, small clinical studies in humans reported that even after large doses of radiation an initial increase in perfusion and reoxygenation (217–222) was seen, which is in agreement with one (reoxygenation) of the basic rules of radiobiology (5Rs) (16). In comparison, with single-doses below 10 Gy or fractionated doses of radiation, little histological or functional evidence of vascular destruction and less effect on the tumour vascular function has been seen (125, 205, 232, 348–351). This might be due to successful repair and release of vascular protective chemokines such as bFGF and VEGF from the irradiated tumour (127, 352, 353).

In later stages of tumour regression and recurrence, less is known. Previous studies have described opposing results when looking at vessel function. While some report a decrease in blood flow and an increase in hypoxia (354, 355) others have shown an increase in blood flow (206, 210). Structurally, vessel density has been described as decreasing initially but then increasing with tumour recurrence (125, 355). More recently, Brown and associates have proposed vasculogenesis in a glioblastoma model as an important factor of vessel recurrence

after high doses of radiation (123, 125, 161). They propose that the regeneration of tumour blood vessels relies on circulating endothelial progenitor cells to build new vessels. In their model, pre-angiogenic bone marrow-derived cells, which are circulating endothelial cells, were attracted by increased expression of the stromal cell-derived factor (SDF-1) generated by hypoxia-induced HIF-1 α signalling. How much of the incorporated circulating endothelial cells contribute to vessel growth after irradiation, or to what extent surviving tumour endothelial cells contribute to recurrent tumour vessel growth, remains disputed and requires further research.

What leads to vessel collapse, death, and even destruction if the dose of radiation is strong enough, is also less understood. Garcia-Barros and colleagues (28) observed early massive death and destruction of tumour vessels within hours when treated with 15 Gy irradiation, suggesting this phenomenon is the major contribution to radiation-induced tumour responses and tumour control. However, studies in the late 20th century, as well as more recent studies (262, 276), have shown different results in a variety of tumour models and radiation doses ranging from 12 to 50 Gy (262, 276, 356) with less impact on the tumour vasculature and its function, and apoptosis of tumour vessels peaking later between 24 and 72 hours (262).

Generally, it has been shown that developing vessels show more sensitivity to radiation than mature vessels (357). In tumours, the vasculature is maintained in a developmental stage, continuously proliferating and moving through the developmental processes of new vessel formation of sprouting, guidance, branching, anastomoses, and lumen formation (31). This continuous process, and specifically the proliferation, results in potentially higher susceptibility to radiation compared to their normal and quiescent counterparts. Moding et al. used genetic knockout of the cell cycle checkpoint kinase ATM in endothelial cells, which is required for effective DNA damage repair, to investigate the response to radiation. Knock out of this protein in endothelial cells resulted in higher sensitivity to radiation (262, 263). Park suggested that an

increase in vascular permeability and vasodilation in tumours after irradiation (273, 358) leads to plasma extravasation. This, in turn, might lead to increased erythrocyte concentration within narrow capillaries and retardation or stasis of perfusion. Eventually, this could lead to microvessel collapse and destruction. While irradiation damages the DNA with all the accompanying consequences, the suggestion by Park would add another physiological layer to tumour vascular response to irradiation and these responses are not mutually exclusive.

Studies on the tumour vasculature network and quantification after irradiation have been sparse. Analysis by Hilmas and Gillette (208) some 45 years ago described an increase of the length and a decrease in the diameter of the tumour vasculature after treatment with 10 or 30 Gy (208). Their study relied on tissue sections of different tumours from various time points. Thus, generally, little is known about tumour vasculature parameter changes after irradiation.

What can we conclude from this? The literature suggests that doses of 15 Gy and higher are needed to affect and enforce changes in the tumour vasculature. Lower single or fractionated dose regimes seem to have little and transient or no effects. Doses above 30 Gy or repeated high doses of irradiation have been suggested to lead to destruction and vascular death measured by leakiness of blood vessels and loss of perfusion to part of the tumour. Some of the wide variations may result from the diversity of models used and particular results may depend on the tumour models which have been described (24, 25). However, most studies have investigated the tumour vasculature response with functional assays. These readouts are highly valuable, yet endothelial cells that are the building blocks of tumour vessels have had little attention. This is not surprising as most of the above-mentioned studies were conducted some 40 years ago and good endothelial cell markers were not available at that time.

4.2 AIMS

The aim of this chapter is to investigate the response of tumour vessels grown in two different tumour models to a single or fractionated dose of irradiation *in vivo*. To this end, we used the model developed in the previous chapter and either applied 15 Gy single-dose or 5 x 3 Gy fractionated irradiation. This has been done through the following workflow:

1) Comparing parameters describing vessel morphology of tumour vessels after different doses of radiation in MC38 tumours
2) Comparing parameters describing vessel morphology of tumour vessel after a single dose of 15 Gy or DC101 antibody treatment in MC38 tumours
3) Comparing parameters describing vessel morphology of tumour vessels after using a dose of 15 Gy irradiation of B16F10 tumours to control
4) Evaluating perivascular cell coverage of tumour vessels in MC38 and B16F10 tumours
5) Evaluating extent of hypoxia in MC38 and B16F10 tumours

4.3 RESULTS

4.3.1 Tumour growth response to single and fractionated irradiation

Here we used the model described in the previous chapter to investigate the tumour vasculature response to 15 Gy single-dose irradiation in MC38 and B16F10 tumours and fractionated irradiation to MC38 tumours. Previous reports described single-doses of 15 Gy to impact the tumour vasculature leading to, for example, apoptosis in endothelial cells (28, 262). To evaluate the effect of irradiation on the growth of the two tumour models used in the previous chapter, we first irradiated MC38 subcutaneous tumours with different doses. When subcutaneous tumours reached approximately a volume of 100 mm^3 mice were randomly allocated into groups of 10 which were put into control and treatment groups and were irradiated either with 15 Gy single-dose or 5 x 3 Gy fractionated irradiation in MC38 tumours.

We are aware that this is not the radiobiological equivalent for the MC38 tumour, but we chose the same dose because the radiobiological equivalent would be different for the tumour from that for the endothelial cells and we wanted the endothelium to receive the same dose in each case. We followed the tumour growth of these treated tumours and measured their growth in response to irradiation (Figure 4.1). MC38 control tumours reached the endpoint volume within 6 to 8 days. Daily radiation doses of in fractions of 3 Gy for five x let to partial regression of the tumours followed by regrowth. 15 Gy led to decrease of tumour volume over a period of 8 days (Figure 4.1), follow up showed no recurrence of tumours treated with 15 Gy (Figure S4.1A).

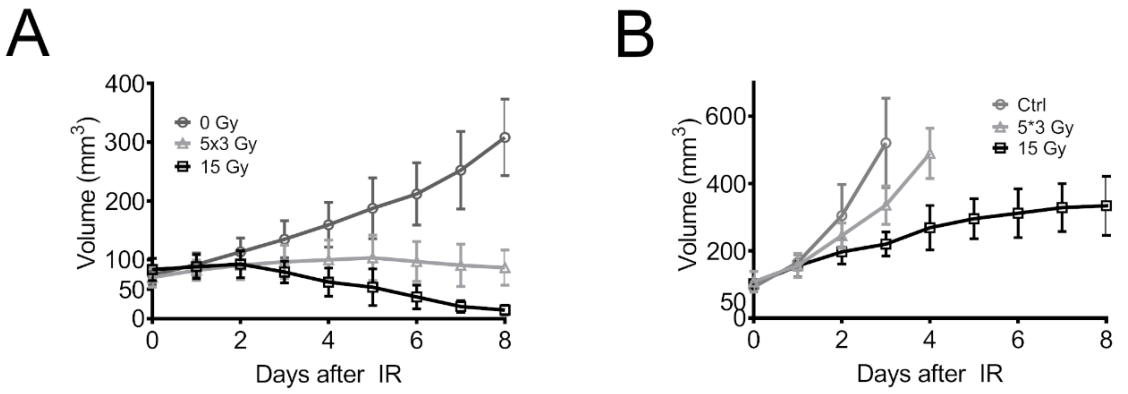


Figure 4.1 Tumour growth and response to irradiation.

(A) Subcutaneous MC38 tumour growth in C57BL/6 mice show dose-dependent respond to ionising radiation. Tumours were separated in three subgroups receiving 0 Gy, 5 x 3 Gy or single-dose 15 Gy irradiation. Tumour growth was followed over eight days. N= 10 mice per group. Error bars ± SEM.

(B) Subcutaneous B16F10 tumours growth in C57BL/6 mice show dose-dependent response to ionising radiation. Tumours were separated in three subgroups receiving 0 Gy, 5 x 3 Gy or single-dose 15 Gy irradiation. Tumour growth was followed over eight days. N= 10 mice per group. Error bars ± SEM.

We then performed the same experiment with B16F10 subcutaneous tumours. Fractionated 5 x 3 Gy irradiation did not result in a statistically significant difference to control tumour growth. 15 Gy single-dose irradiation led to tumour growth retardation but no complete regression was observed in contrast to the MC38 tumour model.

4.3.2 Structural and functional changes of the tumour vasculature after irradiation in MC38 tumours

Tumours were grown in window chamber in VEOM mice to follow changes of the tumour vasculature after irradiation. Mice with tumours < 3 mm diameter were irradiated with a small animal radiation research platform (SARRP). Usage of the SARRP allowed us to target a high dose of irradiation to the tumour, and at the same time, spare the surrounding tissue from

being exposed to higher doses of radiation (See chapter 2 Figure 2.2). After the first day of intravital imaging, animals were irradiated and then imaged following a 24-hour cycle for up to 8 days. Extracted data were compared to control parameters, with some parameters normalised to the first day of imaging in both control and irradiated tumours.

Compared to previous reports, 15 Gy irradiation did not reveal dramatic effects on the tumour vasculature of MC38 nor B16F10 tumours, neither did fractionated 5 x 3 Gy irradiation. We did not observe complete shutdown of perfusion neither in the microvasculature nor larger vessels in either MC38 (Figure 4.2.1B) or B16F10 tumour models (Figure 4.2.2B). In detail, 15 Gy irradiation of MC38 window tumours lead to an initial increase in tumour size followed by growth arrest for several days, tumours then displayed a decline in tumour size (Figure 4.1A and 4.2.1A). B16F10 tumours maintained size and increased slowly throughout the experiment. Thus, tumours followed a similar pattern in the window chamber experiment as compared to the subcutaneous experiment (Figure 3.2.1 and 3.2.4 and Figure 4.1B and 4.2.2A).

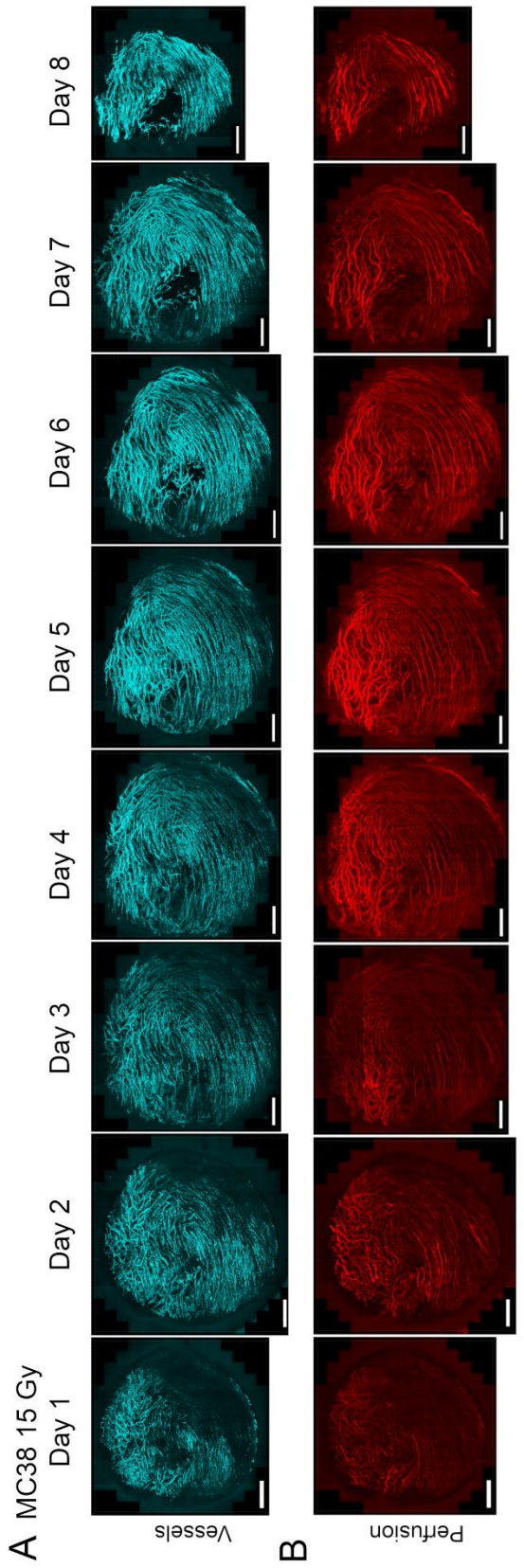


Figure 4.2.1 Time-lapse intravital microscopy of MC38 tumours in VEOM mice after ionizing irradiation

(A) Representative two-photon fluorescent 3D image timeline of MC38 tumour vasculature (cyan) after 15 Gy single-dose ionizing irradiation. Scale bars: 1 mm

(B) Representative two-photon fluorescent 3D image timeline of perfusion (red) in the same MC38 tumour after 15 Gy single-dose ionizing irradiation. Scale bars: 1 mm

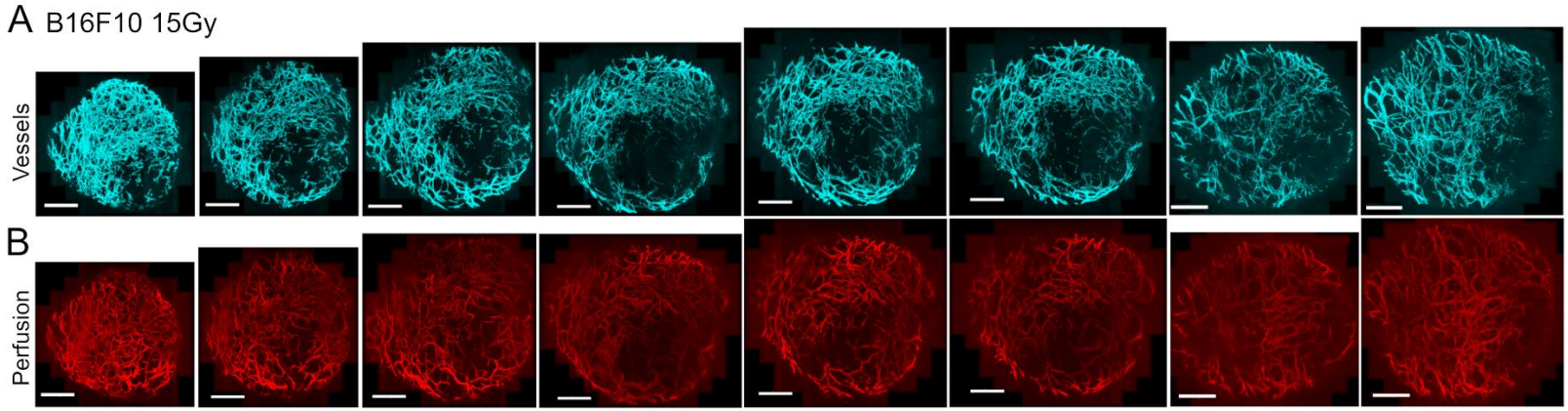


Figure 4.2.2 Time-lapse intravital microscopy of B16F10 tumours in VEOM mice after ionizing irradiation

(C) Representative two-photon fluorescent 3D image timeline of MC38 tumour vasculature (cyan) after 15 Gy single-dose ionizing irradiation. Scale bars: 1 mm

(D) Representative two-photon fluorescent 3D image timeline of perfusion (red) in the same MC38 tumour after 15 Gy single-dose ionizing irradiation. Scale bars: 1 mm

15 Gy single-dose and fractionated 5 × 3 Gy had strong effects on the formation of new branches (Figure 4.4). In control tumours, the number of branches increased with time and tumour growth (Figure 4.3.1A and 4.3.1Ai) together with extensive sprouting angiogenesis. In the treatment groups, inhibition of the formation of new sprouts was observed (Figure 4.3.1B and 4.3.2A). Magnification of the same area within one tumour over consecutive days reinforces this observation (Figure 4.3.1Bi and 4.3.2Ai). Initially, we observed a decrease in the number of sprouts. Sprouting was not completely inhibited but slowed down extensively which enabled us to observe and follow single sprouts over several days. Most sprouts displayed little change in morphology and functionality, which we determined by perfusion with injected qDots 705 (Figure 4.3.2B and Figure S4.2).

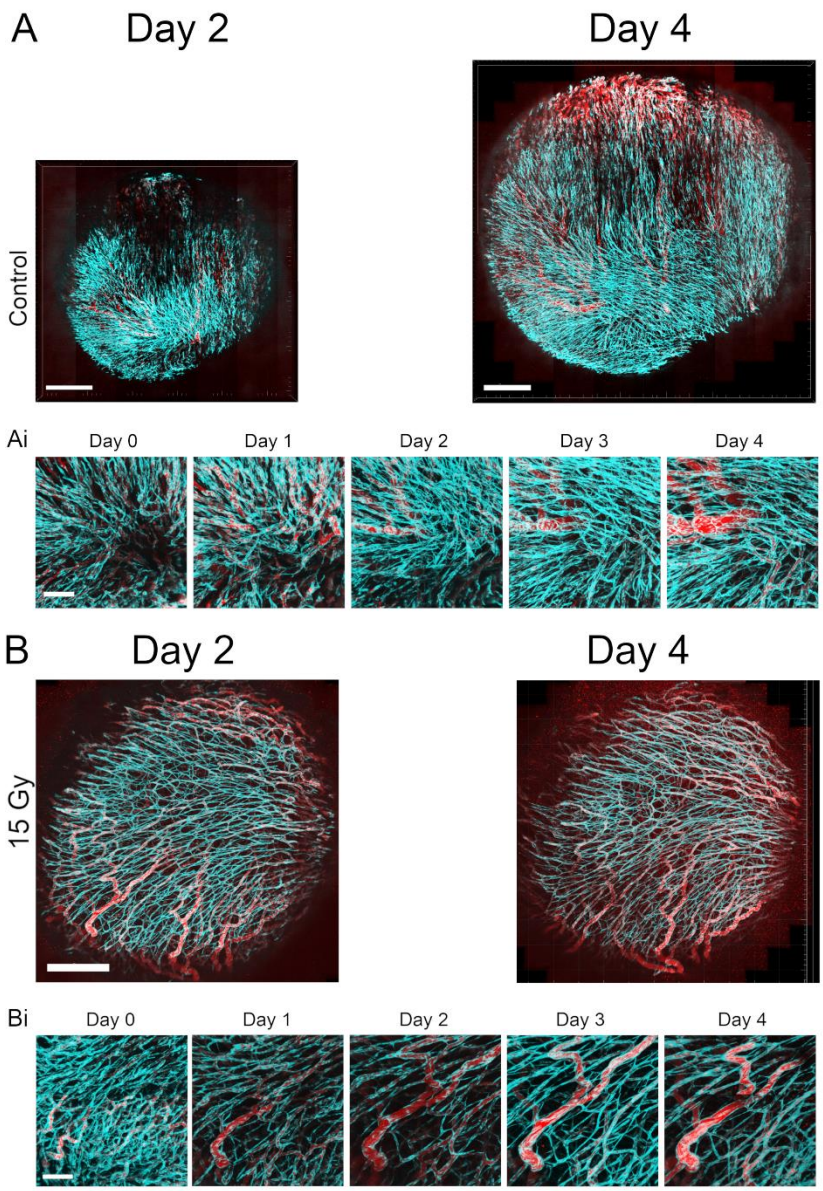


Figure 4.3.1 Time-lapse intravital microscopy of MC38 tumours in VEOM mice after irradiation. The developing MC38 tumour vasculature was imaged in an abdominal window chamber model with two-photon microscopy after irradiation at the indicated x.

- **(A)** Representative two photon images of a control MC38 tumour vasculature (cyan) and perfusion (red) at Day 2and 4. **(Ai)** zoom of the same tumour region from Day 0 to Day 4 of the tumour vasculature (cyan) and perfusion (red). Scale bar: 1 mm in **(A)** and scale bar 0.25 mm in **(Ai)**.
- **(B)** Representative two-photon images of the MC38 tumour vasculature (cyan) treated with single-dose 15 Gy ionizing irradiation and perfusion (red) at Day 2 and 4. **(Bi)** zoom of the same tumour region from Day 0 to Day 4 of the tumour vasculature (cyan) and perfusion (red). Scale bar: 1 mm in **(B)** and scale bar 0.25 mm in **(Bi)**.

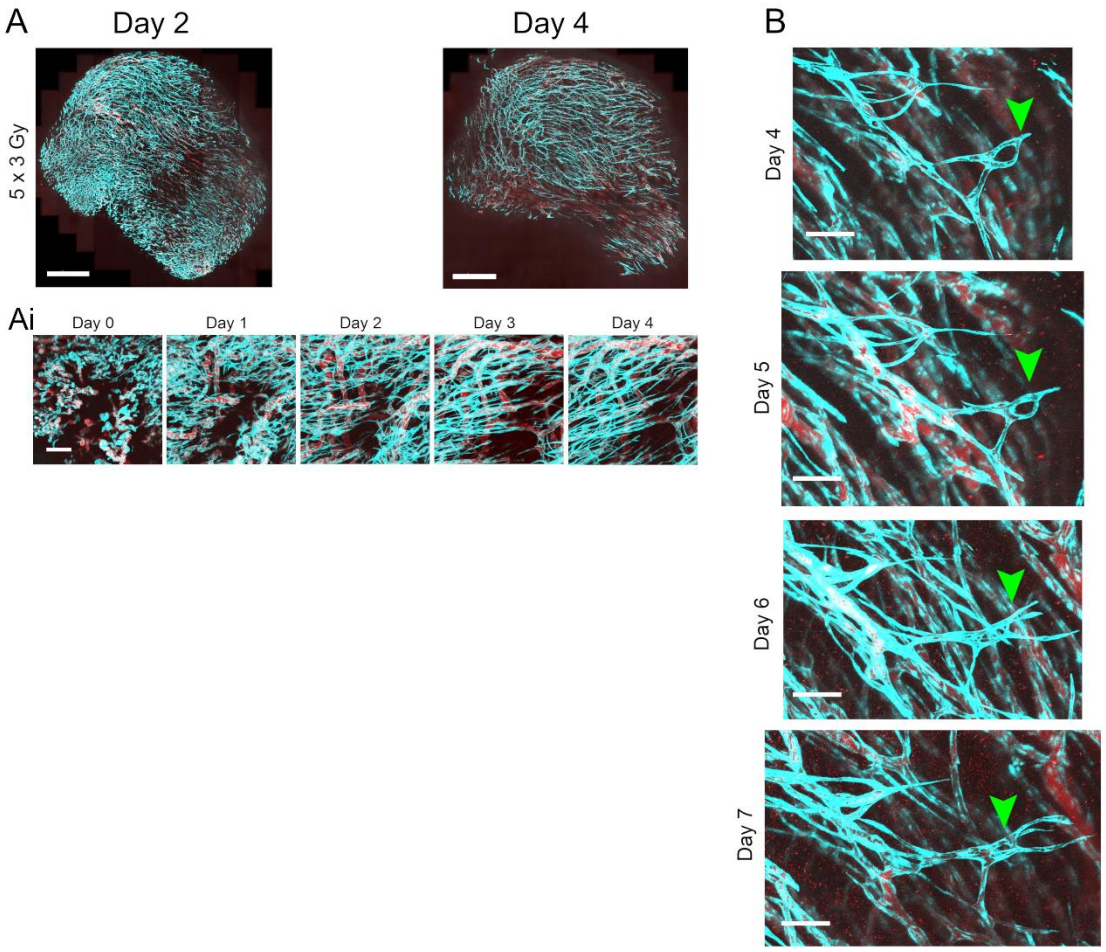


Figure 4.3.2 Time-lapse intravital microscopy of MC38 tumours in VEOM mice after irradiation. The developing MC38 tumour vasculature was imaged in an abdominal window chamber model with two-photon microscopy after irradiation at the indicated Days.

- **(A)** Representative two-photon images of the MC38 tumour vasculature (cyan) treated with fractionated dose 5 x 3 Gy ionizing irradiation and perfusion (red) at Day 2 and 4. **(Ai)** zoom of the same tumour region from Day 0 to Day 4 of the tumour vasculature (cyan) and perfusion (red). Scale bar: 1 mm in **(A)** and scale bar 0.25 mm in **(Ai)**.
- **(B)** Representative two-photon images of MC38 tumour vasculature sprouts (cyan) four to seven days after single-dose 15 Gy ionizing irradiation. Sprouting angiogenesis dramatically slowed with transient perfusion of the microvasculature (red). Scale bars: 25 µm.

To quantify these observations, we applied the previously described segmentation algorithm (289). This allowed us to follow the effect of single and fractionated irradiation on the parameters of the tumour vasculature morphology and compare the obtained values to control tumours. We first measured the change of sprouting behaviour between the control and irradiated tumours. The control tumour exhibited increased sprouting and branch point density

with tumour growth (Figure 3.2.3H and Figure 4.4A -B). In comparison, single and fractionated irradiation inhibited sprouting angiogenesis as well as the formation of new branches between tumour vessels (Figure 4.4A-C). A single dose of 15 Gy irradiation led to early regression of vessel branches within 24 hours (Figure 4.4A); in the fractionated setting, up to three doses were required to see similar effects (Figure S4.2A). In both settings, the density of tumour vessel branches plateaued without showing major changes (Figure 4.4B and S4.2A). This pattern was similar for the total number of vessels (Figure 4.4C) with 15 Gy. Extended inhibition of angiogenesis and no further increase in the total number of branches were seen. In contrast in the fractionated irradiation setting a slight increase in the number of tumour vessels was seen after the first fraction and a decrease after the third fraction of 3 Gy irradiation (Figure 4.4C).

Measuring the inhibition of the formation of further vessels, we next asked whether irradiation affects tumour vessel length as defined by the distance between branches. We quantified the average vessel branch length in MC38 tumours (Figure 4.4D). Average vessel branch length increased from 120 micrometres to approximately 150 micrometres within the first three days after a 15 Gy single-dose irradiation. Thereafter vessel length maintained on a plateau displaying little change. In contrast, fractionated 5 × 3 Gy irradiation did not result in any notable changes within the first three days after the start of irradiation. An upward trend of increasing vessel branch length was observed after the third fraction of radiation. The average length increased from 120 micrometres to approximately 140 micrometres (Figure 4.4D). These were like the results after the single dose.

We were curious whether the change in average vessel length followed a general trend over all the vessels or was due to a change in shorter or longer fractions of the whole vessel population. To answer this question, we measured fractions of the longer or shorter vessel. The fraction of vessels with branches longer than 400 micrometres increased within the first three days after single-dose irradiation of 15 Gy (Figure 4.4E). Tumours treated with fractionated

irradiation did not show such distinct changes of vessel length. In comparison, the fraction of vessels longer than 400 micrometres remained at the same level compared to control values and showed little increase in length after the last fraction of 3 Gy (Figure 4.4E). In the fraction of vessels shorter in length than 80 micrometres, we observed a decrease within the first day after 15 Gy single-dose irradiation (Figure 4.4F). The decrease of short vessels continued and reached a plateau after three days after irradiation and maintained at this level until the end of the experiment. The decrease was likely due to pruning resulting from apoptosis, both were observed within the first three days after single-dose irradiation (Figure S4.2A) Tumours treated with fractionated irradiation displayed no change over the initial time points, but we observed a decrease in vessels with more frequent branches after the third fraction of irradiation. Short branches decreased to a similar degree in the fractionated irradiation setting when compared to the single-dose treated tumours (Figure 4.4F). This indicates that the effect of fractionated irradiation let to similar effects upon dose accumulation.

In the previous chapter, we correlated length and tortuosity in control tumours. The increase in longer vessels and the decrease of shorter vessels let us measure the change of tortuosity after irradiation. We measured a slight decrease in vessel tortuosity in tumour vessels treated with 15 Gy irradiation within 24 hours (to recapitulate: an increase in the cord to length ratio of a vessel branch indicates a straighter vessel, thus less tortuous). In comparison, fractionated irradiation did not show such changes in tortuosity compared to the control (Figure 4.4G and Figure S4.2B). We further measured directional coherence between tumour vessels. Here, we observed opposite effects. No changes in directional coherence in tumours treated with single-dose irradiation were observed (Figure 4.4H). In contrast, fractionated irradiation showed changes at later time points which indicated a more coherent development of vessels and might be explained by ongoing endothelial cell proliferation after fractionated irradiation (Figure 4.4H).

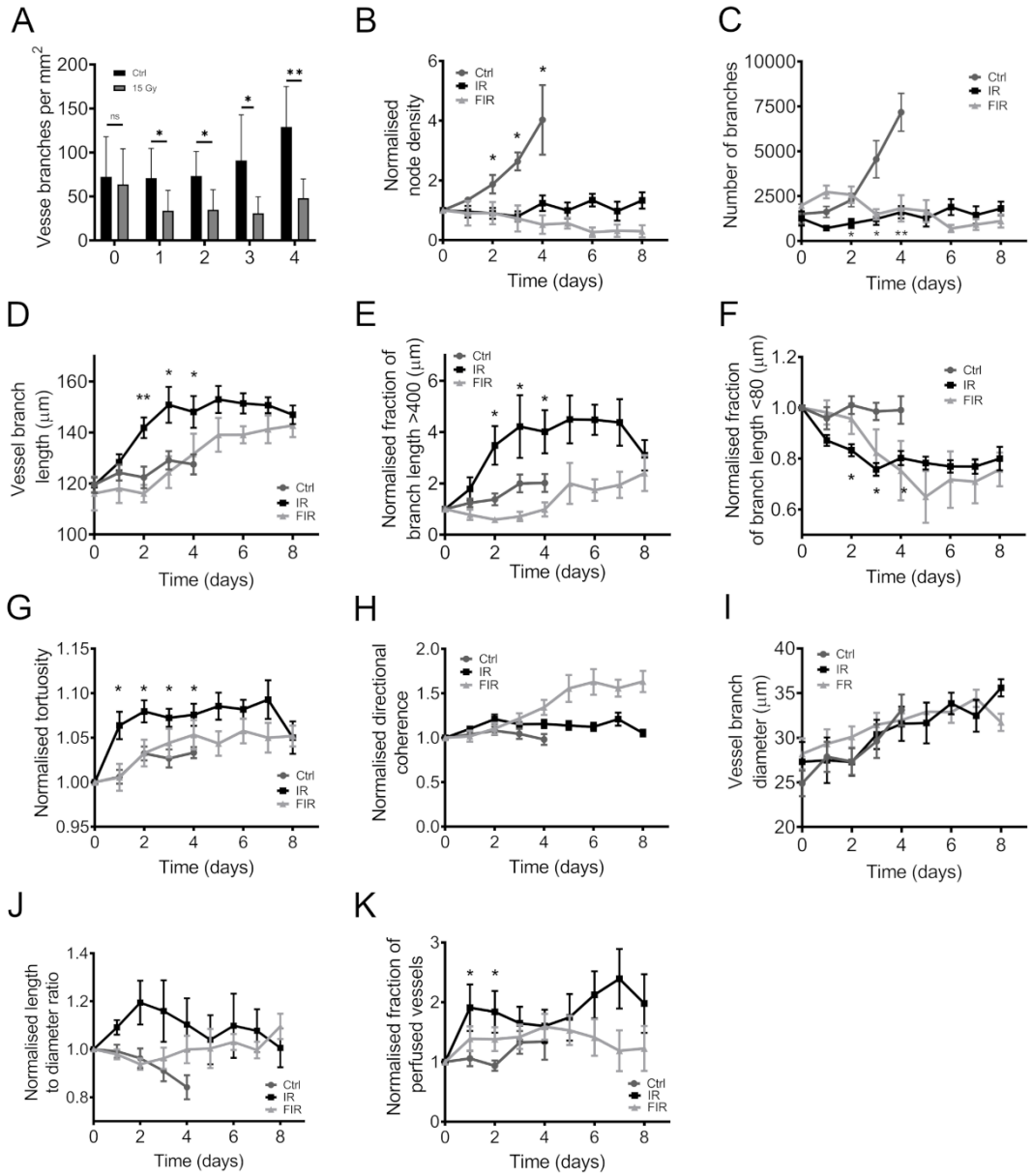


Figure 4.4 Time-lapse intravital microscopy of MC38 tumours in VEOM mice after irradiation. **(A-K)** Quantified vascular parameters, for each day of imaging the following parameters were quantified from segmented images and normalised to Day 1 if indicated: **(A)** number of vessel branching points per mm^2, **(B)** normalised vessel branching point density, **(C)** total number of vessel branches, **(D)** average vessel length, **(E)** normalised vessel branch length > 400µm, **(F)** normalised branch length < 80µm, **(G)** normalised vessel tortuosity, **(H)** normalised vessel directional coherence, **(I)** vessel diameter, **(J)** normalised vessel length to diameter ratio, **(K)** normalised fraction of perfused vessels. Legends in A to K: Ctrl: Control, IR: 15 Gy irradiation, FIR: 5×3 Gy irradiation. N=7 for control and single-dose irradiated samples and N=4 for fractionated irradiated samples. Error bars represents mean ± SEM, *P <0.05, **P <0.01. Statistical analysis of all data by analysis of variance (1 way-ANOVA) with Tuckey's multiple comparison test.

While we observed an increase in diameter in the control MC38 tumours with increased tumour size (Figure 3.2.3C), no change in the diameter of tumour vessels was observed after single or fractionated irradiation when compared to control values (Figure 4.4H). In both settings, vessel diameter increased with time like the control tumours.

Noting that there was a change in the average length of vessel branches, we measured the length to diameter ratio and perfusion in the MC38 tumour model. Tumours treated with single-dose irradiation showed an increase in the length to diameter ratio over time compared to control which decreased over time (Figure 4.4J). Tumours treated with fractionated irradiation showed no changes (Figure 4.4J). The change in length to diameter was accompanied by a transient increase in perfusion within 48 hours after single-dose irradiation (Figure 4.4K).

Taken together, these results show that single-dose irradiation adversely affects sprouting in the MC38 tumour vasculature. Further, the branch length increases and longer vessels become more frequent. At the same time, shorter vessels disappear and further a thinning of interconnectivity was observed leading to increased interstitial space between tumour vessels. The formation of vessel bifurcation decreased. This was accompanied by a slight decrease in tortuosity, but no change was observed in directional coherence after a single dose. Overall, most changes were observed within a short timeframe after irradiation in the single-dose treatment group, thereafter little change was observed in this setting. Fractionated irradiation showed similar changes over a little longer period and upon dose accumulation.

4.3.3 Comparison of vessel parameters between single-dose and anti-angiogenic treatment

Anti-angiogenic treatment in preclinical experiments has been shown to affect multiple parameters in a tumour including vasculature network properties (359, 360) for example, vessel length as well as the formation of vessel sprouts that are highly dependent on the VEGF concentration in the microenvironment and the ligand-receptor interaction activating the VEGF-VEGFR signalling axis. Antiangiogenic treatment with an anti-VEGFR-antibody in mice led, for example to the development of longer vessels and abrogated sprouting angiogenesis (94, 361). These changes during anti-angiogenic treatment have been termed vasculature normalisation. However, further research suggested that this phenomenon seems to be only transient. While there is a vast amount of research looking at different aspects of vasculature normalisation, vessel network properties have had less attention. Reports regarding tumour vasculature normalisation specifically looking at tumour vessel parameters have described a decrease in microvessel density and a decrease in tortuosity. We were curious whether we could observe similar parameter changes over the first days comparing anti-angiogenic treatment to single-dose irradiation.

Therefore, mice with MC38 window tumours were combined with intraperitoneally administered DC101 antibodies to mice. This antibody targets the murine VEGF-Receptor 2, blocking the interaction between the VEGF growth factor and its receptor (86). We followed the initial tumour vasculature response to DC101 (Figure 4.5A) and quantified parameters that showed changes after irradiation (Figure 4.5B-E). Like irradiation, anti-angiogenic treatment leads to a decrease in branch point density (Figure 4.5B). Further, we observed an increase in the average branch length between two vessel branch bifurcations (Figure 4.5C). This was accompanied by a decrease in the fraction of short vessels over time (Figure 4.5D). We then

measured the length to diameter ratio, which displayed a similar slope in comparison to 15 Gy irradiation with an increase of the length to diameter ratio within the first days after treatment initiation (Figure 4.5E).

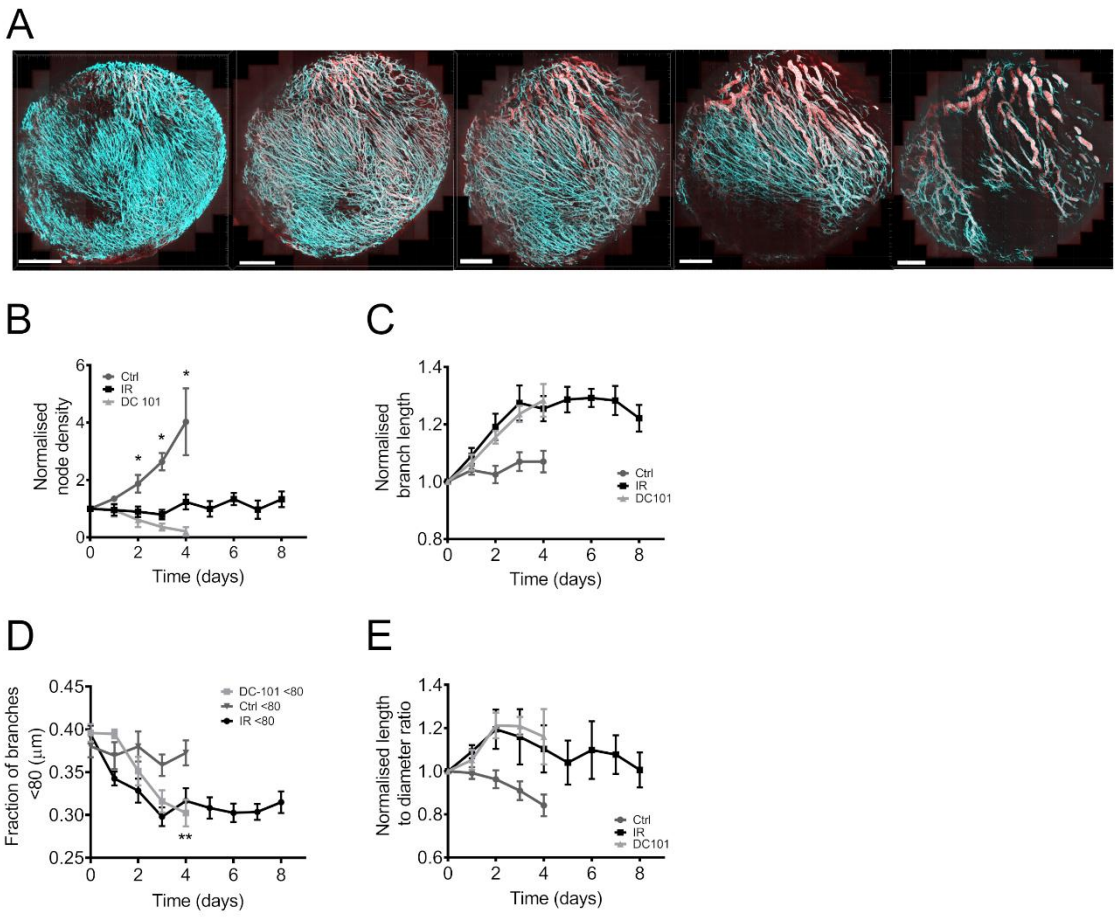


Figure 4.5 Time-lapse intravital microscopy of MC38 tumours in VEOM mice after DC101 antibody treatment.

(A) Representative two-photon image timeline of a tumour treated with the anti-VEGFR antibody DC101. Tumour vasculature (cyan), Perfusion (red). Scale bar 1 mm.

(B) to **(E)** Quantification of vessel parameters compared to control and 15 Gy single-dose irradiated tumours. Data normalised to Day 0. **(B)** Normalised node density. **(C)** Normalised vessel branch length. **(D)** The fraction of vessel branches shorter than 80 micrometres. **(E)** Normalised length to diameter ratio. N = seven for control and single-dose irradiated samples and N = five for DC101 treated tumours. Ctrl: Control, IR: 15 Gy irradiation, DC101: Anti-VEGFR antibody treatment. Error bars represents mean ± SEM, *P <0.05, **P <0.01. Statistical analysis of all data by analysis of variance (1 way-ANOVA) with Tuckey's multiple comparison test.

4.3.4 Structural and functional changes of the tumour vasculature after irradiation in B16F10 tumours

We next examined how the tumour vasculature developed in the B16F10 tumour would respond to 15 Gy single-dose irradiation in the same window chamber model. The window chamber experiment revealed a similar response in tumour growth compared to the subcutaneous experiment with a decreased growth speed of the tumour after irradiation. Like subcutaneous tumours, no regression of the tumour was observed. Like the MC38 tumour model (Figure 4.2.2A), we did not see major destruction of tumour blood vessels or shutdown of perfusion (Figure 4.2.2B). As previously described, B16F10 displayed less vascularity and smaller vessels. (Figure 3.2.5H and Figure 4.7B) We now asked what effect ionizing irradiation would have on the tumour vasculature in this model.

Intravital imaging revealed that after 15 Gy irradiation sprouts of the tumour vasculature initially maintained their development. Areas that were not populated with vessels showed tumour vessel growth although in a much slower fashion. Towards later time points after irradiation, active sprouting did diminish and no recovery and formation of new sprouts was observed (Figure 4.6.2B (arrows) and Figure 4.7B). The tumour, on the contrary, started to grow again. The tumour vasculature at later time points showed signs of pruning and apoptosis and (Figure S4.3A), as a result, we observed an increase in the distance between vessels (Figure 4.7B). Generally, larger vessels maintained their shape and function in most cases (Figure 4.2 and Figure 4.6.2A). Remaining sprouts showed no further development after irradiation and expansion of the vascular network diminished (Figure 4.2 and Figure 4.6.1A and 4.6.2A). We quantified vasculature network parameters and compared them to non-irradiated controls. Most vasculature network parameters did not show significant differences between controls and 15 Gy single-dose irradiated tumours.

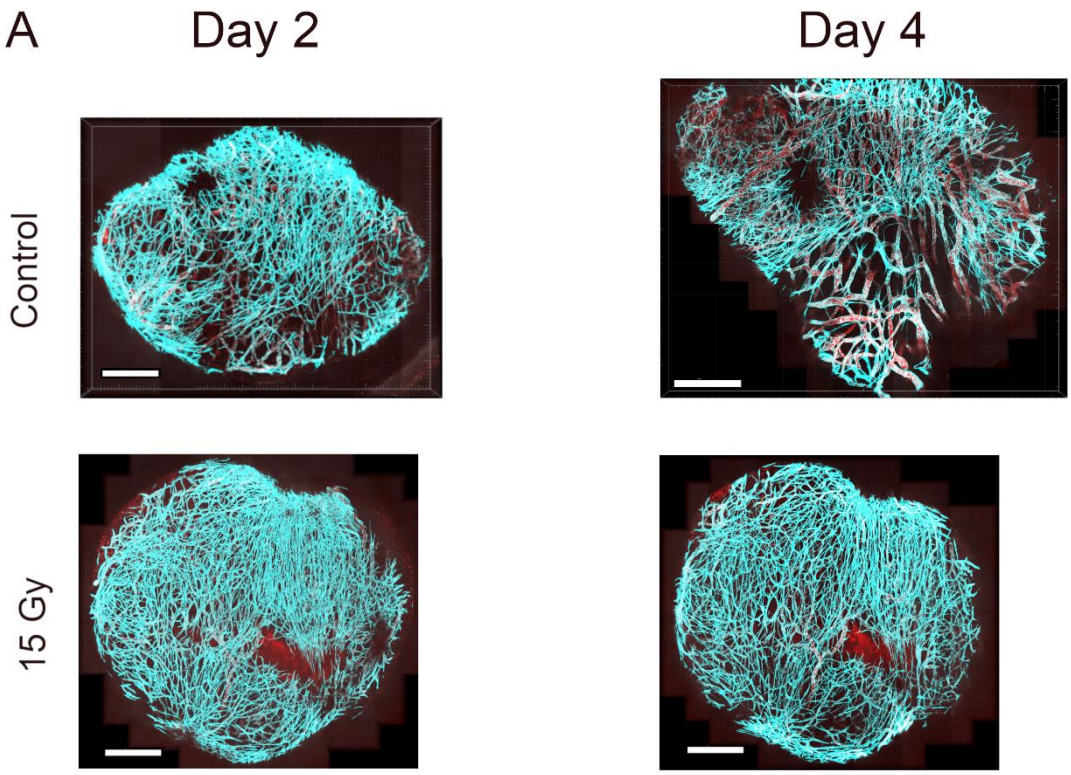


Figure 4.6.1 Time-lapse intravital microscopy of a B16F10 tumour in VEOM mice after irradiation. The developing B16F10 tumour vasculature was imaged in an abdominal window chamber model with two-photon microscopy after irradiation at the indicated time points.

(A) Representative two-photon images of control and 15 Gy single-dose irradiated B16F10 tumours. Vasculature (cyan) and perfusion (red) on Day2 and 4. Scale bar: 1 mm

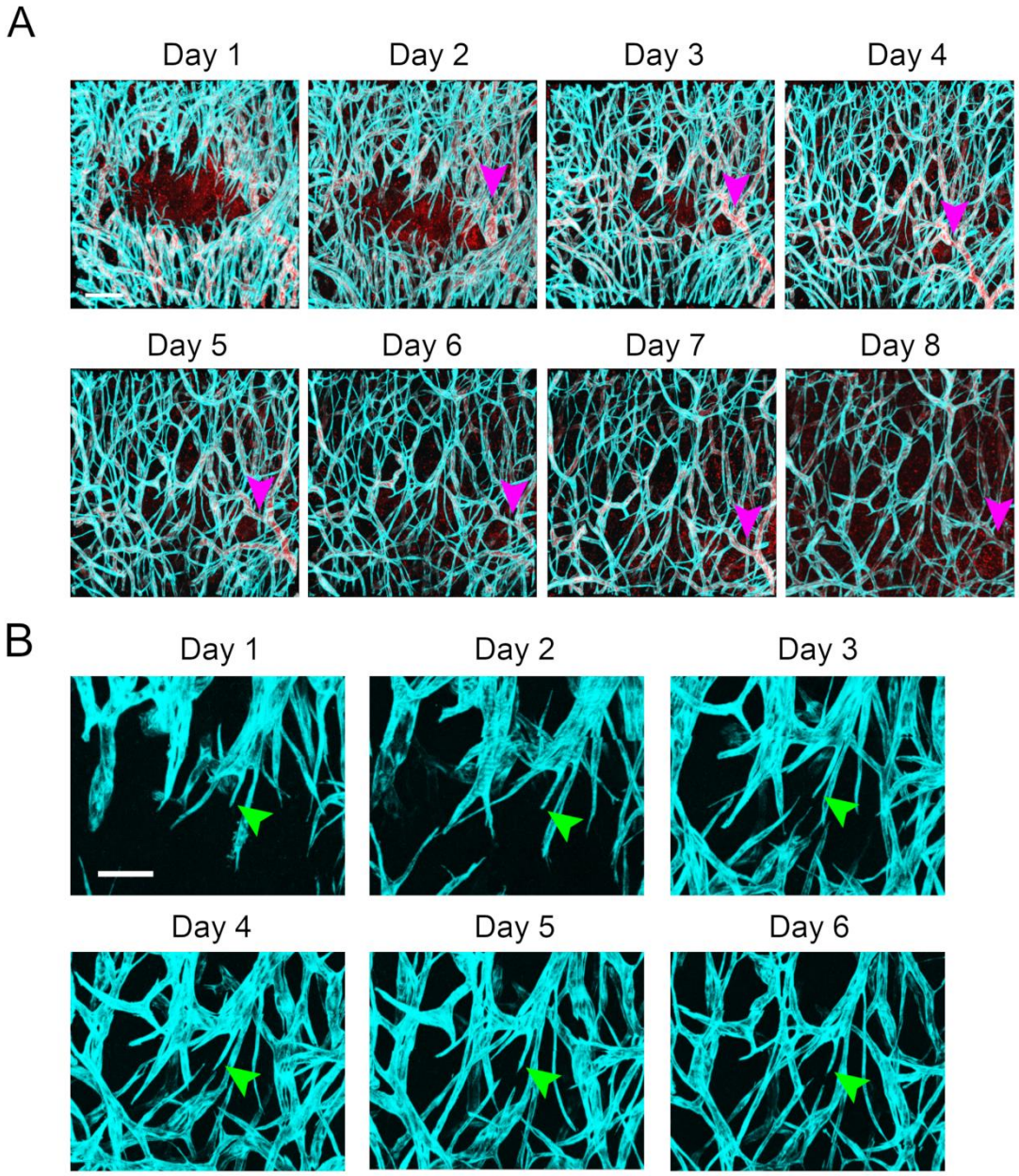


Figure 4.6.2 Time-lapse intravital microscopy of a B16F10 tumour in VEOM mice after irradiation. The developing B16F10 tumour vasculature was imaged in an abdominal window chamber model with two-photon microscopy after irradiation at the indicated time points.

(A) Representative two-photon images of the B16F10 tumour vasculature (cyan) treated with single-dose 15 Gy ionizing irradiation and perfusion (red). Zoom of the same tumour region from Day 1 to Day 8. Arrowheads: larger vessels display initially little change after irradiation only at Day 8 a change in the perfusion of some larger vessels was observed. Scale bar: 100 µm

(B) Zoom of **(A).** Some sprouts remain over several days, displaying little change and do not show further growth or fusion with other vessels. Arrowheads: maintaining sprouts displaying little change. Scale bar: 50 µm

Compared to B16F10 controls we observed a decrease in branch density after irradiation (Figure 4.7A); this decreased continued throughout the experiment after 15 Gy irradiation and can be explained by a loss of sprouts and the steady increase of the tumour volume even after irradiation. Branch density in control tumours slightly increased while tumours treated with 15 Gy showed an initial plateau of branch density followed by a decrease from day three onwards that also showed significant difference compared to control tumours (Figure 4.7B). This change indicates that further sprouting and formation of new vessels was abrogated and arrows in figure 4.6.2A indicate this further. This change in the behaviour of sprouting was maintained for the duration of the experiment and no recovery of tumour vessel sprouting occurred (Figure 4.6.1B).

The average vessel branch length showed only minor changes in general with an average branch length increasing from less than 100 to 110 to 120 micrometres in both control and treatment groups (Figure 4.7C). In control tumours, we observed a slight increase in the fraction of long branches. This was, however, also evident in irradiated tumours (Figure 4.7E). Irradiated tumour vessels continued their upward slope slightly towards the later time points, times at which the controls had to be sacrificed due to tumour volumes reaching volume limits.

Interestingly, while we observed changes in small vessels after irradiation in MC38 tumours this phenomenon did occur to a lesser extent in tumour blood vessels of B16F10 tumours. Instead, little and statistical non-significant change was seen after irradiation and most small vessels maintained their structural integrity (Figure 4.6.2B and Figure 4.7E). No change in tortuosity was observed over the period of imaging (Figure 4.7F) between control and irradiated tumours. Further, no change in directional coherence was observed (Figure 4.7G). We also did not observe a change in the diameter between control and irradiated tumours (Figure 4.7H).

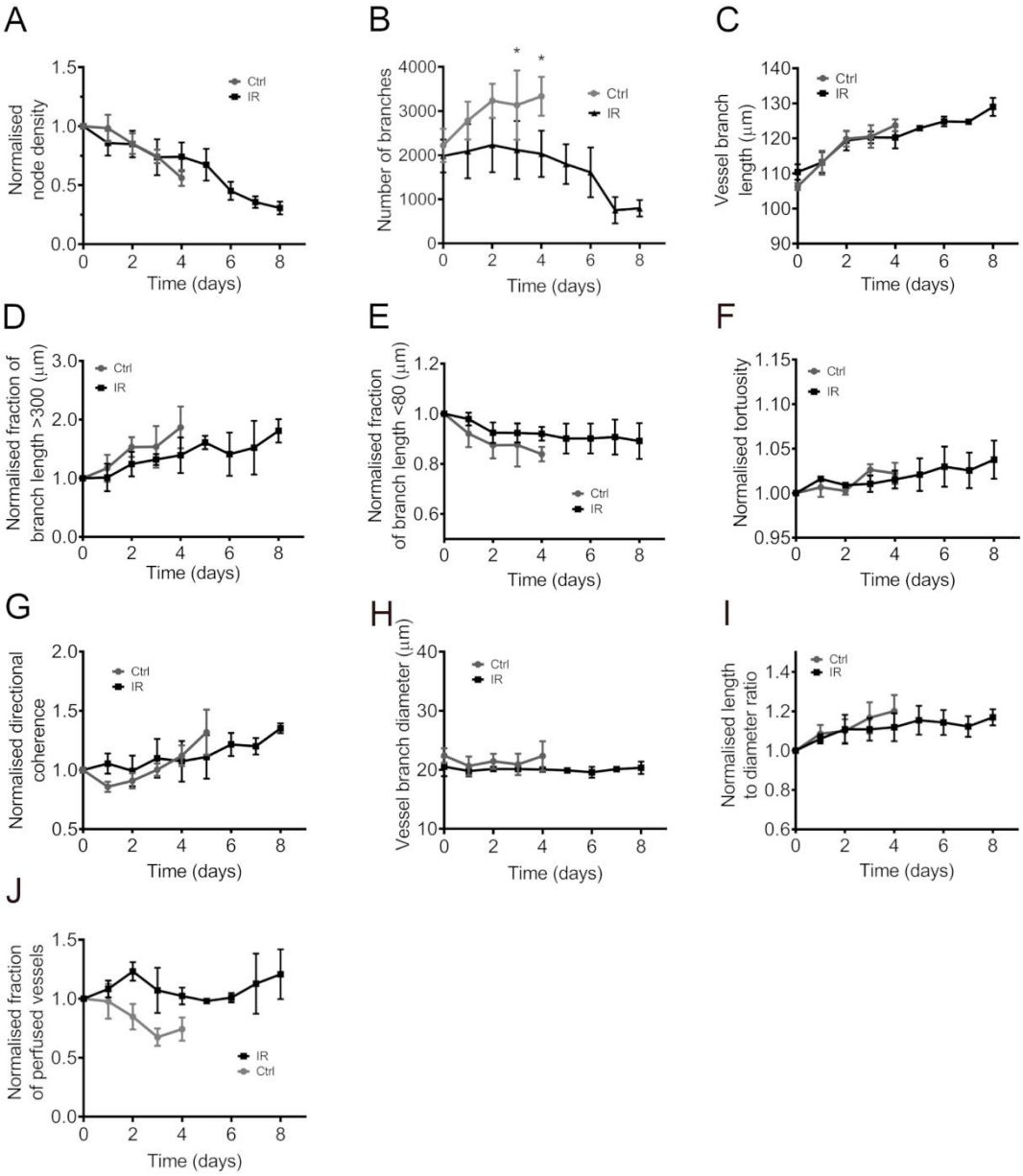


Figure 4.7 Time-lapse intravital microscopy of B16F10 tumours in VEOM mice after 15 Gy irradiation. (A-J) Quantified vascular parameters, for each day of imaging. The following parameters were quantified from segmented images. Parameters were normalised to Day 1 if indicated: **(A)** normalised node density, **(B)** normalised total count of branches, **(C)** average vessel length, **(D)** normalised branch length >300 µm, **(E)** normalised branch length < 80 µm, **(F)** normalised vessel tortuosity, **(G)** normalised directional coherence, **(H)** average vessel diameter, **(I)** normalised length to diameter ratio, **(J)** the normalised fraction of perfused vessels. Legends in A to J: Ctrl: Control, IR: 15 Gy irradiation. N=4 for control and single-dose irradiated samples. Error bars represent mean ± SEM, *P <0.05. Statistical analysis of all data by analysis of variance (1 way-ANOVA) with Tuckey's multiple comparison test.

Interestingly, while we observed changes in small vessels after irradiation in MC38 tumours this phenomenon did occur to a lesser extent in tumour blood vessels of B16F10 tumours. Instead, little and statistical non-significant change was seen after irradiation and most small vessels maintained their structural integrity (Figure 4.6.2B and Figure 4.7E). No change in tortuosity was observed over the period of imaging (Figure 4.7F) between control and irradiated tumours. Further, no change in directional coherence was observed (Figure 4.7G). We also did not observe a change in the diameter between control and irradiated tumours (Figure 4.7H).

Next, we calculated the length to diameter ratio of these tumours, but no obvious changes were observed (Figure 4.7I). This is perhaps not surprising because quantification did not reveal differences between vessel length and the distribution of the smaller and larger fraction of tumour blood vessels (Figure 4.7 C-E). Although less vascular in general, tumour vessels in B16F10 tumours were well perfused with initially a slight upward slope in perfusion at two days after irradiation compared to control (Figure 4.7J).

Together, these data suggest that high, single doses, of irradiation have a limited effect on the structure and function of tumour blood vessels. Our data suggest that smaller vessels and sprouts are more sensitive to radiation than medium and larger established vessel structures in the MC38 tumour model. Medium and larger tumour vessels maintain their structure and function. In addition, the change in parameters after a single high dose of radiation initially follows similar trends compared to antiangiogenic treatment in the MC38 tumour model. However, we have also seen that response to radiation is likely tumour model dependent. Since we did not observe any difference of the tumour vasculature parameters in the B16F10 model to 15 Gy single-dose irradiation and also there was no response to fractionated irradiation to tumour growth(Figure 4.1B, 4.6 and 4.7), we decided not to pursue fractionated irradiation in the intravital setting further for this tumour model.

4.3.5 Characterisation of vessels and hypoxia in MC38 and B16F10 tumours

We then wished to explain the differences in the vessel parameters we observed in the MC38 and the B16F10 models after radiation and to ask whether tumours grown subcutaneously instead of in the window chambers had similar characteristics. We used subcutaneous grown control, irradiated tumours, and immunofluorescence to investigate the parameters that can contribute to the response of tumour vessel to irradiation. Differences between the two models could be due to not only to endothelial cell-intrinsic factors but also to extrinsic factors influencing the response to irradiation, for example, from the tumour microenvironment. The microenvironment can influence the response of the tumour vasculature and endothelial cells to irradiation (352, 356). One of the factors that is known to affect tumour response to radiation is hypoxia (362), which is a result of the fast proliferation of tumour cells, the change in metabolism, and of the chaotic nature of the tumour blood vessel network. Hypoxia often leads to the expression of HIF-1 α which has recently been shown to protect endothelial cells from radiation damage (361). HIF-1 α is expressed in B16F10 tumours *in vivo* (363, 364). We, therefore, used tumour sections from subcutaneous derived MC38 and B16F10 tumours and determined the area of hypoxia in these tumours by staining for a hypoxia marker EF5 (362). The MC38 tumours, in general, displayed little hypoxia (Figure 4.8.1A) and we measured between 1 and 3% of the tumour area to be positive for hypoxia (Figure 4.8.1C). B16F10 tumours, in contrast, expressed greater areas of hypoxia (Figure 4.8.1B) throughout the tumour. Hypoxia in B16F10 was higher and EF5 positive areas correspond to around 10% of the total tumour area (Figure 4.8.1C). This difference in the presence of hypoxia in the tumour could be one of several factors affecting tumour vessels response to radiation.

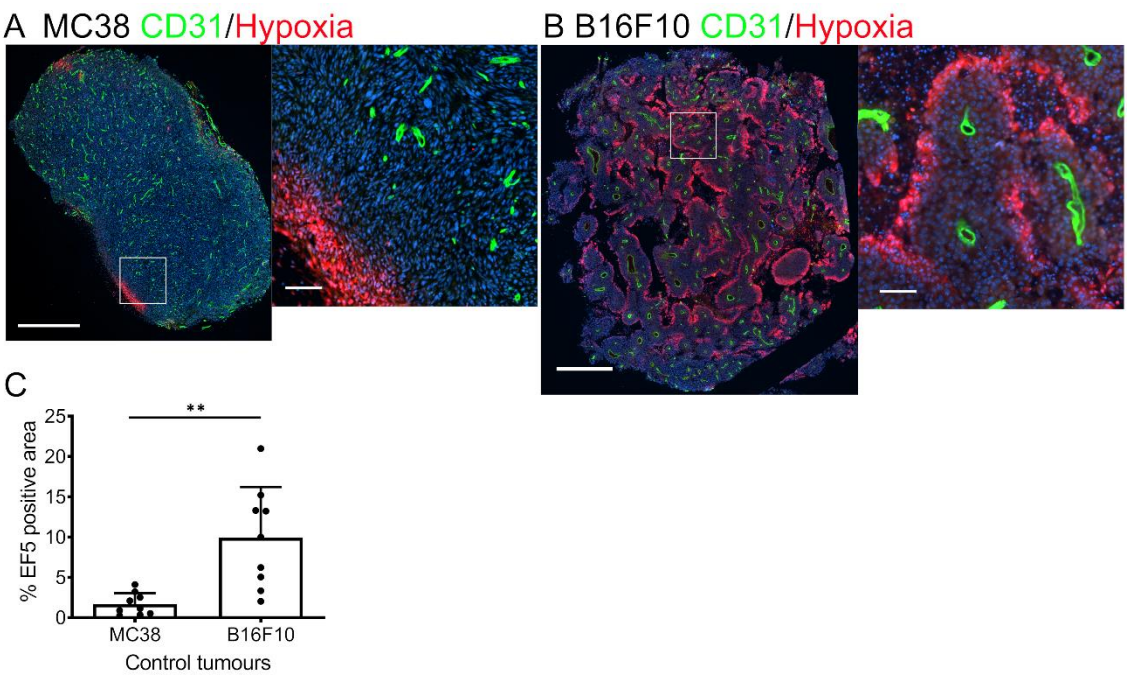


Figure 4.8.1 Tumour hypoxia in MC38 and B16F10 tumours.

(A) Representative fluorescent image of MC38 tumour labelled for hypoxia (red) with EF5, tumour vessels (green) anti-CD31 and nuclei (blue) Hoechst. The right panel of A: magnification of rectangle depicted in the left of A. Scale bars: 1 mm and 25 µm respectively.

(B) Representative fluorescent image of B15F10 tumour labelled for hypoxia (red) with EF5, tumour vessels (green) with anti-CD31 and nuclei (blue) with Hoechst. Right panel, magnification of rectangle depicted in the left panel. Scale bars: 1 mm and 25 µm respectively.

(C) Quantification of hypoxia by measuring EF5 area over the whole tumour area of MC38 and B16F10 tumours. Error bars represent mean + SD, **P <0.005. Statistical analysis of data by unpaired t-test.

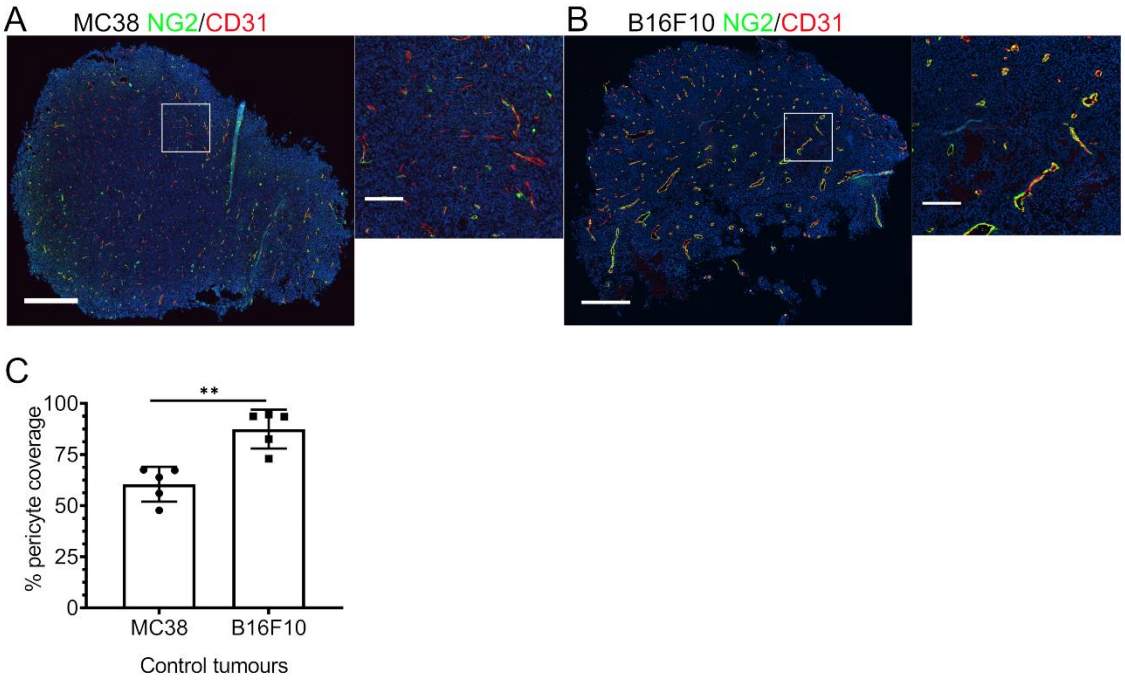


Figure 4.8.2 Tumour vessel coverage by mural cells in MC38 and B16F10 tumours.

(A) Representative fluorescent image of MC38 tumour labelled for mural cells coverage (green) anti-NG2, tumour vessels (red) anti-CD31 and nuclei (blue) Hoechst. The right panel of D: magnification of rectangle depicted in the left panel of D. Scale bars: 1 mm and 50 µm respectively.

(B) Representative fluorescent image of B16F10 tumour labelled for mural cells coverage (green) anti-NG2, tumour vessels (red) anti-CD31 and nuclei (blue) Hoechst. The right panel of E: magnification of rectangle depicted in the left panel of E. Scale bars: 1 mm and 50 µm respectively.

(C) Quantification of tumour vessel coverage by measuring NG2 area over the tumour vessel area of MC38 and B16F10 tumours. Error bars represent mean + SD, **P <0.005. Statistical analysis of data by unpaired t-test.

In normal vasculature, several layers of cells around the endothelial cells, including mural cells, such as pericytes and vascular smooth muscle cells, define the structure of a vessel. A feature of tumour vessels is the low coverage or absence of these types of cells. We were curious whether we could detect differences between the MC38 and the B16F10 tumour model. We used immunofluorescence staining to label pericytes in order to quantify tumour vessel coverage with mural cells (Figure 4.8.2A to C). Quantification revealed that the vasculature of

the MC38 tumours displayed a lower level of mural cell coverage than the B16F10 tumours (Figure 4.D and F).

4.4 DISCUSSION

4.4.1 Irradiation has limited effect on tumour vascular structure and function

In the previous chapter, we established an *in vivo* GEM model to fluorescently label endothelial cells. This allowed us to follow the development of the tumour vasculature within an intravital video microscopy setting. We then used the data and a custom-made algorithm to quantify changes in vessel morphology parameters throughout tumour growth.

In this chapter, we have attempted to analyse the effects of different radiation doses on the same parameters describing the vessel morphology. In order to investigate the radiation response of the tumour vasculature, developing tumours in the intravital model were irradiated with a single high dose of 15 Gy or fractionated irradiation of 5 × 3 Gy. We then followed the tumour vasculature over eight days and measured changes in the parameters describing vessel morphology.

In the literature, 15 Gy has been described as having a strong and lasting structural and functional impact on the tumour vasculature. Regarding the tumour growth response, we observed different radiation response in both models. While 15 Gy in the MC38 model led to tumour regression, in the B16F10 model we observed minor effects displayed in tumour growth delay. Fractionated irradiation of 5 × 3 Gy over five days led to growth delay in MC38 tumour with no change in tumour size during treatment. In the B16F10 tumours, however, only a slight delay of two days was observed, suggesting that it is a more radiation-resistant tumour. This had been shown previously (359). Reasons for the different responses could be due to microenvironmental factors such as the different levels of hypoxia displayed in the two models.

It is recognised that hypoxia affects radiation response in tumours and that hypoxic tumours are more radioresistant than those tumours that are primarily normoxic.

Generally, tumour vessels seemed relatively stable during the experiments with changes in the morphological parameters mainly observed in the first three days after single-dose irradiation. Looking at the tumour vasculature response to single-dose 15 Gy radiation we observed changes in structural, as well as functional, parameters in MC38 tumours. One study stated that the dramatic death of tumour endothelial cells and tumour vessels might have contributed to tumour cell response to irradiation (28). We did not, however, observe an immediate and major occurrence of endothelial cell death and vessel collapse after 15 Gy. Thus, our data questions the microvascular influence on the regulation of tumour cell response to radiation. Rather than the annihilation of tumour blood vessels, we saw an immediate and lasting inhibition of the formation of new tumour blood vessel sprouts after a single dose. Yet most vessels maintained their structural and functional integrity. Thus, 15 Gy does seem to be effective in inhibiting further sprouting angiogenesis but neither does it lead to the immediate destruction of functional blood vessels in the tumour models described here. In the fractionated irradiation setting, we observed similar changes in vessel parameters but in a delayed fashion. Several tumour vessel parameters changed in a similar way yet were not as pronounced as in the single-dose setting. This delayed change of parameters might be explained by the effect of dose accumulation through each fraction delivered to the tumour.

Angiogenesis is the result of the growth of small vessels, built from endothelial cells that are proliferating. Small vessels are guided by endothelial tip cells at the vessel front and proliferating stalk cells lining the newly formed vessels. While there is predominately only one guiding tip cell (365), stalk cells are thought to be higher in numbers. Stalk cells are the proliferating cells in a developing blood vessel (113, 366, 367). These proliferating endothelial cells that mainly occur in small vessels should be more susceptible to irradiation than non-

proliferating cells (368). Thus, stalk cells exposed to radiation could contribute to the inhibition of further sprout formation. The inhibition of the proliferation of stalk cells, therefore, could explain our observation of inhibited sprouting angiogenesis after irradiation. This inhibition may be due to DNA damage in endothelial cells, preventing them from further sprouting and proliferation. Natsuko and colleagues showed sprouting suppression in a matrigel plug assay after irradiation as well as p53 induced expression in endothelial cells after irradiation *in vitro* (255), which points towards DNA damage-induced inhibition of proliferation and angiogenesis.

We observed a decrease of the fraction of shorter vessels initially after 15 Gy irradiation and slightly later in the fractionated irradiation setting after the third fraction. The mechanism behind the decrease of the fraction of shorter vessels could be two-fold, by either vessel pruning or regression or by apoptosis. We investigated further apoptosis of tumour endothelial cells in the next chapter. We observed both phenomena after tumour irradiation (Figure 4.3) in the MC38 and the B16F10 tumour model.

The inhibition of the formation of new sprouts and short vessels as well as the destruction or pruning of short vessels could affect the measurement of other vessel parameters. For example, vessel length is measured by the distance from one to the next vessel bifurcation. By apoptosis or pruning of a short vessel, the mother vessel from which the sprout originated would become longer (because a bifurcation disappears) and thus would influence this measurement. In addition, we observed little change in larger vessels, indicating a larger better-established vessel seems to be more stable and displays greater resistant to radiation than a smaller vessel. We have observed this by measuring an increase in their fraction over all vessels. To add to that, any decrease of the fraction of shorter vessel branches would affect the length to diameter ratio and we have observed a change in this parameter. Together, this could lead to decreased tumour blood vessel network complexity. In a recently submitted article (369), we suggest that the increase of the length to diameter ratio could influence haematocrit

or the red blood cell density in blood vessels, contributing to perfusion within the tumour vasculature. In turn, this could explain the increase in perfusion we have observed in this model. Further, a decrease in the tumour cell density after irradiation, leading to decreased interstitial fluid pressure that can increase vessel diameter, is a possible contributor to an increase in perfusion (370).

The phenomenon of a less complex vascular network with increased perfusion has been coined *vascular normalisation* (360), occurring after anti-angiogenic treatment. Indeed, when we performed intravital imaging with the anti-angiogenic antibody DC101, tumour vessels parameters changed in a similar fashion to 15 Gy single-dose irradiation. Parameters like sprouting, vessel length and the decrease of the smaller vessel followed a similar pattern. However, the anti-angiogenic treatment showed more pronounced effects after the initial days of treatment initiation, eventually leading to large gaps between tumour vessels and thus indicating the limited time window of this type of treatment (58, 71). In contrast, in the irradiated setting tumour vessel maintained a more even vasculature network indicating a more subtle effect (350). The strong effect of DC101 treatment on the tumour vasculature is likely to be dose-dependent which has been shown by Jain *et al* (360, 372). Administration of lower concentrations could have perhaps led to more subtle effects on the tumour vasculature. This was not however the focus of this study.

Other parameters such as vessel tortuosity changed slightly. Whilst we observed a correlation between length and tortuosity which might be explained by the initial increase in tumour size after irradiation or inhibition of vessel development. Vessel diameter did not show significant differences between control and irradiated tumours.

The results discussed above have been made on the observation of the MC38 tumour model. This model showed high angiogenesis with a great fraction of small vessels. The B16F10 model, in contrast, did not show such high levels of angiogenesis. Yet irradiation did impact on

the formation of new sprouts in this tumour as well. Other parameters, however, did not appear to change compared to the control. On one hand, this could be because tumour vessels originating from this tumour seemed to be less proliferating (which we have investigated in the next chapter) making them less susceptible to radiation damage (357). On the other hand, B16F10 displays higher levels of hypoxia which has been shown to influence tumour vessel response to radiation by upregulation of HIF-1 α (361). Further, tumour vessels in the B16F10 model displayed a higher level of vessel coverage of mural cells. This indicates more mature vessels, which are also supported by a lower degree of the formation of new sprouts. These differences could influence the effect of radiation on the tumour vessels.

In both tumour models, we have observed angiogenesis by which new vessels emerge from pre-existing vessels. In the literature, several other mechanisms such as vasculogenesis (126), vessel co-option (330), and vascular mimicry (157) of vessel development have been described. In the previous chapter, we discussed their potential contribution to vessel growth in our model system. Several reports have suggested that some of these mechanisms of vessel growth contribute to vessel recurrence after radiation. If vasculogenesis in our GEM model contributed to tumour vessel development after radiation treatment, it would occur in a later stage, for example in tumour recurrence. If so, we would be not be able to observe it. If vasculogenesis appeared earlier within our timeframe, the contribution would have been small as we did not observe an increase in sprouting after irradiation. That is to say, if vasculogenesis occurred, it would only compensate for the number of vessels undergoing apoptosis or pruning. Further, our model would permit the observation of these newly formed vessels from circulating endothelial cells because the endothelial progenitor cells would not be labelled with tdTomato. This is because the tamoxifen was given to mice before irradiation and we commenced the experiments after the reported clearance time for tamoxifen. We have, however, not observed development of un-labelled tumour vessels in control or the irradiated settings suggesting that this type of vessel growth in our model does not majorly contribute to the development of new

vessel. In the case that vascular mimicry or the incorporation of transformed tumour stem cells to endothelial cells had taken place, it would also lead to un-labelled vasculature.

Another type of angiogenesis called intussusceptive angiogenesis, by which an initial pillar is formed in an existing vessel that then propagates to form two separate vessels, has been observed. We have seen pillars in small tumour blood vessels after radiation, yet the contribution seemed only minor compared to the already pre-existing tumour vasculature before radiation, and no major vessel occurred from this type of vessel development. Other means of angiogenesis, such as vessel co-option, does not apply in our setting because tumours do not grow within an existing organ and rely on sprouting angiogenesis. Taken together other means of angiogenesis seemed to play no or only minor roles in our model.

4.4.2 CONCLUSION

In this chapter, the occurring changes of the tumour vessel architecture after fractionated as well as a single high dose of radiation have been described. However, the shut-down of perfusion and the annihilation of tumour vessels was not observed. Nonetheless, we did see some changes in the MC38 tumour model with a decrease in shorter vessel branches, an increase in longer branches, and a decrease in the complexity of the network. The function and structure of the tumour vessels seemed generally able to withstand even higher doses of irradiation over the time measured. In addition, the changes we have observed seemed to be tumour-model dependent. Factors from the microenvironment might help to explain the different responses of the tumour vessels to radiation treatment. In the next chapter, we turn our eye more closely on endothelial cells themselves and how are they affected by irradiation on a cellular level.

Generally, our timeframe captures the initial response to irradiation. Later stages as described in the introduction of this chapter, for example, the phase of tumour recurrence, were not possible to observe for a variety of reasons such as complete tumour regression, experimental restrictions, licensing and ethical restrictions. In the wider context of tumour blood vessel contribution to tumours and their response to irradiation, we have looked at the effect of irradiation on angiogenic tumours. Whilst there are other types of angiogenesis, they do not appear to play a critical role in the development of tumour vasculature. Their roles, such as vessel mimicry by tumour cells and the contribution of vasculogenesis in the growth of tumour vessels have been contested. A phenomenon called vascular co-option (330), by which tumour cells grow along pre-existing blood vessels, however, was not possible to investigate within our model. This has been described, for example, in liver tumours. To answer questions about these phenomena, other experimental setups are needed which are beyond the scope of this study.

CHAPTER 5

Tumour Endothelial Cell Response to Single and Fractionated Irradiation

5.1 INTRODUCTION

In the previous chapter, we investigated how tumour vessel morphology changes to single and fractionated irradiation over time by using an intravital imaging approach in combination with a GEMM mouse model. In this chapter, we will investigate how tumour endothelial cells, the building blocks of tumour vessels, respond to single and fractionated irradiation on a cellular and molecular level.

5.1.1 Tumour endothelial cell proliferation

Tumour endothelial cell proliferation is one of several steps in tumour angiogenesis. It can be divided into the following discrete steps: the release of angiogenic factors, alteration in tumour endothelial cell morphology, release of proteolytic enzymes, migration, proliferation, capillary morphogenesis, and microvessel differentiation. The proliferation of endothelial cells in tumours is initiated by hypoxic conditions through hypoxia-inducible factor - 1α (HIF-1α)-mediated upregulation and secretion of growth factors such as VEGF-A. While endothelial tip cells spearhead the sprouting process, the resulting endothelial stalk cells are thought to be the main proliferating cells (64, 75, 373). Tumour endothelial cells have been shown to proliferate at a higher level than normal endothelial cells in fully developed organs but to a comparable level of angiogenesis in the developmental stage of the placenta (102, 163). During the process of angiogenesis, vessels are immature, with low coverage of perivascular cells and less developed basement membrane. In a tumour setting with a continuous proliferation of tumour cells, parts of the tumour vasculature also remain in an ever-immature state thanks to secreted growth factors from tumour cells. While the mature larger vasculature structures are relatively resistant to irradiation, capillaries and the more immature tumour vasculature, with its higher

level of proliferation, poorly developed vessel wall structure and little support through innervation, are radiosensitive (64, 101, 374–376).

5.1.2 Radiation-induced apoptosis

Damage done to DNA is a major problem for maintaining life. Radiation has been shown to result in DNA damage in a dose-dependent manner. The detection of DNA damage occurs within seconds and, upon repair, cells undergo cell cycle arrest mediated through Ataxia Telangiectasia Mutated (ATM) protein as primary DNA damage sensors. This leads to the inhibition of proliferation (377–380). Interestingly, Moding *et al.*et al. have shown that whilst ATM deletion in proliferating tumour endothelial cells enhances radiosensitivity, its does not do so in non-proliferating endothelial cells (263). Different types of DNA damage have been described in the literature to occur after irradiation, such as single-strand brakes and more severe double-strand brakes, leading to various chromosomal aberrations (381). Other types of damage to the DNA can also occur, such as damage to the sugar backbone and DNA-DNA cross-linking (382). Cells have acquired several repair pathways to cope with the different types of DNA damage for single and double-strand repair, such as base excision repair, and non-homologous end-joining (383, 384). While cells treated with lower doses are often capable of repairing the DNA damage caused by irradiation, repeated doses or larger doses of irradiation can lead to a significant accumulation of DNA damage. This can lead to a situation where cells are not capable of compensating and fully repairing their DNA damage. In such cases, cells have different mechanisms of responding, one of which is cell death.

Apoptosis is one of several types of programmed cell death (385, 386) which have been shown to occur also in endothelial cells (28, 262, 263, 274, 387, 388) and can be triggered through different mechanisms and pathways. These pathways can be intrinsic, such as DNA

damage caused through radiation, but also extrinsic through immune cells such as cytotoxic T cells. If the cell fate is determined to enter into apoptosis, it is based on the relative abundance of pro-apoptotic and anti-apoptotic proteins and their activation/inhibition and executed through the common activation of the caspase protease cascade (386). However, there are cell type-specific but also more common pathways that can lead to apoptosis, helping a complex organisation of cells maintaining integrity through effective cell removal depending on tissue type. In normal endothelial cells and vasculature, several pro- and anti-apoptotic factors have been described that exert influence upon whether apoptosis proceeds. Pro-apoptotic factors are, for example, low shear stress; pro-inflammatory mediators, such as interferon-gamma or interleukin 1; and vasoactive substances such as angiopoietin II, Fas signalling, caspases, perforin and granzyme B (389). Anti-apoptotic mediators are normal and high shear stress; adhesion proteins; anti-inflammatory cytokines like interleukin 10; and growth factors, such as vascular endothelial cell growth factor (VEGF) or fibroblast growth factor 2 (FGF2) (389).

In tumour endothelial cells, several mechanisms have been proposed to lead to apoptosis. Moding *et al.* suggest that by the deletion of the protein BAX in the tumour endothelium, cell death through apoptosis is induced in a p53/bcl-2 independent manner. Moding further suggest this causes mitotic catastrophe (262, 390). They have further shown that apoptosis in tumour endothelial cells occurs between 24 and 72 hours after irradiation. On the other hand, researchers around Fuks and Kolesnick have found that tumour endothelial cell apoptosis peaking between 4 and 12 hours can also occur after irradiation in a p53 independent manner through cell membrane generated ceramides/acid sphingomyelinase (261, 274, 391, 392).

While normal and tumour endothelial cells can undergo apoptosis after irradiation, in the previous chapter, we have seen that large parts of the tumour vasculature retain their structure and function after fractionated and single-dose irradiation. While we have observed

apoptosis in vessels, other means of cell response to radiation have been described previously. Kim *et al.* have suggested that endothelial cells in human umbilical veins go into radiation-induced senescence (249, 376, 393).

5.1.3 Radiation-induced inflammation

Another factor after irradiation is the inflammatory response that, regardless of apoptosis or senescence, manifests as a response of the tumour endothelial cell response to irradiation. This has been reported to manifest in increased expression of cell adhesion molecules, like intercellular adhesion molecule (ICAM)-1 or vascular cell adhesion molecule (VCAM)-1 *in vitro* (394, 395). Reactive oxygen species have also been reported as a result of irradiation, leading to NFκB activation that can induce an inflammatory state, increasing the expression of cytokines (396, 397). However, nearly all these studies have been done in vitro and on normal endothelial cells in a non-tumour microenvironment.

5.2 AIMS

The aim of this chapter is to describe the effect of single and fractionated irradiation on tumour endothelial cell proliferation and apoptosis *in vivo*. Further, we will investigate the change in gene expression in tumour endothelial cells after 15 Gy of irradiation. This has been done through the following workflow:

1) Quantifying the change of proliferation in tumour endothelial cells from subcutaneous tumour through flow cytometry and immunofluorescence
2) Quantifying apoptosis in tumour endothelial cells from subcutaneous tumours through flow cytometry and immunofluorescence
3) Investigating in which compartment of the tumour vasculature apoptosis predominately occurs
4) Investigating RNA sequencing data to explore potential pathways that shed light on the RNA expression in tumour endothelial cells after irradiation

5.3 RESULTS

5.3.1 Endothelial cell proliferation decreases after irradiation

In the previous chapter, we investigated the response of tumour vasculature to single and fractionated irradiation. To further explore how tumour vessels respond to radiation, we turned to tumour endothelial cells, the building blocks of the tumour vasculature. We used subcutaneously grown control and irradiated tumours and performed flow cytometry and immunofluorescence studies to precisely decipher endothelial cell response to irradiation *in vivo* at different time points after radiation. Previously we have observed a strong inhibition of sprouting angiogenesis after irradiation. We were therefore interested in how endothelial cells change their proliferative status after single and fractionated irradiation over the initial time course of 4 days after single and fractionated irradiation. Tumour sections of control and irradiated MC38 and B16F10 subcutaneous derived tumours were immunofluorescently labelled with antibodies to microscopically visualise tumour blood vessels, endothelial cell nuclei, and their proliferative status by quantifying their cell-cycle S-phase status (hereafter defined as proliferative status) (Figure 5.1.1 and 5.1.2). Figure 5.1.1A and B shows control MC38 tumours displaying a high proliferative capacity (EdU in red). We combine EdU with a marker for endothelial cell nuclei (anti-ERG in green), an endothelial cell-specific transcription factor (398–400) and a general marker for tumour vessels (anti-CD31 in orange). Interestingly, ERG , which is a transcription factor of the E26 family, has been shown to be involved in vasculature differentiation and development, driving gene expression of genes such as ICAM-2 and VE-cadherin both of which are crucial for the stability of endothelial junctions. This labelling method allowed us to unambiguously identify endothelial cell nuclei and quantify their proliferative status (Figure 5.1.1B arrows).

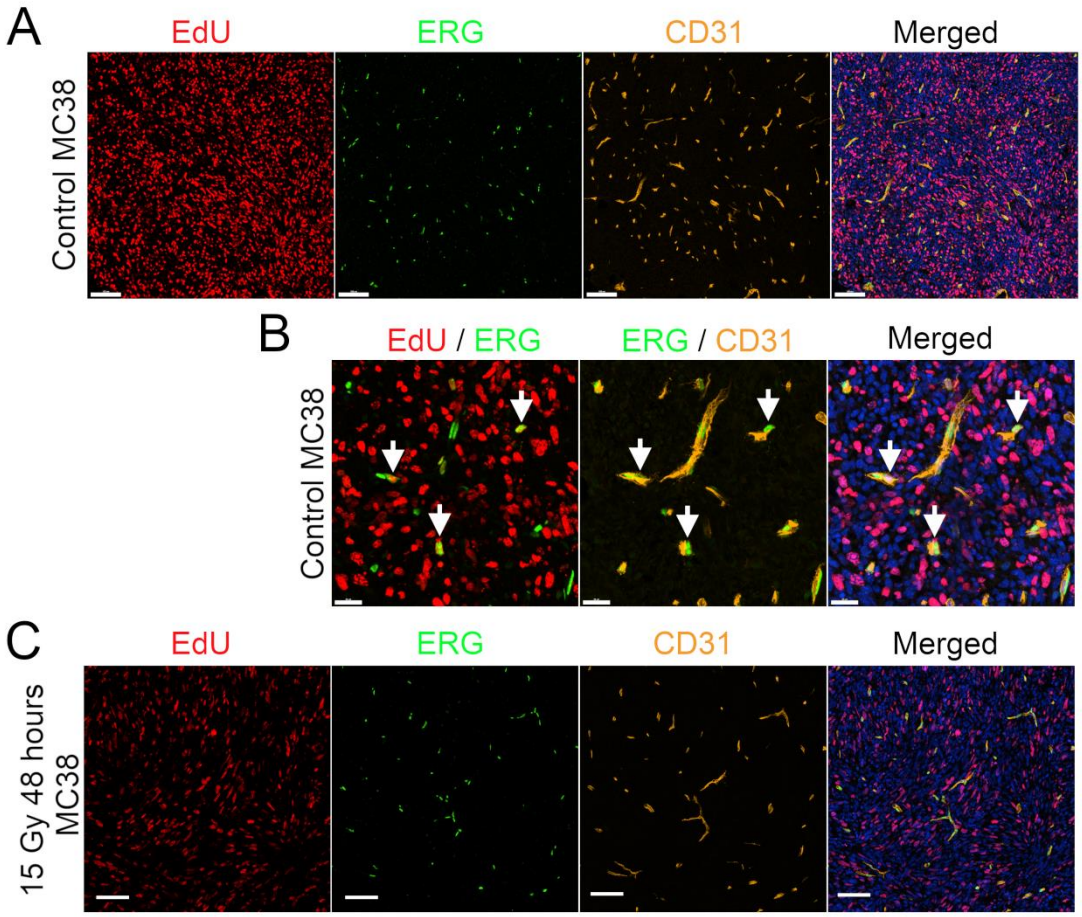


Figure 5.1.1 Proliferation of cells in MC38 tumours after single and fractionated irradiation.

(A) and **(B).** Panel **(A)** Representative immunofluorescent micrograph of non-irradiated MC38 tumours. Tumours are labelled for proliferation (red) with EdU, endothelial nuclei (green) anti-ERG, tumour vessels (orange) anti-CD31 and nuclei (blue) Hoechst. **(B)** High magnification of merged channels of proliferating cells (red) and tumour endothelial cell nuclei (green) tumour vessels (orange) and nuclei (blue) Hoechst. Arrows: proliferating tumour endothelial cells. Scale bars in **A** 100 µm and **B** 25 µm.

(C) Representative immunofluorescent micrograph of 15 Gy irradiated tumours 48 hours after treatment. Tumour labelled for proliferation (red) with EdU, endothelial nuclei (green) anti-ERG, tumour vessels (orange) anti-CD31 and nuclei (blue) Hoechst. Scale bars in **C** 100 µm.

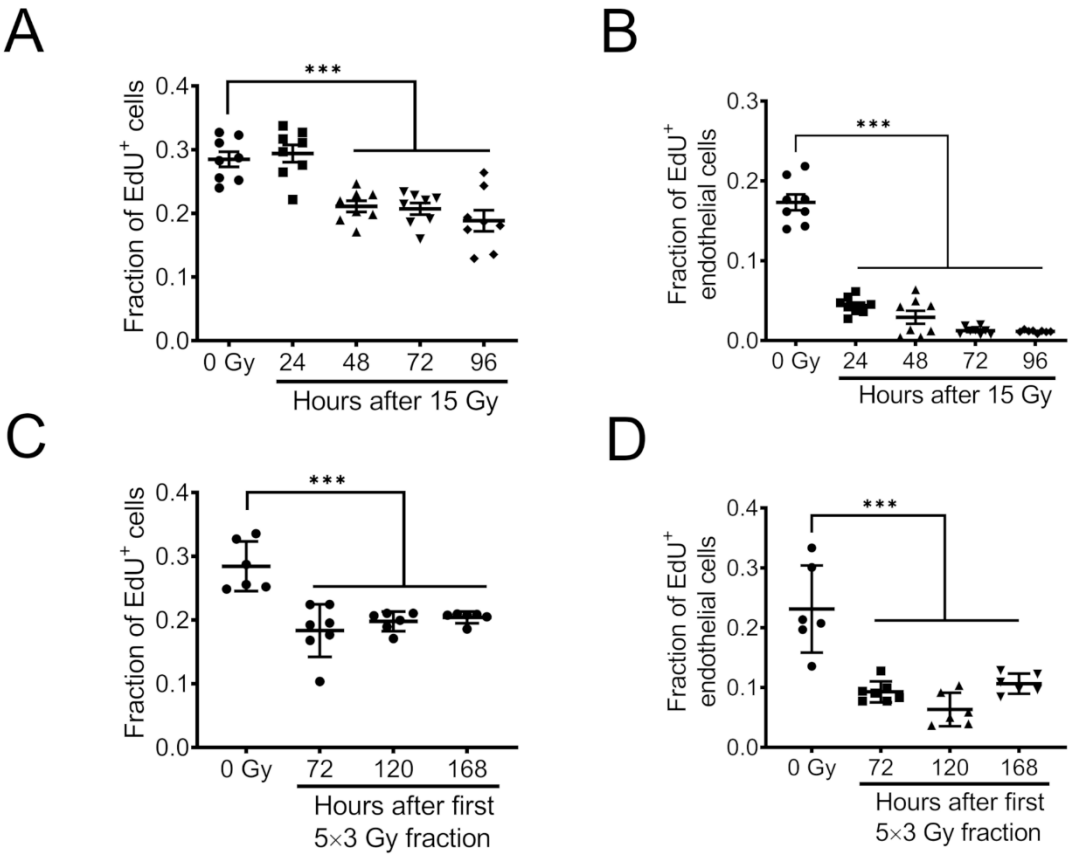


Figure 5.1.2 Quantification of the proliferation of total and tumour endothelial cells in MC38 tumours after single and fractionated irradiation.

(A) Quantification of proliferating cells in control and 15 Gy irradiated MC38 tumours (n = 8 per group) from immunofluorescent images. Fraction of EdU+ cells is the proliferating fraction of all detected cells from a 10 µm thick tumour section. Error bars represent mean ± SD, *P < 0.05, **P < 0.005, ***P < 0.0005 Statistical analysis of data by analysis of variance (one way-ANOVA) with Dunnett's multiple comparison test.

(B) Quantification of proliferating tumour endothelial cells in control and 15 Gy irradiated MC38 tumours (n = 8 per group). Fraction of EdU+ tumour endothelial cells is the proliferating fraction of all detected tumour endothelial cells on one 10 µm thick tumour section. Error bars represent mean ± SD, *P < 0.05, **P < 0.005, ***P < 0.0005 Statistical analysis of data by analysis of variance (one way-ANOVA) with Dunnett's multiple comparison test.

(C) Quantification of proliferating cells in control and fractionated irradiated MC38 tumours (n = 6 to 7 per group). Error bars represent mean ± SD, *P < 0.05, **P < 0.005, ***P < 0.0005 Statistical analysis of data by variance (one way-ANOVA) with Dunnett's multiple comparison test.

(D) Quantification of proliferating tumour endothelial cells in control and fractionated irradiated MC38 tumours (n =5 to 6 per group). Error bars represent mean ± SD, *P < 0.05, **P < 0.005, ***P < 0.0005 Statistical analysis of data by analysis of variance (one way-ANOVA) with Dunnett's multiple comparison test.

We then irradiated subcutaneous tumours with single-dose 15 Gy or fractionated irradiation 5 × 3 Gy and quantified the total proliferative response of all cells, tumour endothelial cells and tumour cells over the initial days after irradiation. In control non-treated MC38 tumours, roughly 30% of all cells are in an active proliferative state (Figure 5.1.2A). With flow cytometry we were able to identify tumour cells (Figure 5.2A to C), in a specific high proliferative status in which roughly 40% of all tumour cells were determined to be in a proliferative state (Figure 5.2D). Tumour endothelial cells in control MC38 tumours displayed a slightly lower proliferative status with an average of 20% of all tumour endothelial cells proliferating (Figure 5.1.2B and 5.2E). Upon single-dose 15 Gy irradiation, the overall proliferation in MC38 tumours did not change significantly within 24 hours (Figure 5.1.2A). A significant decrease of approximately 30% to 20% of overall cell proliferation was observed within 48 hours after 15 Gy irradiation.

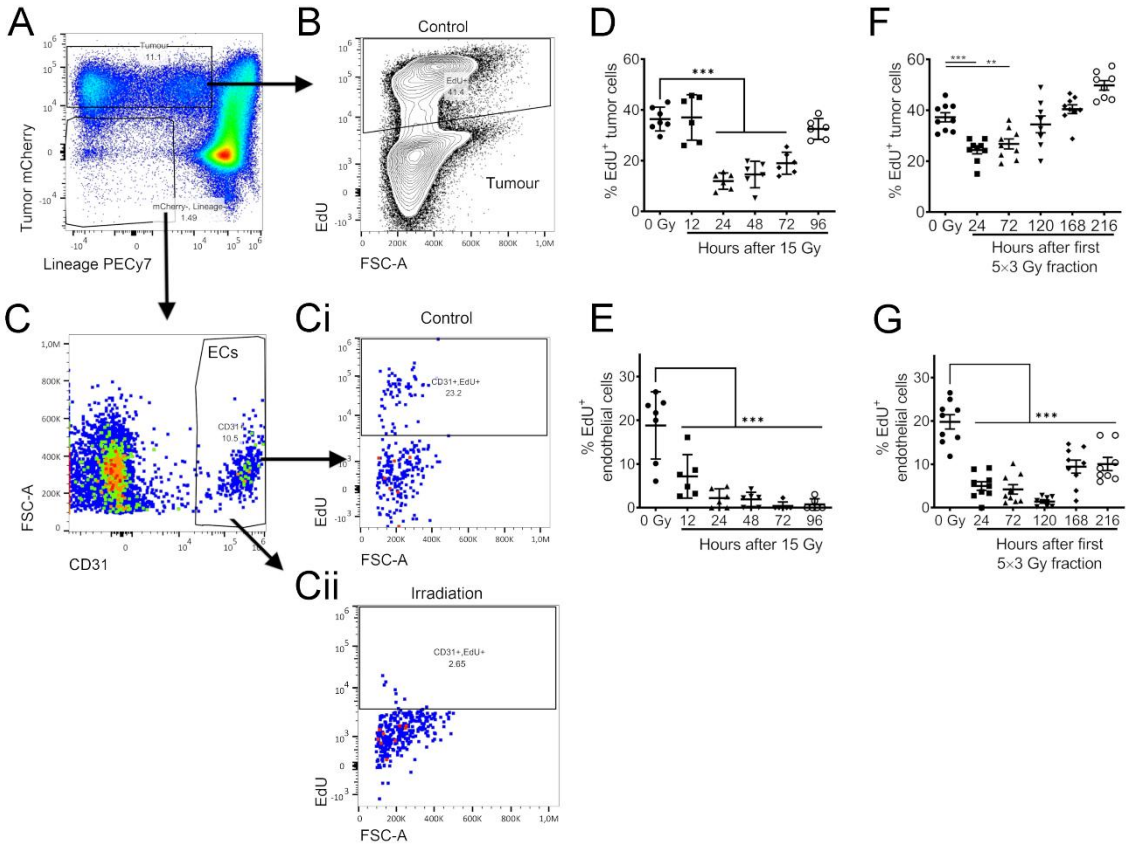


Figure 5.2 Flow cytometry analysis of tumour endothelial cell apoptosis and proliferation after single and fractionated IR.

(A) To **(C)** Representative flow cytometry gating strategy to distinguish tumour endothelial cells from MC38 tumours from live cells (for full gating strategy, see figure 2.2).

(B) A probability contour plot showing the gating to differentiate proliferating, EdU positive tumour cells from non-proliferating tumour cells.

(C) Representative flow cytometry gating strategy to determine proliferating tumour endothelial cells in MC38 tumours **(Ci)** in control and **(Cii)** irradiated tumours.

(D) Quantification of tumour cell proliferation in control and 15 Gy irradiated MC38 tumours (n = 6 to 9 per group). Error bars represent mean ± SD, *P < 0.05, **P < 0.005, ***P < 0.0005 Statistical analysis of data by analysis of variance (one way-ANOVA) with Dunnett's multiple comparison test.

(E) Quantification of tumour endothelial cell proliferation in control and 15 Gy irradiated MC38 tumours (n = 6 to 8 per group). Error bars represent mean ± SD, *P < 0.05, **P < 0.005, ***P < 0.0005 Statistical analysis of data by analysis of variance (one way-ANOVA) with Dunnett's multiple comparison test.

(F) And **(G)** Quantification of tumour cell and tumour endothelial cell proliferation in control and fractionated 5 × 3 Gy irradiated MC38 tumours (n = 8 to 9 per group). Error bars represent mean ± SD, *P <0.05, **P <0.005, ***P <0.0005 Statistical analysis of data by analysis of variance (1 way-ANOVA) with Dunnett's multiple comparison test.

Flow cytometry analysis allowed us to separately measure specific tumour cells and tumour endothelial cells (Figure 5.2A to C). After irradiation with 15 Gy, we observed no decrease in proliferation within 12 hours (Figure 5.2D). However, after 24 hours a significant decrease in proliferation of MC38 tumour cells was observed with a decrease from 40% to roughly 10% of all tumour cells (Figure 5.2D). Tumour cells, however, recovered in their proliferation over the following days and reached a similar level of proliferation 96 hours after single-dose 15 Gy irradiation (Figure 5.2D). Tumour endothelial cells instead showed significant inhibition of proliferation within 12 hours after 15 Gy irradiation determined by immunofluorescence and flow cytometry (Figure 5.1.2B and 5.2E). Their proliferative status did not recover over the consecutive days and maintained a very low level (Figure 5.1.2B and 5.2E). This pattern, observed on a cellular level, confirms the data shown in the previous chapter at the tumour vessel and sprouting level. Fractionated 5 × 3 Gy showed a significant impact on total proliferation on MC38 tumours (Figure 5.1.1C). A decrease of 10% in total proliferation was observed after the third fraction measured by immunofluorescence and was maintained at this level until the last fraction (Figure 5.1.2C). The proliferative response of tumour cells was significantly inhibited 24 hours after the first fraction (Figure 5.2F). Flow cytometry analysis, however, showed that tumour cells recovered quickly after the last fraction of 3 Gy (Figure 5.2F). Tumour endothelial cells in the MC38 model showed a significant decrease in proliferation already after the first fraction of 3 Gy irradiation (Figure 5.2G) and maintained a low level of proliferation during fractionated irradiation (Figure 5.1.2D and 5.2G). Tumour endothelial cell proliferation was inhibited throughout the fractionated irradiation treatment. However, 48 hours after the last fraction, tumour endothelial cell started to recover in their proliferative capacity (Figure 5.2G). In comparison, a single high dose led to strong and prolonged inhibition while fractionated irradiation had only transient effects on the inhibition of tumour endothelial cell proliferation.

Next, we investigated B16F10 tumours and their proliferative capacity in control, single 15 Gy and fractionated 5 × 3 Gy irradiated tumours (Figure 5.3.1A to C). Sections of immunofluorescently labelled B16F10 tumours displayed a similar total proliferation of roughly 30% (Figure 5.3.2D and C first panel). Tumour endothelial cells developing in the B16F10 tumour showed a lower proliferative fraction than in the MC38 model (Figure 5.3.2B and D both left panels). Approximately 10% of tumour endothelial cells proliferated at one time (Figure 5.3.2B). Interestingly, this resembles the observation of lower angiogenesis described previously by intravital microscopy (Figure 4.6). Single-dose 15 Gy irradiation significantly inhibited total proliferation to 20% from 30% without radiation and remained at this level for at least 72 hours (Figure 5.3.2A). Tumour endothelial cells showed a similar response after single-dose 15 Gy, compared to the MC38 tumour endothelial cells (Figure 5.3.2B). Their proliferation decreased roughly by half and was maintained at this level (Figure 5.3.2B). Fractionated irradiation significantly inhibited the proliferation of the total cells, as well as tumour endothelial cells. (Figure 5.3.2C and D). Interestingly, tumour endothelial cells also showed a recovery 48 hours after the last fraction which was also the case in the MC38 model (Figure 5.3.2D).

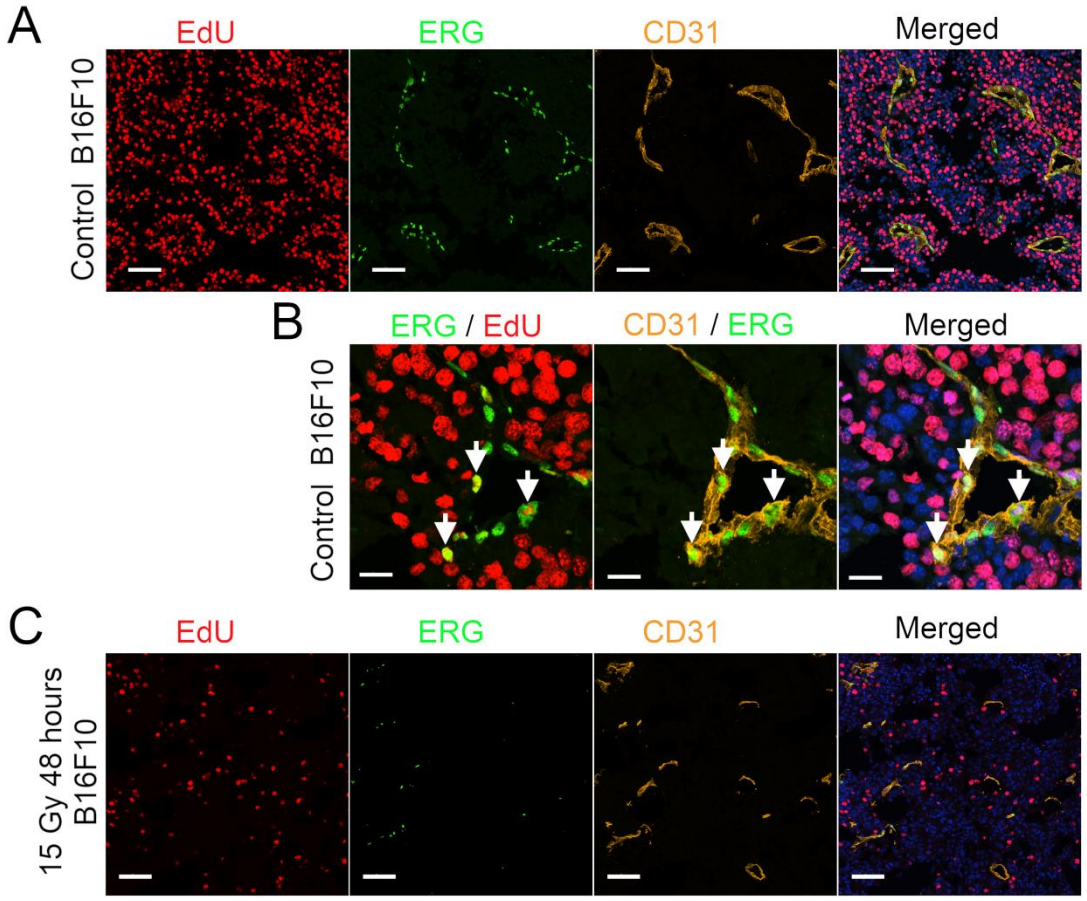


Figure 5.3.1 Proliferation of cells in B16F10 tumours after single and fractionated irradiation.

(A) and **(B).** Panel **(A)** Representative immunofluorescent micrograph of non-irradiated B16F10 tumours. Tumours are labelled for proliferation (red) with EdU, tumour endothelial nuclei (green) anti-ERG, tumour vessels (orange) anti-CD31 and nuclei (blue) Hoechst. **(B)** High magnification of merged channels of proliferating cells (red) and tumour endothelial cell nuclei green and tumour vessels (orange). Arrows: proliferating tumour endothelial cells. Scale bars in **A** 100 µm and **B** 25 µm.

(C) Representative immunofluorescent micrograph of 15 Gy irradiated tumours 48 hours after treatment. Scale bars in **C** 100 µm.

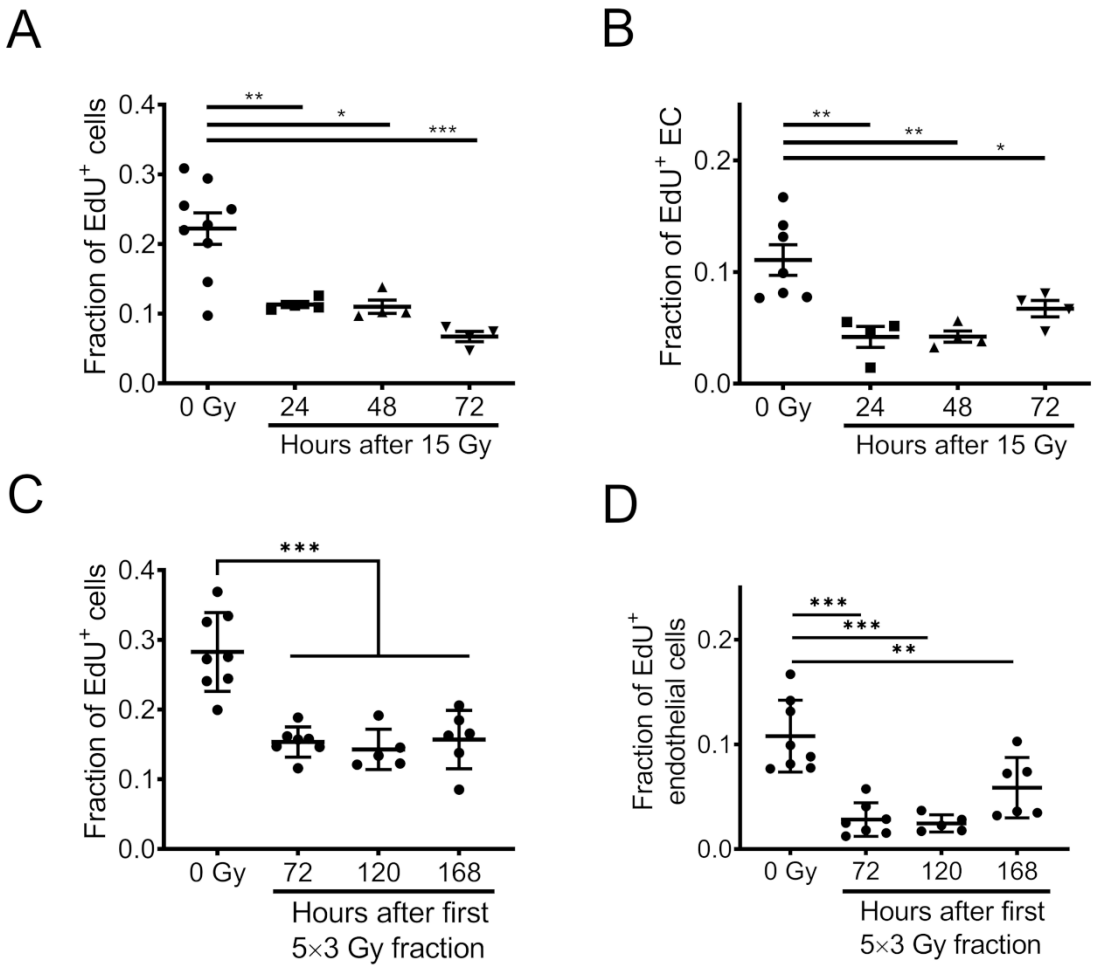


Figure 5.3.2 Proliferation of cells in B16F10 tumours after single and fractionated irradiation.

(A) Quantification of proliferating cells in control and 15 Gy irradiated B16F10 tumours (n = 4 to 8 per group). Error bars represent mean ± SD, *P < 0.05, **P < 0.005, ***P < 0.0005 Statistical analysis of data by analysis of variance (one way-ANOVA) with Dunnett's multiple comparison test.

(B) Quantification of proliferating tumour endothelial cells in control and 15 Gy irradiated B16F10 tumours (n = 4 to 8 per group). Error bars represent mean ± SD, *P < 0.05, **P < 0.005, ***P < 0.0005 Statistical analysis of data by analysis of variance (one way-ANOVA) with Dunnett's multiple comparison test.

(C) Quantification of proliferating cells in control and fractionated irradiated B16F10 tumours (n = 5 to 8 per group). Error bars represent mean ± SD, *P < 0.05, **P < 0.005, ***P < 0.0005 Statistical analysis of data by variance (one way-ANOVA) with Dunnett's multiple comparison test.

(D) Quantification of proliferating tumour endothelial cells in control and fractionated irradiated B16F10 tumours (n =5 to 8 per group). Error bars represent mean ± SD, *P < 0.05, **P < 0.005, ***P < 0.0005 Statistical analysis of data by analysis of variance (one way-ANOVA) with Dunnett's multiple comparison test.

Taken together, we have seen how irradiation affects not only tumour cell proliferation but also proliferation in general. Importantly, irradiation has an even more pronounced effect on the tumour endothelial cells. While tumour cells show quick recovery from irradiation damage, tumour endothelial cells generally seem more susceptible to damage caused by irradiation. We observed prolonged inhibition of proliferation after single-dose 15 Gy irradiation. Fractionated irradiation, in contrast, did not show such prolonged inhibition. Recovery of the proliferation in tumour cells and tumour endothelial cells was observed already within 48 hours after the last fraction.

5.3.2 Radiation-induced apoptosis in tumour vessels

In the previous chapter, we observed a decrease in network density after irradiation with intravital microscopy. Quantification revealed a decline of shorter tumour vessels over time. The decrease of tumour vessels after radiation has been shown to be partly due to apoptosis. We therefore wanted to see whether we could detect apoptosis of tumour endothelial cells after single and fractionated irradiation. To shed light on the timeframe of apoptosis in tumour vessels, we quantified apoptosis by measuring cleaved caspase-3 in tumour endothelial cells in tumour sections and cleaved caspase-3/7 positive tumour endothelial cells with flow cytometry. It was previously reported that apoptosis occurs in tumour endothelial cells as early as 6 to 12 hours after single-dose; others have shown peaks of apoptosis between 48 and 72 hours after irradiation. Subcutaneous tumours treated with single-dose 15 Gy irradiation were subjected to flow cytometry analysis (Figure 5.4).

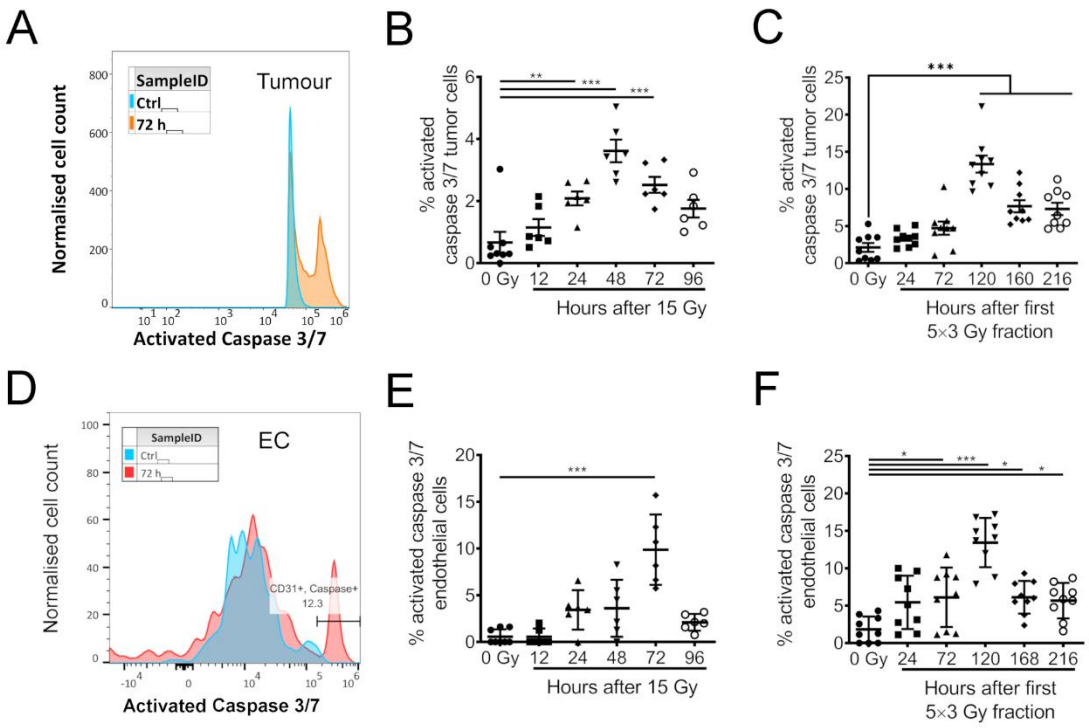


Figure 5.4 Flow cytometry analysis of apoptosis in MC38 tumour and tumour endothelial cells after irradiation.

(A) Histogram to differentiate apoptosis by activated caspase 3/7 in tumour cells from non-apoptotic tumour cells.

(B) Quantification of tumour cell apoptosis in control and 15 Gy irradiated MC38 tumours (n = 6 to 8 per group). Error bars represent mean ± SD, *P < 0.05, **P < 0.005, ***P < 0.0005 Statistical analysis of data by analysis of variance (one way-ANOVA) with Dunnett's multiple comparison test.

(C) Quantification of tumour cell apoptosis in control and 5 × 3 Gy fractionated irradiated MC38 tumours (n = 6 to 8 per group). Error bars represent mean ± SD, *P < 0.05, **P < 0.005, ***P < 0.0005 Statistical analysis of data by analysis of variance (one way-ANOVA) with Dunnett's multiple comparison test.

(D) Histogram to differentiate apoptosis by activated caspase 3/7 in tumour endothelial cells from non-apoptotic tumour endothelial cell cells.

(E) Quantification of tumour endothelial cell apoptosis in control and 15 Gy irradiated MC38 tumours (n = 8 to 9 per group). Error bars represent mean ± SD, *P < 0.05, **P < 0.005, ***P < 0.0005 Statistical analysis of data by analysis of variance (one way-ANOVA) with Dunnett's multiple comparison test.

(F) Quantification of tumour endothelial cell apoptosis in control and 5 × 3 Gy fractionated irradiated MC38 tumours (n = 6 to 8 per group). Error bars represent mean ± SD, *P < 0.05, **P < 0.005, ***P < 0.0005 Statistical analysis of data by analysis of variance (one way-ANOVA) with Dunnett's multiple comparison test.

A time course experiment over the initial days to reveal peaks of apoptosis after single and fractionated irradiation showed the highest value of apoptosis in MC38 tumours cells at 48 hours after 15 Gy single dose (Figure 5.4 A and B) and 120 hours after the start of the 5×3 Gy fractionated irradiation (Figure 5.4C). Apoptosis decreased thereafter to a lower level. Time course flow cytometry analysis of tumour endothelial cells revealed an increase in apoptosis over time with a peak at 72 hours after 15 Gy single-dose irradiation (Figure 5.4D and E). Thereafter apoptosis decreased again (Figure 4.5E). In the fractionated setting tumour endothelial cell apoptosis reached its highest value, like tumour cells, at 120 hours after fractionated irradiation initiation. To confirm this timeline of the induction of apoptosis, we used immunofluorescence staining of whole tumour sections (Figure 5.5A). Similar to flow cytometry analysis, we observed significant induction of apoptosis at 48 and 72 hours after 15 Gy irradiation in MC38 tumours (Figure 5.5B). 5 × 3 Gy fractionated irradiated MC38 tumours also showed a significant increase in apoptosis within 72 hours (after the third fraction). A peak of apoptosis was observed at 120 hours and maintained a higher level for several consecutive days (Figure 5.5C).

Having established a timeline of induction of apoptosis, we next quantified apoptosis in B16F10 tumours after 15 Gy single-dose irradiation via immunofluorescence of whole tumour sections. Confirming that we had seen little change in the morphological structure of tumour vessels after irradiation in this tumour model via intravital imaging, we observed a significant but much smaller induction of apoptosis in B16F10 tumours 72 hours after 15 Gy irradiation (Figure 5.5D). Taken together, we may establish that irradiation-induced apoptosis in both MC38 and B16F10 tumour models show a peak of apoptosis around 72 hours after single-dose radiation and 120 hours after fractionated irradiation in the MC38 model.

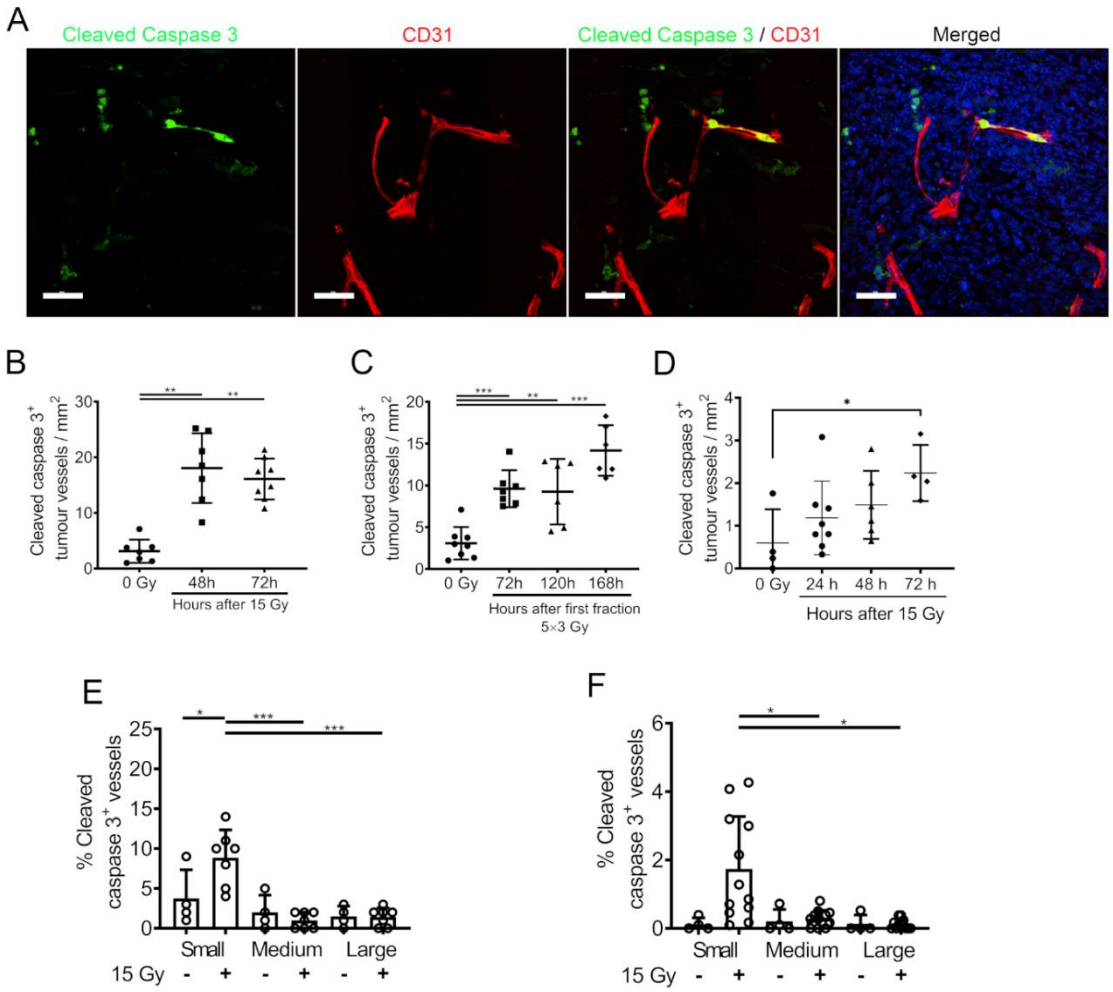


Figure 5.5 Tumour endothelial cell apoptosis after single and fractionated irradiation.

(A) Representative immunofluorescent micrographs 48 hours after 15 Gy irradiation of the tumour vasculature from MC38 tumours. Apoptosis (anti-cleaved caspase 3) in green, tumour vessels (anti-CD31) in red and Nuclei (Hoechst) in blue. Scale bars: 50 µm.

(B) Quantification of apoptotic tumour endothelial cells in control and 15 Gy irradiated MC38 tumours (n = 6 to 7 per group). Error bars represent mean ± SD, *P < 0.05, **P < 0.005. Statistical analysis of data by analysis of variance (one way-ANOVA) with Dunnett's multiple comparison test.

(C) Quantification of apoptosis in tumour endothelial cells in control and 5 × 3 Gy irradiated MC38 tumours (n = 6 to 8 per group). Error bars represent mean ± SD, *P < 0.05, **P < 0.005, ***P < 0.0005 Statistical analysis of data by analysis of variance (one way-ANOVA) with Dunnett's multiple comparison test.

(D) Quantification of apoptosis in tumour endothelial cells in control and 15 Gy irradiated B16F10 tumours (n = 4 to 8 per group). Error bars represent mean ± SD, *P < 0.05, **P < 0.005, ***P < 0.0005 Statistical analysis of data by variance (one way-ANOVA) with Dunnett's multiple comparison test.

(E) Quantification of apoptotic vessels according to size on thin whole MC38 tumour sections (n = 4 to 7 per group). Error bars represent mean ± SD, *P < 0.05, **P < 0.005, ***P < 0.0005 Statistical analysis of data by analysis of variance (one way-ANOVA) with Tukey's multiple comparison test.

(F) Quantification of apoptotic vessels according to size on thin whole B16F10 tumour sections (n = 4 to 7 per group). Error bars represent mean ± SD, *P < 0.05, **P < 0.005, ***P < 0.0005 Statistical analysis of data by analysis of variance (one way-ANOVA) with Tukey's multiple comparison test.

Previously, we observed that the fraction of smaller vessels decreased after radiation and that larger vessels seemed less susceptible to irradiation. We, therefore, wanted to see whether we could detect apoptosis predominately in smaller and not larger vessels. To this end, we separated tumour vessels detected by immunofluorescence staining according to pixel area size in small (less than 300 pixels), medium (from 300 to 1500 pixels), and large vessels (greater than 1500 pixels). We then quantified apoptosis from these immunofluorescence images in both MC38 and B16F10 tumours. When tumours received 15 Gy irradiation apoptosis, this predominately occurred in the smaller compartmented vessels in MC38 (Figure 5.5E) and B16F10 tumours (Figure 5.5F).

To confirm the measurements that we had observed on 10-micrometre thin sections, we used 80-micrometre thick tumour sections that display a more comprehensive tumour vascular network and allow us to identify tumour vessel sprouts. This allows us to detect features more precisely and define large and small vessels such as sprouts. High-resolution fluorescent images were recorded for tumour vessels and apoptosis (Figure 5.6A and B). Segmentation of the vascular network allowed us to precisely measure length, diameter, and area of all vessel branches from a thick tumour section and trace those vessels that are positive for cleave caspase-3 indicating apoptosis. Quantifying the vessels positive for cleaved caspase-3 revealed that sprouts, blind ends, and short vessels, which could be identified by their smaller values in length, diameter, and area, did indeed display higher levels of apoptosis than larger vessels (Figure 5.6C - E).

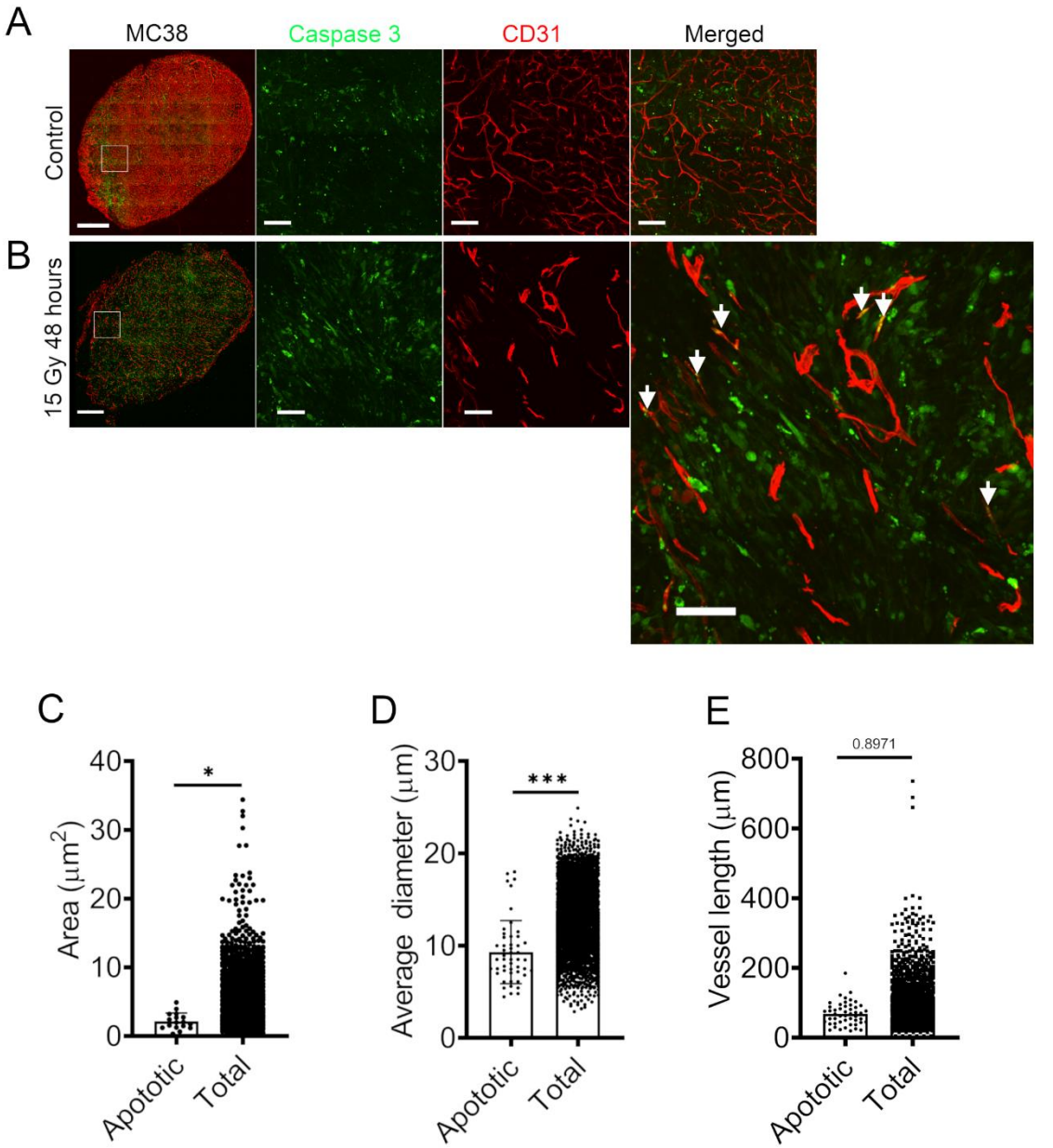


Figure 5.6 Tumour vessels apoptosis after 15 Gy single-dose irradiation in thick tumour sections.

(A) and **(B)** Representative immunofluorescent micrographs of control and 15 Gy treated tumour vasculature from MC38 tumours. Tumour vessels (anti-CD31) and apoptosis (anti-cleaved caspase 3) in **(A)** control and **(B)** 48 hours after 15 Gy irradiation. Scale bars: 100 µm and 25 µm respectively.

(C) to **(E)** tumour vessel area **(C)**, diameter **(D)**, and length **(E)** of apoptotic tumour vessels vs all tumour vessels from segmented thick 80 µm tumour tissue sections (n = 4 per group).). Error bars represent mean ± SD, *P < 0.05, **P < 0.005, ***P < 0.0005 Statistical analysis of data by unpaired t-test with Welch's correction due to sample size and variance differences in C and D.

5.3.3 Tumour endothelial cell gene expression confirms cell cycle arrest and apoptosis

Radiotherapy targets the tumour, stromal and tumour endothelial cells resulting in DNA damage and, in consequence, to the up- or down-regulation of signalling pathways in response to DNA damage. We wanted to know whether our previous observation of the effect of irradiation on proliferation and apoptosis of tumour endothelial cells would also be detectable on a gene expression level. We decided to perform RNA sequencing on MC38 control and irradiated tumours 48 hours after receiving a single dose of 15 Gy of irradiation. This time point was initially chosen because we assumed that most DNA damage should be repaired by this time and that the expression of genes in pathways concerning DNA repair would have dropped to the baseline. This decrease would not mask the expression of other genes in pathways which may be potentially important in subsequent stages of tumour endothelial cells in response to radiation damage. We characterised gene expression by FACS (fluorescent activated cell sorting) separating tumour endothelial cells from MC38 control tumours and from tumours 48 hours after 15 Gy irradiation. The FACS sorted tumour endothelial cells were then subjected to whole RNA sequencing (Figure 2.3).

To ensure sorted cells were actual tumour endothelial cells, we first examined endothelial cell signature genes (Figure 5.7A). Indeed, we were able to detect all major known endothelial cell marker in control and irradiated samples (Figure 5.7A) such as: VE-cadherin; Von Willebrand factor; endoglin; vascular VEGFR-2; PDGFR; and Endothelial Cell Adhesion Molecule (CD31). We then investigated if marker genes for other cell types were present. In both control and irradiated samples we did not detect markers for other cells or detected them at very low levels (Figure 5.7B), indicating successful sorting of tumour endothelial cells in both control and irradiated samples.

Endothelial cells can be subdivided to tip, stalk, and phalanx cells depending on their position within a vessel representing their function. For example, tip cells are endothelial cells at the sprouting and migratory front. Stalk cells in comparison, follow tip cells and are thought to represent the majority of proliferative endothelial cells. Lastly, phalanx cells are thought to represent endothelial cells in larger vessels displaying low levels of proliferation and angiogenesis. Several genes have been attributed to each subcell type based on their function in normal or tumour angiogenesis (67, 401). We wanted to know whether we would be able to detect the presence of these marker genes. We did detect several genes attributed to the different endothelial cell subtypes, confirming that we had a mixed distribution of these cells in our sample (Figure 5.7C-E). While we did find most of these marker genes were present in our samples, we did not observe differences in the gene expression when compared to irradiated samples (Table S5.1). Thus, from the RNA sequencing of our bulk samples, each containing a mixed population of tumour endothelial cells, we could not conclude whether irradiation results differentially affect different subpopulations of tumour endothelial cells.

Further, we detected the majority of transcription factors related to endothelial cell development, putative endothelial cell surface markers as well as major pathways related to endothelial cell development, such as the notch-delta family mentioned in the literature (Table S5.2). However, no significant differential expression in most of those transcription factors was observed between control and irradiated samples. For example, the expression of ERG (an endothelial cell-specific transcription factor which we have also observed via immunofluorescence) linked to vascular homeostasis and the stability of endothelial cell junctions, did not change thus confirming it as a robust marker for tumour endothelial cells.

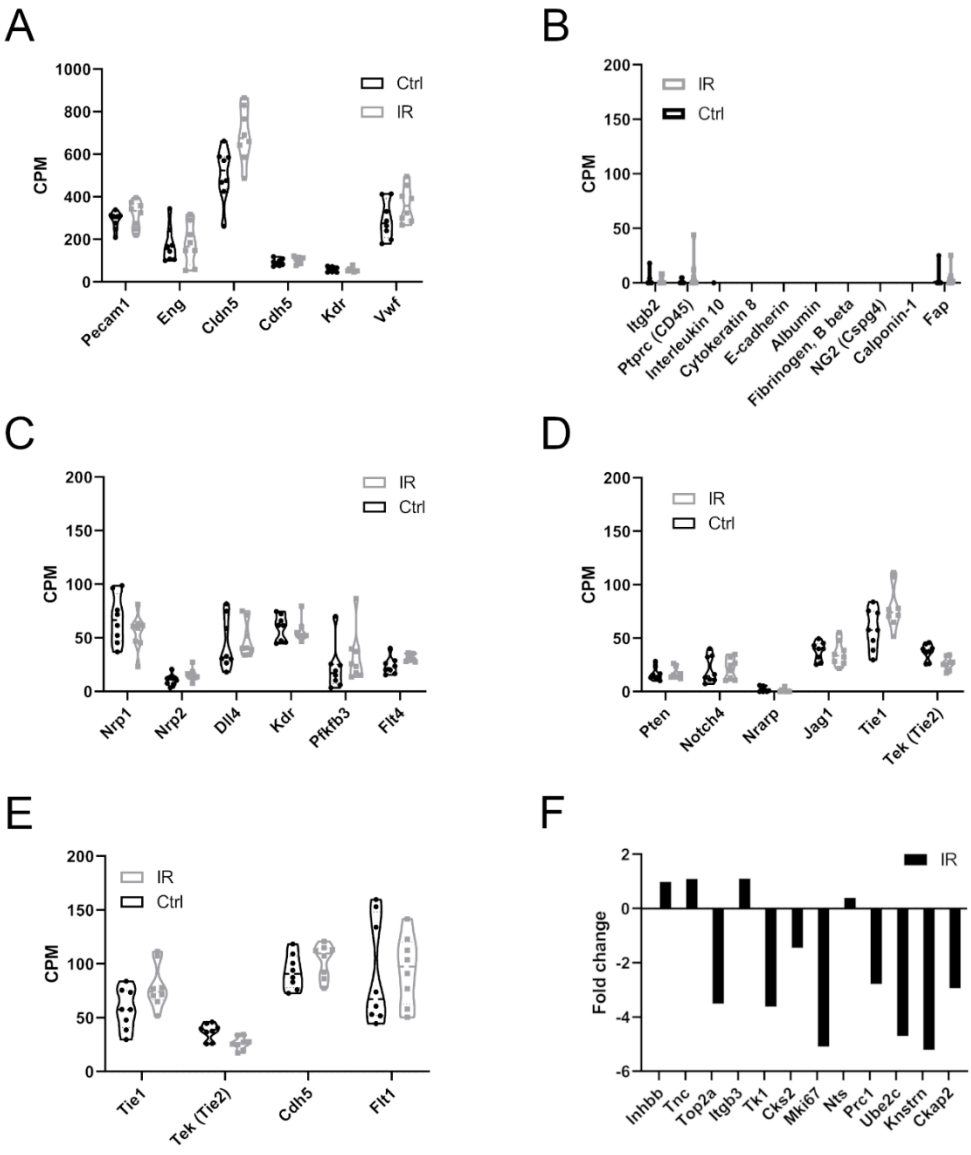


Figure 5.7 Differential expression analysis of tumour endothelial cells after 15 Gy single-dose irradiation.

(A) Violin plots of general endothelial cell genes present in control (black) and irradiated samplers (grey). Read counts are displayed as counts per millions

(B) Violin plots of genes present in non-endothelial cells such as mural cells or immune cells in control (black) and irradiated samples (grey). Read counts are displayed as counts per millions

(C) Violin plots of marker genes attributed to endothelial tip cells. Read counts are displayed as counts per millions

(D) Violin plots of marker genes attributed to endothelial stalk cells. Read counts are displayed as counts per millions

(E) Violin plots of marker genes attributed to endothelial phalanx cells. Read counts are displayed as counts per millions

(F) Histogram of downregulated genes attributed to active tumour angiogenesis as fold changes

To understand potential pathways that are up- or downregulated after irradiation we calculated fold changes of detected genes related to active angiogenesis in control tumours. The genes attributed to angiogenesis remained down-regulated 48 hours after 15 Gy irradiation compared to the control (Figure 5.7F). Other factors that have been reported to inhibit angiogenesis were upregulated after irradiation (Table S5.2), for example, IL-27, genes of the STAT family, CXCL10, and CXCL11 showed upregulation and have been reported to inhibit endothelial cell proliferation and migration (402).

To comprehensively understand differential gene expression after irradiation, we used pathway analysis tools to categorise the genes involved in radiation response. Several tools are available to classify functionally related subfamilies of genes. We chose Panther and MetaCore pathway analysis due to their well-curated gene list. Among the pathways with significant change, MetaCore analysis revealed genes associated to pathways that can be divided into the following categories: DNA damage and cell cycle regulation as well as cytokine signalling and immune response (Figure 5.8). Of the twenty most altered pathways derived from MetaCore, ten were related to DNA damage and cell cycle regulation. For example, genes such as p21 were upregulated at 48 hours after irradiation. Eight more pathways were related to inflammation and immune response, such as interferon pathways. This finding indicates that at this time point an inflammatory and immune attractant response of the tumour endothelial cells takes place.

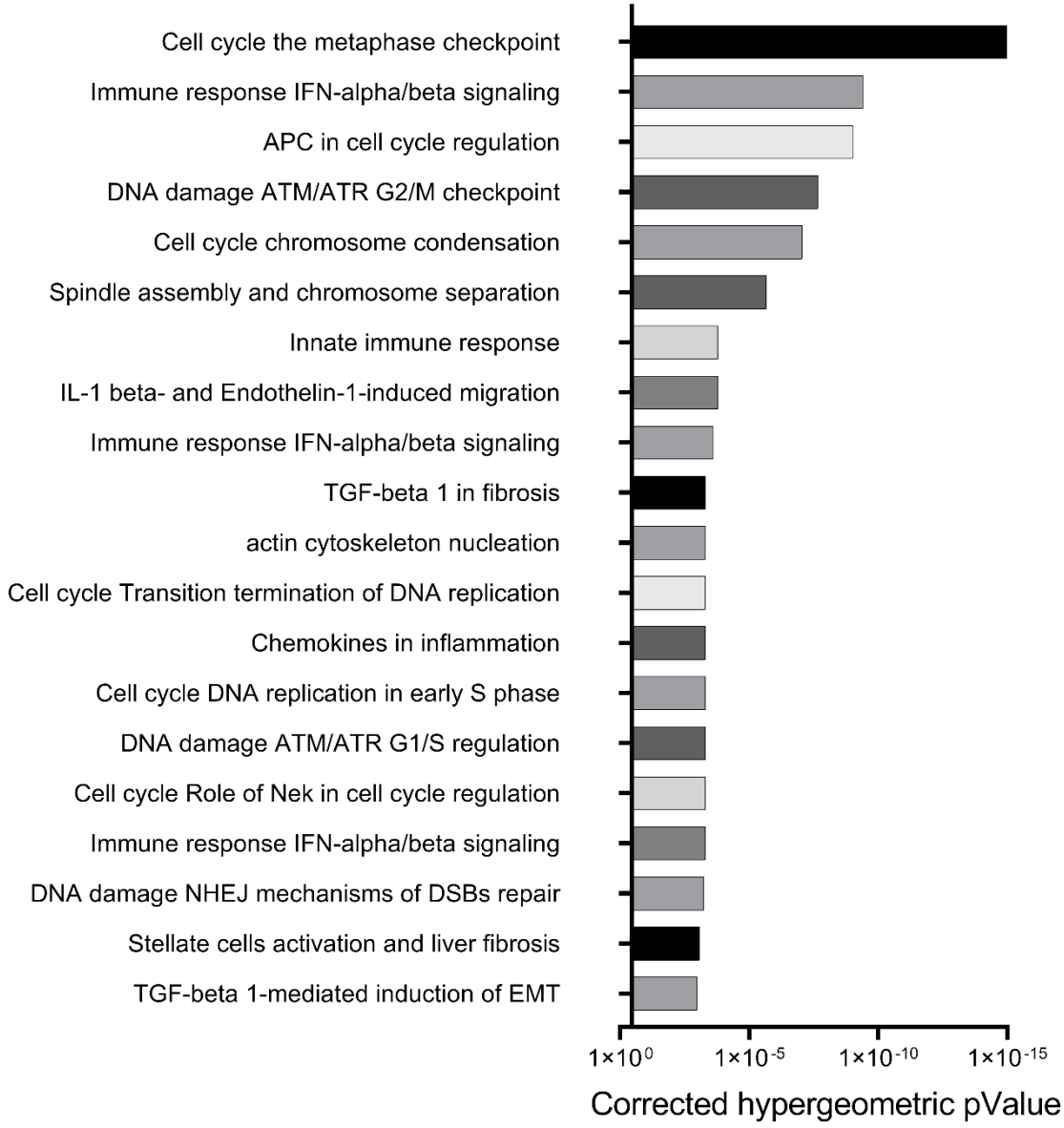


Figure 5.8 MetaCore pathway analysis of tumour endothelial cells 48 hours after 15 Gy irradiation. Top 20 classified signalling pathways in tumour endothelial cells 48 hours after 15 Gy irradiation. Data acquired from 16 tumours with n = 8 per group. Genes were selected based on fold change ≥ ±1 and $P < 0.05$.

Panther pathway analysis similarly revealed upregulation of several pathways that can be divided into the following groups: apoptosis and survival; inflammatory response and immune cell activation; cell cycle regulation and DNA damage (Figure 5.9). Kolesnick et al. suggested the contribution of ceramide-mediated tumour endothelial cells apoptosis initiated

via acid sphingomyelinase (aSMase) at earlier time points. Although our data was collected at a later time point, we did not detect significant upregulation of genes related to this pathway (Table S5.1). We did, however, find upregulation of genes such as Bcl2 and Birc5 that are linked to apoptosis. On the other hand, a gene like FGF2 was upregulated and has been reported to be a pro-survival in endothelial cells. Other pathways were down-regulated. These included for growth factors like EGF, FGF, PDGF, and VEGF; downstream signalling pathways of growth factors, like Wnt and Notch; as well as purine and pyrimidine pathways leading to the de novo biosynthesis of deoxyribonucleotides (Figure 5.10).

Radiation leads to DNA damage and as a consequence several genes in the DNA damage, oxidative stress and damage-associate molecular patterns (DAMPs) were up or down-regulated, suggesting an inflammatory activated state of tumour endothelial cells after irradiation as previously described (273). At 48 hours after 15 Gy irradiation, we found several genes connected to DMAPS upregulated (Table S5.2) suggesting two major responses to irradiation: first, DNA damage and second, cell cycle arrest.

Taken together the pathway analysis augments and confirms our previous observation of decreased proliferation and increased apoptosis in tumour endothelial cells. Our data indicates that irradiation results in a change across a range of pathways including DNA damage, cytokine and growth factor pathways as well as metabolic changes after irradiation. Moreover, the upregulation of genes and pathways linked to inflammation and attraction of immune cells indicates that tumour endothelial cells not only passively respond to DNA damage, resulting in proliferation arrest and apoptosis, but also actively contribute to the activation of immune response and communicate with their microenvironment.

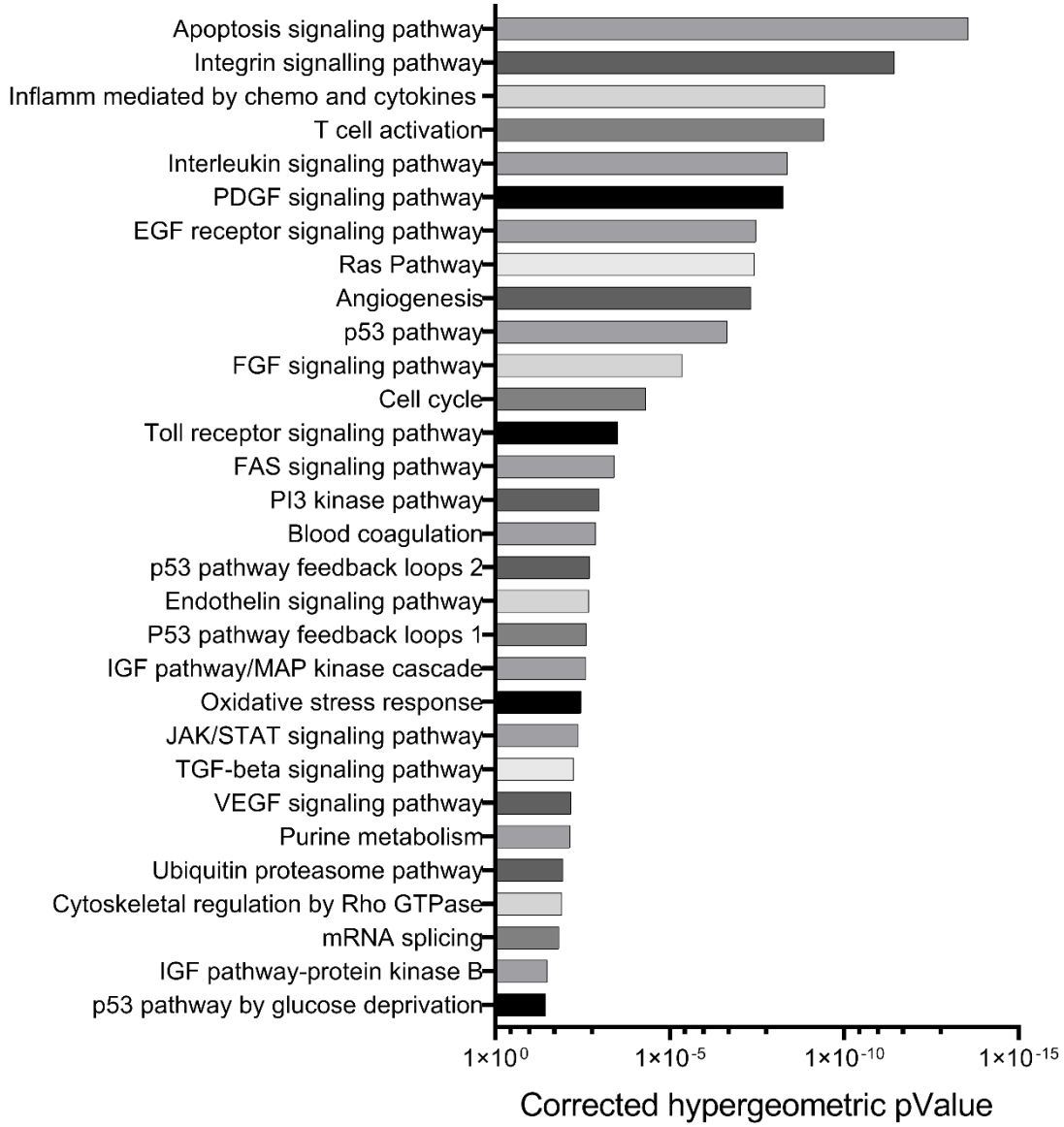


Figure 5.9 Panther pathway analysis of tumour endothelial cells 48 hours after 15 Gy irradiation. Top 30 classified upregulated signalling pathways in tumour endothelial cells 48 hours after 15 Gy irradiation. Data acquired from 16 tumours with n = 8 per group. Genes were selected based on fold change ≥ ±1 and $P < 0.05$.

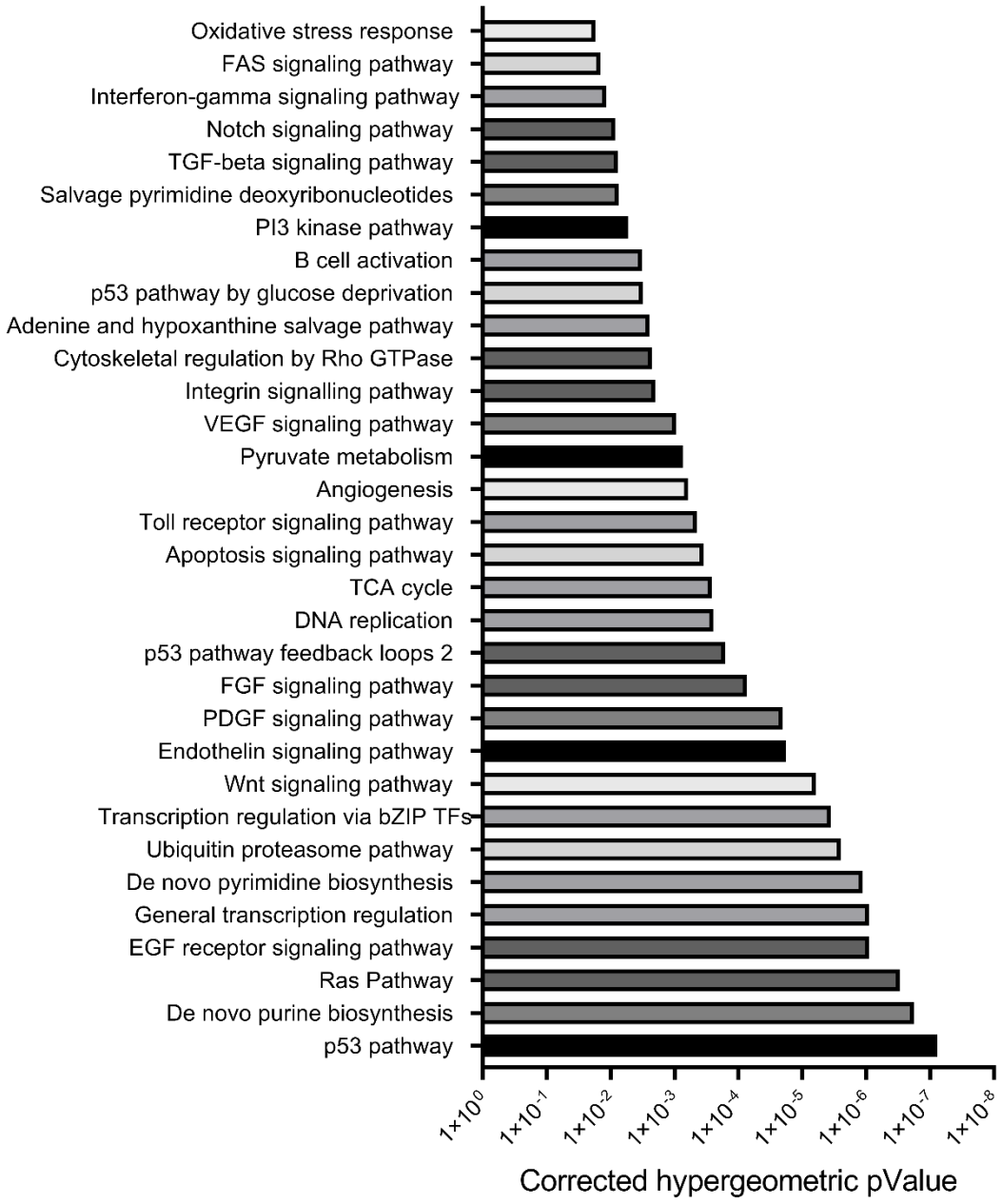


Figure 5.10 Panther pathway analysis of tumour endothelial cells 48 hours after 15 Gy irradiation. Top 32 classified downregulated signalling pathways in tumour endothelial cells 48 hours after 15 Gy irradiation. Data acquired from 16 tumours with n = 8 per group. Genes were selected based on fold change ≥ ±1 and $P < 0.05$.

5.4 DISCUSSION

In the previous chapter, we showed not only that irradiation affects tumour vascular parameters but also that the tumour vasculature maintains its stability after irradiation. Here we have attempted to understand how tumour endothelial cells respond on a cellular level to irradiation, particularly to a high dose of irradiation from a proliferative and apoptotic perspective. We have investigated tumour endothelial cells with immunofluorescence and flow cytometry to quantify proliferation and apoptosis after irradiation. Moreover, we have used whole RNA sequencing to shed light on the underlying pathways that change after irradiation and that might contribute to the tumour endothelial cell response to the single high dose of irradiation.

5.4.1 Tumour endothelial cell proliferation is inhibited after irradiation

In the previous chapter, we observed that in both the MC38 and the B16F10 tumour models an inhibition in the formation of new sprouts occurred after irradiation. Here we have shown that flow cytometry analysis and immunofluorescence in both MC38 and B16F10 tumours, model effective inhibition of proliferation after irradiation, this providing one potential explanation. Our data confirms that proliferation of tumour cells and tumour endothelial cells are affected by irradiation both in the single and fractionated setting. While a single dose of 15 Gy showed a prolonged inhibitory effect on tumour endothelial cell proliferation, fractionated irradiation led to transient inhibition of proliferation, such that tumour endothelial cells recovered their proliferative capacity from radiation damage after the last fraction. While endothelial cells show strong and prolonged inhibition with low capability to recover, tumour cells recovered to a similar proliferative state even after 15 Gy irradiation relatively quickly. It is

well known that irradiation affects proliferation in cells in general (378), our *in vivo* data on tumour endothelial cells confirm similar results previously shown *in vitro* (255, 403). Prolonged inhibition of proliferation after 15 Gy might be due to the cell's inability to repair DNA damage. Our RNA sequencing data confirmed several pathways upregulated in tumour endothelial cells 48 hours after irradiation related to DNA damage pathways. It should be noted that this was done at a relatively early time point at 48 hours after 15 Gy. Evidence at later time points would allow us to draw conclusions about the long-term response of tumour endothelial cells to irradiation. Our *in vivo* imaging data from the previous chapter over the eight initial days after irradiation indicates that tumour blood vessels and tumour endothelial cells, although largely retaining their function, do not recover their proliferative capacity after 15 Gy irradiation.

We observed variation in the percentage of proliferative tumour endothelial cells depending on the tumour type. Although B16F10 tumours display faster tumour growth rate than MC38, tumour endothelial cells in B16F10 tumours display less proliferation. This finding agrees with the less active level of angiogenesis and sprouts formation in the B16F10 tumour type which were investigated in the previous chapter. Differences in the proliferation rate of tumour endothelial cells have been shown previously (102). Irradiation of 15 Gy in B16F10 tumours, however, similarly inhibited proliferation and no differences in response were observed between the tumour endothelial cells originating from the two models, indicating that such high doses effectively inhibits their long-term proliferation.

By use of *in vivo* imaging, we have observed that larger vessels retain their structural integrity. One could argue that endothelial cells in these vessels are less proliferative and should, therefore, be less susceptible to irradiation. Interestingly, our data shows that tumour endothelial cells, unlike tumour cells, do not regain their proliferative capacity after irradiation, indicating the damage received after 15 Gy leads to cell cycle arrest. Whether tumour endothelial cells eventually would recover and start proliferating or undergo senescence

remains an unanswered question as we did not explore this phenomenon here. There is a need for further research looking at these phenomena over a longer period of time.

Interestingly, total proliferation measured by immunofluorescence did not change after irradiation, indicating that either the other cells within the tumour microenvironment maintain their proliferative status or more likely that an increased infiltration of cells that have the proliferative capacity occurs after irradiation. These cells are likely to be immune cells. It has been shown that irradiation induces immune cell infiltration into tumours (404, 405).

Altogether, these data suggest that tumour endothelial cells respond quickly to single-dose irradiation resulting in increased inhibition of proliferation. Fractionated irradiation on the other side results in transient inhibition of proliferation with tumour cells and tumour endothelial cells capable of quickly recovering to a proliferative state after the last fraction of irradiation.

5.4.2 Tumour vessel apoptosis after irradiation

Irradiation in cancer treatment aims to either kill tumour cells or force them into a non-proliferative state. We have observed both phenomena in tumour endothelial cells, with the latter one shown above. If cells are not capable of repairing the damage they have experienced by radiation, they can undergo senescence and/or undergo different types of programmed cell death, such as apoptosis. It has been previously shown that tumour endothelial cell can undergo apoptosis after irradiation through different mechanisms (28, 262, 263). There is still some debate about the timeline when apoptosis occurs in tumour endothelial cells after irradiation and which pathways are involved (28, 262, 263, 274).

In both MC38 and B16F10 tumour models, apoptosis of tumour endothelial cells peaked between 48 and 72 hours after a single dose and at the end of the fractionated regime at 120 hours and beyond. This was measured by labelling tumour endothelial cells for activated caspase 3/7, a common downstream marker for apoptosis and the timeline of apoptosis is in agreement with data from other published reports from Kirsch *et al.* (262, 263, 276). Further, we have observed apoptosis predominately in smaller vessels and sprouts. Additionally, RNA sequencing of tumour endothelial cells 48 hours after 15 Gy irradiation showed upregulation of the genes involved in apoptosis.

Kolesnick *et al.* have shown earlier apoptosis of tumour endothelial cells after a single high dose of irradiation above 15 Gy with a peak of apoptosis around 6 hours (28, 274). They suggested acute apoptosis of tumour endothelial cells, mediated by ceramide and initiated by acid sphingomyelinase (28, 274, 391). Although we have not investigated the early tumour endothelial cells response to irradiation, we found no significant change in the relative gene expression of aSMase pathways after irradiation. They further suggested that the tumour endothelial cells significantly contribute to the general tumour response to radiotherapy. This was contested by several researchers in the field (406), and consequently led to additional investigation of the contribution of tumour and stromal cells to radiation response.

Further research confirmed the notion that there was little contribution of stromal cells to tumour cell response to radiation damage (277, 278, 407, 408). Firstly, our data shows that the larger part of the vasculature remains functional after irradiation, and secondly, that the apoptosis that we have observed particularly happens in smaller tumour vessels and sprouts while larger vessels remain unaffected. Further, the amount of apoptosis was higher in tumour endothelial cells originating in MC38 than in the B16F10 tumour model. Several reasons might explain this. In the previous chapter we showed tumour hypoxia is more prevalent in B16F10 tumours and it has been reported that HIF1alpha can protect cells from radiation-induced

apoptosis (361). Secondly, B16F10 tumour vessels display greater coverage with mural cells indicating a more mature state. In addition, we have seen lower level of angiogenesis and less proliferation of tumour endothelial cells in the B16F10 model. Mature vessels display greater resistance to radiation damage (375). In control B16F10 tumour, a larger fraction of tumour vessels were perfused, leading to shear stress, which has been proposed as an anti-apoptotic factor. All these factors can potentially add to the phenomenon we have observed of little change in the vessel architecture and lower levels of apoptosis in the tumour endothelium in B16F10 tumours. MC38 tumours instead have a larger number of sprouts and we have observed a higher fraction of proliferating tumour endothelial cells. Less vessel coverage was observed, and smaller vessels experience less shear stress as an anti-apoptotic mediator. Taken together, this could explain why we have seen more apoptosis in the tumour endothelial cells of MC38 tumours than in the B16F10 tumours.

With fractionated irradiation of 5 × 3 Gy, we observed a peak of apoptosis around the time of the last fraction. Immunofluorescence indicated prolonged apoptosis after the last fraction. Interestingly our MRI data (see previous chapter) indicates that there is a decrease in perfusion in this treatment setting as well, which could be explained by our observation of increased apoptosis after fractionated irradiation.

5.4.3 Total RNA sequencing after 15 Gy irradiation in MC38 tumour endothelial cells

RNA sequencing of tumour endothelial cells 48 hours after 15 Gy irradiation revealed differential expression of several hundreds of genes. With pathway analysis, we categorised these differentially expressed genes and detected several subgroups. This revealed several cellular processes dominating at this time point after irradiation. This finding confirmed our

observation by flow cytometry and immunofluorescence on the downregulation of proliferation and the upregulation of apoptosis on a gene level. While we have seen apoptosis occurring after 48 hours, clearly, not all tumour endothelial cells undergo apoptosis. The detected expression of genes that has been shown to have an anti-apoptotic role reinforces this. In addition, several pathways related to inflammation and immune cell attraction and interaction with endothelial cells were found to be upregulated after irradiation, indicating an active contribution of the tumour endothelium to the immune response after irradiation. Indeed, others have shown that in response to irradiation a first activation of the immune system occurs soon after irradiation leading to immune cell influx, most probably through the tumour vasculature as the route of entrance (409).

It must be noted, however, here we have only covered a single time point after irradiation allowing us only to comment on an early tumour endothelial cell response. We have observed in the previous chapter that the remaining tumour vessels maintain their shape and function. On a gene level, we observed no significant change of gene expression that could have been associated to vessel structural integrity, for example, leaving us unable to draw conclusions related to the changes in endothelial signature genes. For example, we have detected all major transcription factors but due to redundancy amongst them, it is futile to speculate whether one transcription factor is important or not. In addition, different subtypes of endothelial cells increase the layers of complexity and make it even more difficult to draw conclusions. For example, endothelial cells can be divided by their position within the vasculature structure and, accordingly, they display different tasks and functions. Secondly, subsets, like tip or stalk cells, are constantly competing and phenotypes are temporal and require different genes to be expressed at one time. Thus, a single cell RNA sequencing would have to be performed to answer these open questions.

If a high dose of irradiation in the longer term can be repaired and whether tumour endothelial cells can recover to a proliferative state, or whether there is a second wave of programmed cell death, still needs to be determined. It has also been suggested that tumour endothelial cells undergo senescence, which would perhaps explain our finding that there is no recovery of proliferation and sprouting angiogenesis after a single dose of 15 Gy irradiation. Further time points would help us to better decipher long-term changes in gene expression and would help us to understand how tumour endothelial cells maintain their structure and function at later time points.

These data indicate that tumour endothelial cells not only are affected in their proliferation but also undergo apoptosis after irradiation. Moreover, our data is in agreement with others (409–411) indicating that early on tumour endothelial cells actively contribute in the radiation-induced immune response through several signalling pathways.

5.4.4 Conclusion

In this Chapter, we have shown the response of tumour endothelial cell proliferation to irradiation and how it potentially contributes to tumour vasculature development. By inhibiting proliferation, the formation of new sprouts is inhibited on a cellular level. We have further shown that apoptosis of tumour endothelial cells occurs after irradiation. Our data suggests that this happens not in an immediate fashion but between 48 and 72 hours after single high dose irradiation. Moreover, and perhaps, more importantly, we have shown that it happens predominately in smaller vessels and sprouts and blunt ends that contribute little to overall tumour perfusion. We furthermore have shown that irradiation leads to the upregulation of cell cycle regulating and DNA damage related pathways, as well as pathways involved in apoptosis, the pathways that contribute to the immune response after irradiation. Together these data

shed light on the response of tumour endothelial cells to irradiation on a cellular and molecular level and increase our understanding of how they are connected to the changes in the function of tumour vasculature after irradiation.

CHAPTER 6

Concluding Remarks

6.1 Conclusion

The aim of this thesis has been to increase our understanding of the response of tumour vasculature to different radiation schedules, and to bring together the two opposing views on how tumour vasculature responds to high doses of radiation, a topic that has been vividly discussed over the last two decades (24, 27, 406). On the one hand, it is suggested that irradiation has a modest impact and leads only to limited change of the tumour vasculature, and on the other, that major death and dysfunction of endothelial cells and of the tumour vasculature is seen to arise (28, 262, 263, 274, 392). It is argued in this thesis that both views are partially correct, if differentiated by the size of the tumour vasculature.

Novel findings provided in this thesis are derived from the method of repeated two-photon microscopy imaging on the same tumour in combination with the GEM model. This has allowed us to observe the same vessels over days and to differentiate in vivo perfused and non-perfused parts of the tumour vasculature in high resolution. Furthermore, we have been able to carry out detailed evaluation of the change of gene expression after radiation in tumour endothelial cells. Intravital imaging, in combination with a GEM model, reveals little change in established tumour blood vessels in both tumour models, and only moderate change in the morphological features of the tumour vasculature, after a singular dose of 15 Gy irradiation, with some features of the vessel morphology resembling vascular normalisation (371).

We have also shown that those parts of the tumour vasculature that do undergo changes are, in most cases, smaller vessels, blunt ends and vascular sprouts. We confirmed this with normal subcutaneous models of the same tumour cell lines by investigating proliferation and apoptosis as potential reasons leading to the changes observed in intravital imaging. Proliferation is abrogated in both MC38 and B16F10 tumour models. Apoptosis appears

predominantly in small-sized tumour vessels and is higher in the MC38 tumour model that also displays a greater proliferative capacity compared to the B16F10 model that shows less proliferative capacity. While it has been suggested that apoptosis takes place at very early time points after irradiation, our data, as well as that of others, shows a peak of apoptosis towards later time points, around two to three days after irradiation. Interestingly, this peak in apoptosis is accompanied by a temporal change in perfusion measured by DCE-MRI.

Our intravital data further suggests that the remaining vessels after tumour irradiation maintain or increase their perfusion status. In conclusion, our observations can explain the disjuncture between substantial apoptosis and its limited contribution in the response of the tumour to radiotherapy. If a majority of smaller, less important, and quite probably non-functional, vessels undergo apoptosis, but the functional medium to large vessels that display perfusion are maintained, both observations can be aligned.

Interestingly, repeated lower doses of radiation to tumours in our hands show differential effects in the intravital and in the accompanied experiments. While the morphological changes are subtler and a clear dose-dependent response is visible, accompanied proliferation measurements show the repair capability of the tumour endothelial cells. However, we have also observed prolonged apoptosis, indicating that smaller doses of radiation lead to greater apoptosis, due to the capacity of tumour endothelial cells to repair the damage received through radiation, which might be explained by the 5Rs of radiobiology (16, 18). However, further research is needed to establish this firmly.

6.2 Potential clinical relevance

Although it would be inappropriate to make a direct comparison between our observations and clinical practice, higher doses of radiation have recently seen an increased use

due to technical advances in the delivery of radiation. It is, therefore, expedient to increase our understanding of the response of the tumour vasculature to those higher doses, because of the crucial function that the tumour vasculature provides to metabolites and as a gateway for immune cells. Furthermore, it is also potentially a mediator for the release of inflammatory signals from the endothelial cells themselves, as well as from the surrounding microenvironment. This could be interesting in light of immunotherapy, which has recently seen an increased use in the clinic and in clinical trials exploring its feasibility (20–23, 412, 413). Clearly, human tissue samples would be invaluable for comparison to confirm our results, but are, regretfully, beyond the scope of this thesis.

6.3 Limitations of our research and future perspective

During this research project, we employed an experimental model of intravital imaging in combination with a GEM model. This model is particularly advantageous for investigating temporal questions at a high resolution, allowing for spatially precise measurements of the tumour vasculature, regardless of perfusion status or vessel size. The VEOM mouse model enabled us to fluorescently label specifically endothelial cells. However, the induction efficiency of tdTomato was below our expectations. While there are other endothelial cell-specific mouse lines available, where *cre* is under the expression of a different promoter (see chapter 3), they are often not endothelial cell specific and other types of cells would express reporter protein making them impractical for this type of study. Further research of endothelial cell specific promoters could overcome this issue. Although this might prove difficult due to endothelial cell phenotypic variation.

There are other limitations of this research study from an imaging perspective. While spatial resolution is high in this model by using two-photon microscopy approach, its

penetration depth is limited compared to, say, an MRI approach. This physical limitation, in combination with fluorescent reporter mice, is currently not possible to overcome. Further technical advances could potentially solve this issue. Recently Medea has used optical coherence tomography approach, combined with a dorsal skinfold chamber (214, 348), which allows recording of perfused blood vessels to a greater depth of up to 1 mm (303). While this comes with increased depth compared to two-photon microscopy and a higher resolution compared to DCE-MRI, its application is limited as it relies on well-perfused vessels.

An additional issue is that the average depth of 300 to 400 micrometre in our model does not allow us to draw firm conclusions about changes within the tumour core, as this compartment of the tumour might respond differently to radiotherapy compared to the rim of the tumour (414). Two-photon imaging has achieved imaging depth of up to 1 mm in the brain (329). Tumours, however, display a different tissue composition, thus, we have not been able to image to this depth.

Window chamber experiments resemble subcutaneous approaches as the injection site is similar. However, subcutaneous injections sites generally do not resemble orthotopic environments and parameters of the tumour vasculature might be substantially different in orthotopic models. Initiation of angiogenesis in the window model can only occur from the muscle layer beneath. While this is definitively different to the normal subcutaneous model, where angiogenesis and vessel growth can approach the tumour from every side, little is known of orthotopic tumour angiogenesis, which probably depends on the site of tumour development.

Intravital imaging also reveals the distinct differences of the morphological appearance between tumour types. This was also seen in the measured parameters. Although the growing vasculature arises from the same bed, there seems to be either some factors coming from the tumour cells themselves or from the composition of the microenvironment that influence vessel

morphology. It is interesting to speculate, as has been suggested, that tumours from certain types of tissue similarly influence the morphological appearance of their vasculature (415). These differences of tumour grafting might also have an impact on the level of perfusion and response to radiotherapy. Unfortunately, longitudinal intravital imaging of orthotopic tumours for most organs are not a feasible experimental approach with existing techniques. Nonetheless, recently some first attempts in terminal procedures, such a lung or liver intravital imaging, have been performed (416). An exception would be the use of a mammary imaging window, which would only permit the study of very small tumours, or the use of a cranial window approach (417).

Other important factors that can influence the effect of radiation on tumour endothelial cells are the number of growth factors expressed by the tumour and other stromal cells, and their release from the tumour microenvironment. This can not only lead to differences in the morphology of blood vessels but can also affect the response after irradiation. This is because it has already been shown that the growth factor expression protects normal and tumour endothelial cells from radiation damage (252–254). It would be interesting to measure the growth factor expression of the tumour cell lines that we have used and to see if there are significant differences that might partially explain the different responses we have observed.

Additionally, to obtain insights into tumour endothelial cells, we deployed normal subcutaneous tumours to study proliferation and apoptosis. Sampling over the first days after irradiation enabled us to study the proliferative response. It would have also been interesting to investigate whether tumour endothelial cells regain their proliferative capacity, as we followed the fractionated irradiation setting, and soon after the end of the radiation treatment, observed the recovery of proliferation. In the single dose setting, however, intravital imaging did not indicate a recovery of proliferation and angiogenesis and thus, we decided not to pursue this question further. If angiogenesis does take place at much later stages such as late tumour

recurrence, we would not have been able to establish this, as we did not have any intravital data on this question.

REFERENCES

1. Hanahan, D. and Weinberg, R. A. (2000) The hallmarks of cancer. *Cell* **100**, 57–70

2. Hanahan, D. and Weinberg, R. A. (2011) Hallmarks of cancer: the next generation. *Cell* **144**, 646–674

3. Baskar, R., Lee, K. A., Yeo, R., and Yeoh, K.-W. W. (2012) Cancer and radiation therapy: Current advances and future directions. *Int. J. Med. Sci.* **9**, 193–199

4. Emami, B., Lyman, J., Brown, A., Cola, L., Goitein, M., Munzenrider, J. E., Shank, B., Solin, L. J., and Wesson, M. (1991) Tolerance of normal tissue to therapeutic irradiation. *Int. J. Radiat. Oncol.* **21**, 109–122

5. Brown, J. M., Carlson, D. J., and Brenner, D. J. (2014) The tumor radiobiology of SRS and SBRT: Are more than the 5 Rs involved? *Int. J. Radiat. Oncol. Biol. Phys.* **88**, 254–262

6. Herskind, C., Ma, L., Liu, Q., Zhang, B., Schneider, F., Veldwijk, M. R., and Wenz, F. (2017) Biology of high single doses of IORT: RBE, 5 R's, and other biological aspects. *Radiat. Oncol.* **12**, 24

7. Ogawa, Y., Shibamoto, Y., Hashizume, C., Kondo, T., Iwata, H., Tomita, N., and Ogino, H. (2018) Repeat stereotactic body radiotherapy (SBRT) for local recurrence of non-small cell lung cancer and lung metastasis after first SBRT. *Radiat. Oncol.* **13**, 136

8. Tubin, S., Popper, H. H., and Brcic, L. (2019) Novel stereotactic body radiation therapy (SBRT)-based partial tumor irradiation targeting hypoxic segment of bulky tumors (SBRT-PATHY): improvement of the radiotherapy outcome by exploiting the bystander and abscopal effects. *Radiat. Oncol.* **14**, 21

9. Yeung, R., Hamm, J., Liu, M., and Schellenberg, D. (2017) Institutional analysis of stereotactic body radiotherapy (SBRT) for oligometastatic lymph node metastases. *Radiat. Oncol.* **12**, 105

10. Moore, A., Cohen-Naftaly, M., Tobar, A., Kundel, Y., Benjaminov, O., Braun, M., Issachar, A., Mor, E., Sarfaty, M., Bragilovski, D., Hur, R. Ben, Gordon, N., Stemmer, S. M., and Allen, A. M. (2017) Stereotactic body radiation therapy (SBRT) for definitive treatment and as a bridge to liver transplantation in early stage inoperable Hepatocellular carcinoma. *Radiat. Oncol.* **12**, 163

11. Park, Y., Park, H. J., Jang, W. Il, Jeong, B. K., Kim, H.-J., and Chang, A. R. (2018) Long-term results and PSA kinetics after robotic SBRT for prostate cancer: multicenter retrospective study in Korea (Korean radiation oncology group study 15–01). *Radiat. Oncol.* **13**, 230

12. Bucci, M. K., Bevan, A., and Roach, M. (2005) Advances in Radiation Therapy: Conventional to 3D, to IMRT, to 4D, and Beyond. *CA. Cancer J. Clin.* **55**, 117–134

13. Verellen, D., Ridder, M. De, Linthout, N., Tournel, K., Soete, G., and Storme, G. (2007) Innovations in image-guided radiotherapy. *Nat. Rev. Cancer* **7**, 949–960

14. Bhide, S. and Nutting, C. (2010) Recent advances in radiotherapy. *BMC Med.* **8**, 25

15. Miller, K. D., Nogueira, L., Mariotto, A. B., Rowland, J. H., Yabroff, K. R., Alfano, C. M., Jemal, A., Kramer, J. L., and Siegel, R. L. (2019) Cancer treatment and survivorship statistics, 2019. *CA. Cancer J. Clin.* **69**, 363–385

16. Steel, G. G., Mcmillan, T. J., and Peacock, J. H. (1989) The 5rs of radiobiology. *Int. J. Radiat. Biol.* **56**, 1045–1048

17. Withers, H. R. (1975) Four R's of radiotherapy. *Adv. Radiat. Biol.* **5** pp. **241–2**

18. Good, J. S. and Harrington, K. J. (2013) The hallmarks of cancer and the radiation oncologist: updating the 5Rs of radiobiology. *Clin Oncol (R Coll Radiol)* **25**, 569–577

19. Junttila, M. R. and de Sauvage, F. J. (2013) Influence of tumour micro-environment heterogeneity on therapeutic response. *Nature* **501**, 346–354

20. Sharabi, A. B., Nirschl, C. J., Kochel, C. M., Nirschl, T. R., Francica, B. J., Velarde, E., Deweese, T. L., and Drake, C. G. (2015) Stereotactic Radiation Therapy Augments Antigen-Specific PD-1-Mediated Antitumor Immune Responses via Cross-Presentation of Tumor Antigen. *Cancer Immunol. Res.* **3**, 345–355

21. Luke, J. J., Lemons, J. M., Karrison, T. G., Pitroda, S. P., Melotek, J. M., Zha, Y., Al-Hallaq, H. A., Arina, A., Khodarev, N. N., Janisch, L., Chang, P., Patel, J. D., Fleming, G. F., Moroney, J., Sharma, M. R., White, J. R., Ratain, M. J., Gajewski, T. F., Weichselbaum, R. R., and Chmura, S. J. (2018) Safety and clinical activity of pembrolizumab and multisite stereotactic body radiotherapy in patients with advanced solid tumors. *J. Clin. Oncol.* **36**, 1611–1618

22. Antonia, S. J., Villegas, A., Daniel, D., Vicente, D., Murakami, S., Hui, R., Kurata, T., Chiappori, A., Lee, K. H., de Wit, M., Cho, B. C., Bourhaba, M., Quantin, X., Tokito, T., Mekhail, T., Planchard, D., Kim, Y.-C., Karapetis, C. S., Hiret, S., Ostoros, G., Kubota, K., Gray, J. E., Paz-Ares, L., de Castro Carpeño, J., Faivre-Finn, C., Reck, M., Vansteenkiste, J., Spigel, D. R., Wadsworth, C., Melillo, G., Taboada, M., Dennis, P. A., Özgüroğlu, M., and PACIFIC Investigators. (2018) Overall Survival with Durvalumab after Chemoradiotherapy in Stage III NSCLC. *N. Engl. J. Med.* **379**, 2342–2350

23. Antonia, S. J., Villegas, A., Daniel, D., Vicente, D., Murakami, S., Hui, R., Yokoi, T., Chiappori, A., Lee, K. H., de Wit, M., Cho, B. C., Bourhaba, M., Quantin, X., Tokito, T., Mekhail, T., Planchard, D., Kim, Y.-C., Karapetis, C. S., Hiret, S., Ostoros, G., Kubota, K., Gray, J. E., Paz-Ares, L., de Castro Carpeño, J., Wadsworth, C., Melillo, G., Jiang, H., Huang, Y., Dennis, P. A., Özgüroğlu, M., and PACIFIC Investigators. (2017) Durvalumab after Chemoradiotherapy in Stage III Non–Small-Cell Lung Cancer. *N. Engl. J. Med.* **377**, 1919–1929

24. Kozin, S. V., Duda, D. G., Munn, L. L., and Jain, R. K. (2012) Neovascularization after irradiation: What is the source of newly formed vessels in recurring tumors? *J. Natl. Cancer Inst.* **104**, 899–905

25. Park, H. J., Griffin, R. J., Hui, S., Levitt, S. H., and Song, C. W. (2012) Radiation-Induced Vascular Damage in Tumors: Implications of Vascular Damage in Ablative Hypofractionated Radiotherapy (SBRT and SRS). *Radiat. Res.* **177**, 311–327

26. El Kaffas, A., Giles, A., and Czarnota, G. J. (2013) Dose-dependent response of tumor vasculature to radiation therapy in combination with Sunitinib depicted by three-dimensional high-frequency power Doppler ultrasound. *Angiogenesis* **16**, 443–454

27. Denekamp, J. (1993) Limited role of vasculature-mediated injury in tumor response to radiotherapy. *J. Natl. Cancer Inst.* **85**, 935–937

28. Garcia-Barros, M., Paris, F., Cordon-Cardo, C., Lyden, D., Rafii, S., Haimovitz-Friedman, A., Fuks, Z., and Kolesnick, R. (2003) Tumor Response to Radiotherapy Regulated by Endothelial Cell Apoptosis. *Science (80-.).* **300**, 1155–1159

29. Moding, E. J., Mowery, Y. M., and Kirsch, D. G. (2016) Opportunities for Radiosensitization in the SBRT Era. *Cancer J.* **22**, 267–273

30. Tucker, W. D. and Mahajan, K. (2018) Anatomy, Blood Vessels. In *StatPearls* StatPearls Publishing

31. Potente, M., Gerhardt, H., and Carmeliet, P. (2011) Basic and therapeutic aspects of angiogenesis. *Cell* **146**, 873–887

32. Ahn, G. O. and Brown, J. M. (2009) Role of endothelial progenitors and other bone marrow-derived cells in the development of the tumor vasculature. *Angiogenesis* **12**, 159–164

33. Simons, M., Alitalo, K., Annex, B. H., Augustin, H. G., Beam, C., Berk, B. C., Byzova, T., Carmeliet, P., Chilian, W., Cooke, J. P., Davis, G. E., Eichmann, A., Iruela-Arispe, M. L., Keshet, E., Sinusas, A. J., Ruhrberg, C., Woo, Y. J., and Dimmeler, S. (2015) State-of-the-art methods for evaluation of angiogenesis and tissue vascularization: A scientific statement from The American Heart Association. In *Circulation Research* vol. 116,

34. Goldmann, E. (1908) The Growth of Malignant Disease in Man and the Lower Animals, with special reference to the Vascular System. *Proc. R. Soc. Med.* **1**, 1–13

35. Ribatti, D., Vacca, A., and Dammacco, F. (1999) The role of the vascular phase in solid tumor growth: a historical review. *Neoplasia* **1**, 293–302

36. Algire, G. H. (1943) Microscopic studies of the early growth of a transplantable melanoma of the mouse, using the transparent-chamber technique. *J. Natl. Cancer Inst.* **4**, 13–20

37. Algire, G. H., Chalkley, H. W., Legallais, F. Y., and Park, H. D. (1945) Vasculae Reactions of Normal and Malignant Tissues in Vivo. I. Vascular Reactions of Mice to Wounds and to Normal and Neoplastic Transplants. *JNCI J. Natl. Cancer Inst.* **6**, 73–85

38. Folkman, J. (1971) Tumor Angiogenensis: Therapeutic Implications. *New Engl. Jounral Med.* 1182–1186

39. Folkman, J., Merler, E., Abernathy, C., and Williams, G. (1971) Isolation of a tumor factor responsible for angiogenesis. *J. Exp. Med.* **133**, 275–288

40. Brem, S., Brem, H., Folkman, J., Finkelstein, D., and Patz, A. (1976) Prolonged tumor dormancy by prevention of neovascularization in the vitreous. *Cancer Res.* **36**, 2807–2812

41. Gimbrone, M. A., Leapman, S. B., Cotran, R. S., and Folkman, J. (1972) Tumor dormancy in vivo by prevention of neovascularization. *J. Exp. Med.* **136**, 261–276

42. Bluff, J. E., Menakuru, S. R., Cross, S. S., Higham, S. E., Balasubramanian, S. P., Brown, N. J., Reed, M. W., and Staton, C. A. (2009) Angiogenesis is associated with the onset of hyperplasia in human ductal breast disease. *Br. J. Cancer* **101**, 666–672

43. Gospodarowicz, D., Moran, J. S., and Braun, D. L. (1977) Control of proliferation of bovine vascular endothelial cells. *J. Cell. Physiol.* **91**, 377–385

44. Shing, Y., Folkman, J., Sullivan, R., Butterfield, C., Murray, J., and Klagsbrun, M. (1984) Heparin affinity: purification of a tumor-derived capillary endothelial cell growth factor. *Science (80-.).* **223**, 1296–1299

45. Esch, F., Baird, A., Ling, N., Ueno, N., Hill, F., Denoroy, L., Klepper, R., Gospodarowicz, D., Böhlen, P., and Guillemin, R. (1985) Primary structure of bovine pituitary basic fibroblast growth factor (FGF) and comparison with the amino-terminal sequence of bovine brain

acidic FGF. *Proc. Natl. Acad. Sci. U. S. A.* **82**, 6507–6511

46. Dvorak, H. F. and Gresser, I. (1989) Microvascular injury in pathogenesis of interferon-induced necrosis of subcutaneous tumors in mice. *J. Natl. Cancer Inst.* **81**, 497–502

47. Hanahan, D. and Folkman, J. (1996) Patterns and emerging mechanisms of the angiogenic switch during tumorigenesis. *Cell* **86**, 353–364

48. Okamoto, R., Ueno, M., Yamada, Y., Takahashi, N., Sano, H., Suda, T., and Takakura, N. (2005) Hematopoietic cells regulate the angiogenic switch during tumorigenesis. *Blood* **105**, 2757–2763

49. Baeriswyl, V. and Christofori, G. (2009) The angiogenic switch in carcinogenesis. *Semin. Cancer Biol.* **19**, 329–337

50. Leibovich, S. J., Polverini, P. J., Shepard, H. M., Wiseman, D. M., Shively, V., and Nuseir, N. (1987) Macrophage-induced angiogenesis is mediated by tumour necrosis factor-α. *Nature* **329**, 630–632

51. Leek, R. D., Lewis, C. E., Whitehouse, R., Greenall, M., Clarke, J., Harris, A. L., Qian, H., Xue, X., Pollard, J. W., and Leek, Russell D., Lewis, Claire E., Whitehouse, R., Greenall, M., Clarke, J., and Harris, A. L. (1996) Association of Macrophage Infiltration with Angiogenesis and Prognosis in Invasive Breast Carcinoma. *Cancer Res.* **56**, 4625–4629

52. De Palma, M., Biziato, D., and Petrova, T. V. (2017) Microenvironmental regulation of tumour angiogenesis. *Nat. Rev. Cancer* **17**, 457–474

53. Kimura, Y. N., Watari, K., Fotovati, A., Hosoi, F., Yasumoto, K., Izumi, H., Kohno, K., Umezawa, K., Iguchi, H., Shirouzu, K., Takamori, S., Kuwano, M., and Ono, M. (2007) Inflammatory stimuli from macrophages and cancer cells synergistically promote tumor growth and angiogenesis. *Cancer Sci.* **98**, 2009–2018

54. Hughes, R., Qian, B.-Z., Rowan, C., Muthana, M., Keklikoglou, I., Olson, O. C., Tazzyman, S., Danson, S., Addison, C., Clemons, M., Gonzalez-Angulo, A. M., Joyce, J. A., De Palma, M., Pollard, J. W., and Lewis, C. E. (2015) Perivascular M2 Macrophages Stimulate Tumor Relapse after Chemotherapy. *Cancer Res.* **75**, 3479–3491

55. Clear, A. J., Lee, A. M., Calaminici, M., Ramsay, A. G., Morris, K. J., Hallam, S., Kelly, G., Macdougall, F., Lister, T. A., and Gribben, J. G. (2010) Increased angiogenic sprouting in poor prognosis FL is associated with elevated numbers of CD163+ macrophages within the immediate sprouting microenvironment. *Blood* **115**, 5053–5056

56. Kujawski, M., Kortylewski, M., Lee, H., Herrmann, A., Kay, H., and Yu, H. (2008) Stat3 mediates myeloid cell-dependent tumor angiogenesis in mice. *J. Clin. Invest.* **118**, 3367–3377

57. Nozawa, H., Chiu, C., and Hanahan, D. (2006) Infiltrating neutrophils mediate the initial angiogenic switch in a mouse model of multistage carcinogenesis. *Proc. Natl. Acad. Sci. U. S. A.* **103**, 12493–12498

58. Bergers, G., Brekken, R., McMahon, G., Vu, T. H., Itoh, T., Tamaki, K., Tanzawa, K., Thorpe, P., Itohara, S., Werb, Z., and Hanahan, D. (2000) Matrix metalloproteinase-9 triggers the angiogenic switch during carcinogenesis. *Nat. Cell Biol.* **2**, 737–744

59. Dorrell, M. I. and Friedlander, M. (2006) Mechanisms of endothelial cell guidance and vascular patterning in the developing mouse retina. *Prog. Retin. Eye Res.* **25**, 277–295

60. Barkefors, I., Le Jan, S., Jakobsson, L., Hejll, E., Carlson, G., Johansson, H., Jarvius, J., Park, J. W., Li Jeon, N., and Kreuger, J. (2008) Endothelial cell migration in stable gradients of vascular endothelial growth factor A and fibroblast growth factor 2: effects on chemotaxis and chemokinesis. *J. Biol. Chem.* **283**, 13905–13912

61. Hamerlik, P., Lathia, J. D., Rasmussen, R., Wu, Q., Bartkova, J., Lee, M. H., Moudry, P., Bartek, J., Fischer, W., Lukas, J., Rich, J. N., and Bartek, J. (2012) Autocrine VEGF-VEGFR2-Neuropilin-1 signaling promotes glioma stem-like cell viability and tumor growth. *J. Exp. Med.* **209**, 507–520

62. Grünewald, F. S., Prota, A. E., Giese, A., and Ballmer-Hofer, K. (2010) Structure-function analysis of VEGF receptor activation and the role of coreceptors in angiogenic signaling. *Biochim. Biophys. Acta - Proteins Proteomics* **1804**, 567–580

63. Simons, M., Gordon, E., and Claesson-Welsh, L. (2016) Mechanisms and regulation of endothelial VEGF receptor signalling. *Nat. Rev. Mol. Cell Biol.* **17**, 611–625

64. Gerhardt, H., Golding, M., Fruttiger, M., Ruhrberg, C., Lundkvist, A., Abramsson, A., Jeltsch, M., Mitchell, C., Alitalo, K., Shima, D., and Betsholtz, C. (2003) VEGF guides angiogenic sprouting utilizing endothelial tip cell filopodia. *J. Cell Biol.* **161**, 1163–1177

65. Yana, I., Sagara, H., Takaki, S., Takatsu, K., Nakamura, K., Nakao, K., Katsuki, M., Taniguchi, S., Aoki, T., Sato, H., Weiss, S. J., and Seiki, M. (2007) Crosstalk between neovessels and mural cells directs the site-specific expression of MT1-MMP to endothelial tip cells. *J. Cell Sci.* **120**, 1607–1614

66. van Hinsbergh, V. W. M. and Koolwijk, P. (2008) Endothelial sprouting and angiogenesis: matrix metalloproteinases in the lead. *Cardiovasc. Res.* **78**, 203–212

67. Del Toro, R., Prahst, C., Mathivet, T., Siegfried, G., Kaminker, J. S., Larrivee, B., Breant, C., Duarte, A., Takakura, N., Fukamizu, A., Penninger, J., and Eichmann, A. (2010) Identification and functional analysis of endothelial tip cell-enriched genes. *Blood* **116**, 4025–4033

68. Sorensen, I., Adams, R. H., and Gossler, A. (2009) DLL1-mediated Notch activation regulates endothelial identity in mouse fetal arteries. *Blood* **113**, 5680–5688

69. Saravanakumar, M. and Devaraj, H. (2013) Notch signalling in cardiovasculogenesis: Insight into their role in early cardiovascular development. *Mol. Biol. Rep.* **40**, 3537–3547

70. Andrawes, M. B., Xu, X., Liu, H., Ficarro, S. B., Marto, J. A., Aster, J. C., and Blacklow, S. C. (2013) Intrinsic selectivity of Notch 1 for Delta-like 4 over Delta-like 1. *J. Biol. Chem.* **288**, 25477–25489

71. Suchting, S., Freitas, C., le Noble, F., Benedito, R., Bréant, C., Duarte, A., and Eichmann, A. (2007) The Notch ligand Delta-like 4 negatively regulates endothelial tip cell formation and vessel branching. *Proc. Natl. Acad. Sci. U. S. A.* **104**, 3225–3230

72. Hellström, M., Phng, L.-K., Hofmann, J. J., Wallgard, E., Coultas, L., Lindblom, P., Alva, J., Nilsson, A.-K., Karlsson, L., Gaiano, N., Yoon, K., Rossant, J., Iruela-Arispe, M. L., Kalén, M., Gerhardt, H., and Betsholtz, C. (2007) Dll4 signalling through Notch1 regulates formation of tip cells during angiogenesis. *Nature* **445**, 776–780

73. Ferrara, N., Gerber, H. P., and LeCouter, J. (2003) The biology of VEGF and its receptors. *Nat. Med.* **9**, 669–676

74. Park, J. E., Chen, H. H., Winer, J., Houck, K. A., and Ferrara, N. (1994) Placenta growth

factor. Potentiation of vascular endothelial growth factor bioactivity, in vitro and in vivo, and high affinity binding to Flt-1 but not to Flk-1/KDR. *J. Biol. Chem.* **269**, 25646–25654

75. Gerhardt, H. and Blanco, R. (2013) VEGF and Notch in Tip and Stalk Cell Selection. *Cold Spring Harb. Perspect. Med.* **3**, 1–19

76. Gebala, V., Collins, R., Geudens, I., Phng, L.-K., and Gerhardt, H. (2016) Blood flow drives lumen formation by inverse membrane blebbing during angiogenesis in vivo. *Nat. Cell Biol.* **18**, 443–450

77. Iruela-Arispe, M. L. and Davis, G. E. (2009) Cellular and Molecular Mechanisms of Vascular Lumen Formation. *Dev. Cell* **16**, 222–231

78. Fantin, A., Vieira, J. M., Gestri, G., Denti, L., Schwarz, Q., Prykhozhij, S., Peri, F., Wilson, S. W., and Ruhrberg, C. (2010) Tissue macrophages act as cellular chaperones for vascular anastomosis downstream of VEGF-mediated endothelial tip cell induction. *Blood* **116**, 829–840

79. Simonavicius, N., Ashenden, M., Van Weverwijk, A., Lax, S., Huso, D. L., Buckley, C. D., Huijber, I. J., Yarwood, H., and Isacke, C. M. (2012) Pericytes promote selective vessel regression to regulate vascular patterning. *Blood* **120**, 1516–1527

80. Song, J. W. and Munn, L. L. (2011) Fluid forces control endothelial sprouting. *Proc. Natl. Acad. Sci. U. S. A.* **108**, 15342–15347

81. Franco, C. A., Jones, M., Bernabeu, M. O., Vion, A., Fan, J., Mathivet, T., Ragab, A., Yamaguchi, T. P., Peter, V., Lang, R. A., and Gerhardt, H. (2016) Non-canonical Wnt signalling modulates the endothelial shear stress flow sensor in vascular remodelling. *Elife* 1–22

82. Geudens, I. and Gerhardt, H. (2011) Coordinating cell behaviour during blood vessel formation. *Development* **138**, 4569–4583

83. Pepper, M. S. (1997) Transforming growth factor-beta: Vasculogenesis, angiogenesis, and vessel wall integrity. *Cytokine Growth Factor Rev.* **8**, 21–43

84. Yu, Q. and Stamenkovic, I. (2000) Cell surface-localized matrix metalloproteinase-9 proteolytically activates TGF-beta and promotes tumor invasion and angiogenesis. *Genes Dev.* **14**, 163–176

85. Thomas, M. and Augustin, H. G. (2009) The role of the Angiopoietins in vascular morphogenesis. *Angiogenesis* **12**, 125–137

86. Pate, K. T., Stringari, C., Sprowl-Tanio, S., Wang, K., TeSlaa, T., Hoverter, N. P., McQuade, M. M., Garner, C., Digman, M. A., Teitell, M. A., Edwards, R. A., Gratton, E., and Waterman, M. L. (2014) Wnt signaling directs a metabolic program of glycolysis and angiogenesis in colon cancer. *EMBO J.* **33**, 1454–1473

87. Gelfand, M. V, Hagan, N., Tata, A., Oh, W.-J., Lacoste, B., Kang, K.-T., Kopycinska, J., Bischoff, J., Wang, J.-H., and Gu, C. (2014) Neuropilin-1 functions as a VEGFR2 co-receptor to guide developmental angiogenesis independent of ligand binding. *Elife* **3**

88. Konerding, M. A., Fait, E., and Gaumann, A. (2001) 3D microvascular architecture of pre-cancerous lesions and invasive carcinomas of the colon. *Br. J. Cancer* **84**, 1354–1362

89. Konerding, M. A., Malkusch, W., Klapthor, B., Van Ackern, C., Fait, E., Hill, S. A., Parklns, C., Chaplin, D. J., Presta, M., and Denekamp, J. (1999) Evidence for characteristic vascular

patterns in solid tumours: Quantitative studies using corrosion casts. *Br. J. Cancer* **80**, 724–732

90. Hashizume, H., Baluk, P., Morikawa, S., McLean, J. W., Thurston, G., Roberge, S., Jain, R. K., and McDonald, D. M. (2000) Openings between defective endothelial cells explain tumor vessel leakiness. *Am. J. Pathol.* **156**, 1363–1380

91. Baluk, P., Hashizume, H., and McDonald, D. M. (2005) Cellular abnormalities of blood vessels as targets in cancer. *Curr. Opin. Genet. Dev.* **15**, 102–111

92. Baluk, P., Morikawa, S., Haskell, A., Mancuso, M., and McDonald, D. M. (2003) Abnormalities of basement membrane on blood vessels and endothelial sprouts in tumors. *Am. J. Pathol.* **163**, 1801–1815

93. Baluk, P., Morikawa, S., Kaidoh, T., Haskell, A., Jain, R. K., and Mcdonald, D. M. (2002) Abnormalities in Pericytes on Blood Vessels and Endothelial Sprouts in Tumors. *Am. J. Pathol.* **160**, 985–1000

94. Inai, T., Mancuso, M., Hashizume, H., Baffert, F., Haskell, A., Baluk, P., Hu-Lowe, D. D., Shalinsky, D. R., Thurston, G., Yancopoulos, G. D., and McDonald, D. M. (2004) Inhibition of Vascular Endothelial Growth Factor (VEGF) Signaling in Cancer Causes Loss of Endothelial Fenestrations, Regression of Tumor Vessels, and Appearance of Basement Membrane Ghosts. *Am. J. Pathol.* **165**, 35–52

95. Nagy, J. A., Chang, S. H., Dvorak, A. M., and Dvorak, H. F. (2009) Why are tumour blood vessels abnormal and why is it important to know? *Br. J. Cancer* **100**, 865–869

96. Ruhrberg, C., Gerhardt, H., Golding, M., Watson, R., Ioannidou, S., Fujisawa, H., Betsholtz, C., and Shima, D. T. (2002) Spatially restricted patterning cues provided by heparin-binding VEGF-A control blood vessel branching morphogenesis. *Genes Dev.* **16**, 2684–2698

97. Tozer, G. M., Akerman, S., Cross, N. A., Barber, P. R., Bjorndahl, M. A., Greco, O., Harris, S., Hill, S. A., Honess, D. J., Ireson, C. R., Pettyjohn, K. L., Prise, V. E., Reyes-Aldasoro, C. C., Ruhrberg, C., Shima, D. T., and Kanthou, C. (2008) Blood Vessel Maturation and Response to Vascular-Disrupting Therapy in Single Vascular Endothelial Growth Factor-A Isoform-Producing Tumors. *Cancer Res.* **68**, 2301–2311

98. Helfrich, I. and Schadendorf, D. (2011) Blood vessel maturation, vascular phenotype and angiogenic potential in malignant melanoma: One step forward for overcoming anti-angiogenic drug resistance? *Mol. Oncol.* **5**, 137–149

99. Helfrich, I., Scheffrahn, I., Bartling, S., Weis, J., von Felbert, V., Middleton, M., Kato, M., Ergün, S., Schadendorf, D., Augustin, H. G., and Schadendorf, D. (2010) Resistance to antiangiogenic therapy is directed by vascular phenotype, vessel stabilization, and maturation in malignant melanoma. *J. Exp. Med.* **207**, 491–503

100. Dudley, A. C. (2012) Tumor Endothelial Cells. *Cold Spring Harb. Perspect. Med.* 1–18

101. Denekamp, J. (1984) Vascular endothelium as the vulnerable element in tumours. *Acta Radiol. Oncol.* **23**, 217–225

102. Denekamp, J. and Hobson, B. (1982) Endothelial-cell proliferation in experimental tumours. *Br. J. Cancer* **46**, 711–720

103. Hirst, D. G., Denekamp, J., and Hobson, B. (1980) Proliferation studies of the endothelial and smooth muscle cells of the mouse mesentery after irradiation. *Cell Tissue Kinet.* **13**,

91–104

104. Fukumura, D., Yuan, F., Monsky, W. L., Chen, Y., and Jain, R. K. (1997) Effect of host microenvironment on the microcirculation of human colon adenocarcinoma. *Am. J. Pathol.* **151**, 679–688

105. Monsky, W. L., Mouta Carreira, C., Tsuzuki, Y., Gohongi, T., Fukumura, D., and Jain, R. K. (2002) Role of host microenvironment in angiogenesis and microvascular functions in human breast cancer xenografts: mammary fat pad versus cranial tumors. *Clin. Cancer Res.* **8**, 1008–1013

106. Morrissey, C., True, L. D., Roudier, M. P., Coleman, I. M., Hawley, S., Nelson, P. S., Coleman, R., Wang, Y.-C., Corey, E., Lange, P. H., Higano, C. S., and Vessella, R. L. (2008) Differential expression of angiogenesis associated genes in prostate cancer bone, liver and lymph node metastases. *Clin. Exp. Metastasis* **25**, 377–388

107. Jubb, A. M., Cesario, A., Ferguson, M., Congedo, M. T., Gatter, K. C., Lococo, F., Mulè, A., and Pezzella, F. (2011) Vascular phenotypes in primary non-small cell lung carcinomas and matched brain metastases. *Br. J. Cancer* **104**, 1877–1881

108. Hellström, M., Gerhardt, H., Kalén, M., Li, X., Eriksson, U., Wolburg, H., and Betsholtz, C. (2001) Lack of pericytes leads to endothelial hyperplasia and abnormal vascular morphogenesis. *J. Cell Biol.* **153**, 543–553

109. Cho, H., Kozasa, T., Bondjers, C., Betsholtz, C., and Kehrl, J. H. (2003) Pericyte-specific expression of Rgs5: implications for PDGF and EDG receptor signaling during vascular maturation. *FASEB J.* **17**, 440–442

110. Uemura, A., Ogawa, M., Hirashima, M., Fujiwara, T., Koyama, S., Takagi, H., Honda, Y., Wiegand, S. J., Yancopoulos, G. D., and Nishikawa, S.-I. (2002) Recombinant angiopoietin-1 restores higher-order architecture of growing blood vessels in mice in the absence of mural cells. *J. Clin. Invest.* **110**, 1619–1628

111. Armulik, A., Genove, G., and Betsholtz, C. (2011) Pericytes: Developmental, Physiological, and Pathological Perspectives, Problems, and Promises. *Dev. Cell* **21**, 193–215

112. Abramsson, A., Berlin, O., Papayan, H., Paulin, D., Shani, M., Betsholtz, C., Berlin, Ö., Papayan, H., Paulin, D., Shani, M., and Betsholtz, C. (2002) Analysis of mural cell recruitment to tumor vessels. *Circulation* **105**, 112–117

113. Gerhardt, H. and Betsholtz, C. (2003) Endothelial-pericyte interactions in angiogenesis. *Cell Tissue Res.* **314**, 15–23

114. Anderberg, C., Li, H., Fredriksson, L., Andrae, J., Betsholtz, C., Li, X., Eriksson, U., and Pietras, K. (2009) Paracrine Signaling by Platelet-Derived Growth Factor-CC Promotes Tumor Growth by Recruitment of Cancer-Associated Fibroblasts. *Cancer Res.* **69**, 369–378

115. Furuhashi, M., Sjöblom, T., Abramsson, A., Ellingsen, J., Micke, P., Li, H., Bergsten-Folestad, E., Eriksson, U., Heuchel, R., Betsholtz, C., Heldin, C.-H., and Ostman, A. (2004) Platelet-derived growth factor production by B16 melanoma cells leads to increased pericyte abundance in tumors and an associated increase in tumor growth rate. *Cancer Res.* **64**, 2725–2733

116. Abramsson, A., Lindblom, P., and Betsholtz, C. (2003) Endothelial and nonendothelial sources of PDGF-B regulate pericyte recruitment and influence vascular pattern

formation in tumors. *J. Clin. Invest.* **112**, 1142–1151

117. Greenberg, J. I., Shields, D. J., Barillas, S. G., Acevedo, L. M., Murphy, E., Huang, J., Scheppke, L., Stockmann, C., Johnson, R. S., Angle, N., and Cheresh, D. A. (2008) A role for VEGF as a negative regulator of pericyte function and vessel maturation. *Nature* **456**, 809–813

118. De Palma, M., Venneri, M. A., Roca, C., and Naldini, L. (2003) Targeting exogenous genes to tumor angiogenesis by transplantation of genetically modified hematopoietic stem cells. *Nat. Med.* **9**, 789–795

119. De Palma, M., Venneri, M. A., Galli, R., Sergi, L. S., Politi, L. S., Sampaolesi, M., and Naldini, L. (2005) Tie2 identifies a hematopoietic lineage of proangiogenic monocytes required for tumor vessel formation and a mesenchymal population of pericyte progenitors. *Cancer Cell* **8**, 211–226

120. Lewis, J. S., Landers, R. J., Underwood, J. C., Harris, A. L., and Lewis, C. E. (2000) Expression of vascular endothelial growth factor by macrophages is up-regulated in poorly vascularized areas of breast carcinomas. *J. Pathol.* **192**, 150–158

121. Stockmann, C., Doedens, A., Weidemann, A., Zhang, N., Takeda, N., Greenberg, J. I., Cheresh, D. A., and Johnson, R. S. (2008) Deletion of vascular endothelial growth factor in myeloid cells accelerates tumorigenesis. *Nature* **456**, 814–818

122. Priceman, S. J., Sung, J. L., Shaposhnik, Z., Burton, J. B., Torres-Collado, A. X., Moughon, D. L., Johnson, M., Lusis, A. J., Cohen, D. A., Iruela-Arispe, M. L., and Wu, L. (2010) Targeting distinct tumor-infiltrating myeloid cells by inhibiting CSF-1 receptor: Combating tumor evasion of antiangiogenic therapy. *Blood* **115**, 1461–1471

123. Ahn, G.-O. O. and Brown, J. M. (2008) Matrix Metalloproteinase-9 Is Required for Tumor Vasculogenesis but Not for Angiogenesis: Role of Bone Marrow-Derived Myelomonocytic Cells. *Cancer Cell* **13**, 193–205

124. Kozin, S. V., Kamoun, W. S., Huang, Y., Dawson, M. R., Jain, R. K., and Duda, D. G. (2010) Recruitment of Myeloid but not Endothelial Precursor Cells Facilitates Tumor Regrowth after Local Irradiation. *Cancer Res.* **70**, 5679–5685

125. Kioi, M., Vogel, H., Schultz, G., Hoffman, R. M., Harsh, G. R., and Brown, J. M. (2010) Inhibition of vasculogenesis, but not angiogenesis, prevents the recurrence of glioblastoma after irradiation in mice. *J. Clin. Invest.* **120**, 694–705

126. Brown, J. M. (2014) Vasculogenesis: A crucial player in the resistance of solid tumours to radiotherapy. *Br. J. Radiol.* **87**, 20130686

127. Moeller, B. J. and Dewhirst, M. W. (2006) HIF-1 and tumour radiosensitivity. *Br. J. Cancer* **95**, 1–5

128. Unruh, A., Ressel, A., Mohamed, H. G., Johnson, R. S., Nadrowitz, R., Richter, E., Katschinski, D. M., and Wenger, R. H. (2003) The hypoxia-inducible factor-1α is a negative factor for tumor therapy. *Oncogene* **22**, 3213–3220

129. Zhang, M., Qiu, Q., Li, Z., Sachdeva, M., Min, H., Cardona, D. M., DeLaney, T. F., Han, T., Ma, Y., Luo, L., Ilkayeva, O. R., Lui, K., Nichols, A. G., Newgard, C. B., Kastan, M. B., Rathmell, J. C., Dewhirst, M. W., and Kirsch, D. G. (2015) HIF-1 Alpha Regulates the Response of Primary Sarcomas to Radiation Therapy through a Cell Autonomous Mechanism. *Radiat. Res.* **183**, 594

130. Brown, J. M. and Giaccia, A. J. (1998) The unique physiology of solid tumors: Opportunities (and problems) for cancer therapy. *Cancer Res.* **58**, 1408–1416

131. Heldin, C.-H., Rubin, K., Pietras, K., and Östman, A. (2004) High interstitial fluid pressure — an obstacle in cancer therapy. *Nat. Rev. Cancer* **4**, 806–813

132. Suzuki, A., Andrew, D. P., Gonzalo, J. A., Fukumoto, M., Spellberg, J., Hashiyama, M., Takimoto, H., Gerwin, N., Webb, I., Molineux, G., Amakawa, R., Tada, Y., Wakeham, A., Brown, J., McNiece, I., Ley, K., Butcher, E. C., Suda, T., Gutierrez-Ramos, J. C., and Mak, T. W. (1996) CD34-deficient mice have reduced eosinophil accumulation after allergen exposure and show a novel crossreactive 90-kD protein. *Blood* **87**, 3550–3562

133. Heissig, B., Hattori, K., Dias, S., Friedrich, M., Ferris, B., Hackett, N. R., Crystal, R. G., Besmer, P., Lyden, D., Moore, M. A. S., Werb, Z., and Rafii, S. (2002) Recruitment of stem and progenitor cells from the bone marrow niche requires MMP-9 mediated release of kit-ligand. *Cell* **109**, 625–637

134. Nolan, D. J., Ciarrocchi, A., Mellick, A. S., Jaggi, J. S., Bambino, K., Gupta, S., Heikamp, E., Mcdevitt, M. R., Scheinberg, D. A., Benezra, R., and Mittal, V. (2007) Bone marrow-derived endothelial progenitor cells are a major determinant of nascent tumor neovascularization. *Genes Dev.* **21**, 1546–1558

135. Lyden, D., Hattori, K., Dias, S., Costa, C., Blaikie, P., Butros, L., Chadburn, A., Heissig, B., Marks, W., Witte, L., Wu, Y., Hicklin, D., Zhu, Z., Hackett, N. R., Crystal, R. G., Moore, M. A. S., Hajjar, K. A., Manova, K., Benezra, R., and Rafii, S. (2001) Impaired recruitment of bone-marrow-derived endothelial and hematopoietic precursor cells blocks tumor angiogenesis and growth. *Nat. Med.* **7**, 1194–1201

136. Asahara, T., Masuda, H., Takahashi, T., Kalka, C., Pastore, C., Silver, M., Kearne, M., Magner, M., and Isner, J. M. (1999) Bone Marrow Origin of Endothelial Progenitor Cells Responsible for Postnatal Vasculogenesis in Physiological and Pathological Neovascularization. *Circ. Res.* **85**, 221–228

137. Asahara, T., Takahashi, T., Masuda, H., Kalka, C., Chen, D., Iwaguro, H., Inai, Y., Silver, M., and Isner, J. M. (1999) VEGF contributes to postnatal neovascularization by mobilizing bone marrow-derived endothelial progenitor cells. *EMBO J.* **18**, 3964–3972

138. Ahn, G.-O., Tseng, D., Liao, C.-H., Dorie, M. J., Czechowicz, A., and Brown, J. M. (2010) Inhibition of Mac-1 (CD11b/CD18) enhances tumor response to radiation by reducing myeloid cell recruitment. *Proc. Natl. Acad. Sci.* **107**, 8363–8368

139. Voswinckel, R., Ziegelhoeffer, T., Heil, M., Kostin, S., Breier, G., Mehling, T., Haberberger, R., Clauss, M., Gaumann, A., Schaper, W., and Seeger, W. (2003) Circulating Vascular Progenitor Cells Do Not Contribute to Compensatory Lung Growth. *Circ. Res.* **93**, 372–379

140. Ziegelhoeffer, T., Fernandez, B., Kostin, S., Heil, M., Voswinckel, R., Helisch, A., and Schaper, W. (2004) Bone Marrow-Derived Cells Do Not Incorporate Into the Adult Growing Vasculature. *Circ. Res.* **94**, 230–238

141. He, Y., Rajantie, I., Ilmonen, M., Makinen, T., Karkkainen, M. J., Haiko, P., Salven, P., and Alitalo, K. (2004) Preexisting lymphatic endothelium but not endothelial progenitor cells are essential for tumor lymphangiogenesis and lymphatic metastasis. *Cancer Res.* **64**, 3737–3740

142. Gothert, J. R., Gustin, S. E., van Eekelen, J. A. M., Schmidt, U., Hall, M. A., Jane, S. M.,

Green, A. R., Göttgens, B., Izon, D. J., and Begley, C. G. (2004) Genetically tagging endothelial cells in vivo: bone marrow-derived cells do not contribute to tumor endothelium. *Blood* **104**, 1769–1777

143. Holash, J., Maisonpierre, P. C., Compton, D., Boland, P., Alexander, C. R., Zagzag, D., Yancopoulos, G. D., and Wiegand, S. J. (1999) Vessel Cooption, Regression, and Growth in Tumors Mediated by Angiopoietins and VEGF. *Science (80-.).* **284**, 1994–1998

144. Griveau, A., Seano, G., Shelton, S. J., Kupp, R., Jahangiri, A., Obernier, K., Krishnan, S., Lindberg, O. R., Yuen, T. J., Tien, A. C., Sabo, J. K., Wang, N., Chen, I., Kloepper, J., Larrouquere, L., Ghosh, M., Tirosh, I., Huillard, E., Alvarez-Buylla, A., Oldham, M. C., Persson, A. I., Weiss, W. A., Batchelor, T. T., Stemmer-Rachamimov, A., Suvà, M. L., Phillips, J. J., Aghi, M. K., Mehta, S., Jain, R. K., and Rowitch, D. H. (2018) A Glial Signature and Wnt7 Signaling Regulate Glioma-Vascular Interactions and Tumor Microenvironment. *Cancer Cell* **33**, 874-889.e7

145. Küsters, B., Leenders, W. P. J., Wesseling, P., Smits, D., Verrijp, K., Ruiter, D. J., Peters, J. P. W., Van der Kogel, A. J., and De Waal, R. M. W. (2002) Vascular endothelial growth factor-A165 induces progression of melanoma brain metastases without induction of sprouting angiogenesis. *Cancer Res.* **62**, 341–345

146. Naresh, K. N., Nerurkar, A. Y., and Borges, A. M. (2001) Angiogenesis is redundant for tumour growth in lymph node metastases. *Histopathology* **38**, 466–470

147. Pezzella, F., Pastorino, U., Tagliabue, E., Andreola, S., Sozzi, G., Gasparini, G., Menard, S., Gatter, K. C., Harris, A. L., Fox, S., Buyse, M., Pilotti, S., Pierotti, M., and Rilke, F. (1997) Non-small-cell lung carcinoma tumor growth without morphological evidence of neo-angiogenesis. *Am. J. Pathol.* **151**, 1417–1423

148. Donnem, T., Hu, J., Ferguson, M., Adighibe, O., Snell, C., Harris, A. L., Gatter, K. C., and Pezzella, F. (2013) Vessel co-option in primary human tumors and metastases: an obstacle to effective anti-angiogenic treatment? *Cancer Med.* **2**, 427–436

149. Pezzella, F., Di Bacco, A., Andreola, S., Nicholson, A. G., Pastorino, U., and Harris, A. L. (1996) Angiogenesis in primary lung cancer and lung secondaries. *Eur. J. Cancer* **32**, 2494–2500

150. Carbonell, W. S., Ansorge, O., Sibson, N., and Muschel, R. (2009) The Vascular Basement Membrane as "Soil" in Brain Metastasis. *PLoS One* **4**, e5857

151. Leenders, W. P. J., Küsters, B., Verrijp, K., Maass, C., Wesseling, P., Heerschap, A., Ruiter, D., Ryan, A., and de Waal, R. (2004) Antiangiogenic Therapy of Cerebral Melanoma Metastases Results in Sustained Tumor Progression via Vessel Co-Option. *Clin. Cancer Res.* **10**, 6222–6230

152. Leenders, W. P. J., Küsters, B., and De Waal, R. M. W. (2002) Vessel co-option: How tumors obtain blood supply in the absence of sprouting angiogenesis. *Endothel. J. Endothel. Cell Res.* **9**, 83–87

153. Zhao, C., Yang, H., Shi, H., Wang, X., Chen, X., Yuan, Y., Lin, S., and Wei, Y. (2011) Distinct contributions of angiogenesis and vascular co-option during the initiation of primary microtumors and micrometastases. *Carcinogenesis* **32**, 1143–1150

154. Valiente, M., Obenauf, A. C., Jin, X., Chen, Q., Zhang, X. H.-F., Lee, D. J., Chaft, J. E., Kris, M. G., Huse, J. T., Brogi, E., and Massagué, J. (2014) Serpins Promote Cancer Cell Survival and Vascular Co-Option in Brain Metastasis. *Cell* **156**, 1002–1016

155. Frentzas, S., Simoneau, E., Bridgeman, V. L., Vermeulen, P. B., Foo, S., Kostaras, E., Nathan, M. R., Wotherspoon, A., Gao, Z., Shi, Y., Van den Eynden, G., Daley, F., Peckitt, C., Tan, X., Salman, A., Lazaris, A., Gazinska, P., Berg, T. J., Eltahir, Z., Ritsma, L., van Rheenen, J., Khashper, A., Brown, G., Nyström, H., Sund, M., Van Laere, S., Loyer, E., Dirix, L., Cunningham, D., Metrakos, P., and Reynolds, A. R. (2016) Vessel co-option mediates resistance to anti-angiogenic therapy in liver metastases. *Nat. Med.* **22**, 1294–1302

156. Bridgeman, V. L., Vermeulen, P. B., Foo, S., Bilecz, A., Daley, F., Kostaras, E., Nathan, M. R., Wan, E., Frentzas, S., Schweiger, T., Hegedus, B., Hoetzenecker, K., Renyi-Vamos, F., Kuczynski, E. A., Vasudev, N. S., Larkin, J., Gore, M., Dvorak, H. F., Paku, S., Kerbel, R. S., Dome, B., and Reynolds, A. R. (2017) Vessel co-option is common in human lung metastases and mediates resistance to anti-angiogenic therapy in preclinical lung metastasis models. *J. Pathol.* **241**, 362–374

157. Maniotis, A. J., Folberg, R., Hess, A., Seftor, E. A., Gardner, L. M. G., Pe'er, J., Trent, J. M., Meltzer, P. S., and Hendrix, M. J. C. (1999) Vascular Channel Formation by Human Melanoma Cells in Vivo and in Vitro: Vasculogenic Mimicry. *Am. J. Pathol.* **155**, 739–752

158. Wang, R., Chadalavada, K., Wilshire, J., Kowalik, U., Hovinga, K. E., Geber, A., Fligelman, B., Leversha, M., Brennan, C., and Tabar, V. (2010) Glioblastoma stem-like cells give rise to tumour endothelium. *Nature* **468**, 829–835

159. Caduff, J. H., Fischer, L. C., and Burri, P. H. (1986) Scanning electron microscope study of the developing microvasculature in the postnatal rat lung. *Anat. Rec.* **216**, 154–164

160. Ribatti, D. and Djonov, V. (2012) Intussusceptive microvascular growth in tumors. *Cancer Lett.* **316**, 126–131

161. Liu, S.-C. C., Alomran, R., Chernikova, S. B., Lartey, F., Stafford, J., Jang, T., Merchant, M., Zboralski, D., Zöllner, S., Kruschinski, A., Klussmann, S., Recht, L., and Brown, J. M. (2014) Blockade of SDF-1 after irradiation inhibits tumor recurrences of autochthonous brain tumors in rats. *Neuro. Oncol.* **16**, 21–28

162. Russell, J. S. and Brown, J. M. (2013) The irradiated tumor microenvironment: Role of tumor-associated macrophages in vascular recovery. *Front. Physiol.* **4 JUL**, 1–9

163. Hobson, B. and Denekamp, J. (1984) Endothelial proliferation in tumours and normal tissues: Continuous labelling studies. *Br. J. Cancer* **49**, 405–413

164. Shaifer, C. A., Huang, J., and Lin, P. C. (2010) Glioblastoma cells incorporate into tumor vasculature and contribute to vascular radioresistance. *Int. J. Cancer* **127**, 2063–2075

165. Hlushchuk, R., Riesterer, O., Baum, O., Wood, J., Gruber, G., Pruschy, M., and Djonov, V. (2008) Tumor recovery by angiogenic switch from sprouting to intussusceptive angiogenesis after treatment with PTK787/ZK222584 or ionizing radiation. *Am. J. Pathol.* **173**, 1173–1185

166. Senger, D., Galli, S., Dvorak, A., Perruzzi, C., Harvey, V., and Dvorak, H. (1983) Tumor cells secrete a vascular permeability factor that promotes accumulation of ascites fluid. *Science (80-.).* **219**, 983–985

167. Leung, D., Cachianes, G., Kuang, W., Goeddel, D., and Ferrara, N. (1989) Vascular endothelial growth factor is a secreted angiogenic mitogen. *Science (80-.).* **246**, 1306–1309

168. Keck, P. J., Hauser, S. D., Krivi, G., Sanzo, K., Warren, T., Feder, J., and Connolly, D. T.

(1989) Vascular permeability factor, an endothelial cell mitogen related to PDGF. *Science (80-.).* **246**, 1309–1312

169. Millauer, B., Wizigmann-Voos, S., Schnürch, H., Martinez, R., Møller, N. P., Risau, W., and Ullrich, A. (1993) High affinity VEGF binding and developmental expression suggest Flk-1 as a major regulator of vasculogenesis and angiogenesis. *Cell* **72**, 835–846

170. Welti, J., Loges, S., Dimmeler, S., and Carmeliet, P. (2013) Recent molecular discoveries in angiogenesis and antiangiogenic therapies in cancer. *J. Clin. Invest.* **123**, 3190–3200

171. Brouty-Boye, D. and Zetter, B. (1980) Inhibition of cell motility by interferon. *Science (80-.).* **208**, 516–518

172. Taylor, S. and Folkman, J. (1982) Protamine is an inhibitor of angiogenesis. *Nature* **297**, 307–312

173. Crum, R., Szabo, S., and Folkman, J. (1985) A new class of steroids inhibits angiogenesis in the presence of heparin or a heparin fragment. *Science (80-.).* **230**, 1375–1378

174. Rastinejad, F., Polverini, P. J., and Bouck, N. P. (1989) Regulation of the activity of a new inhibitor of angiogenesis by a cancer suppressor gene. *Cell* **56**, 345–355

175. Good, D. J., Polverini, P. J., Rastinejad, F., Le Beau, M. M., Lemons, R. S., Frazier, W. A., and Bouck, N. P. (1990) A tumor suppressor-dependent inhibitor of angiogenesis is immunologically and functionally indistinguishable from a fragment of thrombospondin. *Proc. Natl. Acad. Sci.* **87**, 6624–6628

176. Eddy, H. A. (1980) Tumor vascular responses following irradiation. *Microvasc. Res.* **20**, 195–211

177. Wang, E. S., Teruya-Feldstein, J., Wu, Y., Zhu, Z., Hicklin, D. J., and Moore, M. A. S. (2004) Targeting autocrine and paracrine VEGF receptor pathways inhibits human lymphoma xenografts in vivo. *Blood* **104**, 2893–2902

178. Sweeney, P., Karashima, T., Kim, S.-J., Kedar, D., Mian, B., Huang, S., Baker, C., Fan, Z., Hicklin, D. J., Pettaway, C. A., and Dinney, C. P. N. (2002) Anti-vascular endothelial growth factor receptor 2 antibody reduces tumorigenicity and metastasis in orthotopic prostate cancer xenografts via induction of endothelial cell apoptosis and reduction of endothelial cell matrix metalloproteinase type 9 production. *Clin. Cancer Res.* **8**, 2714–2724

179. Bruns, C. J., Shrader, M., Harbison, M. T., Portera, C., Solorzano, C. C., Jauch, K.-W., Hicklin, D. J., Radinsky, R., and Ellis, L. M. (2002) Effect of the vascular endothelial growth factor receptor-2 antibody DC101 plus gemcitabine on growth, metastasis and angiogenesis of human pancreatic cancer growing orthotopically in nude mice. *Int. J. Cancer* **102**, 101–108

180. Dameron, K., Volpert, O., Tainsky, M., and Bouck, N. (1994) Control of angiogenesis in fibroblasts by p53 regulation of thrombospondin-1. *Science (80-.).* **265**, 1582–1584

181. Ingber, D., Fujita, T., Kishimoto, S., Sudo, K., Kanamaru, T., Brem, H., and Folkman, J. (1990) Synthetic analogues of fumagillin that inhibit angiogenesis and suppress tumour growth. *Nature* **348**, 555–557

182. Moses, M., Sudhalter, J., and Langer, R. (1990) Identification of an inhibitor of neovascularization from cartilage. *Science (80-.).* **248**, 1408–1410

183. O'Reilly, M., Holmgren, L., Shing, Y., Chen, C., Rosenthal, R. A., Moses, M., Lane, W. S.,

Cao, Y., Sage, E. H., and Folkman, J. (1994) Angiostatin: A novel angiogenesis inhibitor that mediates the suppression of metastases by a lewis lung carcinoma. *Cell* **79**, 315–328

184. D'Amato, R. J., Loughnan, M. S., Flynn, E., and Folkman, J. (1994) Thalidomide is an inhibitor of angiogenesis. *Proc. Natl. Acad. Sci. U. S. A.* **91**, 4082–4085

185. O'Reilly, M. S., Boehm, T., Shing, Y., Fukai, N., Vasios, G., Lane, W. S., Flynn, E., Birkhead, J. R., Olsen, B. R., and Folkman, J. (1997) Endostatin: an endogenous inhibitor of angiogenesis and tumor growth. *Cell* **88**, 277–285

186. Parangi, S., O'Reilly, M., Christofori, G., Holmgren, L., Grosfeld, J., Folkman, J., and Hanahan, D. (1996) Antiangiogenic therapy of transgenic mice impairs de novo tumor growth. *Proc. Natl. Acad. Sci. U. S. A.* **93**, 2002–2007

187. Jain, R. K. (2001) Normalizing tumor vasculature with anti-angiogenic therapy: A new paradigm for combination therapy. *Nat. Med.* **7**, 987–989

188. Park, J.-S., Kim, I.-K., Han, S., Park, I., Kim, C., Bae, J., Oh, S. J., Lee, S., Kim, J. H., Woo, D.-C., He, Y., Augustin, H. G., Kim, I., Lee, D., and Koh, G. Y. (2016) Normalization of Tumor Vessels by Tie2 Activation and Ang2 Inhibition Enhances Drug Delivery and Produces a Favorable Tumor Microenvironment. *Cancer Cell* **30**, 953–967

189. Hattingen, E., Jurcoane, A., Bahr, O., Rieger, J., Magerkurth, J., Anti, S., Steinbach, J. P., and Pilatus, U. (2011) Bevacizumab impairs oxidative energy metabolism and shows antitumoral effects in recurrent glioblastomas: a 31P/1H MRSI and quantitative magnetic resonance imaging study. *Neuro. Oncol.* **13**, 1349–1363

190. DeLay, M., Jahangiri, A., Carbonell, W. S., Hu, Y.-L., Tsao, S., Tom, M. W., Paquette, J., Tokuyasu, T. A., and Aghi, M. K. (2012) Microarray Analysis Verifies Two Distinct Phenotypes of Glioblastomas Resistant to Antiangiogenic Therapy. *Clin. Cancer Res.* **18**, 2930–2942

191. Yopp, A. C., Schwartz, L. H., Kemeny, N., Gultekin, D. H., Gönen, M., Bamboat, Z., Shia, J., Haviland, D., D'Angelica, M. I., Fong, Y., DeMatteo, R. P., Allen, P. J., and Jarnagin, W. R. (2011) Antiangiogenic Therapy for Primary Liver Cancer: Correlation of Changes in Dynamic Contrast-Enhanced Magnetic Resonance Imaging with Tissue Hypoxia Markers and Clinical Response. *Ann. Surg. Oncol.* **18**, 2192–2199

192. Van der Veldt, A. A. M., Lubberink, M., Bahce, I., Walraven, M., de Boer, M. P., Greuter, H. N. J. M., Hendrikse, N. H., Eriksson, J., Windhorst, A. D., Postmus, P. E., Verheul, H. M., Serné, E. H., Lammertsma, A. A., and Smit, E. F. (2012) Rapid Decrease in Delivery of Chemotherapy to Tumors after Anti-VEGF Therapy: Implications for Scheduling of Anti-Angiogenic Drugs. *Cancer Cell* **21**, 82–91

193. Chang, Y. S., Adnane, J., Trail, P. A., Levy, J., Henderson, A., Xue, D., Bortolon, E., Ichetovkin, M., Chen, C., McNabola, A., Wilkie, D., Carter, C. A., Taylor, I. C. A., Lynch, M., and Wilhelm, S. (2007) Sorafenib (BAY 43-9006) inhibits tumor growth and vascularization and induces tumor apoptosis and hypoxia in RCC xenograft models. *Cancer Chemother. Pharmacol.* **59**, 561–574

194. Kanthou, C., Greco, O., Stratford, A., Cook, I., Knight, R., Benzakour, O., and Tozer, G. (2004) The Tubulin-Binding Agent Combretastatin A-4-Phosphate Arrests Endothelial Cells in Mitosis and Induces Mitotic Cell Death. *Am. J. Pathol.* **165**, 1401–1411

195. Gill, J. H., Rockley, K. L., De Santis, C., and Mohamed, A. K. (2019) Vascular Disrupting Agents in cancer treatment: Cardiovascular toxicity and implications for co-

administration with other cancer chemotherapeutics. *Pharmacol. Ther.* **202**, 18–31

196. Chauhan, A., Arnold, S., Wu, J., Slone, S., Dressler, E., Flynn, H., Adams, V., Weiss, H., and Anthony, L. (2019) Abstract CT067: A Phase I study of Fosbretabulin in combination with everolimus in neuroendocrine tumors (Grades 1-3) that have progressed after at least one prior regimen for metastatic disease.

197. Chauhan, A., Arnold, S., Slone, S. A., Flynn, H., Weiss, H., and Anthony, L. B. (2018) A phase I/II study of fosbretabulin in combination with everolimus in neuroendocrine tumors that have progressed after at least one prior regimen for metastatic disease. *J. Clin. Oncol.* **36**, TPS4148–TPS4148

198. Grisham, R., Ky, B., Tewari, K. S., Chaplin, D. J., and Walker, J. (2018) Clinical trial experience with CA4P anticancer therapy: focus on efficacy, cardiovascular adverse events, and hypertension management. *Gynecol. Oncol. Res. Pract.* **5**, 1

199. Libutti, S. K., Anthony, L. B., Chaplin, D. J., and Sosa, J. A. (2017) A phase II study of combretastatin A4-phosphate (CA4P) in the treatment of well-differentiated, low- to intermediate-grade, unresectable, recurrent, or metastatic pancreatic, or GI neuroendocrine tumors/carcinoid (GI-NETs/PNETs) with elevated biomarkers. *J. Clin. Oncol.* **35**, 432–432

200. Kanthou, C. and Tozer, G. M. (2009) Microtubule depolymerizing vascular disrupting agents: novel therapeutic agents for oncology and other pathologies. *Int. J. Exp. Pathol.* **90**, 284–294

201. Nathan, P., Zweifel, M., Padhani, A. R., Koh, D.-M., Ng, M., Collins, D. J., Harris, A., Carden, C., Smythe, J., Fisher, N., Taylor, N. J., Stirling, J. J., Lu, S.-P., Leach, M. O., Rustin, G. J. S., and Judson, I. (2012) Phase I Trial of Combretastatin A4 Phosphate (CA4P) in Combination with Bevacizumab in Patients with Advanced Cancer. *Clin. Cancer Res.* **18**, 3428–3439

202. Solesvik, O. V., Rofstad, E. K., and Brustad, T. (1984) Vascular Changes in a Human Malignant Melanoma Xenograft Following Single-Dose Irradiation. *Radiat. Res.* **98**, 115–128

203. Kalofonos, H., Rowlinson, G., and Epenetos, A. A. (1990) Enhancement of monoclonal antibody uptake in human colon tumor xenografts following irradiation. *Cancer Res.* **50**, 159–163

204. Fokas, E., Hänze, J., Kamlah, F., Eul, B. G., Lang, N., Keil, B., Heverhagen, J. T., Engenhart-Cabillic, R., An, H., and Rose, F. (2010) Irradiation-Dependent Effects on Tumor Perfusion and Endogenous and Exogenous Hypoxia Markers in an A549 Xenograft Model. *Int. J. Radiat. Oncol.* **77**, 1500–1508

205. Song, C. W. and Levitt, S. H. (1971) Vascular Changes in Walker 256 Carcinoma of Rats Following X Irradiation. *Radiology* **100**, 397–407

206. Kallman, R., DeNardo, G., and Stasch, M. (1972) Blood flow in irradiated mouse sarcoma as determined by the clearance of xenon-133. *Cancer Res.* **32**, 483–490

207. Song, C. W., Sung, J. H., Clement, J. J., and Levitt, S. H. (1974) Vascular Changes In Neuroblastoma Of Mice Following X-Irradiation 1. *Cancer Res.* **34**, 2344–2350

208. Hilmas, D. E. and Gillette, E. L. (1974) Morphometric analyses of the microvasculature of tumors during growth and after x-irradiation. *Cancer* **33**, 103–110

209. Hilmas, D. E. and Gillette, E. L. (1975) Microvasculature of C3H / Bi Mouse Mammary Tumors after X-Irradiation. *Radiat. Res.* **61**, 128–143

210. Tozer, G. M., Myers, R., and Cunningham, V. J. (1991) Radiation-induced modification of blood flow distribution in a rat fibrosarcoma. *Int. J. Radiat. Biol.* **60**, 327–334

211. Dings, R. P. M., Williams, B. W., Song, C. W., Griffioen, A. W., Mayo, K. H., and Griffin, R. J. (2005) Anginex synergizes with radiation therapy to inhibit tumor growth by radiosensitizing endothelial cells. *Int. J. Cancer* **115**, 312–319

212. Brurberg, K. G., Thuen, M., Ruud, E.-B. M., and Rofstad, E. K. (2006) Fluctuations in pO2 in irradiated human melanoma xenografts. *Radiat. Res.* **165**, 16–25

213. Merwing, R., Algire, G. H., Kaplan, H. S., Merwin, R., Algire, G. H., and Kaplan, H. S. (1950) Transparent-chamber observations of the response of a transplantable mouse mammary tumor to local roentgen irradiation. *J. Natl. Cancer Inst.* **11**, 593–623

214. Demidov, V., Maeda, A., Sugita, M., Madge, V., Sadanand, S., Flueraru, C., and Vitkin, I. A. (2018) Preclinical longitudinal imaging of tumor microvascular radiobiological response with functional optical coherence tomography. *Sci Rep* **8**, 38

215. Kim, D. W. N., Huamani, J., Niermann, K. J., Lee, H., Geng, L., Leavitt, L. L., Baheza, R. A., Jones, C. C., Tumkur, S., Yankeelov, T. E., Fleischer, A. C., and Hallahan, D. E. (2006) Noninvasive Assessment of Tumor Vasculature Response to Radiation-Mediated, Vasculature-Targeted Therapy Using Quantified Power Doppler Sonography. *J. Ultrasound Med.* **25**, 1507–1517

216. Emami, B., Ten Haken, R. K., Nussbaum, G. H., and Hughes, W. L. (1981) Effects of single-dose irradiation in tumor blood flow studied by 15O decay after photon activation in situ. *Radiology* **141**, 207–209

217. Mäntylä, M. J., Toivanen, J. T., Pitkänen, M. A., and Rekonen, A. H. (1982) Radiation-induced changes in regional blood flow in human tumors. *Int. J. Radiat. Oncol.* **8**, 1711–1717

218. Pirhonen, J. P., Grenman, S. A., Bredbacka, Å. B., Bahado-Singh, R. O., and Salmi, T. A. (1995) Effects of external radiotherapy on uterine blood flow in patients with advanced cervical carcinoma assessed by Color Doppler ultrasonography. *Cancer* **76**, 67–71

219. Lyng, H., Sundfør, K., and Rofstad, E. K. (2000) Changes in tumor oxygen tension during radiotherapy of uterine cervical cancer: relationships to changes in vascular density, cell density, and frequency of mitosis and apoptosis. *Int. J. Radiat. Oncol. Biol. Phys.* **46**, 935–946

220. Mayr, N. A., Yuh, W. T. C., Magnotta, V. A., Ehrhardt, J. C., Wheeler, J. A., Sorosky, J. I., Davis, C. S., Wen, B. C., Martin, D. D., Pelsang, R. E., Buller, R. E., Oberley, L. W., Mellenberg, D. E., and Hussey, D. H. (1996) Tumor perfusion studies using fast magnetic resonance imaging technique in advanced cervical cancer: A new noninvasive predictive assay. *Int. J. Radiat. Oncol. Biol. Phys.* **36**, 623–633

221. Ng, Q.-S., Goh, V., Milner, J., Padhani, A. R., Saunders, M. I., and Hoskin, P. J. (2007) Acute tumor vascular effects following fractionated radiotherapy in human lung cancer: In vivo whole tumor assessment using volumetric perfusion computed tomography. *Int. J. Radiat. Oncol. Biol. Phys.* **67**, 417–424

222. Janssen, M. H. M., Aerts, H. J. W. L., Kierkels, R. G. J., Backes, W. H., Ollers, M. C., Buijsen,

J., Lambin, P., and Lammering, G. (2010) Tumor perfusion increases during hypofractionated short-course radiotherapy in rectal cancer: sequential perfusion-CT findings. *Radiother. Oncol.* **94**, 156–160

223. Lock, S., Perrin, R., Seidlitz, A., Bandurska-Luque, A., Zschaeck, S., Zophel, K., Krause, M., Steinbach, J., Kotzerke, J., Zips, D., Troost, E. G. C., and Baumann, M. (2017) Residual tumour hypoxia in head-and-neck cancer patients undergoing primary radiochemotherapy, final results of a prospective trial on repeat FMISO-PET imaging. *Radiother Oncol* **124**, 533–540

224. Lock, S., Linge, A., Seidlitz, A., Bandurska-Luque, A., Nowak, A., Gudziol, V., Buchholz, F., Aust, D. E., Baretton, G. B., Zophel, K., Steinbach, J., Kotzerke, J., Overgaard, J., Zips, D., Krause, M., Baumann, M., and Troost, E. G. C. (2019) Repeat FMISO-PET imaging weakly correlates with hypoxia-associated gene expressions for locally advanced HNSCC treated by primary radiochemotherapy. *Radiother Oncol* **135**, 43–50

225. Shibuya, K., Tsushima, Y., Horisoko, E., Noda, S. E., Taketomi-Takahashi, A., Ohno, T., Amanuma, M., Endo, K., and Nakano, T. (2011) Blood flow change quantification in cervical cancer before and during radiation therapy using perfusion CT. *J Radiat Res* **52**, 804–811

226. Song, C. W., Glatstein, E., Marks, L. B., Emami, B., Grimm, J., Sperduto, P. W., Kim, M. S., Hui, S., Dusenbery, K. E., and Cho, L. C. (2019) Biological Principles of Stereotactic Body Radiation Therapy (SBRT) and Stereotactic Radiation Surgery (SRS): Indirect Cell Death. *Int. J. Radiat. Oncol. Biol. Phys.*

227. Howes, A. E., Page, A., and Fowler, J. F. (1972) The effect of single and fractionated doses of X rays on the effective proportion of hypoxic cells in C_3H mouse mammary tumours. *Br. J. Radiol.* **45**, 250–256

228. Howes, A. E. (1969) An estimation of changes in the proportions and absolute numbers of hypoxic cells after irradiation of transplanted C_3H mouse mammary tumours. *Br. J. Radiol.* **42**, 441–447

229. Dorie, M. J. and Kallman, R. F. (1984) Reoxygenation in the RIF-1 tumor. *Int. J. Radiat. Oncol.* **10**, 687–693

230. Vaupel, P., Frinak, S., and O'Hara, M. (1984) Direct measurement of reoxygenation in malignant mammary tumors after a single large dose of irradiation. *Adv. Exp. Med. Biol.* **180**, 773–782

231. Vaupel, P., Kelleher, D. K., and Höckel, M. (2001) Oxygen status of malignant tumors: pathogenesis of hypoxia and significance for tumor therapy. *Semin. Oncol.* **28**, 29–35

232. Yaromina, A., Kroeber, T., Meinzer, A., Boeke, S., Thames, H., Baumann, M., and Zips, D. (2011) Exploratory study of the prognostic value of microenvironmental parameters during fractionated irradiation inhuman squamous cell carcinoma xenografts. *Int. J. Radiat. Oncol. Biol. Phys.* **80**, 1205–1213

233. Brizel, D. M., Dodge, R. K., Clough, R. W., and Dewhirst, M. W. (1999) Oxygenation of head and neck cancer: Changes during radiotherapy and impact on treatment outcome. *Radiother. Oncol.* **53**, 113–117

234. Seymour, C. B. and Mothersill, C. (2004) Radiation-induced bystander effects — implications for cancer. *Nat. Rev. Cancer* **4**, 158–164

235. Galluzzi, L. and Vitale, I. (2018) Molecular mechanisms of cell death: recommendations of the Nomenclature Committee on Cell Death 2018. *Cell Death Differ.* **25**, 486–541

236. Eriksson, D. and Stigbrand, T. (2010) Radiation-induced cell death mechanisms. *Tumor Biol.* **31**, 363–372

237. Eriksson, D., Lofroth, P.-O., Johansson, L., Riklund, K. A., and Stigbrand, T. (2007) Cell Cycle Disturbances and Mitotic Catastrophes in HeLa Hep2 Cells following 2.5 to 10 Gy of Ionizing Radiation. *Clin. Cancer Res.* **13**, 5501s-5508s

238. Dodson, H., Wheatley, S. P., and Morrison, C. G. (2007) Involvement of Centrosome Amplification in Radiation-Induced Mitotic Catastrophe. *Cell Cycle* **6**, 364–370

239. Bourke, E., Dodson, H., Merdes, A., Cuffe, L., Zachos, G., Walker, M., Gillespie, D., and Morrison, C. G. (2007) DNA damage induces Chk1-dependent centrosome amplification. *EMBO Rep.* **8**, 603–609

240. Kawamura, K., Fujikawa-Yamamoto, K., Ozaki, M., Iwabuchi, K., Nakashima, H., Domiki, C., Morita, N., Inoue, M., Tokunaga, K., Shiba, N., Ikeda, R., and Suzuki, K. (2004) Centrosome hyperamplification and chromosomal damage after exposure to radiation. *Oncology* **67**, 460–470

241. Lowe, S. W., Schmitt, E. M., Smith, S. W., Osborne, B. A., and Jacks, T. (1993) p53 is required for radiation-induced apoptosis in mouse thymocytes. *Nature* **362**, 847–849

242. Soussi, T. and Béroud, C. (2001) Assessing TP53 status in human tumours to evaluate clinical outcome. *Nat. Rev. Cancer* **1**, 233–239

243. Soussi, T. and Lozano, G. (2005) p53 mutation heterogeneity in cancer. *Biochem. Biophys. Res. Commun.* **331**, 834–842

244. Hollstein, M., Sidransky, D., Vogelstein, B., and Harris, C. (1991) p53 mutations in human cancers. *Science (80-.).* **253**, 49–53

245. Turcotte, S. and Giaccia, A. J. (2010) Targeting cancer cells through autophagy for anticancer therapy. *Curr. Opin. Cell Biol.* **22**, 246–251

246. Radford, I. R., Murphy, T. K., Radley, J. M., and Ellis, S. L. (1994) Radiation Response of Mouse Lymphoid and Myeloid Cell Lines. Part II. Apoptotic Death is Shown by all Lines Examined. *Int. J. Radiat. Biol.* **65**, 217–227

247. Shinomiya, N. (2001) New concepts in radiation-induced apoptosis: 'premitotic apoptosis1 and "postmitotic apoptosis." *J. Cell. Mol. Med.* **5**, 240–253

248. Igarashi, K., Sakimoto, I., Kataoka, K., Ohta, K., and Miura, M. (2007) Radiation-induced senescence-like phenotype in proliferating and plateau-phase vascular endothelial cells. *Exp. Cell Res.* **313**, 3326–3336

249. Kim, K. S., Kim, J. E., Choi, K. J., Bae, S., and Kim, D. H. (2014) Characterization of DNA damage-induced cellular senescence by ionizing radiation in endothelial cells. *Int. J. Radiat. Biol.* **90**, 71–80

250. Panganiban, R. A. M., Mungunsukh, O., and Day, R. M. (2013) X-irradiation induces ER stress, apoptosis, and senescence in pulmonary artery endothelial cells. *Int. J. Radiat. Biol.* **89**, 656–667

251. Langley, R. E., Bump, E. A., Quartuccio, S. G., Medeiros, D., and Braunhut, S. J. (1997) Radiation-induced apoptosis in microvascular endothelial cells. *Br. J. Cancer* **75**, 666–672

252. Haimovitz-Friedman, A., Vlodavsky, I., Chaudhuri, A., Witte, L., and Fuks, Z. (1991) Autocrine effects of fibroblast growth factor in repair of radiation damage in endothelial cells. *Cancer Res.* **51**, 2552–2558

253. Fuks, Z., Persaud, R. S., Alfieri, A., McLoughlin, M., Ehleiter, D., Schwartz, J. L., Seddon, A. P., Cordon-Cardo, C., and Haimovitz-Friedman, A. (1994) Basic fibroblast growth factor protects endothelial cells against radiation-induced programmed cell death in vitro and in vivo. *Cancer Res.* **54**, 2582–2590

254. Karsan, A., Yee, E., Poirier, G. G., Zhou, P., Craig, R., and Harlan, J. M. (1997) Fibroblast growth factor-2 inhibits endothelial cell apoptosis by Bcl-2-dependent and independent mechanisms. *Am. J. Pathol.* **151**, 1775–1784

255. Imaizumi, N., Monnier, Y., Hegi, M., Mirimanoff, R. O., and Rüegg, C. (2010) Radiotherapy suppresses angiogenesis in mice through TGF-βRI/ALK5-dependent inhibition of endothelial cell sprouting. *PLoS One* **5**, e11084

256. Kobayashi, T., Ruan, S., Jabbur, J. R., Consoli, U., Clodi, K., Shiku, H., Owen-Schaub, L. B., Andreeff, M., Reed, J. C., and Zhang, W. (1998) Differential p53 phosphorylation and activation of apoptosis-promoting genes Bax and Fas/APO-1 by irradiation and ara-C treatment. *Cell Death Differ.* **5**, 584–591

257. Alvarez, S., Drané, P., Meiller, A., Bras, M., Deguin-Chambon, V., Bouvard, V., and May, E. (2006) A comprehensive study of p53 transcriptional activity in thymus and spleen of γ irradiated mouse: High sensitivity of genes involved in the two main apoptotic pathways. *Int. J. Radiat. Biol.* **82**, 761–770

258. Jin, Z. and El-Deiry, W. S. (2005) Overview of cell death signaling pathways. *Cancer Biol. Ther.* **4**, 139–163

259. Erlacher, M., Michalak, E. M., Kelly, P. N., Labi, V., Niederegger, H., Coultas, L., Adams, J. M., Strasser, A., and Villunger, A. (2005) BH3-only proteins Puma and Bim are rate-limiting for γ-radiation- and glucocorticoid-induced apoptosis of lymphoid cells in vivo. *Blood* **106**, 4131–4138

260. Michalak, E. M., Villunger, A., Adams, J. M., and Strasser, A. (2008) In several cell types tumour suppressor p53 induces apoptosis largely via Puma but Noxa can contribute. *Cell Death Differ.* **15**, 1019–1029

261. Haimovitz-Friedman, A., Kan, C. C., Ehleiter, D., Persaud, R. S., McLoughlin, M., Fuks, Z., and Kolesnick, R. N. (1994) Ionizing radiation acts on cellular membranes to generate ceramide and initiate apoptosis. *J. Exp. Med.* **180**, 525–535

262. Moding, E. J., Castle, K. D., Perez, B. A., Oh, P., Min, H. D., Norris, H., Ma, Y., Cardona, D. M., Lee, C.-L., and Kirsch, D. G. (2015) Tumor cells, but not endothelial cells, mediate eradication of primary sarcomas by stereotactic body radiation therapy. *Sci. Transl. Med.* **7**, 278ra34

263. Moding, E. J., Lee, C. L., Castle, K. D., Oh, P., Mao, L., Zha, S., Min, H. D., Ma, Y., Das, S., and Kirsch, D. G. (2014) ATM deletion with dual recombinase technology preferentially radiosensitizes tumor endothelium. *J. Clin. Invest.* **124**, 3325–3338

264. Rombouts, C., Aerts, A., Beck, M., De Vos, W. H., Van Oostveldt, P., Benotmane, M. A., and Baatout, S. (2013) Differential response to acute low dose radiation in primary and immortalized endothelial cells. *Int. J. Radiat. Biol.* **89**, 841–850

265. Rödel, F., Frey, B., Capalbo, G., Gaipl, U., Keilholz, L., Voll, R., Hildebrandt, G., and Rödel, C. (2010) Discontinuous induction of X-linked inhibitor of apoptosis in EA.hy.926 endothelial cells is linked to NF-κB activation and mediates the anti-inflammatory properties of low-dose ionising-radiation. *Radiother. Oncol.* **97**, 346–351

266. Pluder, F., Barjaktarovic, Z., Azimzadeh, O., Mörtl, S., Krämer, A., Steininger, S., Sarioglu, H., Leszczynski, D., Nylund, R., Hakanen, A., Sriharshan, A., Atkinson, M. J., and Tapio, S. (2011) Low-dose irradiation causes rapid alterations to the proteome of the human endothelial cell line EA.hy926. *Radiat. Environ. Biophys.* **50**, 155–166

267. Wang, Y., Boerma, M., and Zhou, D. (2016) Ionizing Radiation-Induced Endothelial Cell Senescence and Cardiovascular Diseases. *Radiat. Res.* **186**, 153–161

268. Rombouts, C., Aerts, A., Quintens, R., Baselet, B., El-Saghire, H., Harms-Ringdahl, M., Haghdoost, S., Janssen, A., Michaux, A., Yentrapalli, R., Benotmane, M. A., Van Oostveldt, P., and Baatout, S. (2014) Transcriptomic profiling suggests a role for IGFBP5 in premature senescence of endothelial cells after chronic low dose rate irradiation. *Int. J. Radiat. Biol.* **90**, 560–574

269. Oh, C. W., Bump, E. A., Kim, J. S., Janigro, D., and Mayberg, M. R. (2001) Induction of a senescence-like phenotype in bovine aortic endothelial cells by ionizing radiation. *Radiat. Res.* **156**, 232–240

270. Yentrapalli, R., Azimzadeh, O., Sriharshan, A., Malinowsky, K., Merl, J., Wojcik, A., Harms-Ringdahl, M., Atkinson, M. J., Becker, K. F., Haghdoost, S., and Tapio, S. (2013) The PI3K/Akt/mTOR Pathway Is Implicated in the Premature Senescence of Primary Human Endothelial Cells Exposed to Chronic Radiation. *PLoS One* **8**, e70024

271. Costa-Silva, B., Aiello, N. M., Ocean, A. J., Singh, S., Zhang, H., Thakur, B. K., Becker, A., Hoshino, A., Mark, M. T., Molina, H., Xiang, J., Zhang, T., Theilen, T.-M., García-Santos, G., Williams, C., Ararso, Y., Huang, Y., Rodrigues, G., Shen, T.-L., Labori, K. J., Lothe, I. M. B., Kure, E. H., Hernandez, J., Doussot, A., Ebbesen, S. H., Grandgenett, P. M., Hollingsworth, M. a, Jain, M., Mallya, K., Batra, S. K., Jarnagin, W. R., Schwartz, R. E., Matei, I., Peinado, H., Stanger, B. Z., Bromberg, J., and Lyden, D. (2015) Pancreatic cancer exosomes initiate pre-metastatic niche formation in the liver. *Nat. Cell Biol.* **17**, 1–7

272. Muramoto, G. G., Chen, B., Cui, X., Chao, N. J., and Chute, J. P. (2006) Vascular Endothelial Cells Produce Soluble Factors That Mediate the Recovery of Human Hematopoietic Stem Cells after Radiation Injury. *Biol. Blood Marrow Transplant.* **12**, 530–540

273. Baselet, B., Sonveaux, P., Baatout, S., and Aerts, A. (2019) Pathological effects of ionizing radiation: endothelial activation and dysfunction. *Cell. Mol. Life Sci.* **76**, 699–728

274. Garcia-Barros, M., Thin, T. H., Maj, J., Cordon-Cardo, C., Haimovitz-Friedman, A., Fuks, Z., and Kolesnick, R. (2010) Impact of Stromal Sensitivity on Radiation Response of Tumors Implanted in SCID Hosts Revisited. *Cancer Res.* **70**, 8179–8186

275. Fuks, Z. and Kolesnick, R. (2005) Engaging the vascular component of the tumor response. *Cancer Cell* **8**, 89–91

276. Torok, J. A., Oh, P., Castle, K. D., Reinsvold, M., Ma, Y., Luo, L., Lee, C. L., and Kirsch, D. G. (2019) Deletion of ATM in tumor but not endothelial cells improves radiation response in a primary mouse model of lung adenocarcinoma. *Cancer Res.* **79**, 773–782

277. Budach, W., Taghian, A., Freeman, J., Gioioso, D., and Suit, H. D. (1993) Impact of stromal sensitivity on radiation response of tumors. *J Natl Cancer Inst* **85**, 988–993

278. Ogawa, K., Boucher, Y., Kashiwagi, S., Fukumura, D., Chen, D., and Gerweck, L. E. (2007) Influence of tumor cell and stroma sensitivity on tumor response to radiation. *Cancer Res* **67**, 4016–4021

279. Krause, D. S. and Van Etten, R. A. (2005) The new england journal of medicine n engl j med 353;2 www.nejm.org july 14. *N Engl J Med* **353**

280. Greening, G. J., Miller, K. P., Spainhour, C. R., Cato, M. D., and Muldoon, T. J. (2018) Effects of isoflurane anesthesia on physiological parameters in murine subcutaneous tumor allografts measured via diffuse reflectance spectroscopy. *Biomed. Opt. Express* **9**, 2871

281. Szczęsny, G., Veihelmann, A., Massberg, S., Nolte, D., and Messmer, K. (2004) Long-term anaesthesia using inhalatory isoflurane in different strains of mice - The haemodynamic effects. *Lab. Anim.* **38**, 64–69

282. Hill, M. A., Thompson, J. M., Kavanagh, A., Tullis, I. D. C., Newman, R. G., Prentice, J., Beech, J., Gilchrist, S., Smart, S., Fokas, E., and Vojnovic, B. (2017) The Development of Technology for Effective Respiratory-Gated Irradiation Using an Image-Guided Small Animal Irradiator. *Radiat Res* **188**, 247–263

283. Ritsma, L., Steller, E. J., Ellenbroek, S. I., Kranenburg, O., Borel Rinkes, I. H., and van Rheenen, J. (2013) Surgical implantation of an abdominal imaging window for intravital microscopy. *Nat Protoc* **8**, 583–594

284. Yang, R. S., Chang, L. W., Wu, J. P., Tsai, M. H., Wang, H. J., Kuo, Y. C., Yeh, T. K., Yang, C. S., and Lin, P. (2007) Persistent tissue kinetics and redistribution of nanoparticles, quantum Dot 705, in Mice: ICP-MS quantitative assessment. *Environ. Health Perspect.* **115**, 1339–1343

285. Picelli, S., Faridani, O. R., Bjorklund, A. K., Winberg, G., Sagasser, S., Sandberg, R., Björklund, Å. K., Winberg, G., Sagasser, S., Sandberg, R., Bjorklund, A. K., Winberg, G., Sagasser, S., and Sandberg, R. (2014) Full-length RNA-seq from single cells using Smart-seq2. *Nat Protoc* **9**, 171–181

286. Kinchesh, P., Gilchrist, S., Beech, J. S., Gomes, A. L., Kersemans, V., Newman, R. G., Vojnovic, B., Allen, P. D., Brady, M., Muschel, R. J., and Smart, S. C. (2018) Prospective gating control for highly efficient cardio-respiratory synchronised short and constant TR MRI in the mouse. *Magn Reson Imaging* **53**, 20–27

287. Drobizhev, M., Makarov, N. S., Tillo, S. E., Hughes, T. E., and Rebane, A. (2011) Two-photon absorption properties of fluorescent proteins. *Nat. Methods* **8**, 393–399

288. Schindelin, J., Arganda-Carreras, I., Frise, E., Kaynig, V., Longair, M., Pietzsch, T., Preibisch, S., Rueden, C., Saalfeld, S., Schmid, B., Tinevez, J. Y., White, D. J., Hartenstein, V., Eliceiri, K., Tomancak, P., and Cardona, A. (2012) Fiji: an open-source platform for biological-image analysis. *Nat Methods* **9**, 676–682

289. Bates, R., Irving, B., Markelc, B., Kaeppler, J., Brown, G., Muschel, R. J., Brady, S. M., Grau, V., and Schnabel, J. A. (2019) Segmentation of vasculature from fluorescently labeled endothelial cells in multi-photon microscopy images. *IEEE Trans. Med. Imaging* **38**, 1–10

290. Bates, R. (2017) Learning to extract tumour vasculature : techniques in machine learning for medical image analysis.

291. Ronneberger, O., Fischer, P., and Brox, T. (2015) U-net: Convolutional networks for

biomedical image segmentation.

292. Bates, R., Irving, B., Markelc, B., Kaeppler, J., Muschel, R., Grau, V., and Schnabel, J. A. (2017) Extracting 3D Vascular Structures from Microscopy Images using Convolutional Recurrent Networks. *arXiv 2017*

293. Hochreiter, S. and Schmidhuber, J. (1997) Long Short-Term Memory. *Neural Comput.* **9**, 1735–1780

294. Pudney, C. (1998) Distance-Ordered Homotopic Thinning: A Skeletonization Algorithm for 3D Digital Images. *Comput. Vis. Image Underst.* **72**, 404–413

295. Weissleder, R. (2002) Scaling down imaging: molecular mapping of cancer in mice. *Nat. Rev. Cancer* **2**, 11–18

296. Mathivet, T., Bouleti, C., Van Woensel, M., Stanchi, F., Verschuere, T., Phng, L. K., Dejaegher, J., Balcer, M., Matsumoto, K., Georgieva, P. B., Belmans, J., Sciot, R., Stockmann, C., Mazzone, M., De Vleeschouwer, S., and Gerhardt, H. (2017) Dynamic stroma reorganization drives blood vessel dysmorphia during glioma growth. *EMBO Mol. Med.* **9**, 1629–1645

297. Bremer, D., Pache, F., Günther, R., Hornow, J., Andresen, V., Leben, R., Mothes, R., Zimmermann, H., Brandt, A. U., Paul, F., Hauser, A. E., Radbruch, H., and Niesner, R. (2016) Longitudinal intravital imaging of the retina reveals long-term dynamics of immune infiltration and its effects on the glial network in experimental autoimmune uveoretinitis, without evident signs of neuronal dysfunction in the ganglion cell layer. *Front. Immunol.* **7**, 642

298. Norrby, K. (2006) In vivo models of angiogenesis. *J. Cell. Mol. Med.* **10**, 588–612

299. Folarin, A. A. A., Konerding, M. A. A., Timonen, J., Nagl, S., and Pedley, R. B. B. (2010) Three-dimensional analysis of tumour vascular corrosion casts using stereoimaging and micro-computed tomography. *Microvasc. Res.* **80**, 89–98

300. Pittet, M. J. and Weissleder, R. (2011) Intravital Imaging. *Cell* **147**, 983–991

301. Kobat, D., Horton, N. G., and Xu, C. (2011) In vivo two-photon microscopy to 1.6-mm depth in mouse cortex. *J. Biomed. Opt.* **16**, 106014

302. Palmer, G. M., Fontanella, A. N., Shan, S., Hanna, G., Zhang, G., Fraser, C. L., and Dewhirst, M. W. (2011) In vivo optical molecular imaging and analysis in mice using dorsal window chamber models applied to hypoxia, vasculature and fluorescent reporters. *Nat. Protoc.* **6**, 1355–1366

303. Maeda, A. and DaCosta, R. S. (2014) Optimization of the dorsal skinfold window chamber model and multi-parametric characterization of tumor-associated vasculature. *Intravital* **3**, e27935

304. Jain, R. K., Munn, L. L., and Fukumura, D. (2002) Dissecting Tumour Pathophysiology Using Intravital Microscopy. *Nat. Rev. Cancer* **2**, 266–276

305. Payne, S., Val, S. De, and Neal, A. (2018) Endothelial-specific cre mouse models is your cre CREdibile? *Arterioscler. Thromb. Vasc. Biol.* **38**, 2550–2561

306. Feil, S., Valtcheva, N., and Feil, R. (2009) Inducible Cre Mice. *Methods Mol. Biol.* **530**, 343–363

307. Feil, R., Wagner, J., Metzger, D., and Chambon, P. (1997) Regulation of Cre Recombinase

Activity by Mutated Estrogen Receptor Ligand-Binding Domains. *Biochem. Biophys. Res. Commun.* **237**, 752–757

308. Zhong, Z. A., Sun, W., Chen, H., Zhang, H., Lay, Y. A. E., Lane, N. E., and Yao, W. (2015) Optimizing tamoxifen-inducible Cre/loxp system to reduce tamoxifen effect on bone turnover in long bones of young mice. *Bone* **81**, 614–619

309. Metzger, D., Clifford, J., Chiba, H., and Chambon, P. (1995) Conditional site-specific recombination in mammalian cells using a ligand-dependent chimeric Cre recombinase. *Proc. Natl. Acad. Sci. U. S. A.* **92**, 6991–6995

310. Schwenk, F., Kühn, R., Angrand, P. O., Rajewsky, K., and Stewart, A. F. (1998) Temporally and spatially regulated somatic mutagenesis in mice. *Nucleic Acids Res.* **26**, 1427–1432

311. Adams, R. H. (2007) Investigation of the angiogenic programme with tissue-specific and inducible genetic approaches in mice.

312. Monvoisin, A., Alva, J. A., Hofmann, J. J., Zovein, A. C., Lane, T. F., and Iruela-Arispe, M. L. (2006) VE-cadherin-CreERT2 transgenic mouse: A model for inducible recombination in the endothelium. *Dev. Dyn.* **235**, 3413–3422

313. Alva, J. A., Zovein, A. C., Monvoisin, A., Murphy, T., Salazar, A., Harvey, N. L., Carmeliet, P., and Iruela-Arispe, M. L. (2006) VE-cadherin-cre-recombinase transgenic mouse: A tool for lineage analysis and gene deletion in endothelial cells. *Dev. Dyn.* **235**, 759–767

314. Wang, Y., Nakayama, M., Pitulescu, M. E., Schmidt, T. S., Bochenek, M. L., Sakakibara, A., Adams, S., Davy, A., Deutsch, U., Lüthi, U., Barberis, A., Benjamin, L. E., Mäkinen, T., Nobes, C. D., and Adams, R. H. (2010) Ephrin-B2 controls VEGF-induced angiogenesis and lymphangiogenesis. *Nature* **465**, 483–486

315. Okabe, K., Kobayashi, S., Yamada, T., Kurihara, T., Tai-Nagara, I., Miyamoto, T., Mukouyama, Y. S., Sato, T. N., Suda, T., Ema, M., and Kubota, Y. (2014) Neurons limit angiogenesis by titrating VEGF in retina. *Cell* **159**, 584–596

316. Chen, M. J., Yokomizo, T., Zeigler, B. M., Dzierzak, E., and Speck, N. A. (2009) Runx1 is required for the endothelial to haematopoietic cell transition but not thereafter. *Nature* **457**, 887–891

317. Kogata, N., Arai, Y., Pearson, J. T., Hashimoto, K., Hidaka, K., Koyama, T., Somekawa, S., Nakaoka, Y., Ogawa, M., Adams, R. H., Okada, M., and Mochizuki, N. (2006) Cardiac ischemia activates vascular endothelial cadherin promoter in both preexisting vascular cells and bone marrow cells involved in neovascularization. *Circ. Res.* **98**, 897–904

318. Madisen, L., Zwingman, T. A., Sunkin, S. M., Oh, S. W., Zariwala, H. A., Gu, H., Ng, L. L., Palmiter, R. D., Hawrylycz, M. J., Jones, A. R., Lein, E. S., and Zeng, H. (2010) A robust and high-throughput Cre reporting and characterization system for the whole mouse brain. *Nat. Neurosci.* **13**, 133–140

319. Potez, M., Trappetti, V., Bouchet, A., Fernandez-Palomo, C., Güç, E., Kilarski, W. W., Hlushchuk, R., Laissue, J., and Djonov, V. (2018) Characterization of a B16-F10 melanoma model locally implanted into the ear pinnae of C57BL/6 mice. *PLoS One* **13**, e0206693

320. Heffner, C. S., Herbert Pratt, C., Babiuk, R. P., Sharma, Y., Rockwood, S. F., Donahue, L. R., Eppig, J. T., and Murray, S. A. (2012) Supporting conditional mouse mutagenesis with a comprehensive cre characterization resource. *Nat. Commun.* **3**, 1218

321. Lawson, H. A., Cheverud, J. M., and Wolf, J. B. (2013) Genomic imprinting and parent-of-

origin effects on complex traits. *Nat. Rev. Genet.* **14**, 609–617

322. Dewhirst, M. W., Kimura, H., Rehmus, S. W., Braun, R. D., Papahadjopoulos, D., Hong, K., and Secomb, T. W. (1996) Microvascular studies on the origins of perfusion-limited hypoxia. *Br. J. Cancer. Suppl.* **27**, S247-51

323. Pigott, K. H., Hill, S. A., Chaplin, D. J., and Saunders, M. I. (1996) Microregional fluctuations in perfusion within human tumours detected using laser Doppler flowmetry. *Radiother. Oncol.* **40**, 45–50

324. Durand, R. E. and Lepard, N. E. (1995) Contribution of Transient Blood Flow to Tumour Hypoxia in Mice. *Acta Oncol. (Madr).* **34**, 317–323

325. Larson, D. R., Zipfel, W. R., Williams, R. M., Clark, S. W., Bruchez, M. P., Wise, F. W., and Webb, W. W. (2003) Water-Soluble Quantum Dots for Multiphoton Fluorescence Imaging in Vivo. *Science (80-.).* **300**, 1434–1436

326. Ballou, B., Lagerholm, B. C., Ernst, L. A., Bruchez, M. P., and Waggoner, A. S. (2004) Noninvasive Imaging of Quantum Dots in Mice. *Bioconjug. Chem.* **15**, 79–86

327. Jacques, S. L. (2013) Optical properties of biological tissues: A review. *Phys. Med. Biol.* **58**, R37–R61

328. Ingaramo, M., York, A. G., Wawrzusin, P., Milberg, O., Hong, A., Weigert, R., Shroff, H., and Patterson, G. H. (2014) Two-photon excitation improves multifocal structured illumination microscopy in thick scattering tissue. *Proc. Natl. Acad. Sci. U. S. A.* **111**, 5254–5259

329. Helmchen, F. and Denk, W. (2005) Deep tissue two-photon microscopy. *Nat. Methods* **2**, 932–940

330. Kuczynski, E. A., Vermeulen, P. B., Pezzella, F., Kerbel, R. S., and Reynolds, A. R. (2019) Vessel co-option in cancer. *Nat. Rev. Clin. Oncol.* **16**, 469–493

331. Moccia, S., De Momi, E., El Hadji, S., and Mattos, L. S. (2018) Blood vessel segmentation algorithms — Review of methods, datasets and evaluation metrics. *Comput. Methods Programs Biomed.* **158**, 71–91

332. Hilmas D., G. E. (1973) Morphometric Analysis of the microvasculature of tumors during growth and after x-irradiation. *Cancer* **50**, 936–946

333. Tozer, G. M., Ameer-Beg, S. M., Baker, J., Barber, P. R., Hill, S. A., Hodgkiss, R. J., Locke, R., Prise, V. E., Wilson, I., and Vojnovic, B. (2005) Intravital imaging of tumour vascular networks using multi-photon fluorescence microscopy. *Adv. Drug Deliv. Rev.* **57**, 135–152

334. Langenkamp, E., vom Hagen, F. M., Zwiers, P. J., Moorlag, H. E., Schouten, J. P., Hammes, H.-P., Gouw, A. S. H., and Molema, G. (2011) Tumor Vascular Morphology Undergoes Dramatic Changes during Outgrowth of B16 Melanoma While Proangiogenic Gene Expression Remains Unchanged. *ISRN Oncol.* **2011**, 1–14

335. Gomez-Iturriaga, A., Casquero, F., Urresola, A., Ezquerro, A., Lopez, J. I., Espinosa, J. M., Minguez, P., Llarena, R., Irasarri, A., Bilbao, P., and Crook, J. (2016) Dose escalation to dominant intraprostatic lesions with MRI-transrectal ultrasound fusion High-Dose-Rate prostate brachytherapy. Prospective phase II trial. *Radiother. Oncol.* **119**, 91–96

336. Gomez, D. R., Blumenschein Jr., G. R., Lee, J. J., Hernandez, M., Ye, R., Camidge, D. R.,

Doebele, R. C., Skoulidis, F., Gaspar, L. E., Gibbons, D. L., Karam, J. A., Kavanagh, B. D., Tang, C., Komaki, R., Louie, A. V, Palma, D. A., Tsao, A. S., Sepesi, B., William, W. N., Zhang, J., Shi, Q., Wang, X. S., Swisher, S. G., and Heymach, J. V. (2016) Local consolidative therapy versus maintenance therapy or observation for patients with oligometastatic non-small-cell lung cancer without progression after first-line systemic therapy: a multicentre, randomised, controlled, phase 2 study. *Lancet Oncol* **17**, 1672–1682

337. Iyengar, P., Wardak, Z., Gerber, D. E., Tumati, V., Ahn, C., Hughes, R. S., Dowell, J. E., Cheedella, N., Nedzi, L., Westover, K. D., Pulipparacharuvil, S., Choy, H., and Timmerman, R. D. (2018) Consolidative Radiotherapy for Limited Metastatic Non-Small-Cell Lung Cancer: A Phase 2 Randomized Clinical Trial. *JAMA Oncol* **4**, e173501

338. Ning, M. S., Gomez, D. R., Heymach, J. V, and Swisher, S. G. (2019) Stereotactic ablative body radiation for oligometastatic and oligoprogressive disease. *Transl Lung Cancer Res* **8**, 97–106

339. Palma, D. A., Olson, R., Harrow, S., Gaede, S., Louie, A. V, Haasbeek, C., Mulroy, L., Lock, M., Rodrigues, G. B., Yaremko, B. P., Schellenberg, D., Ahmad, B., Griffioen, G., Senthi, S., Swaminath, A., Kopek, N., Liu, M., Moore, K., Currie, S., Bauman, G. S., Warner, A., and Senan, S. (2019) Stereotactic ablative radiotherapy versus standard of care palliative treatment in patients with oligometastatic cancers (SABR-COMET): a randomised, phase 2, open-label trial. *Lancet* **393**, 2051–2058

340. Zeng, K. L., Tseng, C. L., Soliman, H., Weiss, Y., Sahgal, A., and Myrehaug, S. (2019) Stereotactic Body Radiotherapy (SBRT) for Oligometastatic Spine Metastases: An Overview. *Front Oncol* **9**, 337

341. Song, C. W., Cho, L. C., Yuan, J., Dusenbery, K. E., Griffin, R. J., and Levitt, S. H. (2013) Radiobiology of stereotactic body radiation therapy/stereotactic radiosurgery and the linear-quadratic model. *Int. J. Radiat. Oncol. Biol. Phys.* **87**, 18–19

342. Kim, M. S., Kim, W., Park, I. H., Kim, H. J., Lee, E., Jung, J. H., Cho, L. C., and Song, C. W. (2015) Radiobiological mechanisms of stereotactic body radiation therapy and stereotactic radiation surgery. *Radiat Oncol J* **33**, 265–275

343. Spence, A. M., Graham, M. M., Abbott, G. L., Muzi, M., and Lewellen, T. K. (1988) Blood Flow Changes Following 137 Cs Irradiation in a Rat. *Radiat. Res.* **115**, 586–594

344. Crokart, N., Jordan, B. F., Baudelet, C., Ansiaux, R., Sonveaux, P., Grégoire, V., Beghein, N., DeWever, J., Bouzin, C., Feron, O., and Gallez, B. (2005) Early reoxygenation in tumors after irradiation: Determining factors and consequences for radiotherapy regimens using daily multiple fractions. *Int. J. Radiat. Oncol. Biol. Phys.* **63**, 901–910

345. Sonveaux, P., Dessy, C., Brouet, A., Jordan, B. F., Grégoire, V., Gallez, B., Balligand, J. L., and Feron, O. (2002) Modulation of the tumor vasculature functionality by ionizing radiation accounts for tumor radiosensitization and promotes gene delivery. *FASEB J.* **16**, 1979–1981

346. Horsman, M. R., Nielsen, T., Østergaard, L., and Overgaard, J. (2006) Radiation administered as a large single dose or in a fractionated schedule: Role of the tumour vasculature as a target for influencing response. *Acta Oncol. (Madr).* **45**, 876–880

347. Ljungkvist, A. S. E., Bussink, J., Kaanders, J. H. A. M., Wiedenmann, N. E., Vlasman, R., and van der Kogel, A. J. (2006) Dynamics of Hypoxia, Proliferation and Apoptosis after Irradiation in a Murine Tumor Model. *Radiat. Res.* **165**, 326–336

348. Maeda, A., Leung, M. K. K., Conroy, L., Chen, Y., Bu, J., Lindsay, P. E., Mintzberg, S., Virtanen, C., Tsao, J., Winegarden, N. A., Wang, Y., Morikawa, L., Vitkin, I. A., Jaffray, D. A., Hill, R. P., and DaCosta, R. S. (2012) In vivo optical imaging of tumor and microvascular response to ionizing radiation. *PLoS One* **7**, e42133

349. Moding, E. J., Clark, D. P., Qi, Y., Li, Y., Ma, Y., Ghaghada, K., Johnson, G. A., Kirsch, D. G., and Badea, C. T. (2013) Dual-energy micro-computed tomography imaging of radiation-induced vascular changes in primary mouse sarcomas. *Int J Radiat Oncol Biol Phys* **85**, 1353–1359

350. Potiron, V. A., Abderrahmani, R., Clément-Colmou, K., Marionneau-Lambot, S., Oullier, T., Paris, F., and Supiot, S. (2013) Improved Functionality of the Vasculature during Conventionally Fractionated Radiation Therapy of Prostate Cancer. *PLoS One* **8**, e84076

351. Horsman, M. R. and Siemann, D. W. (2006) Therapies the Implications for Combination with Conventional Pathophysiologic Effects of Vascular-Targeting Agents and Pathophysiologic Effects of Vascular-Targeting Agents and the Implications for Combination with Conventional Therapies. *Cancer ResCancer Res* **66**, 11520–11539

352. Moeller, B. J., Dreher, M. R., Rabbani, Z. N., Schroeder, T., Cao, Y., Li, C. Y., and Dewhirst, M. W. (2005) Pleiotropic effects of HIF-1 blockade on tumor radiosensitivity. *Cancer Cell* **8**, 99–110

353. Moeller, B. J., Cao, Y., Li, C. Y., and Dewhirst, M. W. (2004) Radiation activates HIF-1 to regulate vascular radiosensitivity in tumors: role of reoxygenation, free radicals, and stress granules. *Cancer Cell* **5**, 429–441

354. Maeda, A., Chen, Y., Bu, J., Mujcic, H., Wouters, B. G., and DaCosta, R. S. (2017) In Vivo Imaging Reveals Significant Tumor Vascular Dysfunction and Increased Tumor Hypoxia-Inducible Factor-1α Expression Induced by High Single-Dose Irradiation in a Pancreatic Tumor Model. *Int. J. Radiat. Oncol. Biol. Phys.* **97**, 184–194

355. Chen, F.-H., Chiang, C.-S., Wang, C.-C., Tsai, C.-S., Jung, S.-M., Lee, C.-C., McBride, W. H., and Hong, J.-H. (2009) Radiotherapy Decreases Vascular Density and Causes Hypoxia with Macrophage Aggregation in TRAMP-C1 Prostate Tumors. *Clin. Cancer Res.* **15**, 1721–1729

356. Torok, J. A., Oh, P., Castle, K. D., Reinsvold, M., Ma, Y., Luo, L., Lee, C. L., and Kirsch, D. G. (2019) Deletion of Atm in Tumor but not Endothelial Cells Improves Radiation Response in a Primary Mouse Model of Lung Adenocarcinoma. *Cancer Res* **79**, 773–782

357. Grabham, P., Hu, B., Sharma, P., and Geard, C. (2011) Effects of Ionizing Radiation on Three-Dimensional Human Vessel Models: Differential Effects According to Radiation Quality and Cellular Development. *Radiat. Res.* **175**, 21–28

358. Sonveaux, P., Brouet, A., Havaux, X., Grégoire, V., Dessy, C., Balligand, J. L., and Feron, O. (2003) Irradiation-induced angiogenesis through the up-regulation of the nitric oxide pathway: Implications for tumor radiotherapy. *Cancer Res.* **63**, 1012–1019

359. Yuan, F., Chen, Y., Dellian, M., Safabakhsh, N., Ferrara, N., and Jain, R. K. (1996) Time-dependent vascular regression and permeability changes in established human tumor xenografts induced by an anti-vascular endothelial growth factor/vascular permeability factor antibody. *Proc. Natl. Acad. Sci. U. S. A.* **93**, 14765–14770

360. Jain, R. K. (2005) Normalization of Tumor Vasculature: An Emerging Concept in Antiangiogenic Therapy. *Science (80-.).* **58**, 58–62

361. Lee, H. J., Yoon, C., Park, D. J., Kim, Y. J., Schmidt, B., Lee, Y. J., Tap, W. D., Eisinger-Mathason, T. S. S. K., Choy, E., Kirsch, D. G., Simon, M. C., and Yoon, S. S. (2015) Inhibition of vascular endothelial growth factor a and hypoxia-inducible factor 1α maximizes the effects of radiation in sarcoma mouse models through destruction of tumor vasculature. *Int. J. Radiat. Oncol. Biol. Phys.* **91**, 621–630

362. Bush, R. S., Jenkin, R. D., Allt, W. E., Beale, F. A., Bean, H., Dembo, A. J., and Pringle, J. F. (1978) Definitive evidence for hypoxic cells influencing cure in cancer therapy. *Br. J. Cancer. Suppl.* **3**, 302–306

363. Alupei, M. C., Licarete, E., Cristian, F. B., and Banciu, M. (2014) Cytotoxicity of lipophilic statins depends on their combined actions on HIF-1α expression and redox status in B16.F10 melanoma cells. *Anticancer. Drugs* **25**, 393–405

364. Licarete, E., Sesarman, A., Rauca, V. F., Luput, L., Patras, L., and Banciu, M. (2017) HIF-1α acts as a molecular target for simvastatin cytotoxicity in B16.F10 melanoma cells cultured under chemically induced hypoxia. *Oncol. Lett.* **13**, 3942–3950

365. Jakobsson, L., Franco, C. A., Bentley, K., Collins, R. T., Ponsioen, B., Aspalter, I. M., Rosewell, I., Busse, M., Thurston, G., Medvinsky, A., Schulte-Merker, S., and Gerhardt, H. (2010) Endothelial cells dynamically compete for the tip cell position during angiogenic sprouting. *Nat. Publ. Gr.* **12**

366. Mazzone, M., Dettori, D., Leite de Oliveira, R., Loges, S., Schmidt, T., Jonckx, B., Tian, Y. M., Lanahan, A. A., Pollard, P., Ruiz de Almodovar, C., De Smet, F., Vinckier, S., Aragonés, J., Debackere, K., Luttun, A., Wyns, S., Jordan, B., Pisacane, A., Gallez, B., Lampugnani, M. G., Dejana, E., Simons, M., Ratcliffe, P., Maxwell, P., and Carmeliet, P. (2009) Heterozygous Deficiency of PHD2 Restores Tumor Oxygenation and Inhibits Metastasis via Endothelial Normalization. *Cell* **136**, 839–851

367. Phng, L. K. and Gerhardt, H. (2009) Angiogenesis: A Team Effort Coordinated by Notch. *Dev. Cell* **16**, 196–208

368. Bergonié, J., Tribondeau, L., and Bergonie, J. (1959) Interpretation of Some Results of Radiotherapy and an Attempt at Determining a Logical Technique of Treatment. *Radiat. Res.* **11**, 587

369. Bernabeu, M. O., Köry, J., Grogan, J. A., Markelc, B., Ricol, A. B., D'Avezac, M., Kaeppler, J., Daly, N., Hetherington, J., Krüger, T., Maini, P. K., Pitt-Francis, J. M., Muschel, R. J., Alarcón, T., and Byrne, H. M. (2019) Abnormal morphology biases haematocrit distribution in tumour vasculature and contributes to heterogeneity in tissue oxygenation. *bioRxiv* 640060

370. Griffon-Etienne, G., Boucher, Y., Brekken, C., Suit, H. D., and Jain, R. K. (1999) Taxane-induced apoptosis decompresses blood vessels and lowers interstitial fluid pressure in solid tumors: Clinical implications. *Cancer Res.* **59**, 3776–3782

371. Winkler, F., Kozin, S. V, Tong, R. T., Chae, S. S., Booth, M. F., Garkavtsev, I., Xu, L., Hicklin, D. J., Fukumura, D., Di Tomaso, E., Munn, L. L., and Jain, R. K. (2004) Kinetics of vascular normalization by VEGFR2 blockade governs brain tumor response to radiation: Role of oxygenation, angiopoietin-1, and matrix metalloproteinases. *Cancer Cell* **6**, 553–563

372. Goel, S., Wong, A. H., and Jain, R. K. (2012) Vascular Normalization as a Therapeutic Strategy. *Cold Spring Harb Perspect Med* **2**, 1–24

373. Carmeliet, P. and Jain, R. K. (2011) Molecular mechanisms and clinical applications of

angiogenesis. *Nature* **473**, 298–307

374. Dimitrievich, G. S., Fischer-Dzoga, K., and Griem, M. L. (1984) Radiosensitivity of Vascular Tissue: I. Differential Radiosensitivity of Capillaries: A Quantitative in Vivo Study. *Radiat. Res.* **99**, 511

375. Bouchet, A., Serduc, R., Laissue, J. A., and Djonov, V. (2015) Effects of microbeam radiation therapy on normal and tumoral blood vessels. *Phys. Medica* **31**, 634–641

376. Mendonca, M. S., Chin-Sinex, H., Dhaemers, R., Mead, L. E., Yoder, M. C., and Ingram, D. A. (2011) Differential mechanisms of x-ray-induced cell death in human endothelial progenitor cells isolated from cord blood and adults. *Radiat. Res.* **176**, 208–216

377. Dulić, V., Kaufmann, W. K., Wilson, S. J., Tisty, T. D., Lees, E., Harper, J. W., Elledge, S. J., and Reed, S. I. (1994) p53-dependent inhibition of cyclin-dependent kinase activities in human fibroblasts during radiation-induced G1 arrest. *Cell* **76**, 1013–1023

378. Brugarolas, J., Chandrasekaran, C., Gordon, J. I., Beach, D., Jacks, T., and Hannon, G. J. (1995) Radiation-induced cell cycle arrest compromised by p21 deficiency. *Nature* **377**, 552–557

379. Canman, C. E., Lim, D. S., Cimprich, K. A., Taya, Y., Tamai, K., Sakaguchi, K., Appella, E., Kastan, M. B., and Siliciano, J. D. (1998) Activation of the ATM Kinase by Ionizing Radiation and Phosphorylation of p53. *Science (80-.).* **281**, 1677–1679

380. Banin, S., Moyal, L., Shieh, S., Taya, Y., Anderson, C. W., Chessa, L., Smorodinsky, N. I., Prives, C., Reiss, Y., Shiloh, Y., and Ziv, Y. (1998) Enhanced Phosphorylation of p53 by ATM in Response to DNA Damage. *Science (80-.).* **281**, 1674–1677

381. Pfeiffer, P., Goedecke, W., and Obe, G. (2000) Mechanisms of DNA double-strand break repair and their potential to induce chromosomal aberrations. *Mutagenesis* **15**, 289–302

382. Fornace, A. J. and Little, J. B. (1977) DNA crosslinking induced by X-rays and chemical agents. *BBA Sect. Nucleic Acids Protein Synth.* **477**, 343–355

383. Liang, L., Deng, L., Chen, Y., Li, G. C., Shao, C., and Tischfield, J. A. (2005) Modulation of DNA end joining by nuclear proteins. *J. Biol. Chem.* **280**, 31442–31449

384. Moore, J. K. and Haber, J. E. (1996) Cell cycle and genetic requirements of two pathways of nonhomologous end-joining repair of double-strand breaks in Saccharomyces cerevisiae. *Mol. Cell. Biol.* **16**, 2164–2173

385. Kerr, J. F. R., Wyllie, A. H., and Currie, A. R. (1972) Apoptosis: A Basic Biological Phenomenon with Wideranging Implications in Tissue Kinetics. *Br. J. Cancer* **26**, 239–257

386. Elmore, S. (2007) Apoptosis: A Review of Programmed Cell Death. *Toxicol. Pathol.* **35**, 495

387. Najafov, A., Chen, H., and Yuan, J. (2017) Necroptosis and Cancer. *Trends in cancer* **3**, 294–301

388. Venkatesulu, B. P., Mahadevan, L. S., Aliru, M. L., Yang, X., Bodd, M. H., Singh, P. K., Yusuf, S. W., Abe, J. I., and Krishnan, S. (2018) Radiation-Induced Endothelial Vascular Injury: A Review of Possible Mechanisms. *JACC Basic Transl Sci* **3**, 563–572

389. Mallat, Z. and Tedgui, A. (2000) Apoptosis in the vasculature: mechanisms and functional importance. *Br. J. Pharmacol.* **130**, 947

390. Vakifahmetoglu, H., Olsson, M., and Zhivotovsky, B. (2008) Death through a tragedy: Mitotic catastrophe. *Cell Death Differ.* **15**, 1153–1162

391. Truman, J.-P., García-Barros, M., Kaag, M., Hambardzumyan, D., Stancevic, B., Chan, M., Fuks, Z., Kolesnick, R., and Haimovitz-Friedman, A. (2010) Endothelial Membrane Remodeling Is Obligate for Anti-Angiogenic Radiosensitization during Tumor Radiosurgery. *PLoS One* **5**, e12310

392. Bodo, S., Campagne, C., Thin, T. H., Higginson, D. S., Vargas, H. A., Hua, G., Fuller, J. D., Ackerstaff, E., Russell, J., Zhang, Z., Klingler, S., Cho, H., Kaag, M. G., Mazaheri, Y., Rimner, A., Manova-Todorova, K., Epel, B., Zatcky, J., Cleary, C. R., Rao, S. S., Yamada, Y., Zelefsky, M. J., Halpern, H. J., Koutcher, J. A., Cordon-Cardo, C., Greco, C., Haimovitz-Friedman, A., Sala, E., Powell, S. N., Kolesnick, R., and Fuks, Z. (2019) Single-dose radiotherapy disables tumor cell homologous recombination via ischemia/reperfusion injury. *J. Clin. Invest.* **129**, 786–801

393. Coppé, J.-P., Desprez, P.-Y., Krtolica, A., and Campisi, J. (2010) The Senescence-Associated Secretory Phenotype: The Dark Side of Tumor Suppression. *Annu. Rev. Pathol. Mech. Dis.* **5**, 99–118

394. Hallahan, D., Clark, E. T., Kuchibhotla, J., Gewertz, B. L., and Collins, T. (1995) E-selectin gene induction by ionizing radiation is independent of cytokine induction. *Biochem. Biophys. Res. Commun.* **217**, 784–795

395. Prabhakarpandian, B., Goetz, D. J., Swerlick, R. A., Chen, X., and Kiani, M. F. (2001) Expression and functional significance of adhesion molecules on cultured endothelial cells in response to ionizing radiation. *Microcirculation* **8**, 355–364

396. Mollà, M., Gironella, M., Salas, A., Closa, D., Biete, A., Gimeno, M., Coronel, P., Piqué, J. M., and Panés, J. (2005) Protective effect of superoxide dismutase in radiation-induced intestinal inflammation. *Int. J. Radiat. Oncol.* **61**, 1159–1166

397. Turer, A. T. and Hill, J. A. (2010) Pathogenesis of Myocardial Ischemia-Reperfusion Injury and Rationale for Therapy. *Am. J. Cardiol.* **106**, 360–368

398. Randi, A. M., Sperone, A., Dryden, N. H., and Birdsey, G. M. (2009) Regulation of angiogenesis by ETS transcription factors. *Biochem. Soc. Trans.* **37**, 1248–1253

399. Birdsey, G. M., Shah, A. V., Dufton, N., Reynolds, L. E., Almagro, L. O., Yang, Y., Aspalter, I. M., Khan, S. T., Mason, J. C., Dejana, E., G??ttgens, B., Hodivala-Dilke, K., Gerhardt, H., Adams, R. H., and Randi, A. M. (2015) The endothelial transcription factor erg promotes vascular stability and growth through Wnt/beta-catenin signaling. *Dev. Cell* **32**, 82–96

400. Shah, A. V, Birdsey, G. M., Peghaire, C., Pitulescu, M. E., Dufton, N. P., Yang, Y., Weinberg, I., Almagro, L. O., Payne, L., Mason, J. C., Gerhardt, H., Adams, R. H., and Randi, A. M. (2017) The endothelial transcription factor ERG mediates. *Nat. Commun.* **8**, 1–16

401. Strasser, G. A., Kaminker, J. S., and Tessier-Lavigne, M. (2010) Microarray analysis of retinal endothelial tip cells identifies CXCR4 as a mediator of tip cell morphology and branching. *Blood* **115**, 5102–5110

402. Nielsen, S. R., Hammer, T., Gibson, J., Pepper, M. S., Nisato, R. E., Dissing, S., and Tritsaris, K. (2013) IL-27 Inhibits Lymphatic Endothelial Cell Proliferation by STAT1-Regulated Gene Expression. *Microcirculation* **20**, 555–564

403. Mao, X. W. (2006) A quantitative study of the effects of ionizing radiation on endothelial

cells and capillary-like network formation. *Technol. Cancer Res. Treat.* **5**, 127–134

404. Dovedi, S. J., Cheadle, E. J., Popple, A. L., Poon, E., Morrow, M., Stewart, R., Yusko, E. C., Sanders, C. M., Vignali, M., Emerson, R. O., Robins, H. S., Wilkinson, R. W., Honeychurch, J., and Illidge, T. M. (2017) Fractionated radiation therapy stimulates antitumor immunity mediated by both resident and infiltrating polyclonal T-cell populations when combined with PD-1 blockade. *Clin. Cancer Res.* **23**, 5514–5526

405. Twyman-Saint Victor, C., Rech, A. J., Maity, A., Rengan, R., Pauken, K. E., Stelekati, E., Benci, J. L., Xu, B., Dada, H., Odorizzi, P. M., Herati, R. S., Mansfield, K. D., Patsch, D., Amaravadi, R. K., Schuchter, L. M., Ishwaran, H., Mick, R., Pryma, D. A., Xu, X., Feldman, M. D., Gangadhar, T. C., Hahn, S. M., Wherry, E. J., Vonderheide, R. H., and Minn, A. J. (2015) Radiation and dual checkpoint blockade activate non-redundant immune mechanisms in cancer. *Nature* **520**, 373–377

406. Suit, H. D., Willers, H., Brown, M., Bristow, R., Glazer, P., Hill, R., McBride, W., McKenna, G., and Muschel, R. (2003) Comment on "Tumor Response to Radiotherapy Regulated by Endothelial Cell Apoptosis" (II). *Science (80-.).* **302**, 1894c – 1894

407. Budach, W., Freeman, J., and Suit, H. D. (1993) Impact of Stromal Sensitivity. **85**, 988–993

408. Gerweck, L. E., Vijayappa, S., Kurimasa, A., Ogawa, K., and Chen, D. J. (2006) Tumor Cell Radiosensitivity Is a Major Determinant of Tumor Response to Radiation. *Cancer Res.* **66**, 8352–8355

409. Hallahan, D., Kuchibhotla, J., and Wyble, C. (1996) Cell adhesion molecules mediate radiation-induced leukocyte adhesion to the vascular endothelium. *Cancer Res.* **56**, 5150–5155

410. Strom, T., Harrison, L. B., Giuliano, A. R., Schell, M. J., Eschrich, S. A., Berglund, A., Fulp, W., Thapa, R., Coppola, D., Kim, S., Frakes, J., Foekens, J., Mulé, J. J., and Torres-Roca, J. F. (2017) Tumour radiosensitivity is associated with immune activation in solid tumours. *Eur. J. Cancer* **84**, 304–314

411. Hallahan, D. E. and Virudachalam, S. (1997) Ionizing radiation mediates expression of cell adhesion molecules in distinct histological patterns within the lung. *Cancer Res.* **57**, 2096–2099

412. Deng, L., Liang, H., Fu, S., Weichselbaum, R. R., and Fu, Y.-X. (2016) From DNA Damage to Nucleic Acid Sensing: A Strategy to Enhance Radiation Therapy. *Clin. Cancer Res.* **22**, 20–25

413. Formenti, S. C., Rudqvist, N.-P., Golden, E., Cooper, B., Wennerberg, E., Lhuillier, C., Vanpouille-Box, C., Friedman, K., Ferrari de Andrade, L., Wucherpfennig, K. W., Heguy, A., Imai, N., Gnjatic, S., Emerson, R. O., Zhou, X. K., Zhang, T., Chachoua, A., and Demaria, S. (2018) Radiotherapy induces responses of lung cancer to CTLA-4 blockade. *Nat. Med.* **24**, 1845–1851

414. Fontanella, A. N., Boss, M.-K., Hadsell, M., Zhang, J., Schroeder, T., Berman, K. G., Dewhirst, M. W., Chang, S., and Palmer, G. M. (2015) Effects of High-Dose Microbeam Irradiation on Tumor Microvascular Function and Angiogenesis. *Radiat. Res.* **183**, 147

415. Siemann, D. W. and Horsman, M. R. (2015) Modulation of the tumor vasculature and oxygenation to improve therapy. *Pharmacol. Ther.* **153**, 107–124

416. Looney, M. R., Thornton, E. E., Sen, D., Lamm, W. J., Glenny, R. W., and Krummel, M. F. (2011) Stabilized imaging of immune surveillance in the mouse lung. *Nat. Methods* **8**, 91–96

417. Kedrin, D., Gligorijevic, B., Wyckoff, J., Verkhusha, V. V, Condeelis, J., Segall, J. E., and van Rheenen, J. (2008) Intravital imaging of metastatic behavior through a mammary imaging window. *Nat. Methods* **5**, 1019–1021

APPENDIX

Supplementary Figures and Tables

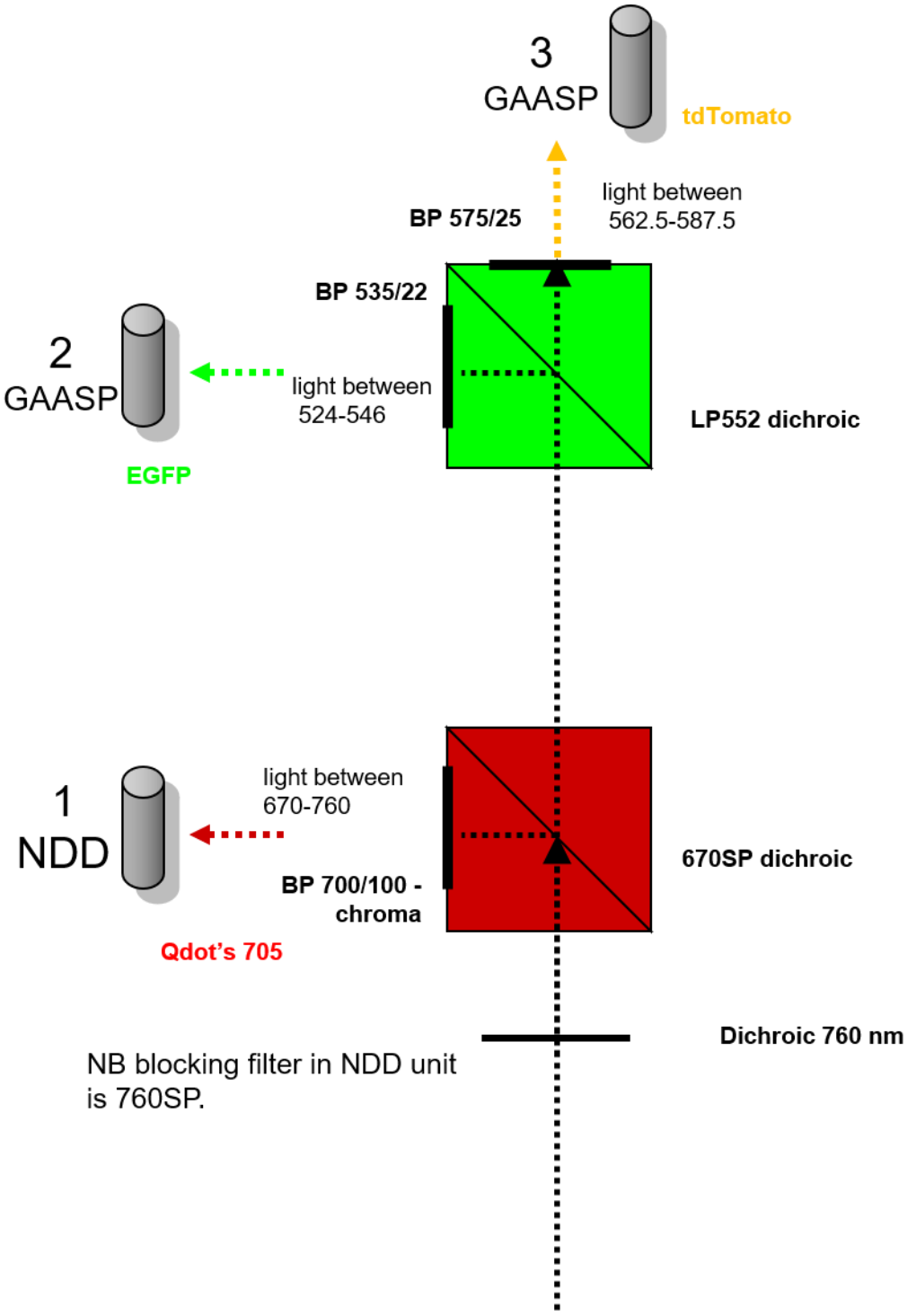


Figure S2 Filter and filter set arrangement of the two-photon microscope. Collected light passes through a dichroic 760 shortpass filter. Remaining light is then split with a 670 shortpass dichroic splitter into longer and shorter wavelengths than 670 nm. Longer wavelengths are filtered by a chroma bandpass 700/100 filter to collect light with a NDD detector between 650 and 750 (qdots705). Shorter wavelengths proceed to the next filter cube where light longer than 552 nm is passed through and collected with a GaAsp detector with a 535/22 bandpass filter in front, while shorter wavelengths of light are reflected and collected by a second GaASP detector with a 535/22 bandpass filter in front.

Table S2.1.1
Nuclei [Algorithm]
Enable Region Of Interest = false
Enable Region Growing = true
Enable Tracking = false
Enable Shortest Distance = false
[Source Channel]
Source Channel Index = 1
Enable Smooth = true
Surface Grain Size = 0.800 um
Enable Eliminate Background = true
Diameter Of Largest Sphere = 8.00 um
[Threshold]
Enable Automatic Threshold = false
Manual Threshold Value = 10
Active Threshold = true
Enable Automatic Threshold B = true
Manual Threshold Value B = 2704.97
Active Threshold B = false
Region Growing Estimated Diameter = 5.00 um
[Classify Seed Points]
"Quality" above 10.0
[Classify Surfaces]
"Number of Voxels Img=1" above 10.0
"Intensity Center Ch=5" above 30.0

Table S2.1.2
EdU [Algorithm]
Enable Region Of Interest = false
Enable Region Growing = true
Enable Tracking = false
Enable Shortest Distance = false
[Source Channel]
Source Channel Index = 4
Enable Smooth = true
Surface Grain Size = 0.800 um
Enable Eliminate Background = true
Diameter Of Largest Sphere = 8.00 um
[Threshold]
Enable Automatic Threshold = false
Manual Threshold Value = 200
Active Threshold = true
Enable Automatic Threshold B = true
Manual Threshold Value B = 3407.45
Active Threshold B = false
Region Growing Estimated Diameter = 6.00 um
[Classify Seed Points]
"Quality" above 150
[Classify Surfaces]
"Number of Voxels Img=1" above 100
"Intensity Center Ch=5 Img=1" above 30.0

Table S2.1.3
CD31 [Algorithm]
Enable Region Of Interest = false
Enable Region Growing = false
Enable Tracking = false
Enable Shortest Distance = false
[Source Channel]
Source Channel Index = 3
Enable Smooth = true
Surface Grain Size = 2.00 um
Enable Eliminate Background = true
Diameter Of Largest Sphere = 10.0 um
[Threshold]
Enable Automatic Threshold = false
Manual Threshold Value = 150
Active Threshold = true
Enable Automatic Threshold B = true
Manual Threshold Value B = 2489.11
Active Threshold B = false
[Classify Surfaces]
"Number of Voxels Img=1" above 25.0
"Intensity Center Ch=5 Img=1" above 30.0

Table S2.1.4
ERG [Algorithm]
Enable Region Of Interest = false
Enable Region Growing = true
Enable Tracking = false
Enable Shortest Distance = false
[Source Channel]
Source Channel Index = 2
Enable Smooth = true
Surface Grain Size = 0.800 um
Enable Eliminate Background = true
Diameter Of Largest Sphere = 8.00 um
[Threshold]
Enable Automatic Threshold = false
Manual Threshold Value = 300
Active Threshold = true
Enable Automatic Threshold B = true
Manual Threshold Value B = 2480.42
Active Threshold B = false
Region Growing Estimated Diameter = 6.00 um
[Classify Seed Points]
"Quality" above 100
[Classify Surfaces]
"Number of Voxels Img=1" above 5.00
"Intensity Center Ch=6 Img=1" between 0.00 and 2.00
"Intensity Center Ch=5 Img=1" above 30.0

Table S2.1.5
EC nuclei [Algorithm]
Enable Region Of Interest = false
Enable Region Growing = true
Enable Tracking = false
Enable Shortest Distance = false
[Source Channel]
Source Channel Index = 2
Enable Smooth = true
Surface Grain Size = 0.800 um
Enable Eliminate Background = true
Diameter Of Largest Sphere = 8.00 um
[Threshold]
Enable Automatic Threshold = false
Manual Threshold Value = 300
Active Threshold = true
Enable Automatic Threshold B = true
Manual Threshold Value B = 3407.45
Active Threshold B = false
Region Growing Estimated Diameter = 6.00 um
[Classify Seed Points]
"Quality" above 100
[Classify Surfaces]
"Number of Voxels Img=1" above 5.00
"Intensity Center Ch=5 Img=1" above 30.0
"Intensity Center Ch=6 Img=1" between 0.00 and 2.50

Table S2.2.1
EF5 [Algorithm]
Enable Region Of Interest = false
Enable Region Growing = false
Enable Tracking = false
Enable Shortest Distance = false
[Source Channel]
Source Channel Index = 3
Enable Smooth = true
Surface Grain Size = 1.30 um
Enable Eliminate Background = false
Diameter Of Largest Sphere = 4.88 um
[Threshold]
Enable Automatic Threshold = false
Manual Threshold Value = 176.373
Active Threshold = true
Enable Automatic Threshold B = true
Manual Threshold Value B = 1300.75
Active Threshold B = false
[Classify Surfaces]
"Number of Voxels" above 400
"Intensity Center Ch=5" above 30.0

Table S2.3.1
Vessels [Algorithm]
Enable Region Of Interest = false
Enable Region Growing = false
Enable Tracking = false
Enable Shortest Distance = false
[Source Channel]
Source Channel Index = 3
Enable Smooth = true
Surface Grain Size = 2.00 um
Enable Eliminate Background = true
Diameter Of Largest Sphere = 10.0 um
[Threshold]
Enable Automatic Threshold = false
Manual Threshold Value = 150
Active Threshold = true
Enable Automatic Threshold B = true
Manual Threshold Value B = 2500
Active Threshold B = false
[Classify Surfaces]
"Number of Voxels Img=1" above 25.0
"Intensity Center Ch=4 Img=1" above 30.0

Table S.2.3.2
Ng2 on vessels [Algorithm]
Enable Region Of Interest = false
Enable Region Growing = false
Enable Tracking = false
Enable Shortest Distance = false
[Source Channel]
Source Channel Index = 5
Enable Smooth = true
Surface Grain Size = 1.00 um
Enable Eliminate Background = true
Diameter Of Largest Sphere = 10.0 um
[Threshold]
Enable Automatic Threshold = false
Manual Threshold Value = 350
Active Threshold = true
Enable Automatic Threshold B = true
Manual Threshold Value B = 3229.15
Active Threshold B = false
[Classify Surfaces]
"Number of Voxels" above 5.00

Table S.2.4.1
small vessels [Algorithm]
Enable Region Of Interest = false
Enable Region Growing = false
Enable Tracking = false
Enable Shortest Distance = false
[Source Channel]
Source Channel Index = 3
Enable Smooth = true
Surface Grain Size = 1.00 um
Enable Eliminate Background = true
Diameter Of Largest Sphere = 50.0 um
[Threshold]
Enable Automatic Threshold = false
Manual Threshold Value = 200
Active Threshold = true
Enable Automatic Threshold B = true
Manual Threshold Value B = 3838.9
Active Threshold B = false
[Classify Surfaces]
"Number of Voxels Img=1" between 5.00 and 1500
"Intensity Center Ch=4 Img=1" above 30.0

Table S.2.4.2
medium vessels [Algorithm]
Enable Region Of Interest = false
Enable Region Growing = false
Enable Tracking = false
Enable Shortest Distance = false
[Source Channel]
Source Channel Index = 3
Enable Smooth = true
Surface Grain Size = 1.00 um
Enable Eliminate Background = true
Diameter Of Largest Sphere = 50.0 um
[Threshold]
Enable Automatic Threshold = false
Manual Threshold Value = 200
Active Threshold = true
Enable Automatic Threshold B = true
Manual Threshold Value B = 3838.9
Active Threshold B = false
[Classify Surfaces]
"Number of Voxels Img=1" between 1500 and 3000
"Intensity Center Ch=4 Img=1" above 30.0

Table S.2.4.3
Large vessel [Algorithm]
Enable Region Of Interest = false
Enable Region Growing = false
Enable Tracking = false
Enable Shortest Distance = false
[Source Channel]
Source Channel Index = 3
Enable Smooth = true
Surface Grain Size = 1.00 um
Enable Eliminate Background = true
Diameter Of Largest Sphere = 50.0 um
[Threshold]
Enable Automatic Threshold = false
Manual Threshold Value = 200
Active Threshold = true
Enable Automatic Threshold B = true
Manual Threshold Value B = 3838.9
Active Threshold B = false
[Classify Surfaces]
"Number of Voxels Img=1" above 3000
"Intensity Center Ch=4 Img=1" above 30.0

Table S2.4.4
Cleaved caspase 3/7 on vessels [Algorithm]
Enable Region Of Interest = false
Enable Region Growing = false
Enable Tracking = false
Enable Shortest Distance = false
[Source Channel]
Source Channel Index = 2
Enable Smooth = true
Surface Grain Size = 1.00 um
Enable Eliminate Background = true
Diameter Of Largest Sphere = 10.0 um
[Threshold]
Enable Automatic Threshold = false
Manual Threshold Value = 300
Active Threshold = true
Enable Automatic Threshold B = true
Manual Threshold Value B = 3002.61
Active Threshold B = false
[Classify Surfaces]
"Number of Voxels Img=1" above 5.00
"Intensity Center Ch=4 Img=1" above 30.0
"Intensity Center Ch=10 Img=1" between 0.00 and 1.00

Table S2.5.1
vessel surface [Algorithm]
Enable Region Of Interest = false
Enable Region Growing = false
Enable Tracking = false
Enable Shortest Distance = false
[Source Channel]
Source Channel Index = 3
Enable Smooth = true
Surface Grain Size = 2.00 um
Enable Eliminate Background = true
Diameter Of Largest Sphere = 30.0 um
[Threshold]
Enable Automatic Threshold = false
Manual Threshold Value = 2000
Active Threshold = true
Enable Automatic Threshold B = true
Manual Threshold Value B = 57631.8
Active Threshold B = false
[Classify Surfaces]
"Number of Voxels Img=1" above 500

Table S.2.5.2
Filament vessel tracer [Algorithm]
Name = Threshold (loops)
Track (over time) = false
[Preprocessing]
Channel Index = 4
Enable Preprocessing = false
Approximate Diameter = 8.00 um
Preserve Edges = false
[Segmentation]
Fill Cavities = true
Connected BaseLine = true
Threshold Low = 1500.000
Threshold High = 1600.000
[Graph Compilation]
Branch Length Ratio = 3.000
Find Dendrite Beginning Point = false
[Finish]
Build all Time Points = true
Delete Working Channel = true

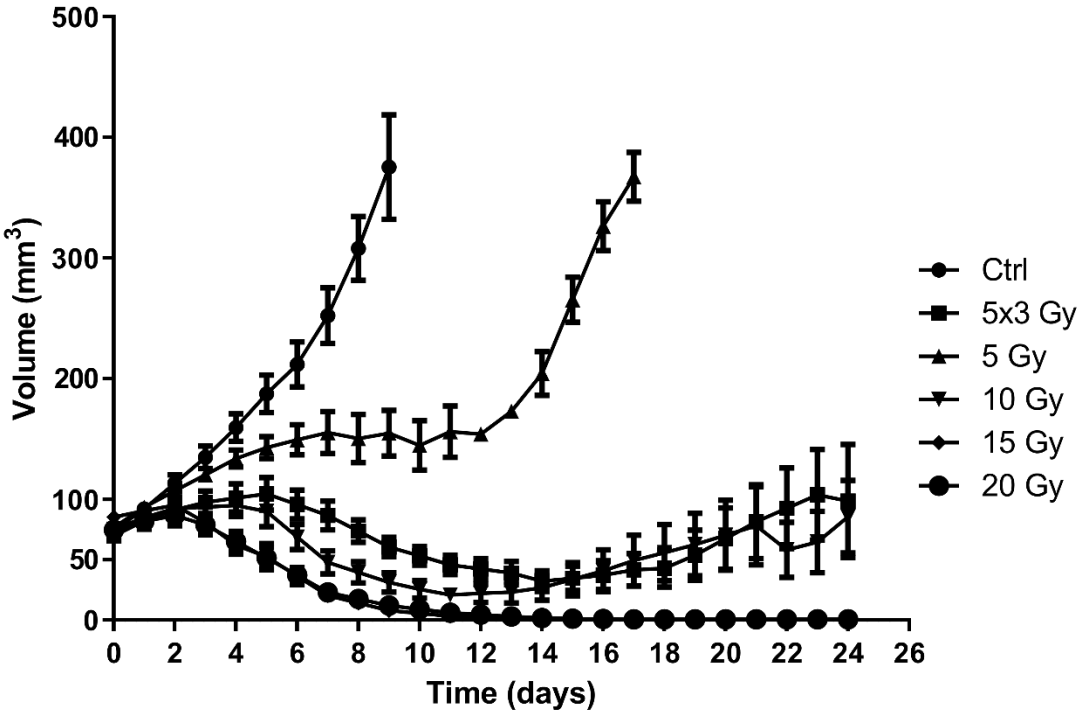


Figure S4.1 Tumour growth and response to irradiation. Subcutaneous MC38 tumour growth in C57BL/6 mice show dose-dependent respond to ionising radiation. Tumours were separated subgroups receiving 0 Gy, 5 Gy, 5 times 3 Gy, 10 Gy, 15 Gy or 20 Gy irradiation. Tumour growth was followed over 24 days. N= 10 mice per group. Error bars ± SEM.

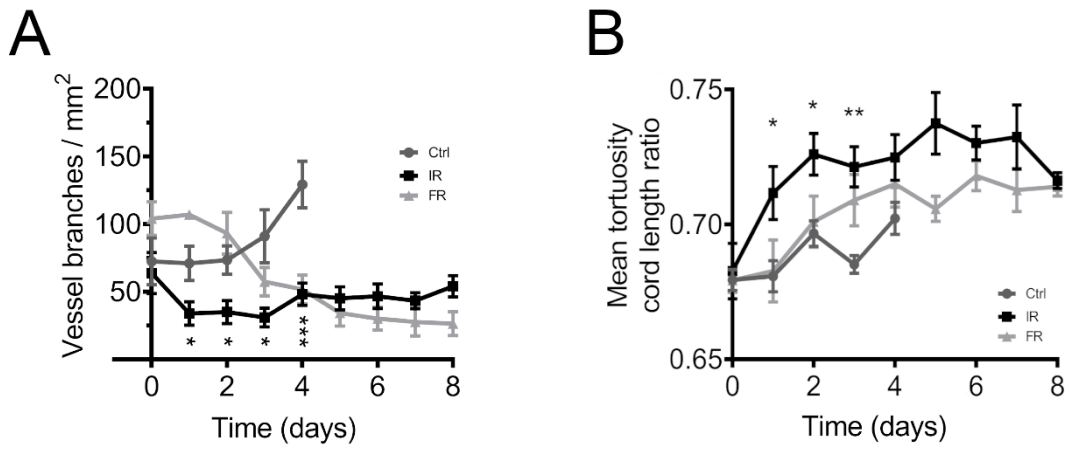


Figure S4.2. Quantified parameters from intravital imaging and DCE-MRI imaging of MC38 tumours.

(A) and (B) non-normalised MC38 tumour vascular parameters of vessel branch density and tortuosity Error bars represent mean ± SEM, *P <0.05, **P <0.01 by analysis of variance (one-way ANOVA) with multiple comparison.

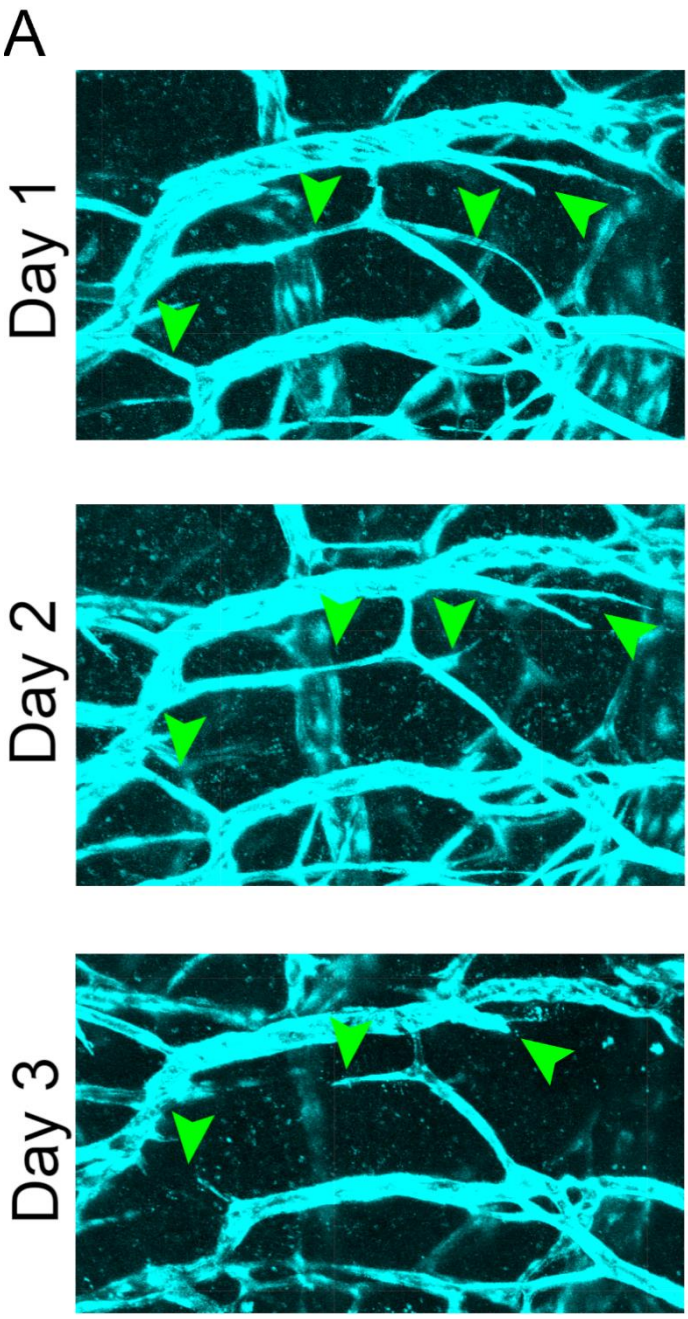


Figure S4.3A Time-lapse intravital microscopy of a B16F10 tumour in VEOM mice after irradiation. The developing B16F10 tumour vasculature was imaged in an abdominal window chamber model with two-photon microscopy after irradiation at the indicated time points. 15 Gy single dose irradiated B16F10 tumours. Vasculature (cyan) is visible with small vessels undergo destruction or pruning (green arrows).

Table S5.1 Differential gene expression of ceramide associated genes in tumour endothelilal cells 48 hours after 15 Gy irradiation

p-value	Fold-change	ENSEMBL gene ID	Gene name
Cermide associated genes			
4.92E-06	0.571588525	ENSMUSG00000028978	Nos3
0.005442	0.927414036	ENSMUSG00000020826	Nos2
	not detected		Cers1
2.22E-16	0.430810145	ENSMUSG00000028381	Ugcg
	not detected		Nos1
0.991507	-0.407836485	ENSMUSG00000032487	Ptgs2
2.22E-16	-0.572991642	ENSMUSG00000025747	Tyms
0.00017	-0.402241061	ENSMUSG00000037049	Smpd1
0.996049	-0.618823347	ENSMUSG00000057177	Gsk3a
0.738415	0.040643556	ENSMUSG00000024401	Tnf
2.22E-16	0.662907614	ENSMUSG00000023021	Cers5
6.15E-07	0.384178259	ENSMUSG00000031591	Asah1
0.023714	-0.033329068	ENSMUSG00000025153	Fasn
6.15E-07	0.811827219	ENSMUSG00000008206	Cers4
0.050336	0.095489656	ENSMUSG00000015714	Cers2
0.995135	-0.591389036	ENSMUSG00000027035	Cers6
2.22E-16	-0.532946633	ENSMUSG00000040451	Sgms1
0.998747	-0.623674338	ENSMUSG00000050931	Sgms2

Table S5.2 Differential gene expression of damage-associated molecular pattern, cytokines and stat pathway in tumour endothelial cells 48 hours after 15 Gy irradiation

p-value	Fold-change	ENSEMBL gene ID	Gene name
Damage-associated molecular pattern			
2.22E-16	1.397224143	ENSMUSG00000024260	Sap130
2.22E-16	1.287418538	ENSMUSG00000031375	Bgn
0.521879	1.404475175	ENSMUSG00000021614	Vcan
0.006737	0.782710603	ENSMUSG00000028763	Hspg2
1.23E-06	0.378272009	ENSMUSG00000026193	Fn1
2.22E-16	1.087622547	ENSMUSG00000028364	Tnc
4.31E-06	1.928350798	ENSMUSG00000040928	S100pbp
0.006737	0.782710603	ENSMUSG00000028763	Hspg2
2.22E-16	0.923702603	ENSMUSG00000091971	Hspa1a
0.003817	0.925438948	ENSMUSG00000025757	Hspa4l
2.22E-16	1.09790553	ENSMUSG00000041548	Hspb8
0.056692	0.746673554	ENSMUSG00000090877	Hspa1b
2.22E-16	0.734335631	ENSMUSG00000004951	Hspb1
2.22E-16	1.981082133	ENSMUSG00000027995	Tlr2
2.22E-16	1.237404414	ENSMUSG00000031639	Tlr3
2.22E-16	3.612750234	ENSMUSG00000037860	Aim2
0.998899	0.989783453	ENSMUSG00000040249	Lrp1
proinflamatory cytokines			
2.22E-16	1.624348711	ENSMUSG00000035385	Ccl2
2.22E-16	0.995889002	ENSMUSG00000025746	Il6
0.132964	1.6693608	ENSMUSG00000027947	Il6ra
Stat pathway related proteins			
2.22E-16	1.209446445	ENSMUSG00000040033	Stat2
0.045608	1.204943741	ENSMUSG00000002147	Stat6
2.22E-16	0.950148531	ENSMUSG00000026104	Stat1
0.904	0.826409825	ENSMUSG00000004043	Stat5a
0.000557	0.643785078	ENSMUSG00000020919	Stat5b
2.22E-16	0.630293469	ENSMUSG00000004040	Stat3
2.22E-16	0.883262053	ENSMUSG00000034855	Cxcl10
2.22E-16	1.894857448	ENSMUSG00000060183	Cxcl11
2.22E-16	4.4923575	ENSMUSG00000044701	Il27